

APPLICATION AND DEVELOPMENT OF HIGH-DENSITY FUNCTIONAL NEAR INFRARED SPECTROSCOPY FOR TRAUMATIC BRAIN INJURY

by

MICHAEL CLANCY

A thesis submitted to
The University of Birmingham
for the degree of
DOCTOR OF PHILOSOPHY

PSIBS Doctoral Training Centre
College of Engineering and Physical Sciences
The University of Birmingham
March 2017

UNIVERSITY OF
BIRMINGHAM

University of Birmingham Research Archive

e-theses repository

This unpublished thesis/dissertation is copyright of the author and/or third parties. The intellectual property rights of the author or third parties in respect of this work are as defined by The Copyright Designs and Patents Act 1988 or as modified by any successor legislation.

Any use made of information contained in this thesis/dissertation must be in accordance with that legislation and must be properly acknowledged. Further distribution or reproduction in any format is prohibited without the permission of the copyright holder.

Abstract

Functional near infrared spectroscopy (fNIRS) is a non-ionising, non-invasive, portable and relatively inexpensive method of measuring cerebral oxygen saturation. It has been suggested as a monitoring modality for patients with traumatic brain injury (TBI) in order to guide therapy in both the emergency and clinical settings. Despite its potential for use in TBI, current literature describes it as a 'work in progress' and is currently not suitable as a standalone technique to replace x-ray computerised tomography or invasive intracranial pressure monitors, due to uncertainty in signal origins (superficial contamination).

This thesis examined the viability of existing fNIRS devices, Atlas-based reconstruction algorithms, and a prototype, high-density near infrared spectroscopy probe, for quantitative assessment of TBI, which is investigated and presented.

Healthy volunteer investigations and simulations with existing fNIRS devices confirmed the ability for the imaging modality to measure relative changes in cerebral oxygen saturation in the presence of signal contamination from superficial tissues such as skin and bone. However, these superficial signals confounded the quantitative accuracy of the cerebral saturation data and therefore confirmed that fNIRS devices, in their current form, are insufficient to be used for monitoring TBI in isolation.

Simulations using a high-density fNIRS probe, providing a 3-wavelength, 168 channel measurement set over a 18 cm^2 region of interest (ROI), and a 4-point registered Atlas model (ICBM152) for accurate spatial prior information, was sufficient to recover cerebral saturation values with greater quantitative accuracy than standard fNIRS devices; mapping the simulated values to within $10 \pm 2\%$.

This concept was extended to healthy volunteer studies, using a high-density probe at 2-wavelengths and 96 channels, over a 16 cm² ROI. Results showed that although there was a clear improvement in terms of the magnitude of recovered saturation changes, the quantitative accuracy of the recovered parameters was still not sufficient to progress fNIRS into the clinic at this stage. The source of the limitations in quantitative accuracy is suggested to be due to tissue thickness mismatches between the subject and the Atlas model used, as well as the choice of scattering parameters in the reconstruction model.

A prototype version of the 3-wavelength, 196 channel high-density probe, controlled by an Arduino Due, was constructed for less than £300, and was capable of data collection at 1.3 Hz. The probe was shown to be able to track qualitative changes in oxygen saturation in both arm cuff occlusion and *Valsalva Manoeuvre* studies. The cost and portability of the probe make it an attractive option for large scale monitoring of TBI patients.

Acknowledgements

There are many people I would like to thank in relation to their input into this project. Without their guidance and support this project would not have been possible.

Firstly I would like to thank my lead supervisor Dr Hamid Dehghani. Hamid's support and guidance have been invaluable, without his knowledge and driven approach to research I would not be where I am today! Dr Samuel Lucas has also been a superb supervisor, as well as being an exceptional academic, his enthusiasm always made long lab sessions bearable! I would also like to thank Prof. Antonio Belli for driving the clinical aspect of my work and also for providing the finest collaborator I could have asked for, Mr David Davies. Over the course of this project Dave has been a constant source of inspiration, motivation and clinical expertise.

I would also like to thank my collaborators from the Institute of Biomedical Engineering and Biocybernetics in Warsaw, Poland. Not only did they provide us with the equipment to test our reconstruction algorithms, they were also willing volunteers to participate in the study! In particular I would like to thank Prof Adam Liebert, Dr Piotr Sawosz and Dr Stanislaw Wojtkiewicz.

For valuable teaching and support when I first started this project a special thanks must go to Dr Jamie Guggenheim and Dr Xue Wu who gave me the introduction to NIRFAST and the Atlas models on which my research was built. Also the knowledge and support I have received from my time in the PSIBS doctoral training centre, from both lecturers and course mates, has been exceptional. Again special thanks must go to Chris Stepanek, Hayley Floyd, Emily Guggenheim and Shelley Taylor for being there with motivation and entertainment during difficult times and also to Prof. Mike Hannon,

Dr Iain Styles and Hamid for running the centre so well.

One final acknowledgement goes to my family, especially my mum who has always been there to correct my grammatical mistakes!

Financially, this work was supported by engineering and physical sciences research council (EPSRC) grant EP/F50053X/1 (funding the PSIBS Doctoral Training Centre).

Publications arising from this work

Journal Publications

A review of the current uses of near-infrared in the field of traumatic brain injury was published in the Journal of Neurotrauma and formed the basis for this research.

Davies DJ, Su Z, Clancy MT, Lucas SJ, Dehghani H, Logan A, Belli A. Near-infrared spectroscopy in the monitoring of adult traumatic brain injury: a review. Journal of neurotrauma. 2015 Jul 1;32(13):933-41.

The simulation studies of the Atlas-based reconstruction method covered in Chapter 5 was published in the Journal of Biophotonics.

Clancy M, Belli A, Davies D, Lucas SJ, Su Z, Dehghani H. Improving the quantitative accuracy of cerebral oxygen saturation in monitoring the injured brain using Atlas-based Near Infrared Spectroscopy models. Journal of biophotonics. 2016

Other publications include an investigation into the the use of frequency domain and continuous wave fNIRS devices when observing controlled hypoxia.

Davies DJ, Clancy M, Lighter D, Balanos GM, Lucas SJ, Dehghani H, Su Z, Forcione M, Belli A. Frequency-domain vs continuous-wave near-infrared spectroscopy devices: a comparison of clinically viable monitors in controlled hypoxia. Journal of Clinical Monitoring and Computing. 2016 Oct 24:1-8.

Conference Proceedings

The first conference abstract relating to this work was presented at the Optical Society of America conference in 2015, and looked at the sensitivity of near infrared spectroscopy probes.

Clancy M, Belli A, Davies D, Lucas S, Dehghani H. Quantitative Evaluation of NIRS Probes and Imaging Protocol for Traumatic Brain Injury (TBI). In Biomedical Optics 2014 Apr 26 (pp. BM3A-8). Optical Society of America.

Work on the effects of superficial contamination in near infrared spectroscopy devices was presented at the European Conference of Biomedical Optics in 2015.

Clancy M, Belli A, Davies D, Lucas SJ, Su Z, Dehghani H. Comparison of neurological NIRS signals during standing Valsalva maneuvers, pre and post vasoconstrictor injection. In European Conferences on Biomedical Optics 2015 Jul 16 (pp. 953817-953817). International Society for Optics and Photonics.

Preliminary work on the Atlas-based reconstruction method was also presented at the European Conference of Biomedical Optics in 2015 and was awarded runner up prize in the best student poster category.

Clancy M, Belli A, Davies D, Lucas SJ, Su Z, Dehghani H. Monitoring the injured brain: registered, patient specific Atlas models to improve accuracy of recovered brain saturation values. In European Conferences on Biomedical Optics 2015 Jul 16 (pp. 95381C-95381C). International Society for Optics and Photonics.

Preliminary work on the applying the Atlas-based reconstruction method to data recorded on a high-density probe was presented at the Optical Society of America conference in 2016.

Clancy M, Lucas SJ, Davies D, Belli A, Su Z, Wojtkiewicz S, Sawosz P, Dehghani H. Monitoring the Injured Brain - High-density near infrared probes and registered Atlas models improve cerebral saturation recovery. In Optical Tomography and Spectroscopy 2016 Apr 25 (pp. OM4C-4). Optical Society of America.

An abstract of a comparison between near infrared spectroscopy and functional magnetic resonance imaging was published in the Lancet in 2016.

Davies D, Evans S, Clancy M, Su Z, Hansen P, Dehghani H, Belli A, Lucas S. Comparison of near infrared spectroscopy with functional MRI for detection of physiological changes in the brain independent of superficial tissue. *The Lancet*. 2016 Feb 25;387:S34.

Work assessing the quantitative accuracy of near infrared spectroscopy devices was presented at the Optical Society of America conference in 2016.

Lighter D, Clancy M, Davies D, Balanos GM, Lucas SJ, Dehghani H. Assessing the quantitative accuracy of continuous wave and frequency domain near infrared spectroscopy for detecting hypoxia in patients with traumatic brain injury. In *Clinical and Translational Biophotonics* 2016 Apr 25 (pp. JW3A-44). Optical Society of America.

CONTENTS

1	Introduction	1
1.1	Background	1
1.1.1	Biological Motivation	1
1.1.2	Introduction to Near Infrared Techniques	2
1.2	Traumatic Brain Injury	6
1.2.1	Treatment of Traumatic Brain Injury	7
1.2.2	Monitoring Modalities in Traumatic Brain Injury	8
1.2.3	Application of Near Infrared Spectroscopy to Traumatic Brain Injury	11
1.3	Research Aims	15
1.4	Summary	17
2	Near Infrared Imaging and Spectroscopy - Tissue Optics	18
2.1	Physical Principles	19
2.1.1	Light Interactions in Biological Tissue	19
2.2	The Radiative Transport Equation and the Diffusion Approximation	25
2.2.1	Modified Beer-Lambert Law	26
2.3	NIR Instrumentation	28
2.3.1	Source Modes	29
2.3.2	Probe Geometries	30
2.4	Summary	34
3	Near Infrared Imaging and Spectroscopy - Reconstruction and Mod-	

elling	36
3.1 Analytical Methods	36
3.1.1 Numerical Methods	42
3.2 Methods for reducing Superficial Signal Contamination	50
3.3 Summary	54
4 Near Infrared Spectroscopy - Device Simulation and Testing	56
4.1 Introduction and Aims	56
4.2 Sensitivity simulations on existing fNIRS probe geometries	57
4.2.1 Jacobian Analysis	57
4.2.2 Singular Value Analysis	63
4.3 Healthy Volunteer Investigation testing method - The <i>Valsalva Manoeuvre</i>	67
4.3.1 What is the <i>Valsalva Manoeuvre</i> ?	67
4.3.2 Predicted Haemodynamic changes during a <i>Valsalva Manoeuvre</i> . .	70
4.4 Spatially Resolved Spectroscopy - Simulation Studies	78
4.4.1 Conclusions	85
4.5 ISS Oxiplex TS Vasopressor Studies	86
4.5.1 Methodology	86
4.5.2 Results and Discussion	88
4.5.3 Conclusions	93
4.6 Summary	94
5 High-Density Near infrared Spectroscopy Reconstructions using Registered Atlas Models	96
5.1 Introduction	97
5.2 Methodology - Simulation Studies	99
5.2.1 Production of Patient Specific head Models	100
5.2.2 Production of registered Atlas models	101
5.2.3 Proposed continuous wave probe design	102

5.2.4	Simulation of Forward Data	104
5.2.5	Reconstruction Routines - Simulation Studies	105
5.3	Results and Discussion - Simulation Studies	107
5.3.1	Registration Process	107
5.3.2	Reconstructions	111
5.3.3	Conclusions - Simulation Studies	119
5.4	Direction Of Future Studies - Healthy Volunteer testing with existing DOT probe	120
5.5	Methodology - <i>In Vivo</i> Testing	121
5.5.1	High-Density Probe for Data Collection	121
5.5.2	Recording <i>Valsalva</i> Data	122
5.5.3	Production and Registration of Head Models	122
5.5.4	Reconstruction Regime	126
5.5.5	Results and Discussion	129
5.5.6	Conclusions - Healthy Volunteer Testing	136
5.6	Frequency Domain Simulations	138
5.6.1	Methodology	139
5.6.2	Results and Discussion	140
5.6.3	Conclusions - Frequency Domain Simulations	143
5.7	Summary	143

6 High-Density Near infrared Spectroscopy Probe Design and Validation Studies 146

6.1	Probe design	147
6.1.1	Electronics	148
6.1.2	Probe Casing	151
6.2	Probe Characterisation	153
6.2.1	Dark Noise	153
6.2.2	Silicon Photodiode responsivity	156

6.2.3	Light Emitting Diode intensity variation	158
6.2.4	Light Emitting Diode spectra response	161
6.2.5	Voltage - Intensity Calibration	164
6.2.6	Probe repeatability tests	167
6.2.7	Solid phantom measurements	168
6.2.8	Pre-amplifier testing	171
6.2.9	Curved probe calibration	173
6.3	Conclusions	175
7	High-Density Near infrared Spectroscopy Probe Testing	177
7.1	Arm Cuff Studies	178
7.1.1	Methodology	179
7.1.2	Results and Discussion	184
7.1.3	Conclusions	191
7.2	Valsalva Studies	192
7.2.1	Methodology	192
7.2.2	Results and Discussion	195
7.3	Conclusions	198
8	Conclusions and Future Work	201
8.1	Conclusions	201
8.2	Future Work	204
.1	Appendix 1 - Near Infrared Spectroscopy Probe Geometries for Simulation	207
.2	Appendix 2 - Atlas model Optical Properties	207
.3	Appendix 3 - Optical Properties of ISS Calibration Phantoms	208
.4	Appendix 4 - Blood pressure comparisons from Vasopressor studies	209
.5	Appendix 5 - Reconstructed arm cuff data from second participant	213
.6	Appendix 6 - Reconstructed VM data from second participant	214
	List of References	215

LIST OF FIGURES

1.1	Absorption spectra for oxyhaemoglobin, deoxyhaemoglobin, and water showing the relatively low absorption levels in the NIR region [18].	3
1.2	Examples of reflectance (A) and transmission (B) NIR measurements . . .	4
1.3	Examples of NIRS (A) and DOT (B) probe geometries, positioned on the forehead.	5
1.4	Example CT of a subject with a TBI used to calculate ideal monitoring depth in TBI patients. A Corpus Callosum, B Contact Point to start measurement, C Haematoma and D Third Ventricle (axis origin). . . .	9
1.5	Example of ICP monitor surgically implanted in the skull of a TBI patient (indicated by red circle).	10
2.1	A High energy photon transport through biological tissue. B NIR photon transport through biological tissue. C Example of scattered light from a single source.	19
2.2	Example spectra for reduced scattering [63] and absorption coefficients [64] to show the area of high scattering and relatively low absorption in the NIR region.	20
2.3	Jablonski energy diagram showing an example set of energy transitions for an electron. The energy of the transition is denoted by $h \nu$ where h is Plancks constant and ν is the frequency of the photon (referred to as f in Equation 2.1). The letters A, F, p and R represent absorption, fluorescence, phosphorescence, and Raman respectively [65].	21

2.4	Illustration Beer-Lambert Law (A) and Modified Beer-Lambert Law (B). .	27
2.5	NIR source modes - A - Continuous Wave, B - Frequency Domain and C - Time Domain [72]	29
2.6	A NIRO-200NX (Hamamtsu, Japan) fNIRS probe. B Diffuse optical tomography probe developed by Washing University in St Louis [62]. . . .	31
2.7	Examples of other fNIRS probe geometries, Top - FORE-SIGHT (CAS Medical Systems Inc; Branford, CT), Middle - INVOS 5100C-PB (Covi- dien; Boulder, CO) and Bottom - EQUANOX Classic 7600 (Nonin Medical Inc; Plymouth, MN) [26]	32
2.8	Examples of different DOT geometries the square (Left) and Triangular (centre) are considered to be spare arrays usually used for topography measurements and the high-density array (Right) is usually used for to- mography [88].	33
2.9	NIRSport portable NIR head cap [89].	34
3.1	Example routine for obtaining optical properties from forward modelling of boundary data.	39
3.2	Example of intensity (A) and phase (B) data produced in NIRFAST ready for fitting to an analytical model [63].	40
3.3	Example of a finite element model of a head [58].	44
3.4	Structure of Jacobian matrix for a single wavelength case. The optical properties μ are separated into absorption μ_a and the diffusion coefficient κ (referred to previously as D). $\frac{\delta \ln(I_i)}{\delta \kappa_j}$ and $\frac{\delta \ln(I_i)}{\delta \mu_{a,j}}$ are sub-matrices showing the change in log intensity arising from the small change in optical properties at the i th measurement at the j th mesh nodes. $\frac{\delta \Theta_i}{\delta \kappa_j}$ and $\frac{\delta \Theta_i}{\delta \mu_{a,j}}$ are similar sub matrices corresponding to changes in phase data from frequency domain measurements [19].	45

3.5	Structure of the Jacobian matrix for a spectral, multi wavelength case. There is a sub-matrix for each chromophore (c), the scatter amplitude (a) and scatter power (b) for each measurement wavelength, each having dimensions of the number of mesh nodes by the number of measurements [19]. NN is the number of unknown parameters and NM is the number of boundary measurements.	46
3.6	Illustration of time resolved spectroscopy.	51
3.7	Example of physiological noise in fNIRS signals [107].	52
3.8	Illustration of NIRO 300 (Hamamatsu, Japan) setup to obtain spatially resolved spectroscopy measurements [76].	53
3.9	A - Illustration of the spatially resolved spectroscopy measurements of light attenuation (A) at distance (ρ) from the source. B Plotting gradient of light attenuation measurements (A) over distance (ρ) to give ($\frac{\delta A}{\delta \rho}$)	53
4.1	Atlas model used for NIRFAST simulations. A - Whole head, B - Clipped head showing internal structure, C - Cropped forehead region. The region labels are: 1 - Skin, 2 - Bone, 3 - Cerebral spinal fluid (CSF), 4 - White matter and, 5 - Grey matter.	59
4.2	Details and schematics of the five probe geometries being modelled in this investigation. For the schematic diagrams X represents a detector and O represents a source.	60
4.3	Example of fNIRS probe geometry modelled on the Atlas	61
4.4	Sensitivity profiles for the 5 fNIRS probe geometries modelled on the Atlas. Each probe is normalised to its own maximum sensitivity. The region of interest is the 'ideal' target depth measured from 50 CT scans of TBI patients and has its lower bound at A - 17 mm and its upper band at B - 25 mm (shown by the black dashed lines).	62

4.5	Magnitude of singular values obtain from Jacobian sensitivity values corresponding the brain nodes in the Atlas-head model from each of the 5 fNIRS probe geometries. The magnitude of the singular values are normalised to its local maximum. The noise threshold is shown as 1% of the normalised maximum.	65
4.6	Magnitude of singular values over the noise threshold for each of the 5 probe geometries normalised to their own maximum value	66
4.7	Diagrammatic representation of the stages in a Valsalva from A to D . . .	68
4.8	Four phases of the VM in terms of mean arterial pressure blood response [124].	69
4.9	Blood pressure response during a 10 s VM over 9 subjects recorded as part of the preliminary investigations into using the VM for fNIRS testing (Average over all subjects).	71
4.10	Percentage change from mean flow velocity in the middle cerebral artery measured with transcranial Doppler over a 10s VM [118]. The triangle, square and diamond markers represent 30 %, 60 % and 90 % maximal VMs.	72
4.11	Percentage change in cardiac output during a 15s (non maximal) VM [117].	72
4.12	Predicted changes in total haemoglobin concentration over a 30 s period including 10 s baseline, 10 s maximal VM and 10 s of recovery. Values are show for three different tissues, Skin, Bone and Brain.	74
4.13	Normalised average change in fMRI BOLD (ROI in extracranial tissue in the same field of view as the fNIRS probe) and fNIRS oxygen saturation data from somatic tissue on the zygoma during a 10 s maximal, supine VM [129].	75
4.14	Normalised average change in fMRI BOLD (region of interest at white/grey matter junction of the middle frontal gyrus (brodman area 10)) and fNIRS signal from cerebral tissue during a 10 s maximal, supine VM [129].	76

4.15	Predicted changes in oxygen saturation over a 30 s period including 10 s baseline, 10s maximal VM and 10 s of recovery. Values are show for three different tissues, Skin, Bone and Brain.	77
4.16	Recovered TOI values during a simulated 10 s VM using the SRS method on homogeneous and heterogeneous head models. Results are all offset to start at the simulated baseline level	81
4.17	Recovered TOI values during a simulated 10 s VM using the SRS method on a heterogeneous head model with varying concentrations of superficial haemoglobin. Results are all offset to start at the simulated baseline level .	82
4.18	Example Jacobian sensitivity plot for NIRO-200NX probe geometry on a heterogeneous 2D model for one source-detector pair.	83
4.19	Example SRS (difference between Jacobians from each detector) sensitivity plot for NIRO-200NX probe geometry on a heterogeneous 2D model. . . .	84
4.20	Comparison of sensitivity to different tissues (skin, bone and brain) with and without the SRS-method employed on the NIRO-200NX geometry modelled on a 3-layer heterogeneous head Atlas.	85
4.21	Recovered saturation values from frequency domain reconstruction using ISS Oxiplex TS probe geometry before and after a 50 % reduction in skin haemoglobin concentration (Left). Simulated VM saturation values in skin and brain (Right)	88
4.22	Average change in forehead flux measured with laser Doppler during a 10 s VM over 4 subjects.	89
4.23	Single subject example of recovered saturation (Top) and total haemoglobin concentration (Bottom) values from the ISS Oxiplex TS probe during a 10s VM before (Left) and after (Right) a vasopressor injection to the forehead.	90

4.24	Group average of recovered saturation (Top) and total haemoglobin concentration (Bottom) values from the ISS Oxiplex TS probe during a 10 s VM before (Left) and after (Right) a vasopressor injection to the forehead across 14 subjects.	92
5.1	Flow chart of model generation from a patient MRI scan. A Original T1 weighted MRI scan. B MRI scan segmented into skin, bone, CSF, white matter and grey matter. C Masks created in NIRVIEW using the segmented MRI scan. D Mesh created in NIRFAST using masks.	100
5.2	Comparison of the ICBM152 Atlas (Left) and the new Atlas used for the simulations (Right).	102
5.3	Design of high-density NIR spectroscopy probe	103
5.4	High-density NIR spectroscopy probe positioned on the forehead	104
5.5	Predicted changes in oxygen saturation over a 30 s period including 10 s baseline, 10 s maximal VM and 10 s of recovery. Values are show for three different tissues: Skin, Bone and Brain.	105
5.6	Heat map showing average registration error between each subject-specific and the corresponding registered Atlas model (Left). Cropped and rescaled heat map to show registration error on the desired region of interest (forehead) (Top Right). A zoom in on the region of the forehead where DOT pad is positioned (Bottom Right).	108
5.7	Average coordinates positions of the DOT pad on the original subject-specific models (red) and on the registered Atlas models (blue).	109
5.8	Maximum error in individual source/detector positioning across all the registered-Atlas models. This is a 2D representation of a 3D error.	110

5.9	Inverse crime reconstructed saturation values for the skin (top), bone (centre) and brain (bottom) regions (outlined in Figure 4.15) using both regional (green) and tomography (blue) algorithms prior to, during, and immediately following a VM (time points 6-11) . The plotted results are the average over all models with the error bar showing the standard deviation of the dataset. The simulated saturation line (dashed) in the Brain results graph (bottom graph) is not visible as it overlaps the Inverse Crime Regional Reconstruction (Green) line.	113
5.10	Graph illustrating how the sensitivity of DOT in the brain region alters as the saturation in all regions is varied during the VM. The sensitivity is a summation of the Jacobian values corresponding to brain nodes. More negative values indicate higher sensitivity.	114
5.11	Plot of Jacobian (sensitivity) matrix values on the surface of a subject-specific model showing the hot spots of hyper sensitivity under each of the sources and detectors. A smaller sensitivity value represents a higher sensitivity.	116
5.12	Atlas reconstructed saturation values for the skin (top), bone (centre) and brain (bottom) regions using both regional (green) and tomography (blue) algorithms. The plotted results are the average over all models with the error bar showing the standard deviation of the dataset	118
5.13	Layout of the high-density DOT probe on Atlas Model (A) and actual probe (B) designed and built by the Institute of Biocybernetics and Biomedical Engineering (IBIB). Detector positions are shown in blue and source positions in green with the maximum source-detector separations indicated. C shows the probe in position on a subjects forehead.	121
5.14	Example of the 4 landmark points used to register the Atlas model to the geometry of a subjects head.	123

5.15	Examples of the VM grading system used for raw data where 1 is a poor VM, 3 is an good VM and 5 represents a strong VM. This is example data from one detector recording data from all sources at 750 nm source wavelength. The different coloured lines represent different source detector separations.	125
5.16	Surface point representation of cylindrical phantom mesh used for VM data calibration process.	127
5.17	Illustrations of the sections of the recorded data used for the baseline and peak VM data sets.	128
5.18	Baseline variation in saturation for the skin, bone and brain regions over all 10 participants.	130
5.19	Average reconstructed saturation values for the skin, bone and brain regions.	131
5.20	Comparison of superficial layer thicknesses between the Atlas model and two subject-specific models made from segmented MRI data. All distances are measured in millimetres (mm) and the distances shown are skin thickness (top) and cortex depth (bottom).	134
5.21	Comparison of average reconstructed saturation for all tissue layers using the registered Atlas models and the subject-specific models for 2 participants. A and B show the baseline values for the Atlas and MRI models, respectively, and C and D show the VM values for the Atlas and MRI models, respectively.	136
5.22	Reconstructed saturation values for the 3 different frequency domain simulations. The blue line representing the FD reconstructions with on a scatter mismatch and the black line representing the simulated values overlay each other.	141
6.1	Design of high-density NIR spectroscopy probe	147

6.2	Absorption spectra for oxyhaemoglobin (HbO ₂), deoxyhaemoglobin (HHb), and water, showing the relatively low absorption levels in the NIR region and the location of the LED wavelengths used in the probe [18].	148
6.3	Circuit diagram for the LED and SPD grids and their connection to the Arduino Due control board.	149
6.4	Circuit board for probe with component soldered in place.	151
6.5	Sections of probe casing that fit together to house the circuit board. The top curved section is removable to allow for data collection of curved or flat target media.	152
6.6	Fully assembled prototype probe with flat top.	153
6.7	Illustration of the P-N junction of a Silicon Photodiode and the depletion region formed between them. The left of the figure shows the component symbol for a SPD and how it orientates with the P and N type junction. .	154
6.8	Setup used for dark measurements as well as phantom and repeatability measurements for later sections.	155
6.9	Top - Graph showing the dark noise of each detector along with the standard deviation from the average measurement. Bottom - Table of numerical values of Dark correction factors.	156
6.10	Setup of SPD responsivity test for probe.	157
6.11	Results of detector responsivity testing with calibration factors shown below the graph.	158
6.12	Setup of LED intensity testing for probe.	159
6.13	Image taken of 735nm sources using EM CCD.	160
6.14	Results of LED intensity testing with calibration factors shown below the graph.	161
6.15	Setup of LED Spectral testing for probe.	162
6.16	Average spectral response over all LEDs in the probe compare to the expected peak wavelengths.	163

6.17	Peak wavelengths for all the sources in the probe.	164
6.18	Setup of voltage-intensity calibration experiment using an external light source.	165
6.19	Voltage - Intensity calibration plot with fitted equations to convert mV detector readings into intensity for using in NIRFAST reconstructions. . .	166
6.20	Percentage variability in detector measurement over 20 independent read cycles on a solid phantom	167
6.21	Average percentage variation in 735 nm detector measurements, separated by source-detector distance, over 20 repeat reads on a solid phantom . . .	168
6.22	Plot of detector intensity (on logarithmic scale) vs source-detector distance on solid phantom A for 735 nm wavelength	170
6.23	Example of a calibration plot fitting homogeneous phantom data (from 735nm source) to an analytical model to estimate absorption properties - Process explained in Section 2.	171
6.24	Setup of preamplifier testing experiment using PowerLab pre amplifier for a single detector while measuring sources at varying distance along a solid phantom.	172
6.25	Plot of detector intensity vs source-detector separation distance recorded using a PowerLab pre-amplifier. The error bars on the pre-amplifier detec- tor measurements are ± 0.03 mV which was the smallest measurable change in voltage.	173
6.26	Setup of curved probe phantom testing.	174
6.27	Plot of correction factor to compensate for intensity drop due to curvature in the probe mount.	175
7.1	Setup for taking arm cuff measurements on the NIRO-200NX and the in- house high-density probe.	180
7.2	Mesh used for spectral minimisation of arm cuff data.	183

7.3	Raw data from built high-density probe before and after moving average, and frequency domain filtering.	185
7.4	Data from measurement of probe drift over a 20-minute period with fitted line used to calculate a correction factor for drift.	186
7.5	Graphs of optical density change from baseline over the duration of data collection for each respectively source-detector distance and wavelength. . .	187
7.6	Changes in chromophore concentration calculated using the modified Beer lambert law for each source detector separation.	188
7.7	Reconstructed spatially resolved spectroscopy parameter - tissue oxygenation index during arm cuff measurement. Results are shown for each pair of source-detector separations.	189
7.8	Tissue oxygenation index values obtained from the forearm with a NIRO-200NX probe.	190
7.9	Changes in chromophore concentration during arm cuff study obtained through minimisation of spectral data.	191
7.10	Position of high-density and NIRO probe of the subjects head.	193
7.11	Mesh used for spectral minimisation of high-density VM data. Left - Surface mesh showing the position of the sources and detectors on the model. Right - Internal tissue structure of the head model, region 1 is skin, region 2 is bone and regions 3-5 are brain.	194
7.12	Raw data recorded on the forehead during a 10 s VM plotted alongside moving average and frequency domain filter data.	196
7.13	Reconstructed TOI for 10 s VM using high-density probe.	197
7.14	Tissue oxygenation index values obtained from the forehead with a NIRO-200NX probe during a 10 s VM.	198
1	Comparison of blood pressure during the VMs pre and post injection for subject 1.	209

2	Comparison of blood pressure during the VMs pre and post injection for subject 2.	209
3	Comparison of blood pressure during the VMs pre and post injection for subject 3.	210
4	Comparison of blood pressure during the VMs pre and post injection for subject 4.	210
5	Comparison of blood pressure during the VMs pre and post injection for subject 5.	211
6	Comparison of blood pressure during the VMs pre and post injection for subject 6.	211
7	Comparison of blood pressure during the VMs pre and post injection for subject 7.	212
8	Comparison of blood pressure during the VMs pre and post injection for subject 8.	212
9	Reconstructed concentration values and TOI values (using SRS) for second participant in arm cuff studies with the prototype high-density probe. . . .	213
10	Reconstructed TOI for 10 s VM using high-density probe for second participant	214

LIST OF TABLES

4.1	Recovered saturation changes from the ISS probe during a 10s standing VM, before and after vasopressor injection to the forehead. The table shows the average baseline across all subjects and the average desaturation during the 10 s VM with the error shown as 1 standard deviation from the mean. The range of changes in the baseline and the VM desaturation are also shown.	92
5.1	Comparison of reconstructed regional saturation values using registered Atlas models for two participants.	132
5.2	Comparison of reconstructed regional saturation values using registered MRI models for two participants.	135
5.3	New ([142]) and Original ([113]) scattering properties used for the frequency domain simulations.	140
1	Information about the five commercial probes being modelled. Note - Due to the curvature of the head the Euclidean distance between a given source-detector pair with vary by approximately ± 1 -2 mm	207
2	Optical properties for scalp, skull and brain used for simulations [113] . . .	207
3	Optical properties of ISS calibration Phantom A	208
4	Optical properties of ISS calibration Phantom B	208

CHAPTER 1

INTRODUCTION

1.1 Background

1.1.1 Biological Motivation

The primary focus of this research is to explore the application of near infrared (NIR) technology to the clinical field of Traumatic Brain Injury (TBI) monitoring; assessing its current role, its limitations and how best to drive development towards its use as a clinical monitoring tool.

Worldwide, TBI is one of the leading causes of death in young people who are otherwise healthy [1], with up to 20,000 people sustaining a serious head injury annually [2]. The main cause of the high mortality rate (20-40%) [3] in TBI is not due to the initial insult to the brain, instead it is the variety of hypoxic, ischaemic and cytotoxic events that can lead to a profound secondary insult, occurring minutes to hours after the primary event, which poses additional risk to patients [4]. Therefore an important facet of improving the care of TBI patients is the prediction and prevention of secondary injuries through continuous monitoring in pre-clinical and clinical locations, so cerebral perfusion can be tightly manipulated externally.

There is currently a niche in the TBI monitoring domain as all the current modalities, such as x-ray computerised tomography (CT) and intracranial pressure (ICP) monitors

(further details of TBI monitoring modalities provided in Section 1.2.2), are only applicable in the clinical environment and are ionising, invasive or high cost. Therefore it has been suggested that NIR devices could fill this gap in TBI monitoring, with current research showing the potential of NIR devices in other areas such as cardiac and vascular surgery, where clinical studies illustrated that a 13-20% drop in blood oxygen saturation is an indicator of post-operative brain tissue damage [5, 6]. However, within the context of TBI they have been found to not yet be a viable substitute for conventional monitoring being described as a work in progress [7, 8, 9].

1.1.2 Introduction to Near Infrared Techniques

Near infrared light has long been a desirable form of non-invasive imaging and spectroscopy since its first reported use by Jobisis in 1977 [10]. As well as being non-invasive, NIR devices use non-ionising radiation, so they can be used for continuous monitoring. They can be made portable [11, 12] and can be relatively cheap in comparison to other TBI monitoring modalities; therefore they could provide significant advantages to the monitoring of TBI patients, both in and out of clinical settings [13]. Basic forms of the technology, such as pulse oximeters, are well established in the clinical setting for measuring the arterial phase oxygen saturation of blood from a probe on the finger. More complex near infrared technology, such as functional near infrared spectroscopy (fNIRS) and diffuse optical tomography (DOT), have been used in many medical research areas ranging from breast cancer [14, 15] to epilepsy [16, 17].

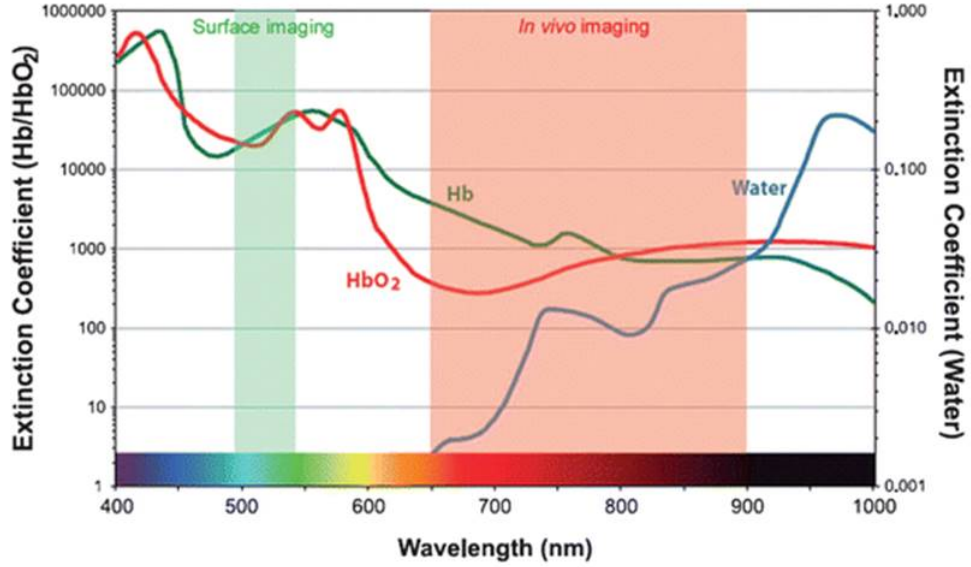


Figure 1.1: Absorption spectra for oxyhaemoglobin, deoxyhaemoglobin, and water showing the relatively low absorption levels in the NIR region [18].

Near infrared light is within the range of 650-1000 nm and can exploit a biological window (Figure 1.1) of relatively low absorption in biological tissue [19, 20, 21]. The main absorption sources are haemoglobin, separated into oxygenated (HbO) and deoxygenated (HHb) components, and water; these are known as chromophores. The low absorption means that scatter is the dominant interaction mechanism significantly altering the light path (examples shown in Figure 1.2). Figure 1.2 shows two different source-detector setups for NIR instrumentation, reflectance (A) and transmittance (B). Reflectance setups (Figure 1.2A) are used for cerebral monitors and the scatter dominated interaction process allows NIR photons to follow a 'banana-shaped' path back to the detector; this provides the ability to probe deeper into tissue than optical techniques operating at visible wavelengths. As NIR photons travel a non-linear path from source to detector data cannot be recon-

structured through simple back projection, as it is in computerised tomography (CT) x-ray imaging, where the light path is linear. For this reason a fundamental principle of NIR technology is that photon diffusion in tissue must be predicted in order to reconstruct a usable parameter from the detected intensity data. Some devices, known as continuous wave instruments, assume a pathlength for NIR photons within a given medium in order to estimate its optical properties. The diffuse (high scattering) nature of the NIR light limits the lateral spatial resolution to approximately 1 cm (depending on the probe and reconstruction methods used) [22]. In terms of spatial resolution and depth penetration, near infrared techniques do not compare to the likes of x-ray and magnetic resonance imaging (MRI), the advantage comes in the form of safe, non-ionising radiation (unlike x-rays) and low cost and portability (unlike MRI). Given that photon diffusion can be predicted, differences in detected light intensity can be attributed to absorption by the aforementioned chromophores. A combination of blood flow and metabolism compete to alter the oxygen saturation of blood [23], changing the concentration HbO and HHb. Then as the absorption spectra for each of the chromophores shown in Figure 1.1 is unique, the individual contributions of each one to the overall detector signal can be unmixed to obtain the relative contribution and concentration from each. This unmixing requires the use of multiple wavelengths in order to obtain chromophore concentrations.

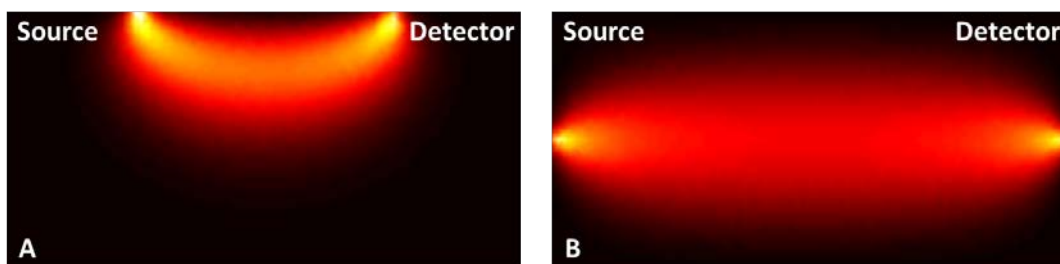


Figure 1.2: Examples of reflectance (A) and transmission (B) NIR measurements

NIR devices can be separated into a variety of categories based on their setup and reconstruction techniques (Full details in Chapter 2.1). For the most part they fall into

two categories; fNIRS (Figure 1.3A) gives single, global values for the chromophores in a target medium using 1 or 2 source-detector pairs, and DOT (Figure 1.3B) uses a large array of sources and detectors, at multiple wavelengths, to produce a spatial resolved map/functional image of the chromophore concentrations in the target medium. The chromophore maps are similar to those produced by positron emission tomography (PET) scanners yet without the need for radionuclide tracers. The observed chromophores HbO, HHb and water are all abundant in the body and are good indicators of patient condition in the context of TBI. Hence no external contrast agents are required, although there are some available (like Cyanine dyes which, can also be used to measure flow rates [24]) depending on the application [25].

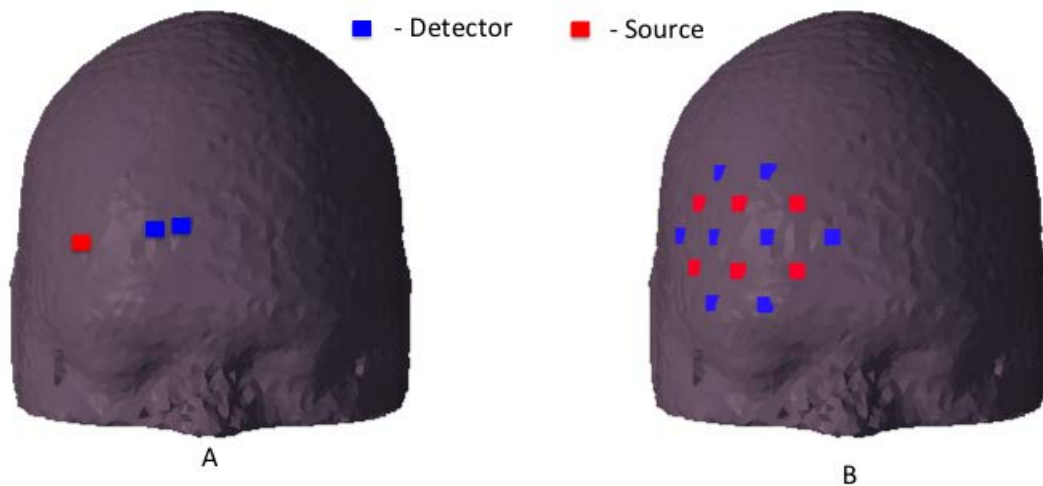


Figure 1.3: Examples of NIRS (A) and DOT (B) probe geometries, positioned on the forehead.

The question remains, with all its potential advantages and current uses in the clinic

and research environments, why has NIR technology not made the leap into TBI monitoring? The main reason is that there are concerns within the NIR field generally about the levels of contamination from superficial layers (i.e., skin and skull) and whether this contamination could confound the neurological NIRS measures which could have a significant impact on TBI monitoring [26, 27, 8, 28, 29]. Thus far investigations into the use of NIR devices in TBI have found results to be highly variable with one of the most prominent issues being the quantitative accuracy of the NIRS data being produced [28, 29, 7]. In a setting where a normal reference baseline can be observed, as in cardiac surgery, this can be used to index relative changes in cerebral haemodynamics and thus be indicative of prognostic clinical outcome (e.g., oxygen saturation decrease from baseline). However, when no normative index baseline is available, as is the case with an acute TBI, the interpretation of changes in NIRS data is problematic as there is a large inter-subject variability in cerebral oxygen saturation. Therefore, improving the quantitative accuracy of NIRS is required to improve its clinical application in TBI.

1.2 Traumatic Brain Injury

Traumatic brain injury is described as an insult to the brain caused by an external mechanical force leading to an alteration or impairment in brain function [30, 31, 32]. The source of the external force ranges from rapid deceleration to blast waves. TBI can be categorised by its severity using the Glasgow Coma Scale (GCS) based on patient response. A mild TBI could be a concussion caused by a sport injury where the patient is awake and responsive. At the other end of the continuum, and the primary focus of this research, a severe TBI would be from a more significant impact, such as a motor vehicle collision, where the patient may be unconscious.

The initial impact of a TBI is likely to cause shearing of white matter tracts and rupturing of blood vessels leading to both intra and extracranial haematomas [33]. This often results in inflammation and swelling, and is referred to as the primary insult to the

brain. While these are significant injuries, in themselves they are not fatal, it is instead the repercussions of these injuries further down the line that are the main source of patient mortality; these repercussions are known as secondary insults to the brain [4]. The main issues in the secondary insult process are hypoxia (lack of oxygen) and intracranial hypotension (abnormally low blood pressure) [34, 32], which along with the impaired brain's intrinsic blood regulatory mechanism (cerebral autoregulation), compromise the delivery of oxygen and nutrients to cerebral tissue. Furthermore the swelling in the brain from the initial insult increases intracranial pressure (ICP), which in turn decreases cerebral perfusion pressure (CPP), meaning that adequate cerebral tissue perfusion is further compromised causing further impairment of the brain's intrinsic autoregulation abilities [35]. As these secondary injuries can take place at anytime post injury, the ability to continuously monitor patients from the moment emergency care arrives is essential for securing positive patient outcomes [32].

1.2.1 Treatment of Traumatic Brain Injury

Standard practice for the treatment of most trauma victims (recommended by the National institute for health and care excellence and other bodies) is Permissive Hypotensive Resuscitation (PHR), which helps to reduce the risk of a secondary haemorrhage, lung injury or tissue oedema. PHR is a procedure, which involves gentle fluid infusion in order to increase systemic blood pressure to just below normal levels. The notable exception to this is in the case of TBI. This is due to concerns that PHR will cause an ischaemic insult to the brain, resulting in further damage by reducing blood pressure in a brain that is potentially already hypotensive, a topic which is still controversial. Currently the main goal in pre-hospital treatments is to use fluid therapy to avoid hypoxia and hypotension until the patient can be fully assessed in a hospital. However the information available to emergency medics at this point in order to guide the therapy is limited to blood pressure and systemic blood saturation measurements. It is only on arrival at a hospital that more informative monitoring and assessment modalities (detailed in Section 1.2.2)

can be utilised. More accurate information then allows clinicians to manipulate ICP and CPP safely through fluid and pharmaceutical intervention with surgical techniques also available, such as a decompressive craniectomy [33].

1.2.2 Monitoring Modalities in Traumatic Brain Injury

Currently there are very few monitoring modalities available for pre-hospital management of TBI, which is a key driving force behind this research. Pulse oximetry and blood pressure monitoring are the main modalities available with both only giving a systemic overview of patient health (i.e., not brain specific). The concern with these modalities is that in TBI, the oxygenation and blood pressure in other tissue is not necessarily indicative of that in the brain and could therefore lead to the incorrect therapy. Despite this it has been shown in the literature that maintaining an acceptable peripheral saturation and blood pressure does correlate with positive TBI outcomes [36, 37].

There are several methods of patient monitoring currently used in the clinic, including x-ray computerised tomography (CT), magnetic resonance imaging (MRI), intracranial pressure (ICP) monitors, transcranial Doppler (TCD) and electroencephalography (EEG) [31]; CT and pressure monitors are the most common. There are also invasive monitors like the ICP probes which can measure brain tissue oxygenation (PbtO₂) and provide positive outcomes when used with ICP [38]. CT scans are standard practice for TBI patients and when used with contrast agents can accurately show the position of haematomas in the brain and can guide surgical procedures (Figure 1.4). It is however only useable once the patient arrives in hospital and due to the ionising nature and risk of moving critical patients it is not useful as a continuous monitoring tool. Similarly, ICP and PbtO₂ monitors can only be installed in the hospital by a surgeon.

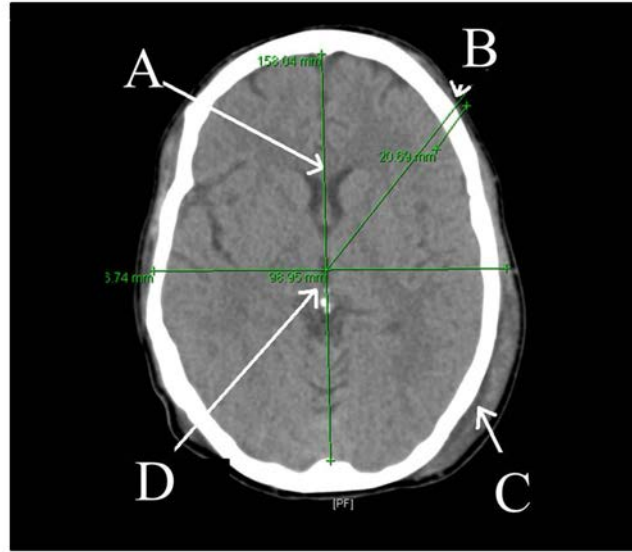


Figure 1.4: Example CT of a subject with a TBI used to calculate ideal monitoring depth in TBI patients. A Corpus Callosum, B Contact Point to start measurement, C Haematoma and D Third Ventricle (axis origin).

The pressure monitors are invasive and are screwed into the skull in order to give a long-term assessment of intracranial pressure and tissue oxygenation (Figure 1.5). They also have their own associated risks with the implantation, specifically a 0.5 % risk of causing a haemorrhage and a 2 % risk of becoming infected [33]. In some literature reviews ICP monitors were not found to have any significant advantage over other imaging and clinical examination [39], although this is a topic of debate [40]. TCD can show blood flow velocity in the brain and has been found useful in guiding therapy to restore cerebral perfusion [41], however the results can be inconclusive and interpretation varies between users.



Figure 1.5: Example of ICP monitor surgically implanted in the skull of a TBI patient (indicated by red circle).

As there is currently no accepted modality/technique for guiding both hospital and pre-hospital therapies, this leaves a gap which could potentially be filled by fNIRS as it has the depth penetration ability to assess the cortex (reaching the ideal TBI monitoring depth of 21 ± 4 mm (Figure 1.4) [42]). The application of fNIRS for assessment of haemodynamics is widely used in clinical research [43] due to its versatility and ease of use. Also as it is non-ionising and significantly cheaper to purchase and run than CT/MRI scanners, it can be used to continuously monitor TBI patients, from the moment emergency medics start treatment. As cerebral oxygen saturation is one of the key parameters clinicians are concerned with when it comes to monitoring TBI patients, the ability to use fNIRS would be advantageous. Evidence indicates that changes in tissue oxygenation index (TOI) and tissue haemoglobin index (THI) as measured by fNIRS can be used as an indicator of ICP [44, 45]. However, other reviews have stated that despite its potential in its current state, fNIRS cannot be relied upon to predict ICP consistently [7]. On balance, research to date indicates that NIRS has the ability to supplement current TBI assessment methods but

it not good enough to replace them [46, 8, 47].

1.2.3 Application of Near Infrared Spectroscopy to Traumatic Brain Injury

The ability to use fNIRS devices to detect changes in cerebral haemodynamics like cerebral oxygen saturation or total haemoglobin concentration is very appealing in TBI monitoring. These parameters potentially give a much more direct measure of whether the brain is hypoxic or under perfused whereas ICP only provides pressure changes from which it can be inferred that the brain may be under perfused. To date there has been a very limited number of studies applying fNIRS to TBI monitoring [8]. The clinical application of fNIRS in TBI have been mainly focused around comparison to current monitoring modalities such as ICP and PbtO₂, which showed that while fNIRS parameters mapped changes well there was a lack of specificity in the output parameters making it difficult to guide therapy choices [48, 7]. The primary reason for this is that despite the apparent advantages and potential of NIRS in this clinical context, there still remains doubt as to the physical origins of the obtained oxygen saturation values from externally measured optical signals, a debate common to the entire fNIRS and DOT field. With the rich vascular nature of facial somatic tissue, questions have been raised about the levels of signal contamination that will occur due to haemodynamic changes in these superficial tissues, and thus obscuring cerebral observations [26, 49, 50]. Due to the diffuse nature of near infrared light and the reflection geometry used by fNIRS devices, it is impossible to avoid all influence from the superficial tissues as the light must physically pass through these regions. A multitude of different approaches to reduce and/or eliminate superficial contamination have been suggested, ranging from probe design to reconstruction algorithms (discussed in detail in Chapter 2). Another limitation of the NIRS approach is that the presence of a sub-dural or extracranial haemorrhage can severely obscure the assessment of cerebral saturation as essentially the probe will be sampling a large pool of

blood, which will slowly desaturate [51]. Interestingly this limitation has actually been adapted to form fNIRS devices, which are designed specifically to locate haemorrhages in TBI patients [52, 53].

As a result of the signal contamination from superficial tissue, the quantitative accuracy of NIRS is limited. The principle of fNIRS is that it provides a global representation of the optical properties of a target tissue, which makes a quantitative assessment of cerebral oxygenation difficult. Additionally there is a distinct lack of standardisation between different fNIRS devices due to the different setups and algorithms used [21], resulting in fNIRS experiments reporting only changes in baseline measurements. While limiting, this approach is applicable in specific situations such as cardiac surgery and cognitive studies where it can be confidently assumed that the patients brains are well perfused. However in the context of the injured brain, no normative baseline measurements are available, as the state of the brain is unknown. A study which used fNIRS devices to measure cerebral oxygenation during a controlled hypoxic event showed that even with a healthy baseline measurement the variation between subjects was too high to put a firm number of what saturation level was indicative of a healthy brain [54]. Thus, a more quantitatively accurate measurement of cerebral oxygenation is required in order to gauge the condition of a patient. The main limiting factor is the measurement of a global saturation value in the target tissue, which effectively averages the saturation changes over all layers (tissue type) of the head, obscuring the true brain changes.

The progression of fNIRS towards a more quantitative assessment of cerebral oxygenation can come in one of two ways. The first is to move to a time domain (TD) fNIRS system, which maintains the real-time and portable advantages of standard fNIRS; however it uses significantly more expensive components capable of individual photon counting. By measuring both intensity and arrival time of the photons, TD fNIRS has intrinsic information about photon flight path, which enables deep and shallow photons to be selected allowing greater quantitative accuracy and increased depth resolution (although still global in the

lateral plane) [55]. The increased cost is a limiting factor when considering large number of devices would be needed.

An alternative method is an adaptation and use of diffuse optical tomography (DOT), mentioned in Section 1.1. DOT differs to conventional fNIRS in both system design and reconstruction, where instead of the linear probe designs used in NIRS systems consisting of one or two sources and detectors (Figure 1.3A), a DOT probe will have a larger array (Figure 1.3B) allowing use of multiple sets of overlapping measurements which can improve both the spatial resolution and quantitative accuracy [22]. Most reconstructions in DOT are model-based, typically using finite element models (FEM) where spatial priors and initial optical property estimates can be used to increase the accuracy of derived optical properties. The limitation of DOT systems is their size and parameter recovery time, which makes them less practical for TBI monitoring. Although relative changes in chromophore concentrations from a baseline can be measured in real time, the quantitatively accurate results (of oxygen saturation, for example) require a non-linear and iterative reconstruction approach to hone in on the best solution. To date, however, truly quantitative results have only been obtained in DOT of the breast [56] and the lack of known baseline optical properties in the brain is currently a limiting factor in achieving quantitative results.

Providing spatial priors regarding the tissue layers of the head, namely the skin, bone and brain in a reconstruction algorithm has shown to help constrain the ill-posed nature of the problem and improve parameter recovery accuracy [57]. Such spatial priors can be obtained from patient MRI or CT scans that can be segmented and formed into subject-specific models, however in the clinical and pre-clinical setting this is not always a feasible option [22, 57, 58]. Alternatively, the use of Atlas-based models has shown good promise to overcome cases where subject-specific MRI/CT data are not available [57, 58, 59].

Although the application of a DOT-based system can produce the data required to monitor TBI patients, in its current format it is not ideal. The first issue is size and expense of the equipment, which may have a relatively simple solution; the sampled area

could be scaled down. Although this would imply a smaller region of interest from which spatially varying parameters would be recovered, such small target regions would be suitable if the results were quantitative. It is worth noting that the invasive ICP probe only target a small volume of the brain also. Therefore, if a small DOT probe is used to give overlapping, multi-distant measurements over a small area, it could be used to reconstruct depth-resolved spectroscopic parameters. A smaller probe is also more portable and cheaper to produce and will also help with the second issue of reconstruction time. Specifically, smaller the number of voxels (spatially varying locations) being reconstructed, the faster the iterative reconstruction will complete [58]. Also having multiple overlapping measurements obtained over a smaller sample area will improve the ill-posed nature of the inverse problem [60]. It is also worth noting that a smaller target area is more likely to avoid clots/haematomas in the brain, which may obscure recovered parameters. With parallel computing and GPU acceleration becoming more prevalent, reconstruction times will only get faster [61], providing additional benefits. The final obstacle in the way of quantitatively accurate DOT reconstructions is the availability of spatial priors. A subject-specific reconstruction model will not typically be available in clinical and pre-clinical TBI cases, hence the utilisation of an Atlas model, using the average spatial priors over a multitude of segmented heads, could be registered to match a patient head and used as a substitute for specific priors [57, 58].

Finally, while portable high-density NIRS system designs are already available and routinely used (e.g., NIRSport, NIRx Medical Technologies and fNIRS300B, BIOPAC System, Inc), the key feature that is currently lacking is the non-trivial base-line parameter recovery needed to obtain information with a reasonable degree of quantitative accuracy (reconstruction methods will be discussed in Chapter 2). At the other extreme, systems such as the Washington University DOT array [62] uses a large-scale probe design, focusing on mapping cerebral activation and connectivity, which incorporate Atlas guided recovery into their reconstruction routines. Thus, there are already system designs

available that are suitable in terms of hardware. A near infrared system suitable for the monitoring of TBI lies somewhere between these aforementioned designs, hybridising the portability of the smaller DOT arrays with the more enhanced reconstruction algorithms of the large scale probes. While this is something that has been explored [59], there has been limited expansion of the Atlas-guided techniques to produce quantitatively accurate results. Therefore this research was aimed to investigate the suitability of a small scale fNIRS/DOT hybrid probe, designed for use on the forehead, for producing quantitatively accurate cerebral oxygen saturation values, using a registered Atlas model for spatial priors to address the limitation of fNIRS in the TBI setting.

1.3 Research Aims

Given the current position on NIR technology in the TBI field the aim of this research is to address the following hypotheses:

1. Signals from superficial tissues are not preventing fNIRS from measuring haemodynamic changes in the brain that would be necessary for guiding TBI patient therapy.
2. Contamination from superficial tissues is limiting the quantitative accuracy of fNIRS measurements and thus it cannot currently be used as a standalone TBI monitoring modality when no normative baseline measurements are available.
3. A small scale hybrid fNIRS/DOT probe and Atlas-based reconstruction algorithm can be used to recover superficial and cerebral haemodynamics simultaneously and thus produce quantitatively accurate results.
4. A low cost, portable, fNIRS device capable of producing these measurements can be built using off-the-shelf components.

By understanding how superficial signals are influencing the NIR parameter recovery, it will potentially allow for improvements to be made. In order to make this technology

a viable option for use in the clinical and pre-clinical environments it needs to be low cost and as simple as possible. Therefore finding ways to improve upon existing fNIRS technology is more desirable than moving to more complex and large-scale DOT devices. The proposed compromise is that a hybrid probe between that of fNIRS and DOT is built. The idea being that the probe would obtain a large number of measurements over a small target area that will allow for more complex parameter recovery without decreasing the portability or affordability of the technology.

Chapter 2 and 3 explains the physical principles behind NIR technology and the different reconstruction techniques that are used to reduce the influence of superficial contamination. It also includes a review of the most commonly used NIR devices and their areas of use. Chapter 4 investigates existing fNIRS devices in both simulation and healthy volunteer studies to work out their pitfalls and also what attributes help in reducing superficial contamination or increasing quantitative accuracy. The idea of this chapter is to provide the foundations for the next stage of research into improving the fNIRS probes and reconstruction to move towards quantitative parameter recovery.

Chapter 5 examines how the quantitative accuracy of NIR reconstructions can be improved by using Atlas models, registered to a subject head, in order to provide prior structural information to guide the parameter recover. A small-scale diffuse optical tomography device, referred to as a high-density near infrared spectroscopy (HD-NIRS) probe is outlined to provide the additional data required for the new reconstruction process. This is assessed in both simulations and healthy volunteer studies using an existing DOT system. Finally Chapters 6 & 7 outline the design, development and testing of the proposed new HD-NIRS probe using a variety of low cost, off-the-shelf, components to demonstrate its viability.

1.4 Summary

This chapter has laid out the background and motivation for the research into applying NIR techniques as a monitoring modality for patients with TBI. The literature so far has shown that NIR modalities have the potential for use in TBI monitoring both in and out of the clinic, however due to uncertainties about the quantitative accuracy and contamination in the recovery data they cannot currently be used other than to supplement current monitoring tools such as CT and ICP probes. The following chapter looks at the underlying physical principles of NIR techniques as the biological origins of the recovered signals.

CHAPTER 2

NEAR INFRARED IMAGING AND SPECTROSCOPY - TISSUE OPTICS

A brief introduction to the use of near infrared light is given in Chapter 1, here this is expanded upon and the physical principles, which underpin diffuse optics (near infrared) as an imaging and spectroscopy modality are explored.

The use of high-energy light (x-rays and gamma rays) to image inside biological tissue is well established within the clinical setting, with Computerised Tomography (CT) x-ray and Positron Emission Tomography (PET) being used routinely in hospitals. Incident light can be assumed to travel in a straight line through a medium with contrast coming from any drop in intensity of the detected light due to absorption. However the propagation of NIR light in biological tissue, as previously mentioned, is a more complex phenomenon. Unlike x-rays, NIR light cannot be assumed to travel in a straight line, as absorption is no longer the dominant interaction process; scattering now plays a major role and light which originates from a point source becomes dispersed as shown in Figures 1.2 and 2.1.

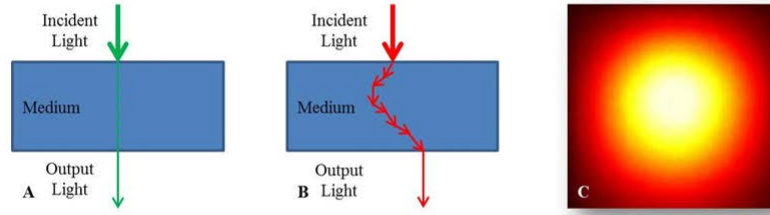


Figure 2.1: A High energy photon transport through biological tissue. B NIR photon transport through biological tissue. C Example of scattered light from a single source.

Therefore, in order to predict or reconstruct the path of NIR light in tissue, and hence its optical properties, computational methods and modelling are required. Modelling can be done using the Radiative Transfer Equation (RTE) or simplifications of the RTE, which will be discussed in Section 2.2.

2.1 Physical Principles

2.1.1 Light Interactions in Biological Tissue

The prediction of photon migration in tissue is based on our understanding of how light interacts with biological media. The main interaction methods of a photon with tissue are scatter and absorption; this section aims to described how these interactions take place and why they cause changes in detected intensity at a given measurement point. Figure 2.2 shows examples of changes in absorption and scattering coefficients over a range of wavelengths, where the area of high scattering and lower absorption in the NIR range can be seen.

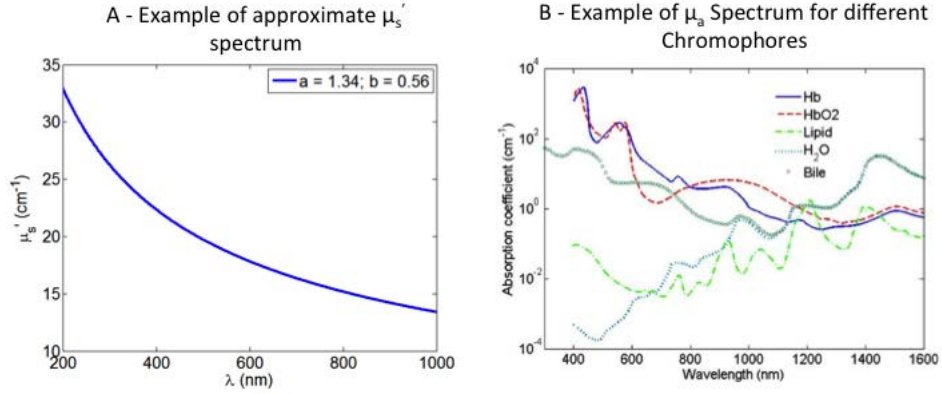


Figure 2.2: Example spectra for reduced scattering [63] and absorption coefficients [64] to show the area of high scattering and relatively low absorption in the NIR region.

A photon is the name given to a 'packet' of energy, with the energy of the photon being directly related to its frequency or wavelength (Planck-Einstein relation); as shown in Equation 2.1, where E is the photon energy, f its frequency, λ its wavelength, c is the speed of light in the medium and h is Planck's constant.

$$E = hf = \frac{hc}{\lambda} \quad (2.1)$$

Absorption

The process of absorption occurs when a photon transfers its energy to molecules inside the medium being traversed. The transfer of energy takes place via excitation of an electron moving it from a lower energy, or ground state, to a higher energy level (illustrated in Figure 2.3). Once the excitation has taken place the electron can return to its original, or

intermediate, state by releasing some or all of the absorbed energy. This can take place through a variety of mechanisms, which can be generalised under luminescence or thermal energy. NIR light is described as 'non ionising' as its photons do not have sufficient energy to excite an electron to a level where it can break free of its parent nucleus, a process which can cause tissue damage.

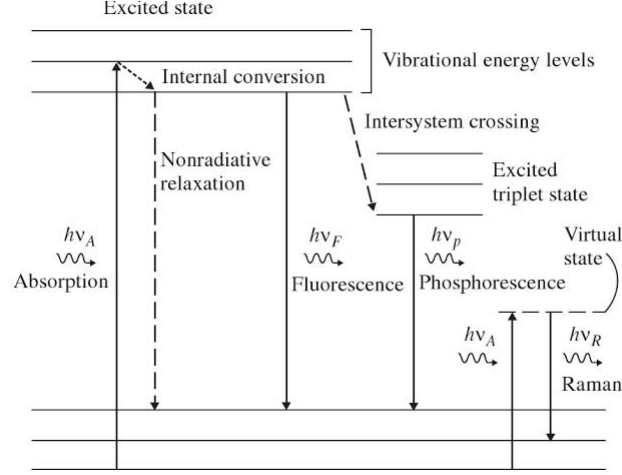


Figure 2.3: Jablonski energy diagram showing an example set of energy transitions for an electron. The energy of the transition is denoted by $h \nu$ where h is Plancks constant and ν is the frequency of the photon (referred to as f in Equation 2.1). The letters A, F, p and R represent absorption, fluorescence, phosphorescence, and Raman respectively [65].

Luminescence is a form of photon emission sub divided into fluorescence and phosphorescence. The process involves relaxation of the excited electron to a lower energy state (Figure 2.3) through the emission of a photon with an energy equal to that of the energy gap traversed. While both involve emission of a photon, fluorescence drops first to an intermediate vibration state while phosphorescence drops first to an excited triple state through inter-system cooling shown in Figure 2.3 [65]. Due to the internal transitions before the emission of the photon, the energy of the new photon is lower than the one initially absorbed.

In terms of thermal energy the photon of light raises the electron into a vibrational energy state where the energy can be dissipated through transfer of heat to surrounding atoms. This absorption process is non-radiative as no photon is released.

The energy levels (Figure 2.3) for electrons in different molecules are specific and as the energy of a photon is directly related to the wavelength of the light there is a wavelength dependence of the amount of absorption by a specific molecule, a principle that is essential for fNIRS.

The probability of a photon, of a particular wavelength, being absorbed within a medium per unit of distance travelled is defined as its absorption coefficient (μ_a). This is a measure of total absorption probability from all absorbing species. The relationship between intensity (I) change over a distance (L) travelled through a non-scattering medium with absorption coefficient μ_a , is exponential and is defined by Equation 2.2 which is referred to as the Lambert-Bouguer Law [66, 67].

$$I(L) = I_0 e^{-\mu_a L} \quad (2.2)$$

The relationship between the absorption coefficient and the concentrations of the constituent absorbing species is defined in Equation 2.3 which was built on by August Beer [68] to become the Beer-Lambert Law (substituting Equation 2.3 into Equation 2.2). The relationship is designed for measuring the transmission through an absorbing, but non-scattering, species dissolved in a non-absorbing medium. The molar extinction coefficient (ϵ) is the probability of light interacting with the species per unit path length. The extinction coefficient is wavelength (λ) specific and accounts for the interaction probability due to absorption in terms of concentration of the absorbing species (C) and the distance travelled (L). For biological tissues scattering is the dominant interaction (which is the reason NIR light can probe deeper into biological tissue than visible light) and to account for this, the modified Beer-Lambert law, discussed in Section 2.2.1 must be used. Equation 2.3 allows the absorption coefficient to be defined in terms the concentration of its absorbing species (oxygenated and deoxygenated haemoglobin in this example).

$$\mu_a(\lambda) = \epsilon(\lambda)_{HbO}C_{HbO} + \epsilon(\lambda)_{HHb}C_{HHb} + \epsilon(\lambda)_{H_2O}C_{H_2O} \quad (2.3)$$

The main absorption species in biological tissue are Haemoglobin (split into oxygenated (HbO) and deoxygenated (HHb) components), Water (H₂O), and others such as cytochrome oxidase and melanin [69]. Recovering concentrations of HbO and HHb can also provide measures of blood oxygen saturation (SO_2) (Equation 2.5) and total Haemoglobin concentration (HbT) (Equation 2.4). The saturation of the blood is an overall value covering both the venous and arterial components of blood, which are usually in the ratio of 75:25 so the venous contributions are stronger [70].

$$HbT = HbO + HHb \quad (2.4)$$

$$SO_2 = \left[\frac{HbO}{(HbO + HHb)} \right] \times 100(\%) \quad (2.5)$$

By measuring the absorption of light at several wavelengths in the NIR region, combined with the extinction coefficients (for each chromophore at each source wavelength) it is possible to calculate the concentration of each chromophore within a sample.

Scattering

Scattering is the process by which the direction of a photon is changed. It can be modelled as a series of interactions between spherical particles and photons (Mie and Rayleigh Theory) which, in the context of NIR light, are elastic meaning no energy is transferred from the photons during the interaction process [65, 71]. There are other forms of scattering which are non elastic and results in the reduction in incident photon energy, such

as Raman scattering (seen on Figure 2.3); but are less likely in the NIR region due to the associated energy level transitions. Elastic scattering dominates when the size of the particles is similar to that of the optical wavelength (NIR), which is the case in biological tissue where cell membranes, nuclei and mitochondria are key scatterers [72]. A mismatch in refractive indices between constituent particles and the background medium can also cause a significant amount of scattering, as governed by Snell's Law.

Just like absorption there is a scattering coefficient (μ_s) that defines the probability of a scattering event per unit length. The reciprocal of the scattering coefficient gives the average distance a photon will travel in a medium before undergoing a scattering event [65]. Another factor to consider with scattering is the angle of direction of the scattered light, known as anisotropy. This is important as the probability of light being scattered in all direction is not equal, so there is often a preference for forward or backward scatter. Therefore, to account for this a reduced scattering coefficient can be used that incorporates an anisotropy factor, g , which can range from -1 (for back scatter) through to 1 (for forward scatter) as shown in Equation 2.6. The anisotropy factor can be estimated experimentally and a typical value for biological tissue is 0.9, indicating forward scattering.

$$\mu'_s = (1 - g)\mu_s = A\lambda^{-B} \quad (2.6)$$

The empirical approximation of the Mie scattering theory (Equation 2.6) has shown a good fit to the reduced scatter coefficient of a tissue (μ'_s) [63, 73]. The scatter amplitude, A and the scatter power B are related to the particle sizes and number density of scatters in a tissue, representing the changes in scatter at different wavelengths (λ), due to different organelles and cellular structures [74].

2.2 The Radiative Transport Equation and the Diffusion Approximation

Based on the scattering and absorption parameters outlined in Section 2.1 the path of diffuse light can be predicted by looking at photon interactions within the medium. The prediction of the light propagation implements the radiative transfer equation (RTE), shown in Equation 2.7. The original basis for the RTE was developed by Boltzmann in the form of the Boltzmann transport equation in 1872. The physical quantities shown in the equation are as follows: \vec{r} is the position; \hat{s} is the unit direction vector; t is time; c is the speed of light in the medium; μ_t is the total attenuation coefficient ($\mu_s + \mu_a$); Ω is the solid angle, $L(\vec{r}, \hat{s}, t)$ represents radiance; $P(\hat{s}', \hat{s})d\Omega'$ represents the scattering phase function and $S(\vec{r}, \hat{s}, t)$ represents photon energy.

$$\begin{aligned} \frac{1}{c} \frac{\partial L(\vec{r}, \hat{s}, t)}{\partial t} = & -\hat{s} \cdot \nabla L(\vec{r}, \hat{s}, t) - \mu_t L(\vec{r}, \hat{s}, t) \\ & + \mu_s \int_{4\pi} L(\vec{r}, \hat{s}', t) P(\hat{s}', \hat{s}) d\Omega' + S(\vec{r}, \hat{s}, t) \end{aligned} \quad (2.7)$$

Given the complexity of the RTE equation it is most commonly simplified into the Diffusion Approximation (DA), which is valid when the following assumptions are applicable [63].

1. Scattering interactions are dominant over absorption.
2. The region of interest is far from the source and boundaries.
3. Light fluence is not changing rapidly with time.

The DA is based on Fick's Law (Equation 2.8), which describes the diffusion of photons in a scattering medium. J is the diffusion flux showing the amount of movement over time, D is the diffusion coefficient defined in Equation 2.9 and Φ is the intensity. μ'_s is the reduced scattering coefficient incorporating the anisotropy factor g .

$$\vec{J}(\vec{r}, t) = -D\nabla\Phi(\vec{r}, t) \quad (2.8)$$

$$D = \frac{1}{3(\mu_a + \mu'_s)} \quad (2.9)$$

Using these principles the RTE can be simplified into Equation 2.10. There are other forms of the DA that can be selected based on the application, for example there is a frequency domain version of the DA that would be used when phase measurements are available and will be discussed in Section 2.3.

$$\frac{\partial\Phi(\vec{r}, t)}{c\partial t} + \mu_a\Phi(\vec{r}, t) - \nabla \cdot [D\nabla\Phi(\vec{r}, t)] = S(\vec{r}, t) \quad (2.10)$$

With fewer variables the diffusion approximation is a simpler equation to solve than the RTE. The solution is usually done in one of two ways either analytically or numerically depending on the instrument setup and application area [63].

2.2.1 Modified Beer-Lambert Law

Given that the propagation of photons within a medium can be predicted using the RTE and DA it is also necessary to be able to translate the changes in detected intensity into concentrations of chromophores in the medium. Modelling photon propagation allows the differential path length at a given wavelength of light for the medium to be estimated. The differential path length factor can also be obtained experimentally using the time domain and frequency domain source modes described in Section 2.3.1. This path length indicates the average distance each photon travels, once this is known then the modified

Beer-Lambert Law (BLL) can be used to obtain the changes in chromophore concentrations. The modified BLL can be used directly with fNIRS measurements to obtain changes in chromophore concentration and as in the later stages of DOT reconstruction, which will be discussed later in Chapter 3.

The original BLL (Section 2.1.1) relates the change in intensity of source light across a medium (optical density $OD = \ln \frac{I}{I_0}$) to the concentration of absorbing species in the medium. The theory is illustrated in Figure 2.4A, where I_0 is the input intensity, and I is the measured output light.

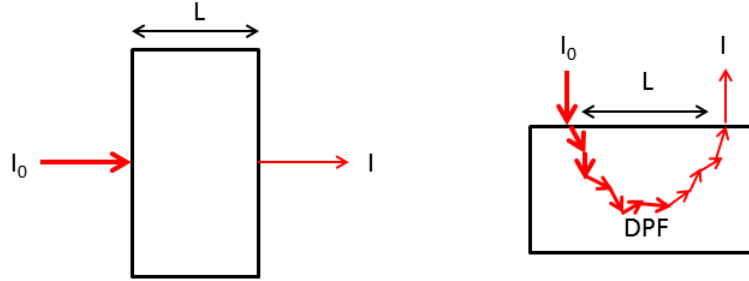


Figure 2.4: Illustration Beer-Lambert Law (A) and Modified Beer-Lambert Law (B).

However the BLL is not designed to take into account scattering effects, which, is problematic for fNIRS measurements. To account for this the BLL was modified to incorporate the differential path length factor (DPF) to calculate the mean photon path and hence the 'thickness' of the sample (Figure 2.4B). While the DPF can be estimated using photon modelling or obtained experimentally [75], using time-domain or frequency-domain methods (discussed in Section 2.3.1) the modified BLL can no longer be used to directly measure chromophore concentration, however it can be used to calculate changes in chromophore concentration Δc . The modification of the BLL includes an additive factor that is dependant on the medium and the geometry of the system which cannot be directly obtained, therefore the factor is assumed to be constant, and hence the reason only changes in chromophore concentrations are calculated [71]. The modified BLL which

includes the DPF is shown in Equation 2.11, instead of using the intensity of input light the modified BLL uses the change in intensity between a reference detector reading (I_{ref}), usually a baseline measurement or the previous measured intensity, and the current detector intensity (I_{meas}), this is used to give a change in optical density (ΔOD). It is possible to compute the chromophore changes without a value for the differential path length, however the concentration changes recovered are offset by a constant factor [76].

$$\Delta OD = L \times DPF \epsilon \Delta C \quad (2.11)$$

As fNIRS measurements are taken at multiple wavelengths, the modified BLL can be solved as a series of simultaneous equation, in matrix form, to calculate the concentrations of the given chromophores in a sample (Equation 2.12).

$$\begin{bmatrix} \Delta HbO \\ \Delta HHb \end{bmatrix} = \frac{1}{L \times DPF} \begin{bmatrix} \epsilon_{HbO\lambda_1} & \epsilon_{HbO\lambda_2} \\ \epsilon_{HHb\lambda_1} & \epsilon_{HHb\lambda_2} \end{bmatrix}^{-1} \begin{bmatrix} \Delta OD_{\lambda_1} \\ \Delta OD_{\lambda_2} \end{bmatrix} \quad (2.12)$$

This example calculates the change in the concentration of oxy (HbO) and deoxy (HHb) haemoglobin for a source and detector a distance L apart, the DPF is the differential pathlength factor for the medium and the change in OD is measured at two wavelengths λ_1 and λ_2 .

2.3 NIR Instrumentation

The design and components that make up a given NIR instrument will vary based on the application and the type of measurement that needs to be acquired for the data reconstruction process (Section 3). In this section an overview of the common components, source modes and probe geometries will be given to show the inherent advantages and

limitations.

2.3.1 Source Modes

There are three distinct types of NIR instruments, which are defined by the source light modes. These are continuous wave (CW), frequency domain (FD) and time domain (TD) modes [77, 78, 79, 80, 69]. A CW instrument is the most simplistic of the three types consisting of Light emitting diodes or laser diode sources and photodiode or avalanche photodiode (for higher sensitivity) detectors. It relies solely on measuring attenuation of the input light (Figure 2.5A). It is thus a fast and relatively inexpensive method, however they cannot give absolute chromophore concentration measurements as there is no way of distinguishing between intensity changes due to scatter and changes due to absorption [81].

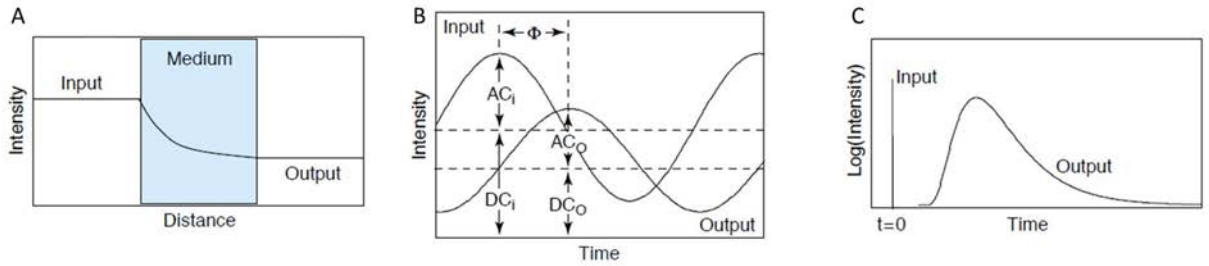


Figure 2.5: NIR source modes - A - Continuous Wave, B - Frequency Domain and C - Time Domain [72]

Frequency domain systems use a similar light source, however the intensity is modulated at frequencies in the MHz range [55]. The high-frequency modulation in FD systems allows measurement of both phase and intensity of light (Figure 2.5B) to provide a more quantitative assessment of optical properties. The phase change of the light indicates the

level of scattering the light has undergone and hence helps distinguish between intensity changes from scatter and absorption sources. For this technique the detectors must be high speed in order to sample at the Nyquist frequency, which in this case would be twice the modulation frequency. These types of detectors, such as photomultiplier tubes, are more expensive and therefore FD instruments to be more expensive to develop [82].

Time domain systems measure both intensity and photon flight time. This gives the the greatest level of depth resolution in comparison to CW and FD instruments. For TD systems both high-speed sources, such as picosecond lasers, and detectors, such as specialised time-gated charge-couple devices (CCD) [83] or PMTs [84], are required. This makes TD system significantly more expensive, which is a limiting factor if large number of instruments were required for a hospital for example. As the detectors count photons from a single laser pulse over time a temporal point spread function is recorded (Figure 2.5C). The spread in the intensity indicates the amount of scattering the light has undergone, the photons that reach the detector last are assumed to be the ones that have travelled the longest path through the medium [55, 85]. It is in this manner that the depth resolution of TD systems is produced. A longer path length implies the greatest scatter and hence the deepest travelling photons. The low scatter photons give shallow signals and the highly scattered photons give deep signals albeit with a poor signal to noise ratio (SNR). This is of course an assumption as a longer flight time does not necessarily mean a deep travelling photon, however it is the most probable path for the photons.

2.3.2 Probe Geometries

Further sub division of NIR instruments come in the form of the probe geometry, a topic briefly explored in Chapter 1. The two main types of probe can be split into two categories, fNIRS probes and DOT probes. Then within these two categories the instruments could be further split based on the 3 sources modes from Section 2.3.1 and by the different reconstruction regimes discussed later in Section 3.

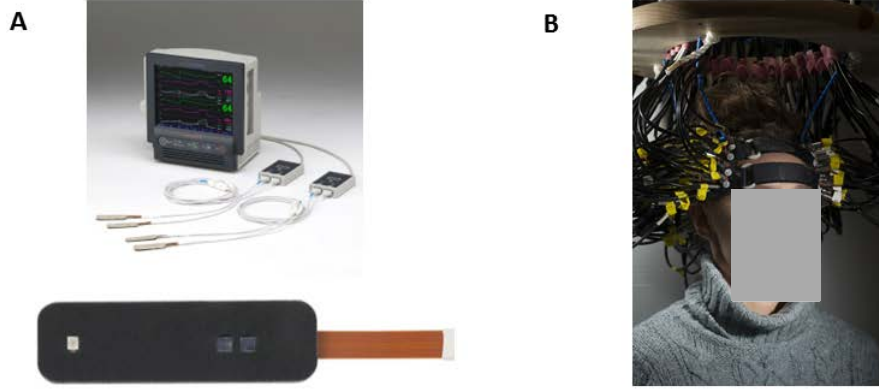


Figure 2.6: A NIRO-200NX (Hamamatsu, Japan) fNIRS probe. B Diffuse optical tomography probe developed by Washing University in St Louis [62].

fNIRS Probe Geometries - An fNIRS probe will consist of a linear array of sources and detectors like the example shown in Figure 2.6A, which is the NIRO-200NX (Hamamatsu, Japan) (other examples in Figure 2.7). As there are only a small number of sources and detectors the number of measurement channels (source-detector combination multiplied by the number of wavelengths) is also small. This means the fNIRS instruments are only suitable for simple reconstruction regimes probing a small target area. Therefore fNIRS instruments will give a global set of recovered parameters representing the entire sampled volume (although techniques are available to improve regional specificity). The typical separation of the sources and detectors ranges from approximately 15 to 55mm and is very dependant on the dynamic range of the detectors being used, as the intensity drop off with increasing distance is exponential. When position on the forehead, the short separations (~ 15 mm) will probe more shallow tissues, for example the skin and bone, while a longer separation of 30 mm upwards will start to probe brain tissue as well. The choice of separation will also influence the maximum depth the probe is capable of sampling, as a general rule the maximum sample depth is $\frac{1}{3}$ to $\frac{1}{2}$ of the source-detector separation [86]. While continually increasing the separation of the source and detectors will increase the sampling depth of the probe, the signal-to-noise ratio (SNR) is the

limiting factor in moving beyond ~ 60 mm, as the signal strength is so low; an effect which is magnified by the need for an ever increasing dynamic range for the detectors.

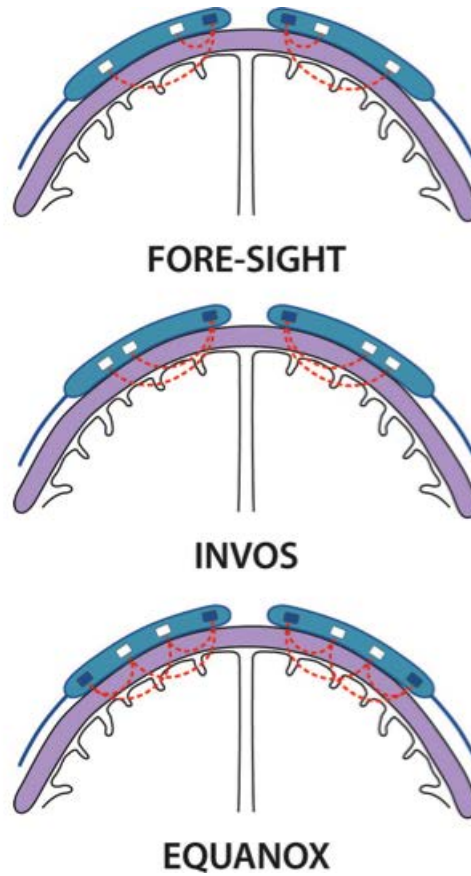


Figure 2.7: Examples of other fNIRS probe geometries, Top - FORE-SIGHT (CAS Medical Systems Inc; Branford, CT), Middle - INVOS 5100C-PB (Covidien; Boulder, CO) and Bottom - EQUANOX Classic 7600 (Nonin Medical Inc; Plymouth, MN) [26]

The setup can be used with all three of the previously mentioned source modes, however the linear nature of the probe gives a very limited ability to locate the spatial origin of any detected signals. Even in the situation where a TD system is being used and photon flight times can be used to work quantitative chromophore concentration by depth, the lateral resolution of the data will be limited.

The advantage of fNIRS probes is that they are small and portable which is of particular interest when looking to move to the pre-clinical environment. They also cost less due to the smaller number of components and the trivial nature of the parameter recovery (see Section 3) means that results are produced in real-time.

DOT Probe Geometries - Diffuse optical tomography probes are large arrays of sources and detectors that provide overlapping measurements over a large region of interest, allowing for more complex parameter recovery than fNIRS geometries. Examples of a DOT probe shown in Figures 2.6B and 2.8, where the sources and detector grid extends around the sides and back of the head to observe haemodynamic changes from different areas of the brain. Having overlapping measures from a 2-dimensional array as opposed to the 1-dimensional fNIRS array means that a 3-dimensional map of chromophore concentrations can be reconstructed with x, y and z dimensions, this is where the 'tomography' comes into play. While DOT produces a spatial map of chromophores, due to the diffuse nature of NIR light the resolution in all directions is limited to approximately 1 cm [22], significantly lower than other functional imaging modalities such as functional MRI, which has resolution in the order of 1mm [87].

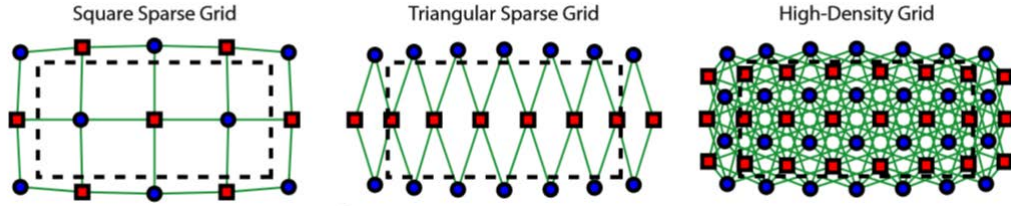


Figure 2.8: Examples of different DOT geometries the square (Left) and Triangular (centre) are considered to be sparse arrays usually used for topography measurements and the high-density array (Right) is usually used for tomography [88].

As well as use in tomography, sparse DOT arrays (shown in Figure 2.8) can also be used to create topography images, these are not depth resolved images and do not require overlapping measurements, instead they are an interpolation of nearest neighbour source-detector combinations, in essence a combination of fNIRS probes over a wide area. The Hitachi ETG-4000 (Hitachi Medical Systems Europe) is an example of a sparse array device.



Figure 2.9: NIRSport portable NIR head cap [89].

Generally DOT systems are very bulky due to the large numbers of optical fibres as well as the housing for all the sources and detectors, which is a limitation to the probability of the instruments. Despite the large array, there systems like the NIRSport (NIRx Medical Technologies) and fNIRS300B (BIOPAC System, Inc) that have been made portable (NIRSport example shown in Figure 2.9).

Although portable versions of DOT probe geometries have been produced they are still expensive in comparison to the fNIRS probes (typically £50k-100k), and therefore are not currently a viable method for mass clinical and pre-clinical monitoring.

2.4 Summary

This chapter discussed the physical principles of absorption and scattering that underpin tissue optics. Using these principles a model of photon transport in tissue, known as the radiative transfer equation, is derived and simplified into the diffusion approximation, which is used as a model of photon migration in a majority of NIR instruments. An understanding of photon migration in tissue and how intensity changes over a given distance forms the basis of the modified Beer-Lambert law, which allows changes in chromophore

concentrations over time to the calculated given a measurement of intensity change.

The different fNIRS and DOT setups were discussed along with their individual limitations and advantages in terms of TBI monitoring. As well as the setup of the instruments, the source modes (CW, FD and TD) were discussed to show the difference in information each could provide. The subject of data reconstruction has been touched upon in this chapter, however the next chapter will go into further detail of how the physical principles discussed can be utilised to reconstruct NIR datasets.

CHAPTER 3

NEAR INFRARED IMAGING AND SPECTROSCOPY - RECONSTRUCTION AND MODELLING

This chapter aims to explain how biologically relevant information is produced from a set of NIR spectroscopy or tomography measurements through the implementation of the diffusion approximation and the modified Beer-Lambert law from Chapter 2. Reconstruction and modelling methods will be grouped into the categories of analytical and numerical reconstructions that can be implemented for both fNIRS and DOT datasets. In general, unless measured intensity is used with the modified Beer-Lambert law to directly calculate chromophore changes, reconstructing optical properties from a dataset will require minimisation of the error between measured and modelled intensity values, which is where the analytical and numerical solutions to the DA come into practice. Modelling intensity values for a given geometry and set of optical values is what is referred to as the 'Forward model'.

3.1 Analytical Methods

An analytical solution is a direct mathematical approach where an exact answer can be found, in this case the equation being solved is the Diffusion Approximation (DA) that is a partial differential equation (Equation 2.10). Depending on the geometry of a

situation, solving the DA equation is not always possible using analytical methods. There are however a series of simple or semi-complex geometries where analytical solutions can be derived that will allow direct calculation of light intensity at a given distance from the source. An analytical solution is the fastest way to calculate light fluence in order to reconstruct measurement data and is used in fNIRS systems where real time data processing is required and the geometries are simple.

In a majority of cases a continuous wave fNIRS device would be used to measure differential changes in chromophore concentrations from a single source-detector pair. In this situation the change in detected intensity can directly be used with the modified BLL equation and a value for differential path length (obtained analytically or experimentally) in order to obtain a value of global chromophore changes in the target volume.

The analytical solution to the diffusion approximation can also be used to find more accurate estimates of the absorption and scattering coefficients (depending on the measurement type) to improve the accuracy of the recovered chromophore concentrations. Analytical solutions to the diffusion approximation for various geometries (such as slabs, cylinders and spheres) have been derived using Green's functions [75]: these models can be used to provide estimations of the differential path length (DPL) or used for forward modelling of data. These solutions tend to be based on a homogeneous medium although there are analytical solutions to the DA, which are built on more complex heterogeneous layered models such as layered slabs [90]. Even with more complex geometries, analytical solutions can only provide accurate results in certain situations (e.g., Muscle oximetry).

Equation 3.1 shows the analytical solution to the diffusion approximation for a semi infinite half-space geometry for an impulse delta function impulse. Where R give the intensity of the reflected light at time (t) after the impulse, when the detector is a distance ρ from the source, μ_a and μ'_s are the absorption and reduced scattering coefficients, c is the speed of light in the medium, and D is the diffusion coefficient [76]. The light attenuation (A) at a distance from the source ρ is described as the negative log of the integral of R over

all time. So by modelling a small change in absorption ($\delta\mu_a$) to find the change in light attenuation (δA), a value of the differential path length (DPL) can be estimated for the medium (Equation 3.2). Here the attenuation, A, (or OD) is defined as $\log(\frac{I_0}{I})$, the log ratio of input to output intensity or, for δA , the intensity change between measurements.

$$R(\rho, t) = (4\pi Dc)^{-\frac{3}{2}} \frac{1}{\mu'_s} e^{\mu_a ct} e^{-\frac{\rho^2 + \mu_s'^{-2}}{4Dct}} \quad (3.1)$$

$$DPL = \frac{\delta A}{\delta \mu_a} \quad (3.2)$$

In the situation where there are multiple source-detector pairs at different separations, such as a DOT array, the approach for using an analytical solution to the DA is less direct; this is where forward modelling of boundary data is used. Boundary data is simply a simulation of the intensity measured at given points on the boundary of a medium, in this case a semi infinite slab. The fitting routines do vary but a general methodology for fitting measurement data to an analytical model in order to obtain optical property estimates, μ_a and μ'_s is outlined in Figure 3.1. Each time the simulated and measurement dataset are compared the optical properties given to the analytical model are updated, until the mismatch between the two datasets reaches a predefined level, or a set number of iterations are reached. Due to the simplicity of analytical models this process is still very fast even in the event of modelling large arrays of sources and detectors.

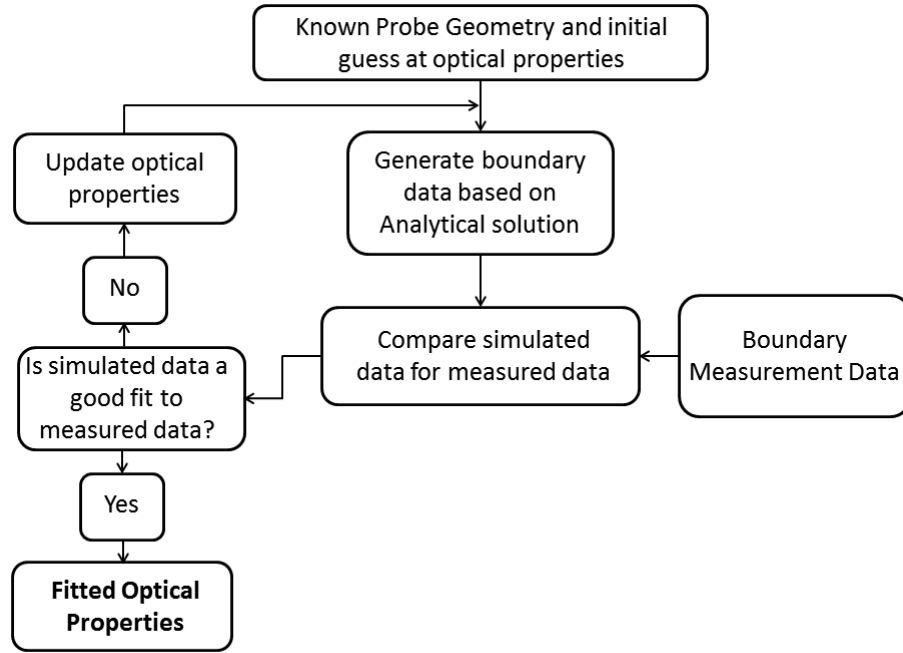


Figure 3.1: Example routine for obtaining optical properties from forward modelling of boundary data.

Using this generalised method to hone in on a set of absorption and reduced scattering coefficients that best fit the measured data, the optical properties can be converted into chromophore concentrations using Equation 2.3. The example shown below is an example of how intensity and phase data can be fitted to an analytical model of an infinite slab, in order to produce a set of global optical properties, this technique, often used for the calibration of data for numerical reconstruction methods (e.g., in NIRFAST), discussed later in this chapter [91, 63]. The iterative fitting algorithm is in itself technically a numerical method however as it is using the analytical solution to generate forward data it is included in this section. This is by no means an exhaustive list of the analytical solutions, but rather an example of its potential applications (analytical solutions for different geometries can be found in Arridge et al [75]).

In this example the measurement data contains both intensity and phase information and therefore fitting forward data to a measured dataset is done with respect to two

parameters. The first parameter ($\frac{\delta\phi}{\delta r}$) is the slope of phase (ϕ) versus source-detector distance (r) and the second parameter is the slope of the log intensity (I) multiplied by source-detector distance (r), versus source-detector distance ($\frac{\delta \ln(rI)}{\delta r}$) (Example shown in figure 3.2). Both of these parameters can be found to be stable in the analytical solution for an infinite medium [91].

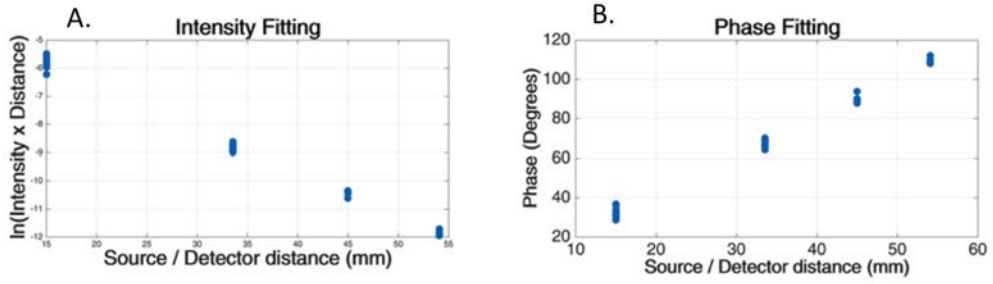


Figure 3.2: Example of intensity (A) and phase (B) data produced in NIRFAST ready for fitting to an analytical model [63].

The fitting is implemented using numerical approximation of the Newton-Raphson method [92], and aims to find a solution for μ_a and μ'_s where the following conditions in Equations 3.3 and 3.4 are met. The Newton-Raphson method requires an initial guess at the suspected root, x_n , (optical properties in this case), with n being the iteration of the fit. A Taylor expansion of the function ($f(x_n)$) up to first order is taken to give a tangent to the function at a given point, x_n , then the root of the tangent is found and used to adjust the value of x_n to a root, x_{n+1} is closer to the actual root of the function using the formula $x_{n+1} = x_n - \frac{f(x_n)}{f'(x_n)}$. The functions being fitted in this situation are shown in

Equations 3.3 and 3.4.

$$\frac{\delta \ln(I_c r)}{\delta r} - \frac{\delta \ln(I_o r)}{\delta r} = 0 \quad (3.3)$$

Where I and ϕ are the intensity and phase at the measurement location for the simulated model (c) and the measurement data (o), r is the distance between the source and detector.

$$\frac{\delta \phi_c}{\delta r} - \frac{\delta \phi_o}{\delta r} = 0 \quad (3.4)$$

For the infinite medium being modelled, the Equations for $(\frac{\delta \ln(rI)}{\delta r})$ and $(\frac{\delta \phi}{\delta r})$ are shown below in Equations 3.5 and 3.6, respectively.

$$\frac{\delta \ln(Ir)}{\delta r} = \left(\frac{\mu_a}{D}\right)^{\frac{1}{2}} \left[1 + \left(\frac{\omega}{\mu_a c}\right)^2\right]^{\frac{1}{4}} \cos \left[\frac{\tan^{-1}\left(\frac{\omega}{\mu_a c}\right)}{2}\right] \quad (3.5)$$

$$\frac{\delta \ln(Ir)}{\delta r} = \left(\frac{\mu_a}{D}\right)^{\frac{1}{2}} \left[1 + \left(\frac{\omega}{\mu_a c}\right)^2\right]^{\frac{1}{4}} \sin \left[\frac{\tan^{-1}\left(\frac{\omega}{\mu_a c}\right)}{2}\right] \quad (3.6)$$

In applying this to the fitting of optical properties the following 'update' equations can be produced, where $\Delta\mu$ is the update to the absorption or reduced scattering coefficient at each iteration and d is a small update to the optical properties (0.0001 in this case [91]). μ represents the measurement data properties being calculated by perturbing the initial guess μ_0 by d to calculate the update parameter.

$$\Delta\mu = \frac{d \left[\frac{\delta \ln(Ir)}{\delta r}(\mu_0) - \frac{\delta \ln(Ir)}{\delta r}(\mu) \right]}{\frac{\delta \ln(Ir)}{\delta r}(\mu_0) - \frac{\delta \ln(Ir)}{\delta r}(\mu_0 + d)} \quad (3.7)$$

$$\Delta\mu = \frac{d \left[\frac{\delta\phi}{\delta r}(\mu_0) - \frac{\delta\phi}{\delta r}(\mu) \right]}{\frac{\delta\phi}{\delta r}(\mu_0) - \frac{\delta\phi}{\delta r}(\mu_0 + d)} \quad (3.8)$$

This method has been shown to converge where the measurement data is good; however, in the situation where the data is noisy or the initial guess at the optical properties is far from the solution, the Newton-Raphson method can break down and give incorrect results. This can also be an issue when the analytical model being used is not truly representative of the measurement geometry or where the changes in optical properties are expected to be large (i.e., the changes are not small enough to be linear). For more complex geometry modelling of a layered head for example, numerical methods are required to obtain more accurate results.

3.1.1 Numerical Methods

When looking at more complex geometries, analytical solution may be either unavailable or inappropriate, instead numerical methods can be used to model forward data for reconstructions. Whereas an analytical solution will most often be fully homogeneous or nearly homogeneous in its interior values, a numerical solution can use fully heterogeneous models to give more accurate results, although the reconstruction time is longer. Numerical solutions are often performed using finite element models (FEM), which are utilised in the following chapters to reconstruct data and will be explained in detail in Section 3.1.1.

Monte Carlo (MC) is another numerical method of modelling the RTE and is often used as a gold standard for validation of other computer models with heterogeneous media [93]. MC uses a statistical approach to modelling and simulates the paths of millions of individual photons through a series of random walks until a set level of counting statistics obtained. The MC techniques are highly versatile and have been implemented for multi-layered tissues geometries, such as that of the human head [94, 95]. The computational

time required to complete the simulations is the reason MC methods are not currently as widely used as FEM-based approaches, however there have been many advances in both parallel computing and utilisation of graphics processing units in order to reduce this computational time [96, 97].

In the following section an outline of how optical properties can be reconstructed using numerical methods will be shown, as a demonstration a FEM-based approach will be used to produce forward data.

Reconstruction Routines

In this section two different types of reconstruction will be discussed, a linear single step routine and an iterative non-linear routine. Linear reconstructions are for measuring small perturbations in the optical proper/chromophore concentration of a medium based on a small change in detected light intensity ($\delta I = \ln(I_{anom}) - \ln(I_{ref})$). A non-linear reconstruction uses an iterative routine to make many small updates to the optical properties until converging on a solution. This method is better suited for finding quantitatively accurate chromophore concentrations and for situations where the changes in chromophore concentration are large, as reconstruction can be done on a single set of intensity values so no 'difference' data is required. Both methods require the use of a forward model for data simulation.

Finite Element Models - are a method of solving partial differential equations such as the diffusion approximation by discretising a complex geometry (see example of a head FEM in Figure 3.3), into a series of small tetrahedral, non-overlapping, elements over which the optical properties can be considered constant (a method that has been validated though MC methods) [98, 63, 99]. As the DA is non-linear with respect to optical properties, breaking down an imaging domain into a series of small elements

acts to create many small areas over which optical properties can be considered linear. Therefore, finding the light fluence at any given point in a model becomes a system of linear algebraic equations that can be solved in matrix form [63]. A tetrahedron is the most common element shape for a 3D geometry, a 2D geometry would be represented using triangles. For 3D geometries each element in the tetrahedron is represented by 4 nodes, apart from the surface of the mesh, which will have three nodes and a triangular element. As the source modelled in the DA is isotropic, the source within a FEM is placed one scattering distance ($\frac{1}{\mu'_s}$) inside the outer boundary [63].

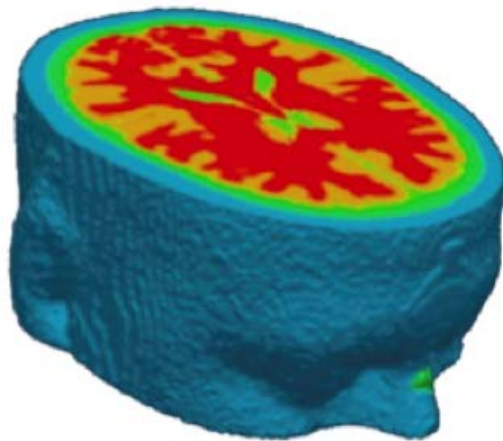


Figure 3.3: Example of a finite element model of a head [58].

The meshes used for FEM-based approaches can be produced in a variety of ways such as segmentation of a 2D imaging stack from modalities like MRI or CT (which will be covered in Chapter 5) or volumes obtained through surface capture. There are numerous software packages available for mesh generation with two open-source examples being iso2mesh [100] and NIRFAST [63], with the latter being the package used within this thesis (see later chapters).

The Jacobian Matrix - The Jacobian defines the relationship between the changes boundary data of a particular model with respect to a small change in optical properties over all nodes. For this reason it is often referred to as the 'sensitivity' matrix. The changes in optical properties can either be 'standard' absorption and scatter coefficients (for single wavelength cases) or chromophore concentrations for spectral (multiple wavelength) cases. In the spectral cases a constrained fit to the modified BLL is used to translate optical properties into chromophore concentrations, and Mie scattering theory is used to translate scattering coefficients into a generalised scatter power and amplitude (from Section 2). The structure of a standard and a spectral Jacobian matrix are shown in Figures 3.4 and 3.5, respectively.

$$J = \begin{bmatrix} \frac{\delta \ln I_1}{\delta \kappa_1} & \frac{\delta \ln I_1}{\delta \kappa_2} & \dots & \frac{\delta \ln I_1}{\delta \kappa_{NN}}; & \frac{\delta \ln I_1}{\delta \mu_{a1}} & \frac{\delta \ln I_1}{\delta \mu_{a2}} & \dots & \frac{\delta \ln I_1}{\delta \mu_{aNN}} \\ \frac{\delta \theta_1}{\delta \kappa_1} & \frac{\delta \theta_1}{\delta \kappa_2} & \dots & \frac{\delta \theta_1}{\delta \kappa_{NN}}; & \frac{\delta \theta_1}{\delta \mu_{a1}} & \frac{\delta \theta_1}{\delta \mu_{a2}} & \dots & \frac{\delta \theta_1}{\delta \mu_{aNN}} \\ \frac{\delta \ln I_2}{\delta \kappa_1} & \frac{\delta \ln I_2}{\delta \kappa_2} & \dots & \frac{\delta \ln I_2}{\delta \kappa_{NN}}; & \frac{\delta \ln I_2}{\delta \mu_{a1}} & \frac{\delta \ln I_2}{\delta \mu_{a2}} & \dots & \frac{\delta \ln I_2}{\delta \mu_{aNN}} \\ \frac{\delta \theta_2}{\delta \kappa_1} & \frac{\delta \theta_2}{\delta \kappa_2} & \dots & \frac{\delta \theta_2}{\delta \kappa_{NN}}; & \frac{\delta \theta_2}{\delta \mu_{a1}} & \frac{\delta \theta_2}{\delta \mu_{a2}} & \dots & \frac{\delta \theta_2}{\delta \mu_{aNN}} \\ \vdots & \vdots & \ddots & \vdots & \vdots & \vdots & \ddots & \vdots \\ \frac{\delta \ln I_{NM}}{\delta \kappa_1} & \frac{\delta \ln I_{NM}}{\delta \kappa_2} & \dots & \frac{\delta \ln I_{NM}}{\delta \kappa_{NN}}; & \frac{\delta \ln I_{NM}}{\delta \mu_{a1}} & \frac{\delta \ln I_{NM}}{\delta \mu_{a2}} & \dots & \frac{\delta \ln I_{NM}}{\delta \mu_{aNN}} \\ \frac{\delta \theta_{NM}}{\delta \kappa_1} & \frac{\delta \theta_{NM}}{\delta \kappa_2} & \dots & \frac{\delta \theta_{NM}}{\delta \kappa_{NN}}; & \frac{\delta \theta_{NM}}{\delta \mu_{a1}} & \frac{\delta \theta_{NM}}{\delta \mu_{a2}} & \dots & \frac{\delta \theta_{NM}}{\delta \mu_{aNN}} \end{bmatrix},$$

Figure 3.4: Structure of Jacobian matrix for a single wavelength case. The optical properties μ are separated into absorption μ_a and the diffusion coefficient κ (referred to previously as D). $\frac{\delta \ln(I_i)}{\delta \kappa_j}$ and $\frac{\delta \ln(I_i)}{\delta \mu_{a,j}}$ are sub-matrices showing the change in log intensity arising from the small change in optical properties at the i th measurement at the j th mesh nodes. $\frac{\delta \Theta_i}{\delta \kappa_j}$ and $\frac{\delta \Theta_i}{\delta \mu_{a,j}}$ are similar sub matrices corresponding to changes in phase data from frequency domain measurements [19].

$$J = \begin{bmatrix} J_{c1,\lambda1} J_{c2,\lambda1} J_{c3,\lambda1} J_{a,\lambda1} J_{b,\lambda1} \\ J_{c1,\lambda2} J_{c2,\lambda2} J_{c3,\lambda2} J_{a,\lambda2} J_{b,\lambda2} \\ \vdots \\ J_{c1,\lambda n} J_{c2,\lambda n} J_{c3,\lambda n} J_{a,\lambda n} J_{b,\lambda n} \end{bmatrix}$$

Figure 3.5: Structure of the Jacobian matrix for a spectral, multi wavelength case. There is a sub-matrix for each chromophore (c), the scatter amplitude (a) and scatter power (b) for each measurement wavelength, each having dimensions of the number of mesh nodes by the number of measurements [19]. NN is the number of unknown parameters and NM is the number of boundary measurements.

The Jacobian matrix can be calculated in a number of ways, the method implemented in NIRFAST and thus the reconstructions in later chapters is known as the adjoint method. The adjoint theorem states that measurement of flux at a detector j on a mesh due to a source at node i is equal to the measurement of photon density at node i that can be attributed to a source at detector j [19]. There are other methods that are more computational intensive, such as the perturbation method where forward data is produced both before and after a small change in optical properties, or the direct method that involves differentiation of the DA equation to obtain the values at each node.

Linear single step reconstructions - As mentioned previously, this reconstruction method is designed to use 'difference' data in order to calculate small changes in chromophore concentration/optical properties within a medium. This method relies on the production of a Jacobian matrix from the forward model. As the Jacobian represents the influence each node in a simulated volume has on the boundary data, by inverting the Jacobian (J^{-1}) and multiplying it by the change in measure boundary data (δI) the change in optical properties ($\delta\mu$) can be obtained as shown in Equations 3.9 and 3.10 [101, 65].

$$\delta I = \ln\left(\frac{I_{anom}}{I_{ref}}\right) = J\delta\mu \quad (3.9)$$

Where I_{ref} represents a reference set of boundary measurements from which to measure the change to the current time point I_{anom} . $\delta\mu$ represents the change in optical properties, which depending on the format of the Jacobian (J) can be either absorption and scattering coefficients or chromophore concentrations.

$$\delta\mu = J^{-1}\delta I \quad (3.10)$$

Non-linear iterative reconstructions - Non-linear reconstruction use the same approach of generating forward data based on an initial set of optical properties, however this time an inverse model to update the optical properties is used to hone in on a quantitatively accurate set of recovered parameters rather than just measuring changes in optical properties. The general steps of the reconstruction routine are as follows [65].

1. Model probe and geometry of medium - initial guess at optical properties. Here the input is a 3D mesh where each node is assigned a set of optical properties. The coordinates of the sources and detectors on the mesh are defined.
2. Run Forward Model - FEM or MC approach. Using the models produced in the previous step the light path from each of the sources is simulated to produce a set of boundary data (i.e. a set of intensity measurements at each detector position), and a Jacobian matrix for the model.
3. Calculate root mean squared error between the simulated boundary data, from the previous step, and the inputted measurement data. This will produce a single error value that can be check against a predefined tolerance value. If the error is within

tolerance the reconstruction will end, if the error is above the tolerance then the reconstruction will move to the next iteration.

4. Inverse problem is set up to update the optical properties of the model. Here the Jacobian matrix is inverted and any regularisation applied before solving Equation 3.10.
5. The inverse problem, Equation 3.10, is solved producing an update for the optical properties at each node in the model.
6. The optical properties of the model are updated and the loop returns to step 2. This process will continue until a predefined error or number of iterations is reached.

The initial guess at optical properties can either be based on a calibration of experimentally derived parameters, which can then be used to produce a set of boundary intensity measurements in the same format as the measurement data. Step 3 is usually performed using a modified version of the Tikhonov minimisation, which looks at the least squares error and is particularly suited to ill-posed problems [102]. The modified version of this minimisation is shown in Equation 3.11 [19].

$$\chi^2 = \min_{\mu} \left\{ \sum_{i=1}^{NM} (\Phi_i^M - \Phi_i^C) + \lambda \sum_{j=1}^{NN} (\mu_j - \mu_0)^2 \right\} \quad (3.11)$$

Φ^M and Φ^C are the measurement data and forward data respectively, with NM being the number of measurements and NN being the number of nodes. λ is the Tikhonov regularisation parameter, μ_j and μ_0 are the calculated and initial guess at absorption coefficient, with χ^2 representing mismatch error between them. To minimise this function the first order derivative is set to 0. λ is defined as the ratio of the variances between the measured and the initial estimate of the optical properties. Generally, for a good estimate large λ values are used in order to make small changes to the model properties. For poor guesses small λ values are used to allow larger updates to the model properties. Step

4 involves calculation of the Jacobian (from the forward model). Once the Jacobian is calculated it is inverted using the Moore-Penrose generalised inverse [103] and regularised to solve the inverse problem (Equation 3.12) to give the optical property value update before starting the next iteration. As the Jacobian is a non-square matrix it must be multiplied by its transpose before it can be inverted.

$$(J^T J + \lambda I) \delta \mu = J^T \delta \Phi - \lambda(\mu_i - \mu_0) \quad (3.12)$$

J and J^T are the Jacobian matrix and its transpose, I is an identity matrix, $\delta \Phi$ is the data mismatch and $\delta \mu$ is the update to the optical properties or chromophore concentration depend on whether standard or spectral reconstruction are being performed. The iterative process will stop once a predefined number of iterations have passed or a set projection error between modelled and measured data is reached.

Numerical methods offer a powerful tool in the accurate reconstruction of chromophore concentrations. The limitation being that large datasets must be collected in order to reconstruct the already ill-posed (meaning that there are more unknowns than there are measurements [19]) problem and the iterative solutions take minutes-hours (unless using single step reconstructions) to hone in on the correct set of values depending on the size of the mesh. This method can also be used to perform dynamic imaging to speed up reconstruction time by pre-calculating and inverting the Jacobian then using a single step calculation rather than iterating through.

3.2 Methods for reducing Superficial Signal Contamination

As the topic of superficial contamination is a prominent issue within NIR imaging and spectroscopy, this next section is designed to explore some of the methods that have been devised to reduce its effects. The methods range from system design to computational processing.

System Design - While it is only necessary to have one source detector pair to calculate changes in chromophore concentration in a medium, this one pair will sample deep signals as well as superficial signals. Therefore, the first method for reducing superficial contamination is the use of multi-distant source-detector combinations. A close source-detector (SD) pair at around 15 mm apart will sample mainly superficial regions and a SD pair at around 30 mm will sample both deep and superficial regions. Therefore the short SD measurement can be used as a regressor to remove the superficial contributions [104, 105, 49]. This is a feature that is almost inherent in DOT devices where 3D reconstructions of optical properties automatically separate contributions by layer [104], also having multiple overlapping measurements obtained over a smaller sample area will improve the ill-posed nature of the inverse problem that can improve reconstruction accuracy [60]. Even though DOT systems reconstruct 3D properties, they still suffer from hypersensitivity in the superficial regions (a side effect of the exponential decrease on light intensity with distance) so the deep signals are still underestimated. To account for this an extra form of regularisation can be added into the Jacobian matrix formation that provides a depth-based weighting to reduced hypersensitivity to superficial changes [106].

Time Resolved Spectroscopy - Systems capable of performing time resolved measurements can also be used to reduce the amount of superficial signal contamination. A time resolved system will use a laser source capable of producing an input pulse in the

picosecond range. Then using a high-speed detector, the output intensity from a single pulse can be measured over time (ns range) to produce a temporal point spread function (example shown in Figure 3.6).

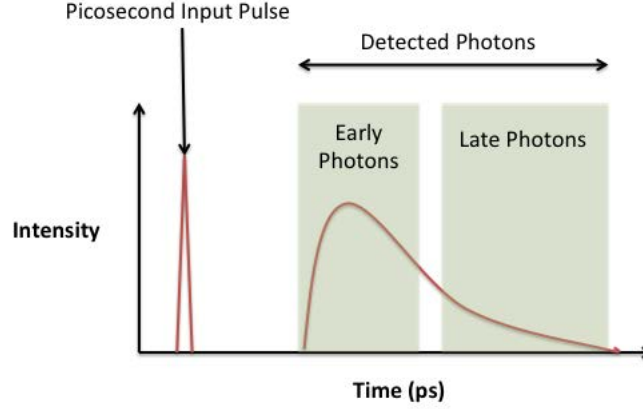


Figure 3.6: Illustration of time resolved spectroscopy.

The 'early' photons have only traversed the shortest distance between the source and detector and the 'late' photons will have travelled the furthest. In the context of performing measurements on the head, the 'early' photons represent shallow photons which have passed mainly through the superficial skin and bone tissues, whereas the 'late' photons will have travelled into the deeper brain tissue. Therefore by using only the 'late' photons in the reconstruction process the influence of the superficial layers can be reduced.

Signal Filtering - Another method of reducing superficial contamination is frequency domain filtering. While this method will not directly affect the quantitative accuracy of recovered parameters, it can be used to remove variations in the signals that are not due to deep tissue changes. The variations in question are physiological signals that are present in superficial tissues such as cardiac pulsation, respiratory changes and blood pressure (Mayer) waves (shown in Figure 3.7 [107]). These signals can be filtered

out using band-pass or high-pass filter after performing a Fourier transform on the time series data. The blood pressure and respiratory signals tend to be between 0.08 Hz and 0.12 Hz, with cardiac signals being at 1 Hz (60 beats per minute).

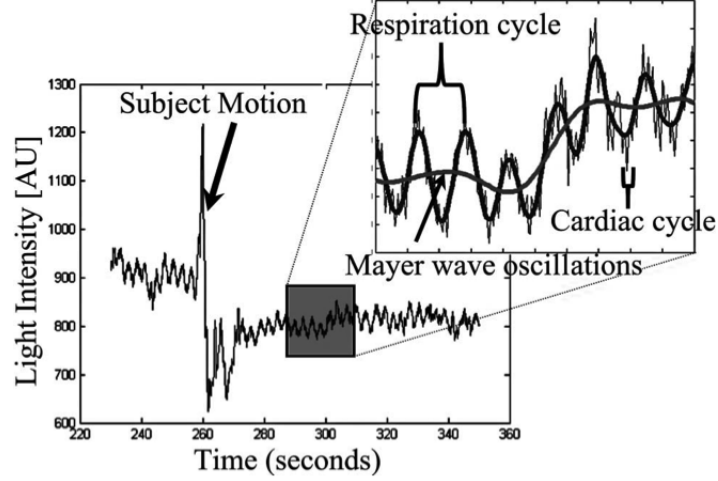


Figure 3.7: Example of physiological noise in fNIRS signals [107].

Reconstruction Models - Another method of reducing superficial contamination and parameter recovery in general is to use more accurate models for forward data simulation. If the model is a good match for the medium in terms of its internal and external structure then this structural prior information can be used to inform the DOT reconstruction process meaning better reconstruction accuracy. Realistic head models can be produced through segmentation and meshing of MRI or CT data [58]. Functional MRI data has also been used as a way to regress out superficial signals in a technique known as extended superficial signal regression (ESSR), where Blood Oxygen Level Dependant (BOLD) MRI changes in scalp voxels are used to inform reconstructions [108].

Spatially Resolved Spectroscopy - Another algorithm, which has been used with fNIRS devices, is spatially resolved spectroscopy (SRS).

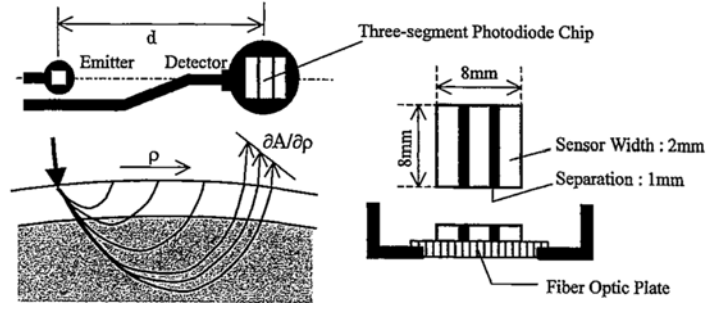


Figure 3.8: Illustration of NIRO 300 (Hamamatsu, Japan) setup to obtain spatially resolved spectroscopy measurements [76].

Spatial resolved spectroscopy (SRS) was a technique developed in 1999 aimed at obtaining a relative index measure of tissue oxygenation (TOI) and tissue haemoglobin (THI) in deep tissues, without contamination from superficial layers by analysing the gradient over a series of multi-distance detectors (see Figures 3.8 and 3.9) [76].

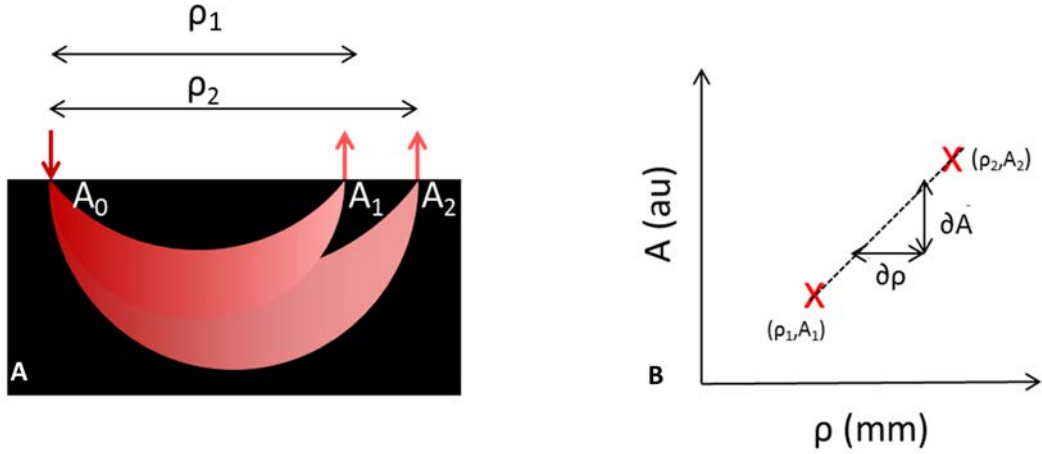


Figure 3.9: A - Illustration of the spatially resolved spectroscopy measurements of light attenuation (A) at distance (ρ) from the source. B Plotting gradient of light attenuation measurements (A) over distance (ρ) to give ($\frac{\partial A}{\partial \rho}$)

SRS is a widely used algorithm (Equations 3.13 and 3.14) and was derived through differentiation of the analytical solution to the DA (Equation 3.1) with respect to the source-

detector distance, ρ .

$$k\mu_a(\lambda) = \frac{1}{3(1 - 6.3E^{-4}\lambda)} \left(\ln(10) \frac{\delta A(\lambda)}{\delta \rho} - \frac{2}{\rho} \right) \quad (3.13)$$

k is an unknown constant, λ is wavelength, μ_a is the absorption coefficient, A is the detector measurement, ρ is the distance between detectors, and ϵ is the extinction coefficient. From the relative concentrations of HbO and HHb the TOI (oxygen saturation equivalent) and THI (HbT equivalent) can be produced. Using the technique requires measuring $\frac{\delta A}{\delta \rho}$; this is change (gradient) in detected light that is attenuated over a series of multi-distance detectors shown in Figure 3.9.

$$\begin{bmatrix} kHbO \\ kHHb \end{bmatrix} = \begin{bmatrix} \epsilon_{i,j}^{-1} \end{bmatrix} \begin{bmatrix} k\mu_a(\lambda_1) \\ k\mu_a(\lambda_2) \\ k\mu_a(\lambda_2) \end{bmatrix} \quad (3.14)$$

This method is not designed to improve quantitative accuracy of recovered parameters; instead its primary focus is to simply map deep signal changes. It has been verified for phantoms and been used for both muscle oximetry work and cerebral monitoring [76, 5, 109]. TOI and THI are calculated in the same way as SO_2 and HbT respectively, however, instead of using HbO and HHb values they use the relative $kHbO$ and $kHHb$ values calculated in Equation 3.14.

3.3 Summary

This section has discussed the different methods that can be used to model NIR light propagation through a medium for use in data reconstruction. With the exception of simple fNIRS, which directly calculates chromophore concentration changes using the modified

BLL, all other reconstructions required a model to produce forward data. Analytical solutions to the DA can be made for simple, often homogeneous media, however numerical methods are required to model more complex heterogeneous media. Numerical methods take longer to produce forward data, however they are more versatile than analytical models.

Reconstruction of small changes in optical parameters can be achieved using back projection of 'difference' data using the inverted Jacobian matrix (sensitivity matrix) in a linear single step process. For a more quantitative reconstruction, a non-linear iterative fitting routine is used to hone in on a more accurate set of optical parameters. All reconstructions will inherently have hypersensitivity to shallow (superficial) signals and therefore a multitude of techniques have been devised to reduce the effect. The use of short SD separation and overlapping measurements are the most common forms of regressing or reconstructing for superficial signals. Filtering of data in the frequency domain can also be used to remove any signal variations due to physiological noise. The SRS technique can also be used to weight reconstructed parameters towards deep tissue changes and hence reduce superficial influence. Testing of the SRS method as well as other fNIRS devices and probe geometries are performed in Chapter 4.

CHAPTER 4

NEAR INFRARED SPECTROSCOPY - DEVICE SIMULATION AND TESTING

4.1 Introduction and Aims

The main aim of this chapter is to address the concerns in the literature (outlined in Chapter 1) that cerebral changes measured by fNIRS devices are obscured by variations in superficial haemodynamics, which is limiting the use of fNIRS in TBI where no normative baseline measurements are available to reference chromophore changes. This is done through a series of simulations and healthy volunteer studies, starting by going back to basics and looking at the sensitivity of a number of commercial fNIRS probe geometries to absorption changes in the brain, through model-based analysis using NIRFAST. Such testing yields information about the desirable features of a fNIRS probe in order to fine tune any future hardware developments and answers the fundamental question of whether we are in fact capable of detecting cerebral signals. The aim of these studies was to confirm the validity of fNIRS signals and assess the accuracy of some of the commercially employed algorithms designed to reduce the effects of superficial contamination.

In order to test fNIRS devices in both simulation and healthy volunteer investigations, a testing protocol was required that would allow differentiation between superficial and cerebral haemodynamics. For this the *Valsalva Manoeuvre* (VM), detailed in Section 4.3,

was used as it can induced profoundly different changes in the superficial and cerebral tissues and thus making the signal origins easier to trace. Using this protocol, two commercial available probes were modelled. The first was the NIRO-200NX (Hamamatsu, Japan), a CW system that uses the Spatially Resolved Spectroscopy (SRS) method to look at relative changes in deep tissue oxygenation. The second was the ISS Oxiplex TS (Imagent, USA), a FD system using multi-distant, AC intensity, measurements, along with phase, to determine quantitative scatter and absorption coefficients. The ISS system was also used in healthy volunteer investigations where the level of superficial contamination was artificially lowered through the use of vasopressor injections to the forehead, in order to investigate the effect on the fNIRS signals when skin blood flow is reduced and therefore the potential for signal contamination.

4.2 Sensitivity simulations on existing fNIRS probe geometries

4.2.1 Jacobian Analysis

As described in Chapter 2, the Jacobian matrix is the differential of the surface measurements with respect to the optical properties of a model at a given point. Therefore, it can be referred to as a sensitivity matrix, describing how much influence a change in optical properties, at a particular point in the model, will have on the overall detector measurements. Thus, analysis of the Jacobian matrix is a good way to assess the sensitivity of different probe geometries to absorption changes in the brain. As the main aim of this work is to develop fNIRS for use in TBI, the sensitivity of the probe geometries will be assessed at a depth of 21 ± 4 mm from the surface of the head as this is the average depth of the white-grey matter interface as measured from patient CT scans [42].

Methodology

For the simulations five commercially available fNIRS probe geometries (details in Appendix .1) were positioned centrally on the forehead region of the ICBM152 Atlas model [58, 110, 111], 3 cm above the nasion point (the air sinus was not included in the model). The ICBM152 Atlas model is based on the average of 152 segmented head MRIs, and was designed for use in brain activation studies [111]. The Atlas model was processed using NIRVIEW [112] to create a series of masks that were imported into NIRFAST [63] and used as a basis for volumetric mesh creation. The node spacing in the meshing process was set to 1.5 mm, which gave a total of 574,999 nodes. To decrease the reconstruction times the Atlas model was cropped to a smaller forehead region and re-meshed at the same node spacing so the number of nodes was reduced to 111,840 (Figure 4.1A and B). The internal structure of the Atlas model consisted of 5 layers, 1 - Skin, 2 - Bone, 3 - Cerebral spinal fluid (CSF), 4 - White matter and 5 - Grey matter, as shown in Figure 4.1C, however for the purpose of the simulations, regions 3-5 were grouped into a single 'brain' region, labelled 3. The optical properties of the mesh used for the simulations were taken from the literature [113] and are shown in Appendix .2.

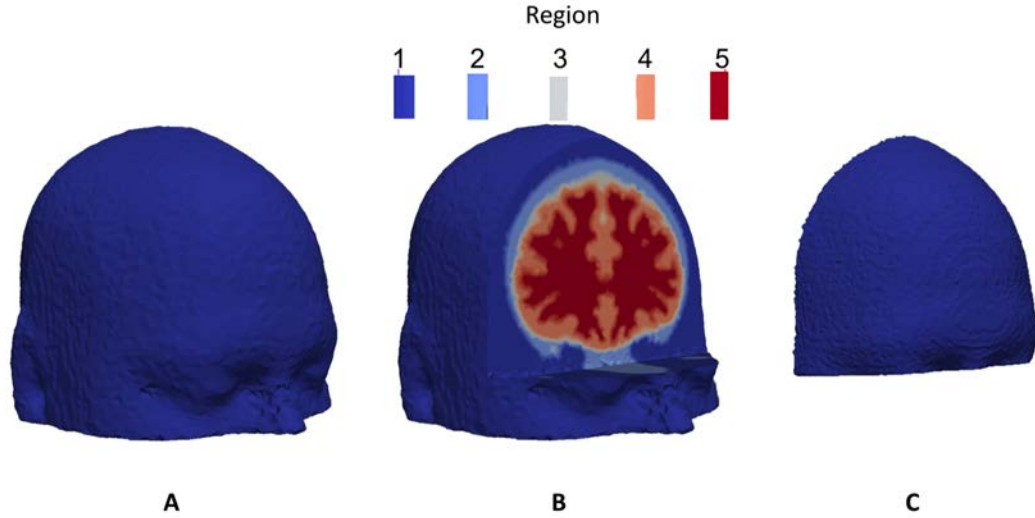


Figure 4.1: Atlas model used for NIRFAST simulations. A - Whole head, B - Clipped head showing internal structure, C - Cropped forehead region. The region labels are: 1 - Skin, 2 - Bone, 3 - Cerebral spinal fluid (CSF), 4 - White matter and, 5 - Grey matter.

The 5 probe geometries modelled were the: INVOS 5100C-PB (Covidien; Boulder, CO); EQUANOX Classic 7600 (Nonin Medical Inc; Plymouth,MN); FORE-SIGHT (CAS Medical Systems Inc; Branford,CT); NIRO-200NX (Hamamatsu, Japan) and ISS Oxiplex TS (ISS Inc, USA). Figure 4.3 shows the positioning of the EQUANOX probe geometry on the Atlas model. The probe details are shown in Figure 4.2.






Probe Name	Wavelengths (nm)	Source-Detector Separation (mm)	No. Sources	No. Detectors	No. Measurements	Schematic
ISS Oxiplex TS	690, 830	30, 35, 40, 45	4	1	8	
INVOS 5100C-PB	730, 810	30, 40	1	2	4	
FORE-SIGHT	690, 780, 805, 850	15, 50	1	2	8	
Equanox Classic 7600	730, 810, 880	20, 40	2	2	12	
Niro 200NX	735, 810, 850	37, 43	1	2	6	

Figure 4.2: Details and schematics of the five probe geometries being modelled in this investigation. For the schematic diagrams X represents a detector and O represents a source.

Usually fNIRS probes would be positioned to the left or right of the forehead in order to avoid the air sinus located centrally on the forehead above the bridge of the nose. However, the sinus is not modelled in the Atlas and so the probes were positioned central for simplicity as the target volume being sample has the same region thicknesses.

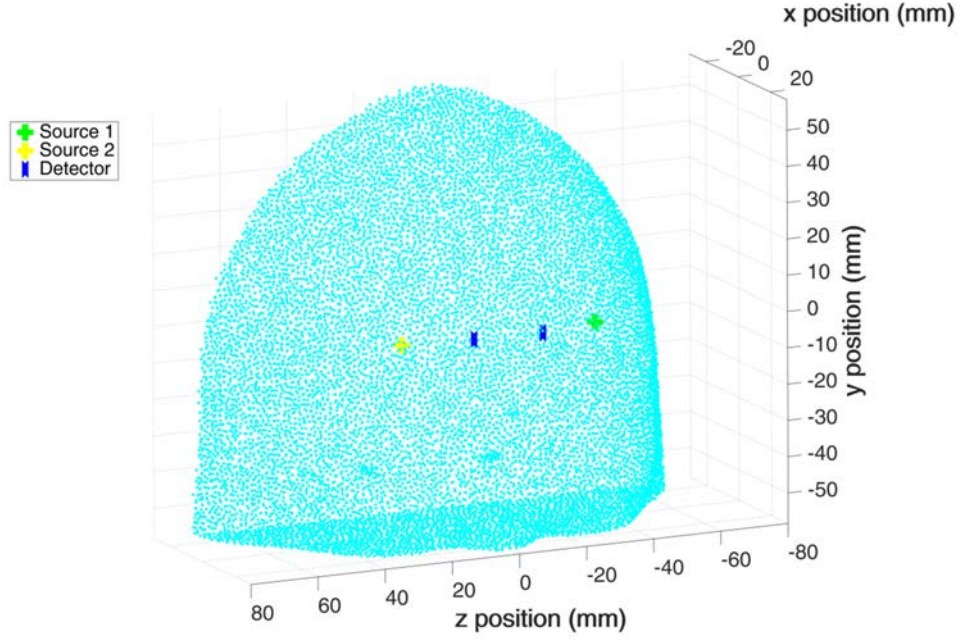


Figure 4.3: Example of fNIRS probe geometry modelled on the Atlas

The Jacobian matrix was calculated in NIRFAST for a continuous wave spectral (at the given wavelengths for each fNIRS probe) model. The Jacobian, as described in Chapter 2, contains sensitivity values for each node with respect to all the source wavelengths and measured chromophore (HbO, HHb, Scatter power and amplitude etc.). Therefore in order to obtain a combined sensitivity the Jacobian was summed over all wavelengths and chromophores to give a singular sensitivity value per node. Starting at the central point of the probe in the axial plane, the sensitivity profile was taken as the values along a path perpendicular to this point in the coronal plane.

Results

It is an inherent part of all fNIRS probes that there will be a majority of the sensitivity in the shallow depths just underneath the sources and detectors. This leads to reconstructed parameters being heavily weighted towards superficial changes. Therefore, the ideal probe geometry would have an even sensitivity with depth, however as this is an unrealistic aim the probe sensitivities are assessed by locally normalising each Jacobian

so then we can look at the sensitivity of the probe geometry as a function of its maximum sensitivity values, showing which has the most 'even' response (shown in Figure 4.4).

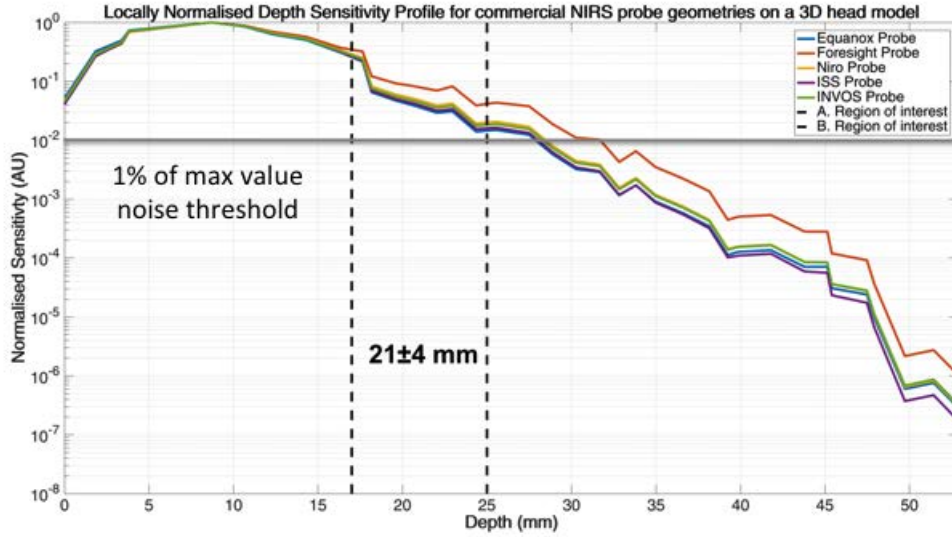


Figure 4.4: Sensitivity profiles for the 5 fNIRS probe geometries modelled on the Atlas. Each probe is normalised to its own maximum sensitivity. The region of interest is the 'ideal' target depth measured from 50 CT scans of TBI patients and has its lower bound at A - 17 mm and its upper band at B - 25 mm (shown by the black dashed lines).

The locally normalised sensitivity data suggested that the FORESIGHT probe had the greatest sensitivity to the brain region as a function of its maximum sensitivity value. This highlights the use of long source-detector separations (50 mm in this case) and the use of multiple wavelengths. The simulations also showed that all the probe geometries are capable of sampling at a depth relevant for monitoring usable TBI parameters. Only sensitivity values greater than the noise threshold of 1% were considered relevant. While the noise threshold of a system will typically be defined by the dynamic range of the detectors and will vary based on the source-detector separation, 1% was used as a repre-

sentative noise floor for the simulations as it is in line with literature values quoting noise levels of 0.12-1.42 % for separation of 13-48 mm respectively [113]. This is an example of one probe location on the head model. If the sensitivity was sampled over multiple probe locations we would expect to see a range differing depth sensitivity values. This is because the composition of the target volume will change, meaning there will be different levels of scatter and absorption.

Conclusion

Jacobian analysis has highlighted that the key to increased sensitivity in the brain region is the use of multiple wavelengths and the use of long source-detector separations (even though in reality the maximum separation will be defined by the signal-to-noise ratio of the system and the dynamic range of the detectors). Over all the probe geometries modelled there was clearly hypersensitivity in the superficial (shallow) regions in comparison to deep (brain) regions. Despite this all probe geometries showed the ability to sample the brain at the depth of 21 ± 4 mm, but had sensitivity values of greater than 1% of their maximum value.

4.2.2 Singular Value Analysis

Singular value analysis of the Jacobian has been used throughout the field of NIR imaging; used to optimise source-detector locations [114] and as a form of regularisation in the reconstruction process [115, 116]. The singular value decomposition of a matrix, in this case the Jacobian, takes the form shown in Equation 4.1.

$$J = USV^T \tag{4.1}$$

Where J is the Jacobian matrix, U and V are orthonormal matrices that contain the eigenvectors of J , and S is a matrix containing the singular vales of J [116]. The matri-

ces U and V can be thought of as the eigenvectors in the detection and imaging space respectively. The magnitude of S defines the 'importance' of paired eigenvectors between U and V . In essence the higher the singular values (with magnitudes over a given noise threshold) the more information there is to link the detection and imaging spaces, thus providing better reconstruction detail or resolution.

Methodology

By extending this principle to Jacobian values corresponding to the brain region only, it is possible to assess the 'information content' a given probe geometry can provide for reconstruction of brain tissue changes. Using the same mesh as was used for the Jacobian analysis in Section 4.2.1, the singular values of the Jacobian nodes corresponding to brain regions only were calculated using the MATLAB SVD function. The probe geometries and optical properties from Appendix .1 and .2, respectively, were used to produce the Jacobian in NIRFAST before singular value decomposition was implemented. The magnitude of the singular values for each probe was normalised to its own maximum values in order to give a comparison between probes. As there was no noise in the simulations the noise level from literature sources was implemented as 1% of the maximum singular value magnitude [116].

Results

The results in Figure 4.5 show that the probe geometry with the greatest information content in the brain region was the EQUANOX. This probe has the largest number of measurement channels and highlights the benefit of collecting overlapping measurements at multiple wavelengths.

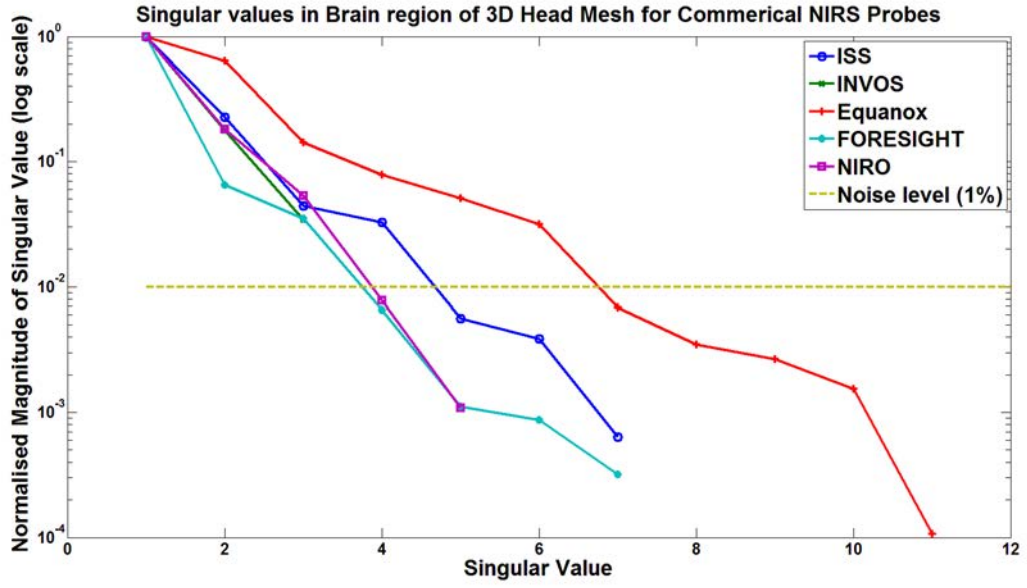


Figure 4.5: Magnitude of singular values obtain from Jacobian sensitivity values corresponding the brain nodes in the Atlas-head model from each of the 5 fNIRS probe geometries. The magnitude of the singular values are normalised to its local maximum. The noise threshold is shown as 1% of the normalised maximum.

Figure 4.6 quantifies the locally normalised magnitude of singular values over the 1% noise threshold. It shows that the probe with the second greatest information content in the brain is the ISS probe; another probe that uses a series of multi-distant, overlapping measurements. All of the probe geometries simulated showed information content in the brain tissue regions; the SVD analysis highlighted the key features of probes, which maximised brain region information content i.e., multiple wavelengths and overlapping source-detector pairs.

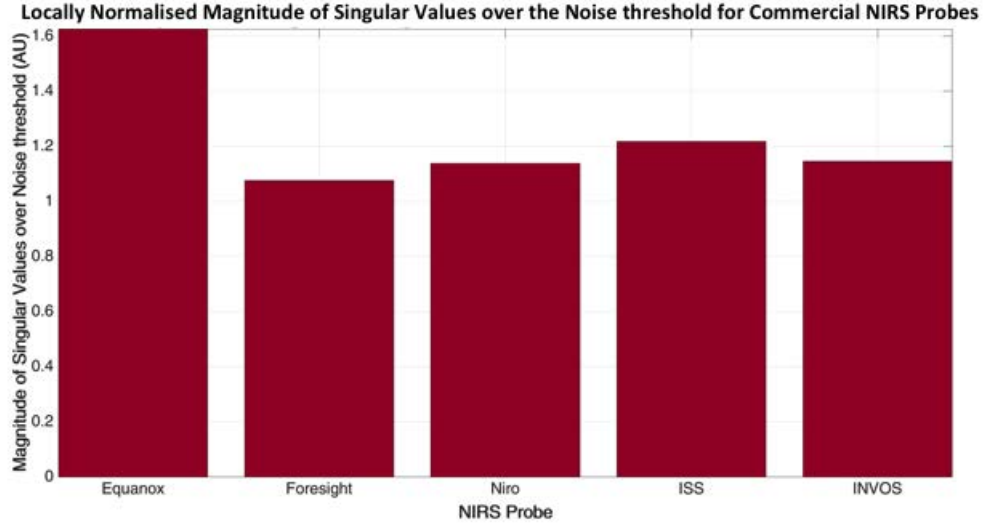


Figure 4.6: Magnitude of singular values over the noise threshold for each of the 5 probe geometries normalised to their own maximum value

Conclusion

Singular value analysis of existing fNIRS probe geometries has highlighted the benefits of using overlapping and multi-distant measurement channels. The analysis also confirms that all the simulated probe geometries do provide information in the brain region. This information is valuable in confirming the validity of current fNIRS systems and also provides further insight into methods of developing the technology further to allow it to be used as a TBI monitoring tool. The Jacobian sensitivity studies showed the need for large source-detector separations for a probe to increase sensitivity to brain tissue; the SVD analysis shows that to maximise this it must also be combined with the use of overlapping measurements at multiple wavelengths.

4.3 Healthy Volunteer Investigation testing method - The *Valsalva Manoeuvre*

For a more in depth assessment of fNIRS, in the context of TBI monitoring, a physiological model is required that will simulate some of the acute changes that clinicians would be looking for, such as a large desaturation (hypoxia) in the brain. As well as cerebral changes it is important for the model to have a unique set of superficial changes so as to provide a test of how well fNIRS devices can separate out cerebral from superficial signals. This is important because in TBI, systemic measures of blood saturation may not mirror that of the brain. Considering these criteria the *Valsalva Manoeuvre* (VM) was selected as an appropriate model.

4.3.1 What is the *Valsalva Manoeuvre*?

In its simplest form the VM is straining and occurs often in day-to-day life. Heavy lifting, coughing and even playing wind instruments are all activities that incorporate some form of the VM of a varying intensity [117, 109]. The main reason the VM is of interest to NIRS investigations is that it will induce profoundly different acute responses in cerebral and somatic tissues. Empirically we know the act of straining can cause people to become dizzy and pass out, we also can see that people become flushed and red-faced. From this evidence it can be deduced that there is clearly a lack of oxygen in the brain, hence the black outs, but at the same time there is clearly a large pooling of blood in the facial tissues. These observations can be backed up but by a wealth of quantitative data discussed later in Section 4.3.2.

The technical terminology for a VM is the act of forced respiratory expiration against a closed glottis, raising intra thoracic pressure (Figure 4.7A and B). During the initial ~ 2 -3 seconds, perfusion pressure is elevated, which is associated with an acute increase in blood flow in the cerebral and systemic circulations [118], this is what causes the subject to go red in the face (Figure 4.7B). As the VM continues, venous return to the heart

is impeded by the raised intra thoracic pressure. This produces a marked reduction in cardiac output and thus blood pressure. The increased intra thoracic pressure also impairs venous outflow from the brain, causing an increase in intra-cranial pressure and venous pooling within the brain and systemic tissue (Figure 4.7C). On release of the VM, the pooled blood is released (Figure 4.7D). It has been used previously as a tool for checking cerebral auto regulation [119, 120, 121] and observing changes in intracranial pressure [122]. The use of the VM has not been limited to brain studies, it has also be used to detect changes in blood pressure response [123], fluid responsiveness [124] and congestive heart defects [125]. Despite its range of use, some research has questioned whether with all the changes induced by a VM, it may be too complex for assessing cerebral autoregulation [126].

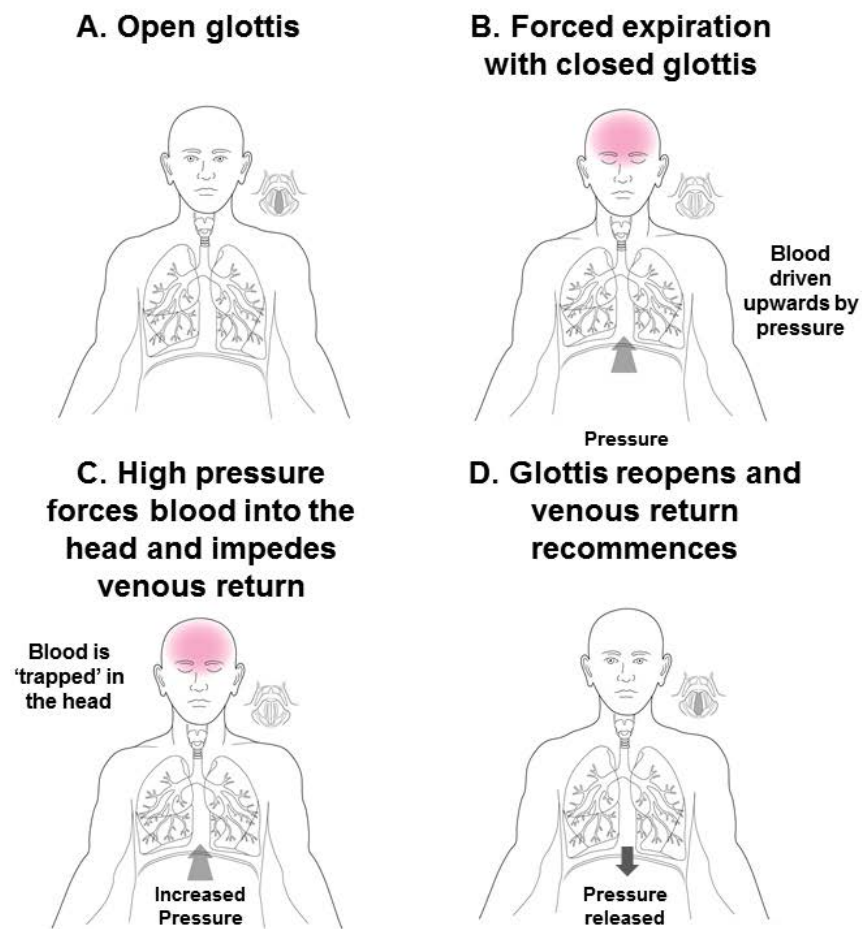


Figure 4.7: Diagrammatic representation of the stages in a Valsalva from A to D

The body's response to a VM has been categorised into 4 phases, which relate to the changes in mean arterial pressure (MAP) and which are outlined in Figure 4.8 [127, 109]. The 4 phase response in Figure 4.8 is for a supine VM, performing a VM while in a supine position will decrease the magnitude of the response in comparison to a standing VM. The mean arterial pressure is a combination of systolic and diastolic pressures, weighted by $\frac{1}{3}$ and $\frac{2}{3}$ respectively [128].

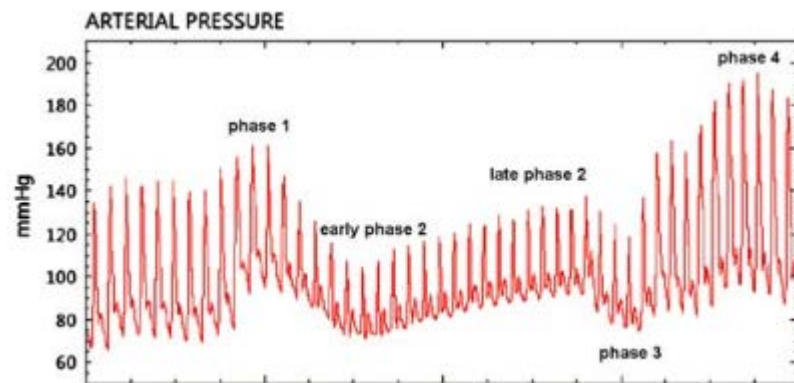


Figure 4.8: Four phases of the VM in terms of mean arterial pressure blood response [124].

1. Phase I - increase in MAP as intrathoracic pressures force blood towards the head.
2. Phase IIa - decrease in MAP as the return of systemic blood to the heart is impeded.
3. Phase IIb - arterial baroreflex responds to drop in MAP, resulting in heart rate increasing.
4. Phase III - As the VM is released the MAP drops rapidly as venous congestion is removed.
5. Phase IV - The MAP overshoots to compensate for the phase III drop.

Maximal Valsalva Manoeuvre - It is possible to grade a VM by measuring the expiratory pressure with respect to a maximal expiratory effort. The model of the

VM implemented for this PhD research was termed a 'maximal' effort, standing, VM where expiratory pressure was at the subjects maximum. The predicted haemodynamic responses shown in the next section are based on a maximal effort VM held for 10 s; a model design to invoke the most dynamic changes in cerebral and somatic tissues. The 10 s maximal VM is capable of causing a subject to faint i.e., the levels of cerebral hypoxia are sufficient to cause dysfunction.

4.3.2 Predicted Haemodynamic changes during a *Valsalva Manoeuvre*

The following section constructs the basis for the predicted changes in haemodynamics occurring over a 10 s, maximal effort, standing VM. While there exists a wealth of information of VM-based changes from a wide variety of monitoring modalities (discussed below), there is no 'gold standard, which can be used to tell us, exactly what changes in haemoglobin concentration and oxygen saturation will occur. Therefore this section aims at deriving the most likely set of changes from the available data, however they are still an estimate. As the Atlas model being used for fNIRS/DOT simulations and reconstructions has three tissue layers (i.e., skin, bone and brain) a set of responses are devised for each layer starting from optical properties used in the literature [113]; one adjustment to these baseline values was the increase in skin saturation from 80% to $\sim 95\%$ to reflect the lower metabolic demand in somatic tissue. Only changes to the skin and brain haemodynamics are predicted, the assumption is made that the bone will show no dramatic change during a VM due to its already low HbT concentration.

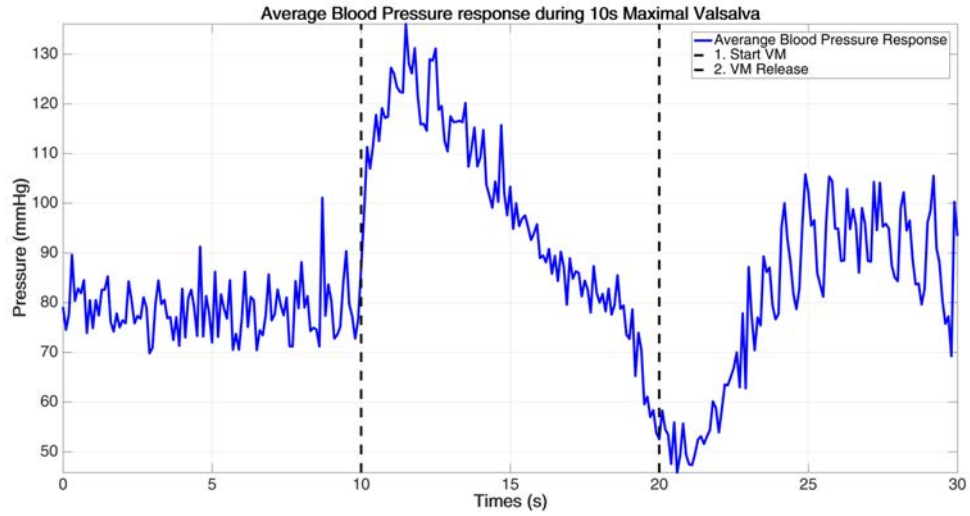


Figure 4.9: Blood pressure response during a 10 s VM over 9 subjects recorded as part of the preliminary investigations into using the VM for fNIRS testing (Average over all subjects).

Immediately after the onset of the VM there is a blood pressure spike (Figure 4.9), indicating that blood is being force upwards into the head via increased perfusion pressure and thus causing an increase in HbT concentration. The skull essentially makes a sealed box around the brain, so there is a limit to how much blood can be forced in during this initial phase, before the reduction in the driving force due to the impaired cardiac output associated with the reduced venous return (phase IIa). Figure 4.10 illustrates this flow response to a VM as measured via blood flow velocity in the middle cerebral artery [118]; and this initial peak response is further supported by the fact that ICP will increase during a VM [122].

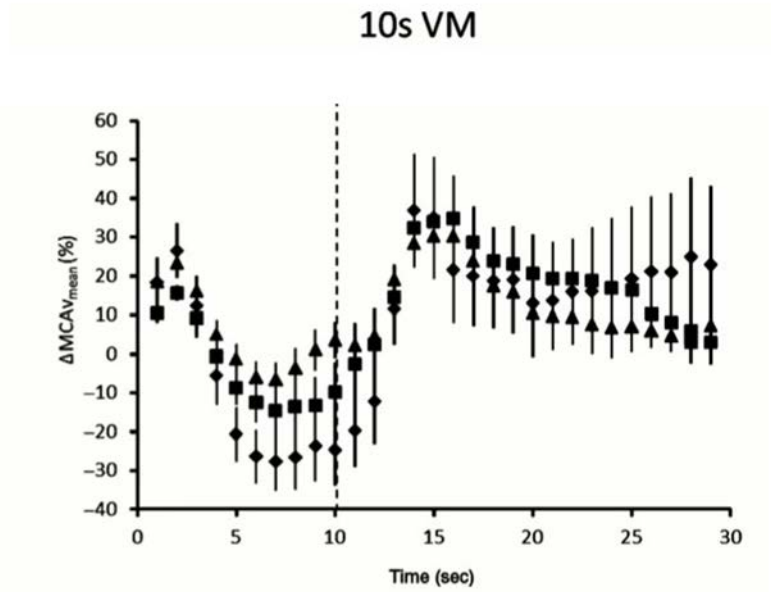


Figure 4.10: Percentage change from mean flow velocity in the middle cerebral artery measured with transcranial Doppler over a 10s VM [118]. The triangle, square and diamond markers represent 30 %, 60 % and 90 % maximal VMs.

The skin however contains blood vessels that can expand and accommodate blood through pooling, so the HbT concentration in somatic tissue can still climb until being limited by the impaired cardiac output (Figure 4.11).

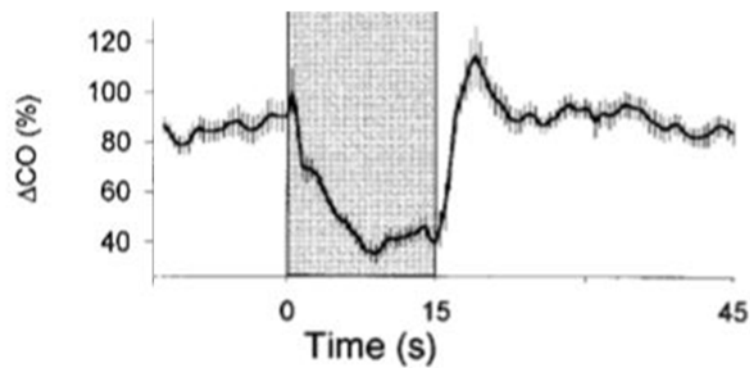


Figure 4.11: Percentage change in cardiac output during a 15s (non maximal) VM [117].

Drawing together all of this information allows prediction of the changes in HbT for the modelled VM as displayed in Figure 4.12. The VM is modelled over a 32 s period split into 2 s sample points, allowing for a 10s VM with a 10/12 s baseline before and after (longer for recovery). The choice to use 2 s samples point was to speed up the reconstruction process in the later simulation studies. Even with a wealth of blood pressure and blood flow metrics available there is currently no gold standard method that can map the changes in HbT during a VM. Therefore, to predict a model for the VM, the focus was on the large-scale changes. Over the course of the VM we know that initially we expect an increase in the amount of blood being forced into the head through increased intrathoracic pressure. This is seen in the blood pressure, middle cerebral artery velocity and cardiac output data (Figures 4.9-11 respectively) that all show an increase of $\sim 20\text{-}40\%$ within the first second of the VM. Therefore, we chose to model the initial increase in HbT concentration as a 30% increase in both the skin and the brain within the first 4 s. From here until the release of the VM the predicted changes are more qualitative. We can see that the blood pressure and cardiac output drop, so we know blood is trapped in the head. In the brain the volume is fix and thus the concentration of HbT maintains a constant level. The skin and facial tissues however can increase in volume; this is why we predict a more gradual increase in HbT initially, which can then start to decrease in the final few seconds of the VM. After the release of the VM we can see from the blood pressure that there is a spike of much smaller magnitude than the initial increase at the VM onset. This we model as a $\sim 10\%$ increase in skin HbT, and then both skin and brain HbT return to baseline values.

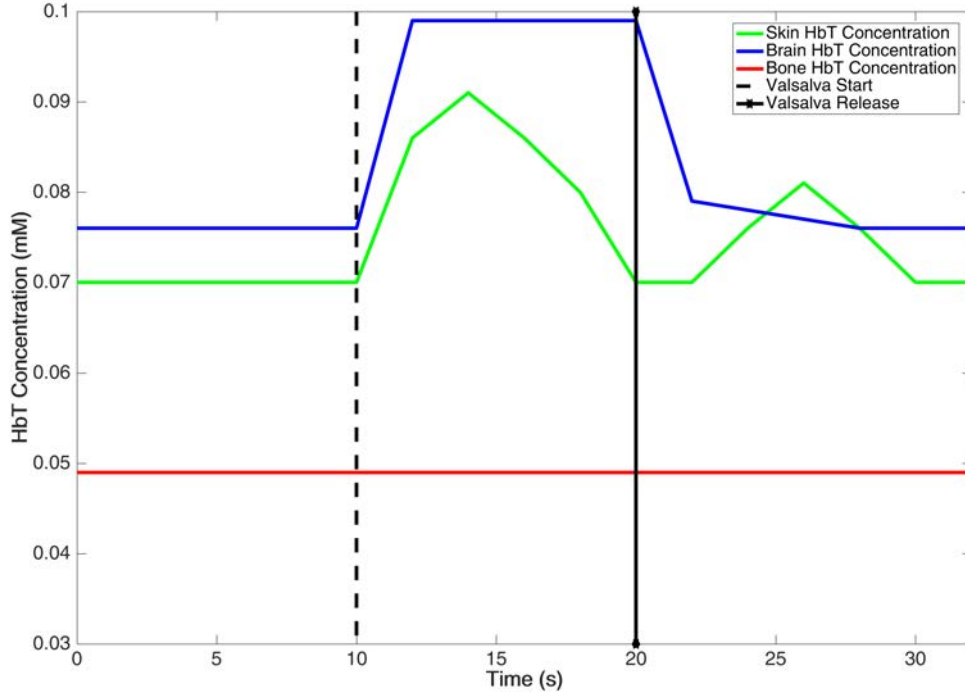


Figure 4.12: Predicted changes in total haemoglobin concentration over a 30 s period including 10 s baseline, 10 s maximal VM and 10 s of recovery. Values are show for three different tissues, Skin, Bone and Brain.

Given the predicted HbT concentration changes, the next consideration is how the oxygen saturation (SO_2 - defined in Equation 4.2) of the blood will change over time during the VM.

$$SO_2 = \left[\frac{HbO}{(HbO + HHb)} \right] \times 100(\%) \quad (4.2)$$

The skin on the forehead, where this response is being modelled, does not have a high metabolic rate and therefore the assumption can be made that the saturation of the pooling blood in the skin, during the VM, will closely match the pressure-driven changes in flow across the VM. Specifically, there will be a small increase in saturation that comes with blood being forced into the facial tissues by the raised intrathoracic pressure at the onset of the VM, then on release of the VM the blood pressure response (i.e., Phase IV) causes a (slightly delayed) influx of oxygenated blood into the head in a

drive to compensate for the VM effects causing a further small spike in skin saturation ~ 2 s after the release (Figure 4.12). Overall changes in skin HbT concentration are fairly profound, however, the associated change in saturation ranges over $\sim 5\%$. This skin response is supported by data collected with fMRI using BOLD measures during a VM [129]; wherein these data demonstrated that there was a correlation between fMRI and fNIRS saturation in the two facial areas assessed (fNIRS probes placed on facial somatic tissue - the zygoma). The trends shown in these data (Figure 4.13) match the predicted haemodynamics of the VM model used within this thesis. While these normalised data do not allow for the absolute quantification of haemodynamic changes, they do confirm the expected pattern of change across the VM.

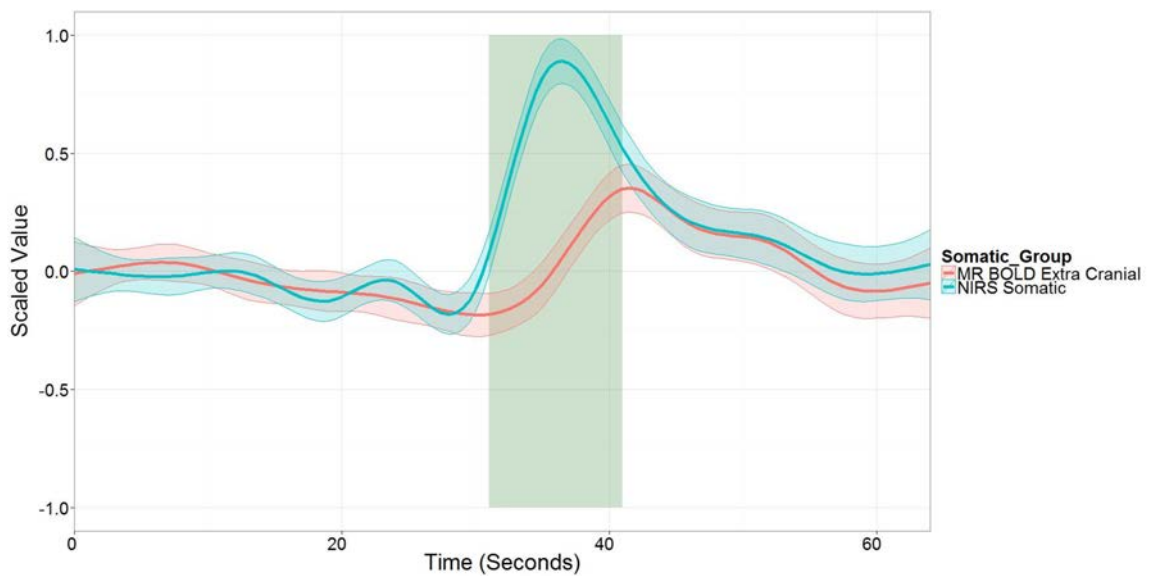


Figure 4.13: Normalised average change in fMRI BOLD (ROI in extracranial tissue in the same field of view as the fNIRS probe) and fNIRS oxygen saturation data from somatic tissue on the zygoma during a 10 s maximal, supine VM [129].

The brain response during a VM was also mapped in the same study along with fNIRS oxygen saturation data (probes on the forehead). These data demonstrated that both modalities show a profound drop in cerebral saturation from the onset of the VM, which then rebound upon release, overshooting the initial baseline saturation before recovery

(Figure 4.14). This pattern of saturation change in the cerebral tissue is consistent with the blood flow data from the middle cerebral artery described above, which showed that blood is initially 'forced' into the brain, then as the ICP increases and venous return is impaired, blood pools within the brain. Therefore, given the high metabolic demand of cerebral tissue, brain saturation will decrease steadily as the oxygen bound to the haemoglobin is extracted and used to meet this metabolic demand.

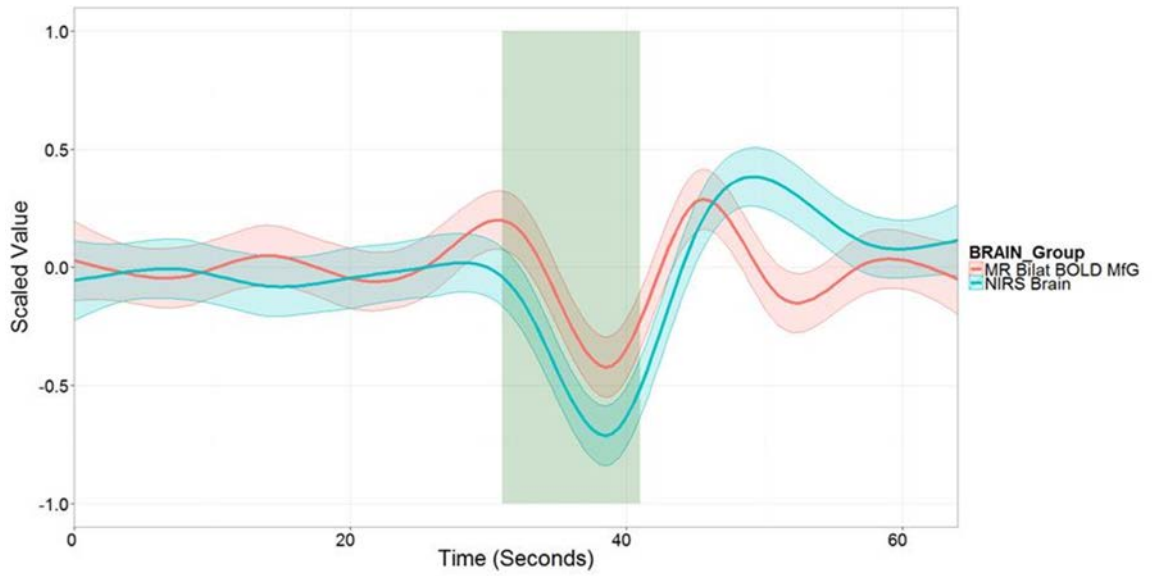


Figure 4.14: Normalised average change in fMRI BOLD (region of interest at white/grey matter junction of the middle frontal gyrus (brodman area 10)) and fNIRS signal from cerebral tissue during a 10 s maximal, supine VM [129].

Predicting how much the saturation drops, however, is another challenge. It is known that holding a maximal VM for too long (e.g., 10-15 s) will result in a loss of consciousness [109], so clearly the saturation drop in the brain is profound. The predicted cerebral saturation drop was estimated using data on the rate of oxygen metabolism in the brain as obtain via fMRI, that being $125.1 \pm 11.4 \mu \text{ mol}/100\text{g}$ per minute [130]. Making the assumption that the active tissue mass in the brain is roughly constant over all subjects and that the ratio of oxygen metabolism to HbO and HHb is 1:1, then it can be calculated that the drop HbO over a 10 s VM is $\sim 20 \mu \text{ mol}$ and the corresponding rise in HHb is

also $\sim 20 \mu \text{ mol}$. Applying these values to the baseline optical properties used for the brain (Appendix .2), the maximum saturation change is $\sim 20 \%$, which when projected onto the changes observed in fMRI give the cerebral saturation changes shown in Figure 4.15.

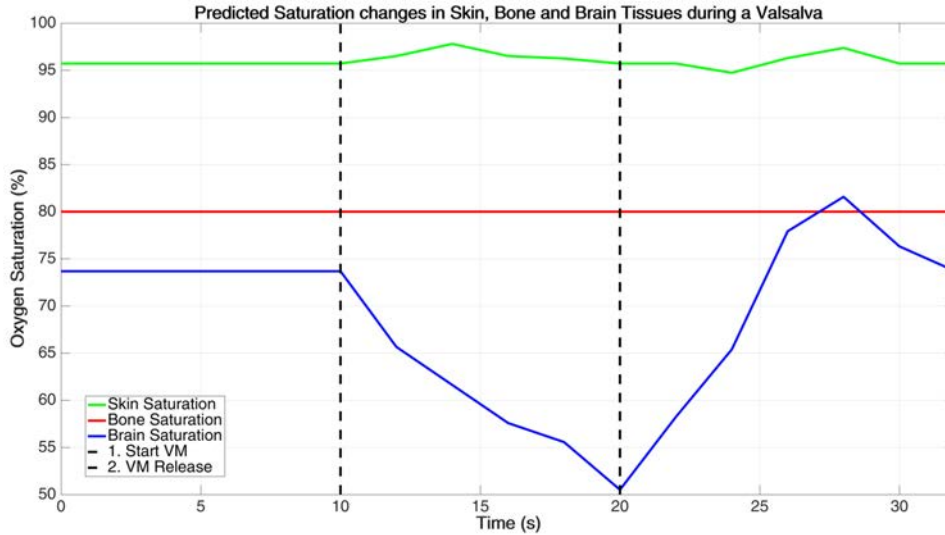


Figure 4.15: Predicted changes in oxygen saturation over a 30 s period including 10 s baseline, 10s maximal VM and 10 s of recovery. Values are show for three different tissues, Skin, Bone and Brain.

The shape of the predicted saturation values shown in Figure 4.15 model the saturation changes seen in the fMRI data during a VM (Figures 4.13 and 4.14) and the HbT predictions in Figure 4.12. The changes are again modelled over a 32 s VM at 2 s intervals in order to reduce computation time in simulations. The magnitude of the drop in brain saturation is modelled quantitatively on the values of oxygen metabolism in the brain ($125.1 \pm 11.4 \mu \text{ mol}/100\text{g}$ per minute) mentioned previously. Taking this rate of oxygen metabolism the saturation was steadily decreased at 2 s intervals to the maximum predicted drop of $\sim 20 \%$. Then on release of the VM the saturation values was modelled as returning to baseline and overshooting by $\sim 8 \%$ due to a secondary spike in blood pressure (Figure 4.9, which occurs within a 10 s time frame. The saturation changes skin

are estimated based on the predicted HbT concentration changes. Working on the basis that the HbT will spike by $\sim 30\%$, and we do not expect the HHb component of the blood in the skin to increase due to low metabolic demand, the HbO concentration was adjusted to give the required HbT change and hence the saturation spikes seen in Figure 4.15.

4.4 Spatially Resolved Spectroscopy - Simulation Studies

Spatially Resolved spectroscopy (SRS - described previously in Chapter 2) is a method of weighting fNIRS data reconstruction to look only at deep tissue changes. As this is a relatively simple technique already available commercially on fNIRS devices like the NIRO-200NX (Hamamatsu, Japan), it is an ideal starting point for TBI monitoring. The SRS method does not claim to be able to quantify deep tissue oxygenation, it only maps relative saturation and total haemoglobin, known as the tissue oxygenation index (TOI) and tissue haemoglobin index (THI) respectively. In this respect a normative baseline reading is still required to map changes, a limitation of application in TBI, however assessment of the technique is a good starting point from which to progress. In order to test the accuracy of the SRS method, a series of simulations designed to mimic the VM were tested. Specifically, these simulations were used to determine the accuracy of the technique for measuring cerebral changes and the determine how much influence the superficial signals were having on the derived TOI and THI parameters.

Methodology

As described in Section 4.2, the probe geometry of the NIRO-200NX (details in Appendix .1) was modelled on the 3-layered (skin, bone and brain tissue regions) ICBM 152 Atlas, and the predicted haemodynamic changes for a 10 s maximal VM from Section 4.3 were applied to the model and forward data produced for each set of values using NIRFAST.

Using the modelled intensity, the TOI and THI values were calculated using Equations 3.13 and 3.14. In the original validation paper for the SRS method [76], the accuracy of the techniques was confirmed using models that were homogeneous in scatter and absorption properties. Therefore, as application to cerebral monitoring is inherently heterogeneous, for completeness, the SRS methods was tested under a series of conditions:

1. The forward model used to produce a set of simulated detector intensity values was given homogeneous brain scattering values and the global absorption changes mapped the predicted brain changes.
2. The forward model used to produce a set of simulated detector intensity values was given homogeneous brain scattering values. Absorption was heterogeneous, skin and bone properties were kept constant and absorption properties were changed in the brain region only.
3. The forward model used to produce a set of simulated detector intensity values was given fully heterogeneous scatter and absorption changes in skin, bone and brain regions.

The effect of superficial contamination was assessed further by simulating the heterogeneous VM haemodynamics while lowering the HbT concentration in the skin region to assess the influence on derived TOI and THI parameters. As the SRS method only shows relative chromophore concentrations, the results were offset to start from the same baseline saturation in order to assess the accuracy of the derived changes.

Results

As the SRS does not assess quantitative level of HbO and HHb the analysis criterion for these results is the magnitude of the recovery saturation (TOI) drop in comparison to the simulation VM values. The saturation drop in the brain being simulated is $\sim 22\%$, and therefore the closer the SRS method is to accurately mapping this change the more

potentially beneficial it will be as a TBI monitoring tool. For the fully homogeneous model saturation changes were made globally (Figure 4.16 - green line) the recovered TOI values were seen to dramatically overshoot the predicted saturation changes giving $\sim 48\%$ drop instead of the simulated 22% . This is most probably due to the fact that while the SRS method is designed to weight reconstruction towards the deep tissue changes there is still influence from shallow signals, which as seen in Section 4.2.1, fNIRS devices are known to be hypersensitive to shallow changes and thus it is enough to cause overestimation of the TOI. This sensitivity issue will be discussed later on in this section. This theory is supported by the results of the simulation where the forward mesh had homogeneous scattering properties and absorption changes were applied to the brain region only (Figure 4.16 - blue line). When there were no changes in the shallow (skin/bone) regions the SRS method mapped the saturation drop in the brain accurately, obtaining a drop of 20% . This indicates that there is still an oversensitivity to shallow changes even with SRS. The third simulation example with fully heterogeneous scattering and changes in absorption over all regions, showed a much lower response to the drop in cerebral saturation (Figure 4.16 - red line). Collectively, these findings demonstrate that the changes in the skin are having an influence on the recovery TOI parameters. For example, the increase in TOI seen just after the onset of the VM is a response that was modelled for the skin region only; the brain saturation was only simulated to decrease during the VM. While there is clear superficial influence in the derived parameters, the SRS method does still observe a drop in the cerebral saturation, albeit at a reduced magnitude ($\sim 12\%$). This reduction in recovered magnitude for the heterogeneous model is not entirely unexpected as the equations for calculating the relative HbO and HHb concentrations for SRS (Equation 3.13) are derived for a medium with homogeneous scattering parameters.

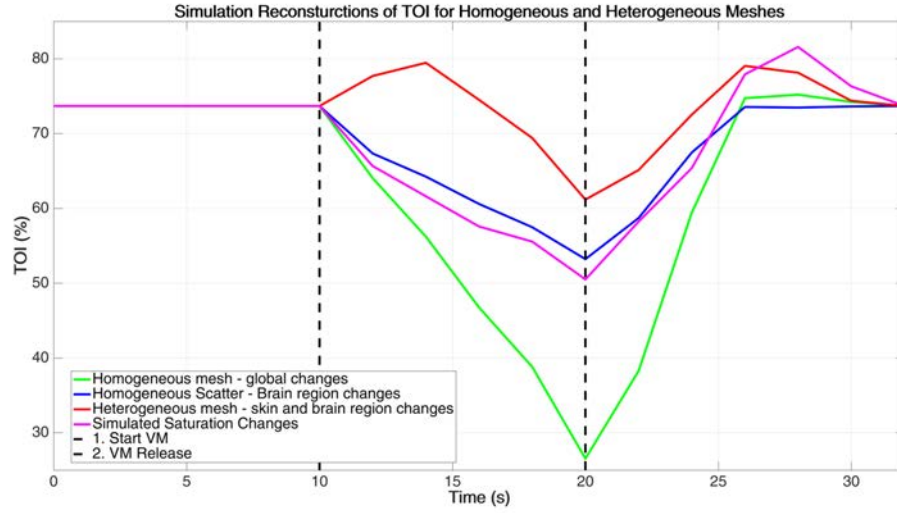


Figure 4.16: Recovered TOI values during a simulated 10 s VM using the SRS method on homogeneous and heterogeneous head models. Results are all offset to start at the simulated baseline level

To further assess the amount of influence the superficial signals have on the recovered TOI values, the simulations were repeated for the heterogeneous model with varying concentrations of HbT in the skin region. The HbT concentrations were taken to be 100, 70, 50, 30 and 10 % of the standard skin value. The results (Figure 4.17) show that as the superficial HbT concentration decreases the magnitude of the recovered cerebral desaturation becomes closer to the true simulated value, until at 10% the magnitude of the change is mapped correctly. The concentration change however does not appear to influence the saturation spike (from the skin region at the VM onset) to the same extent, suggesting that while we can improve the magnitude of the observed cerebral changes there will always be a constant level of superficial contamination. This again may be a side effect of the homogeneous scatter assumptions and residual sensitivity to superficial signals.

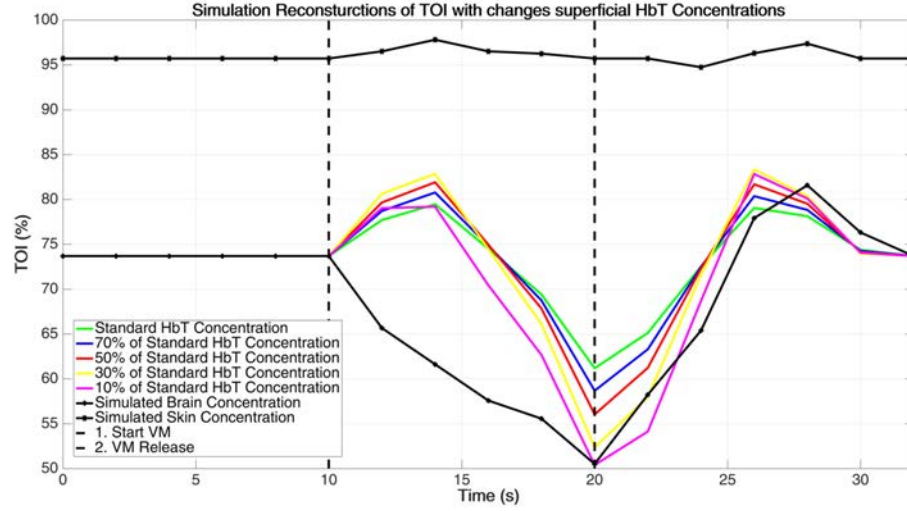


Figure 4.17: Recovered TOI values during a simulated 10 s VM using the SRS method on a heterogeneous head model with varying concentrations of superficial haemoglobin. Results are all offset to start at the simulated baseline level

With reference to the 'sensitivity' of the probe to different regions as discussed in Section 4.2.1 the Jacobian matrix for a model can give a measure of the probes sensitivity to changes occurring at a given point in the model. As an example, the Jacobian for the NIRO-200NX for a 2D heterogeneous rectangle is shown in Figure 4.18. This 2D model has 3 different regions; skin for the first 10mm, bone for the next 10mm and the remainder of the model is brain, the optical properties used where the same as the heterogeneous baseline properties used in the Atlas-head model. The Jacobian, summed over all wavelengths and chromophores, shows that the sensitivity of the probe geometry is focused in the superficial (shallow) regions (more negative values indicate higher sensitivity), as is expected.

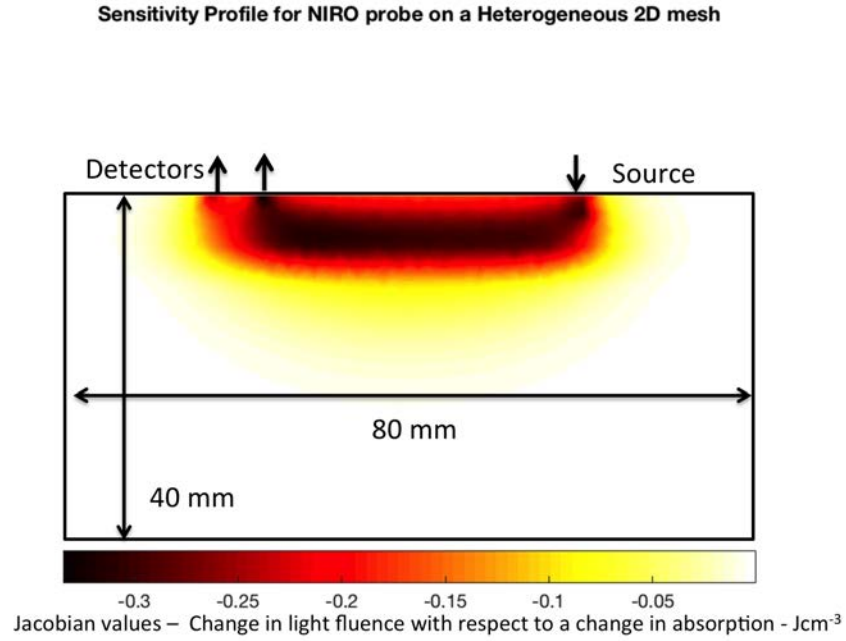


Figure 4.18: Example Jacobian sensitivity plot for NIRO-200NX probe geometry on a heterogeneous 2D model for one source-detector pair.

As the SRS method looks at the difference between two detector measurements, we can build a SRS sensitivity profile by finding the difference between the Jacobians to the two detectors in the NIRO-200NX probe geometry. The results of the SRS sensitivity plot on the same 2D rectangle model are shown in Figure 4.19. It is apparent that there is a section of high and low sensitivity in the superficial region, which may cancel out when the sensitivity is summed over the entire region leaving a low sensitivity to superficial changes and a higher sensitivity to deeper signals.

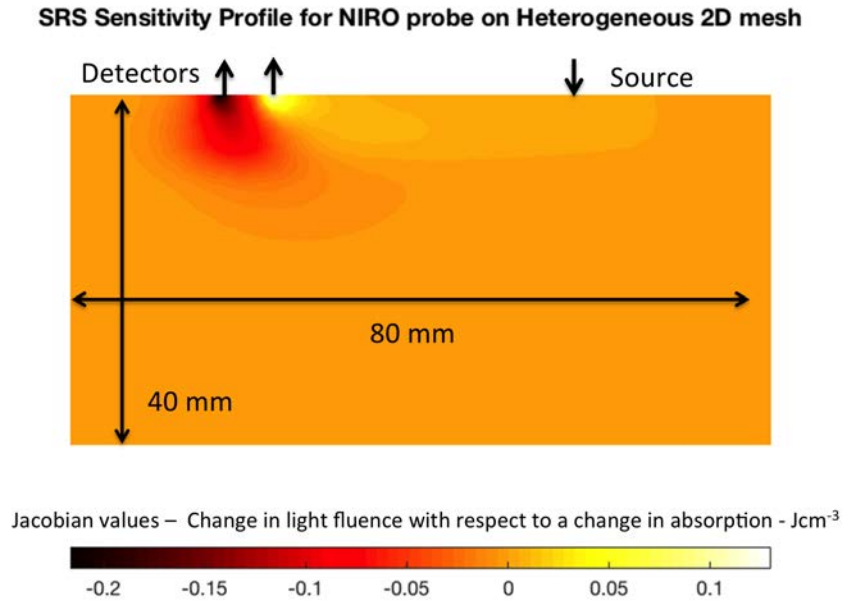


Figure 4.19: Example SRS (difference between Jacobians from each detector) sensitivity plot for NIRO-200NX probe geometry on a heterogeneous 2D model.

When the sensitivity profiles are averaged over the region the percentage of the overall sensitivity in each region can be calculated (Figure 4.20). These data show that even though the SRS method is dramatically decreasing the sensitivity of superficial influences on the recovered TOI, it is not removing it entirely, which explains why there are still superficial changes visible in the VM simulations. Despite this, the sensitivity profile of SRS is significantly more even over the model than the standard fNIRS sensitivity, and therefore represents a profound improvement to the accuracy of recovered deep tissue changes.

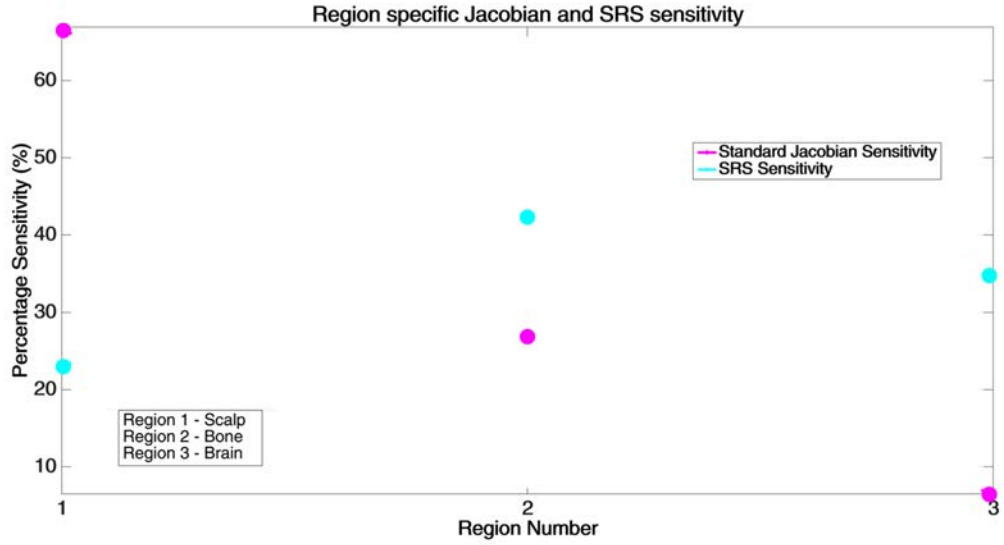


Figure 4.20: Comparison of sensitivity to different tissues (skin, bone and brain) with and without the SRS-method employed on the NIRO-200NX geometry modelled on a 3-layer heterogeneous head Atlas.

4.4.1 Conclusions

The SRS method does provide a more even depth sensitivity profile in comparison to a standard fNIRS probe, allowing changes in cerebral saturation to be obtained with higher confidence of the signal origins. While the SRS method is clearly measuring saturation changes in the brain, even with its more level depth sensitivity profile there is still an element of superficial contamination in the derived TOI values when using a fully heterogeneous model. A potential source for this is the fact that SRS is based upon a homogeneous scatter model, which is an inaccurate model for photon migration in a heterogeneous medium. Collectively, these simulation studies indicate that in its current form SRS is not suitable for TBI monitoring without a normative baseline reading.

4.5 ISS Oxiplex TS Vasopressor Studies

To further investigate the effects of superficial contamination on fNIRS parameters, pharmacological intervention, through use of a vasopressor injection, was used as a means of reducing the overall concentration of haemoglobin in the superficial tissue above the target area of the cortex (similar to simulations performed with the SRS method). The vasopressor acts to constrict the blood vessels to the skin and hence reduce the amount of blood supply to the target region. This will result in a lower volume of blood at the site and therefore subsequent changes in its saturation will have a decreased influence on the fNIRS detector signals and theoretically reduce the contamination from skin changes. While the bone region is still considered as a superficial tissue, there is no practical way of infiltrating it with vasopressor, however as the haemodynamics of bone are insignificant in comparison to the skin and brain, the levels of signal contamination from the region will be generally lower. For comparison, the probes used in the vasopressor study were modelled on the ICBM152 Atlas and the effect of the vasopressor simulated by decreasing the quantity of superficial HbT.

4.5.1 Methodology

Eight healthy volunteers performed a series of 10 s, standing VMs under controlled laboratory conditions, pre and post injection of a potent vasoconstrictor (~ 1.5 -2 mL of 2%xylocaine, with 1:100,000 epinephrine). The magnitude and consistency of the VM was assessed using contemporaneous, beat-to-beat blood pressure monitoring (Portapres, Finapres Medical Systems, The Netherlands). The NIRS monitoring was done using the ISS Oxiplex TS (ISS Inc, USA) with two frequency domain probes positioned on either side of the forehead, centred 2 cm above the superior orbital ridge, with the field of acquisition centred 3 cm from the mid-line. A minimum of 2 satisfactory VMs (i.e., maximal and near identical blood pressure patterns) were recorded for each volunteer for each series of VMs performed. Laser Doppler (Moor Instruments, UK) was also used to

measure blood flow (as indexed by flux) in somatic tissue along the line of the zygoma during forehead NIRS measures. In addition, a repeat set of VMs was completed with laser Doppler measures of the forehead somatic tissue. This protocol was then repeated following injection of the vasoconstrictor into the forehead tissue. Post-injection testing began after capillary refill was observed to be at least 4 s (usually 1-2 s). To ensure that there were no order effects in the repeating of the VM pre and post injection, the blood pressure of the subjects was recorded continuously as a way of gauging the strength of the VM performed. A VM was considered acceptable if the blood pressure dropped to ~ 40 mmHg before release. The blood pressure data for each subject is shown in Appendix .4. The study conformed to the Declaration of Helsinki and was approved by the University of Birmingham Research Ethics Board (Ref.: ERN_30-1031). Individuals recruited had no significant prior medical history.

Simulations of the ISS probe geometry (Appendix .1) were modelled using NIRFAST on the ICBM 152 Atlas model shown in Figures 4.1 and 4.3 (baseline optical properties show in Appendix .2). The Atlas model was separated into 3 tissue layers with the CSF, white matter and grey matter being combined into a single 'brain' region. The effect of the vasopressor was simulated as a 50 % reduction in HbT concentration (chosen from preliminary work) in the skin region modelling the same VM concentration changes outlined in Figure 4.15. Simulated data was then produced in NIRFAST with a 110-MHz frequency modulation to match that of the ISS system. It is important to note that the reconstruction method for the frequency domain data produced in simulation will not directly mimic the output of the ISS system, it is designed as an indicator for how the vasopressor may alter the recovered parameters. The optical properties of the simulated datasets pre and post vasopressor were recovered using the analytical fitting routine outlined in Section 3.1 to find absorption and scatter values, the chromophores were then calculated using the modified BLL (Section 2.2.1). The absorption and scattering properties recovered are a global representation of the haemodynamics in the target volume.

4.5.2 Results and Discussion

The VM simulations (Figure 4.21) predicted that even without the vasoconstrictor injection a frequency domain reconstruction based on the ISS cerebral probe geometry would be capable of observing changes in brain saturation. The magnitude and quantitative accuracy of these changes however is noticeably obscured by the superficial saturation. As mentioned above, the effect of the vasoconstrictor injection acts to decrease the amount of obstruction from the superficial tissues. The main finding of this experiment was that while the magnitude of the change remains constant before and after the vasoconstrictor injection, the quantitative accuracy of the recovered saturation values show a marginal shift towards the simulated brain values when the vasoconstrictor is introduced. The simulation results therefore indicate that the limiting factor in the quantitatively accurate recovery of the brain saturation values is the global nature of the parameter reconstruction.

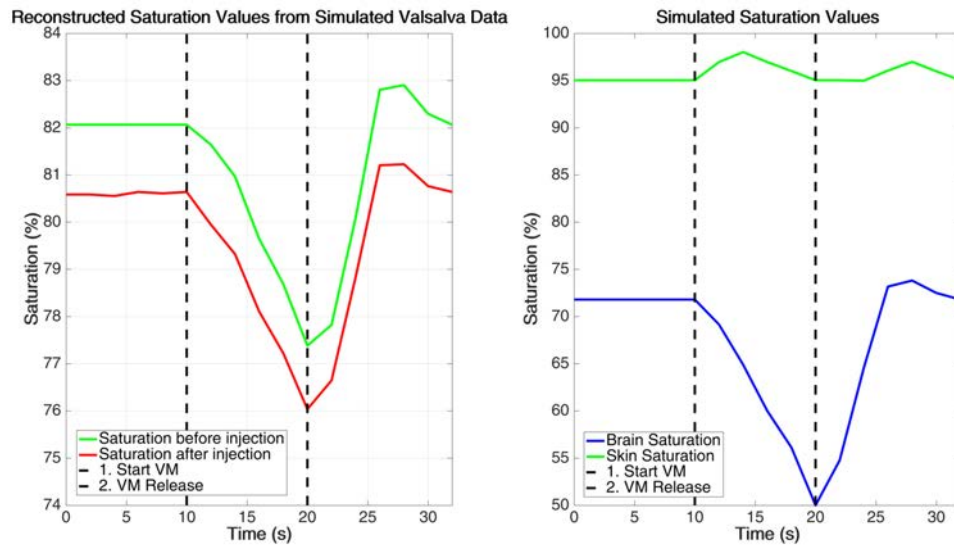


Figure 4.21: Recovered saturation values from frequency domain reconstruction using ISS Oxiplex TS probe geometry before and after a 50 % reduction in skin haemoglobin concentration (Left). Simulated VM saturation values in skin and brain (Right)

The effect of the vasopressor can be seen in Figure 4.22, which shows the Laser Doppler readings taken on the forehead (in the same position as the fNIRS probes) before and after the injection during a 10 s standing VM. Laser Doppler measures flux, which can be taken as a surrogate for flow and only gives a superficial tissue measure. Thus it is clear that the vasopressor injection is dramatically decreasing the blood flow in the skin and also reduces the flow rate induced by the VM. This provides evidence that the vasopressor is working as expected and confirm that the predicted 50 % drop in HbT concentration is valid.

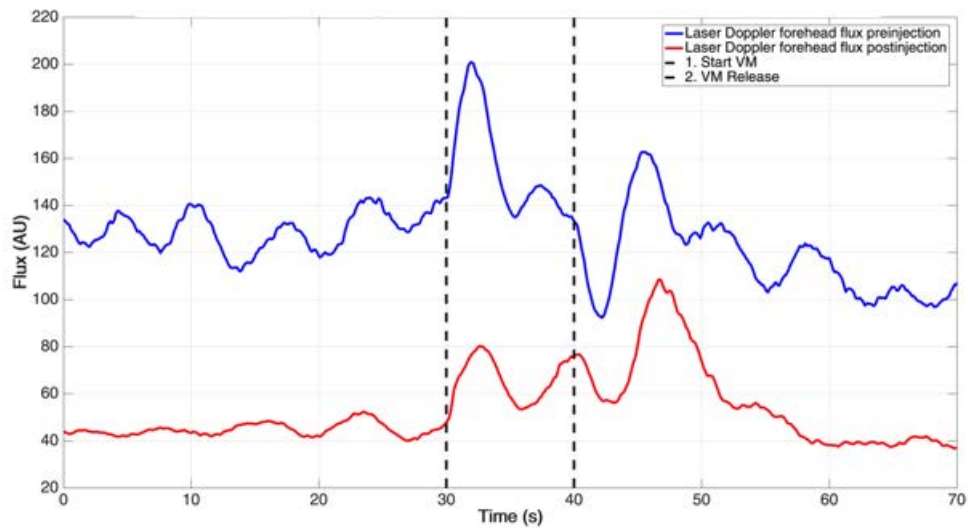


Figure 4.22: Average change in forehead flux measured with laser Doppler during a 10 s VM over 4 subjects.

A two-tailed Wilcoxon signed rank test (MATLAB signrank function) was used to look for statistically significant changes in total haemoglobin and saturation values in both fNIRS probes (left and right) before and after the vasoconstrictor injection; a P-value of less than 0.05 was considered significant. Results from the two-sided hypothesis test showed that the injection did not elicit an alteration in the changes in saturation observed during the 10 s VM, with a P-value of 0.2065 ($z = -0.646$, $N = 16$) and 0.6813

($z = -0.8015$, $N = 16$) for right (channel A) and left (B) side, respectively (Example results plot in Figure 4.23). The fNIRS parameters are sensitive to the probe positioning, therefore care was taken to ensure the probes were placed in the same place before and after the injection. There is also the possibility that the injection itself caused bleeding, and while any blood was cleaned from the probes and the target area before the completing the protocol, there is still a possibility that minor bleeds below the skins surface (in the region of a source or detector) could cause anomalous results.

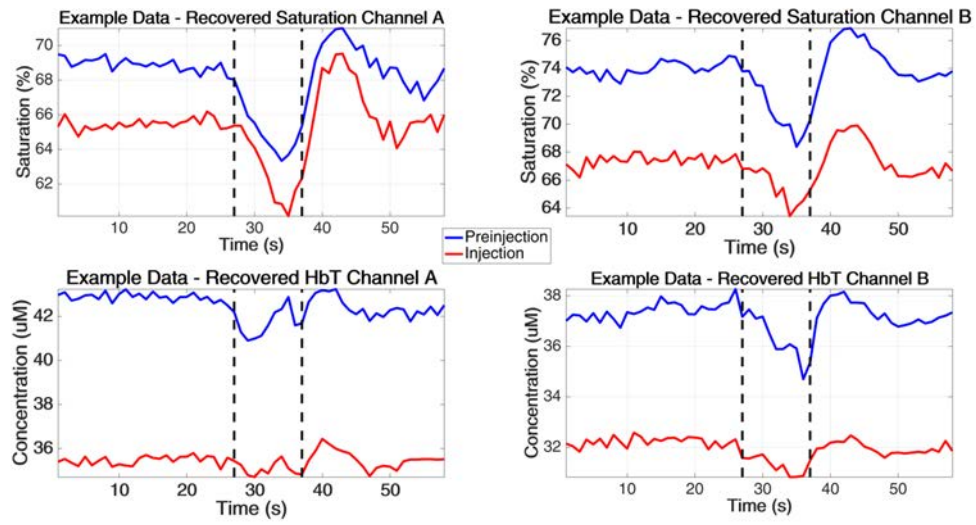


Figure 4.23: Single subject example of recovered saturation (Top) and total haemoglobin concentration (Bottom) values from the ISS Oxiplex TS probe during a 10s VM before (Left) and after (Right) a vasopressor injection to the forehead.

Using a right-tailed hypothesis test (MATLAB signrank function) the total haemoglobin (HbT) showed a statistically significant drop on both channels, with P-values of 0.00003 ($z = 2.6889$, $N = 16$) and 0.0004 ($z = 3.3611$, $N = 16$) for right (A) and left (B) side respectively after the vasoconstrictor was introduced (example data in Figure 4.23). This observation is consistent with the laser Doppler findings and also with the prediction that the vasopressor would decrease the HbT concentration within the probes target volume. The significance of this results confirms that the changes observed were more than

variations due to probe positioning, which was a possibility when looking solely at the saturation data. The drop in HbT over, while not significant in terms of the VM, did prove the effectiveness of the vasopressor injection.

The average saturation and HbT response from all subjects is shown in Figure 4.24. There is a large variation in the baseline measurements (Table 4.1) as was found in other parallel studies conducted within our group [54]. Having a highly variable baseline between patients makes it very difficult to put a number of what constitutes a 'healthy' reading, which is an essential part of TBI monitoring. Despite this, the trend in the saturation changes over the VM is consistent with the shape of predicted changes, further validating the model. This would imply that the fNIRS instrument being used is definitely observing cerebral changes with the superficial contamination only sufficient to obscure the magnitude of the cerebral haemodynamics, with drop in saturation during the VM ranging from 2 - 12 % (Table 4.1), significantly lower than the predicted 24 %. This is also confirmed by the simulation studies where the quantitative accuracy of the recovered saturation as well as the magnitude of the changes was not sufficient to reflect VM changes. It is worth noting that the HbT concentration recovered from the fNIRS data does not follow the trend predicted for a VM, which predicted that the HbT concentration should rise slightly in both the skin and the brain; instead the observed results showed that there is a small drop in HbT during the VM. While this does not fit with the biological prediction there is no obvious reason for it although it could potentially be due to cross talk between wavelengths as both the 690 nm and 830 nm wavelengths used are absorbed by HbO and HHb, perhaps showing the benefit of having additional source wavelengths in order to aid in the unmixing of signals into constituent HbO and HHb elements.

Parameter	Channel A (pre-injection)	Channel B (pre-injection)	Channel A (injection)	Channel B (injection)
Baseline SO ₂ (%)	60 \pm 11	69 \pm 11	64 \pm 7	65 \pm 10
Max SO ₂ drop during VM (%)	7 \pm 3	7 \pm 3	6 \pm 2	6 \pm 3
Baseline SO ₂ Range (%)	40 \rightarrow 74	59 \rightarrow 91	52 \rightarrow 73	47 \rightarrow 73
SO ₂ drop Range during VM (%)	3 \rightarrow 11	4 \rightarrow 12	2 \rightarrow 8	2 \rightarrow 11

Table 4.1: Recovered saturation changes from the ISS probe during a 10s standing VM, before and after vasopressor injection to the forehead. The table shows the average baseline across all subjects and the average desaturation during the 10 s VM with the error shown as 1 standard deviation from the mean. The range of changes in the baseline and the VM desaturation are also shown.

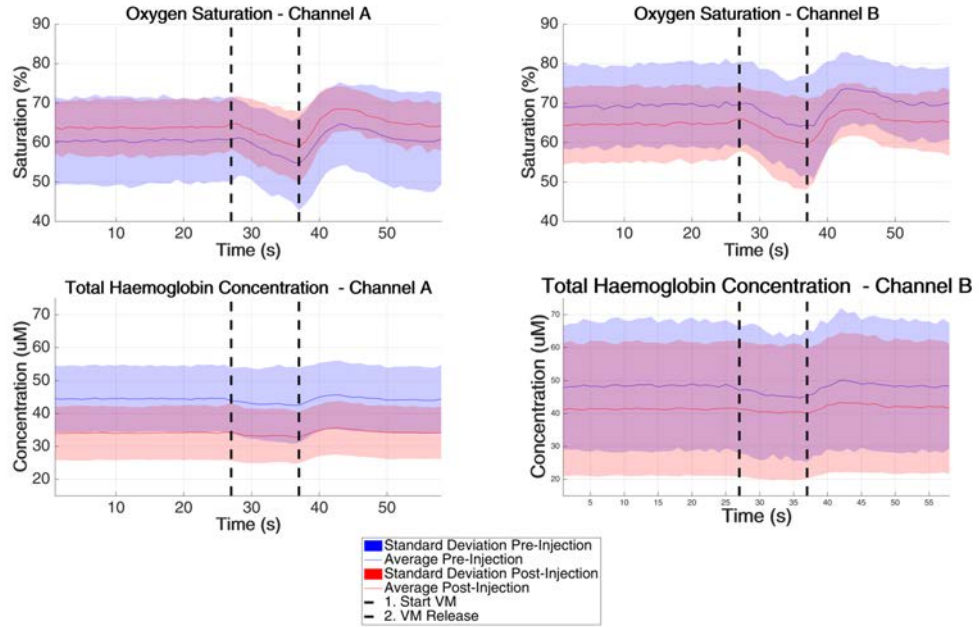


Figure 4.24: Group average of recovered saturation (Top) and total haemoglobin concentration (Bottom) values from the ISS Oxiplex TS probe during a 10 s VM before (Left) and after (Right) a vasopressor injection to the forehead across 14 subjects.

4.5.3 Conclusions

Currently fNIRS has not progressed into the clinic as a gold-standard method of monitoring TBI patients. This is despite its apparent advantages (e.g., cost, portable, non-invasive and non-ionising) as there are still concerns as to the origins and quantitative accuracy of the results being obtained.

The results presented from both simulation and healthy volunteer trials conclusively show that a frequency-domain fNIRS probe can detect neurological changes, in both haemoglobin content and haemoglobin saturation, when positioned on the forehead. The effect of superficial contamination in this instance appeared to be insignificant in the healthy volunteer trials. Even with a significant drop in superficial haemoglobin due to the vasoconstrictor there was no significant change in measured saturation over the volunteer pool. This is supported by simulation findings that showed only a small increase in quantitative accuracy following injection. However, this could be misleading to say that superficial contamination is not affecting the recovered parameters. In terms of quantitative accuracy of the fNIRS, simulations showed that recovered parameters could not be taken as an absolute measure of haemoglobin concentration or oxygen saturation. While the superficial signals do not inhibit fNIRS from being used to measure relative brain changes, the global parameter recovered used by fNIRS effectively give average values that will to some extent include the superficial layers, regardless of the logistical and computational methods used to reduce it.

In order to achieve quantitative accuracy needed for TBI monitoring without a normative baseline measurement, a high-density fNIRS probe with multi-layered parameter recovery could offer a potential solution. Here, instead of a globally reconstructed set of parameters, the reconstruction could take into account the different layers of the head, a topic that will be explored in later Chapters.

4.6 Summary

Simulations and testing of fNIRS geometries and devices has shown they are definitely capable of measuring changes in cerebral haemodynamics, despite inherent limitations from superficial contamination. It would appear that the issue is not necessarily to do with the probe but more to do with the reconstruction process. Frequency domain devices, while providing quantitative chromophore concentrations are not accurate for cerebral values because the concentrations are an average over the whole target volume, a combination of the brain and superficial tissues. Regardless of the fact that Jacobian and singular value analysis confirmed the sensitivity and information content of the simulation probe geometries were detecting cerebral haemodynamic changes, the values were always significantly higher for the superficial regions making depth-related unmixing of the signals untenable. A tomographic reconstruction is ill posed even with the large over lapping datasets of DOT probe, making it an unobtainable goal for small fNIRS probes with CW or FD sources.

Using spatially resolved spectroscopy (SRS) the sensitivity profile of a fNIRS probe can be evened out (with respect to depth) so that not as much weighting is given to superficial regions. A direct comparison between the FD reconstructions and the SRS reconstruction for the same set of simulated VM values showed that the SRS method observes a cerebral saturation change of 12% where as the FD model only observed a 5 % change, with the model predicted change estimate at $\sim 20\%$. While this should not be considered a direct comparison between the two probes, it does highlight that the SRS is providing improvements to obtaining cerebral saturation values. Despite the improvement to the observed change, the SRS method is still far from quantitative and is still not accurate enough to be used as a stand alone monitoring modality in TBI.

Considering a more advanced reconstruction method is required to differentiate the depth of signal origins, it is clear that a high-density probe similar to the DOT devices discussed in Chapter 2 is required in order to obtain the necessary data. However, as the DOT devices to date have been large scale and relatively importable in relation to the

fNIRS devices, a compromise must be reached on the design of the NIR device. Chapter 5 explores the use of a hybrid fNIRS and DOT probe in order to improve upon the current level of quantitative accuracy in fNIRS devices.

CHAPTER 5

HIGH-DENSITY NEAR INFRARED SPECTROSCOPY RECONSTRUCTIONS USING REGISTERED ATLAS MODELS

The aim of this chapter is to address the current limitations of fNIRS application to TBI monitoring by assessing an Atlas-based reconstruction model and algorithm in order to move towards a more quantitative and depth-resolved parameter recovery. The reconstruction algorithm is designed to work with a small scale DOT probe, obtaining overlapping spectral (multiple wavelengths) data from multi-distant source-detector pairs; a probe that has the potential to be made portable and affordable to application to TBI monitoring in the clinical and pre-clinical settings.

This chapter is split into two sections, the first is a simulation study to assess the feasibility of the Atlas reconstruction process with a model DOT probe. The second section entails healthy volunteer investigations, applying of the Atlas model to data obtained on a functioning small scale DOT system (designed by Nalecz Institute of Biocybernetics and Biomedical Engineering Polish Academy of Sciences) during a series of standing VMs in order to assess its current ability to provide clinically beneficial measurements.

5.1 Introduction

As discussed in previous chapters, the current quantitative accuracy of fNIRS devices is currently insufficient for it to progress as a monitoring modality in TBI. The progression of NIRS towards a more quantitative assessment of cerebral oxygenation can come in one of two ways. The first is to move to a time domain (TD) NIRS system that maintains the real-time and portable advantages of standard NIRS, however, such systems require the use of significantly more expensive components capable of individual photon counting. By measuring both intensity and arrival time of the photons, TD NIRS has intrinsic information about photon flight path, and therefore deep and shallow probing photons can be selected that allows greater quantitative accuracy and increased depth resolution (although still global in the lateral plane) [55].

An alternative method is an adaptation and use of diffuse optical tomography (DOT), which, with a denser array of sources and detectors allows use of multiple sets of overlapping measurements that can improve both the spatial resolution and quantitative accuracy [22]. Most reconstructions in DOT are model-based, typically using finite element models (FEM) for which spatial priors and initial optical property estimates can be used to increase the accuracy of derived optical properties. The limitation of DOT systems is their size and parameter recovery time, which makes them less practical for TBI monitoring. Although relative changes in chromophore concentrations from a baseline can be measured in real time, the quantitatively accurate results (of oxygen saturation, for example) require a non-linear and iterative reconstruction approach to hone in on the best solution. To date, however, truly quantitative results have only been obtained with DOT of the breast [56]. The lack of known baseline optical properties in the brain is currently a limiting factor in achieving quantitative result even when using DOT.

Providing spatial priors regarding the tissue layers of the head, namely the skin, bone and brain in a reconstruction algorithm has shown to help constrain the ill-posed nature of the problem and improve parameter recovery accuracy [57]. Such spatial priors can be obtained from patient MRI or CT scans, which can be segmented and formed into

subject-specific models, however in the clinical and pre-clinical setting this is not always a feasible option [22, 57, 58]. Alternatively, the use of Atlas-based models has shown good promise to overcome cases where subject-specific MRI/CT data are not available [57, 58, 59].

Although the application of a DOT-based system can produce the data required to monitor TBI patients, in its current format it is not ideal. The first issue is size and expense of the equipment, which may have a relatively simple solution; the sampled area could be scaled down. Although this would imply a smaller region of interest from which spatially varying parameters would be recovered, such small target regions would be suitable if the results were quantitative. It is worth noting that the invasive ICP probes only target a small area of the brain also. Therefore, if a small DOT probe is used to give overlapping, multi-distant measurements over a small area, it could be used to reconstruct depth-resolved spectroscopic parameters. A smaller probe is also more portable and cheaper to produce and will also help with the second issue of reconstruction time. Specifically, the smaller the number of voxels (spatially varying locations) being reconstructed, the faster the iterative reconstruction will complete [58]. In addition, having multiple overlapping measurements obtained over a smaller sample area will also improve the ill-posed nature of the inverse problem [60]. With parallel computing and GPU acceleration becoming more prevalent, reconstruction times will only get faster [61], providing additional benefits. The final obstacle in the way of quantitatively accurate DOT reconstructions is the availability of spatial priors. A subject-specific reconstruction model will not typically be available in clinical and pre-clinical TBI cases, hence the utilisation of an Atlas model, using the average spatial priors over a multitude of segmented heads, could be registered to match a patient head and used as a substitute for specific priors [57, 58].

Finally, while portable high-density NIRS system designs are already available and routinely used (e.g., NIRSport, NIRx Medical Technologies and fNIRS300B, BIOPAC System, Inc), the key feature that is currently lacking is the non-trivial baseline parameter

recovery needed to obtain information with a reasonable degree of quantitative accuracy. At the other extreme, systems such as the Washington University DOT array [62] uses a large-scale probe design, focusing on mapping cerebral activation and connectivity, which incorporates Atlas-guided recovery into their reconstruction routines. Thus, there are already system designs available that are suitable in terms of hardware. A NIR system suitable for the monitoring of TBI lies somewhere between these aforementioned designs, hybridising the portability of the smaller DOT arrays with the more enhanced reconstruction algorithms of the large scale probes. While this is something that has been explored [59], there has been limited expansion of the Atlas-guided techniques to produce quantitatively accurate results. Therefore this chapter is aimed at investigating the suitability of a small scale DOT probe, designed for use on the forehead, for producing quantitatively accurate cerebral oxygen saturation values, using a registered Atlas model for spatial priors.

5.2 Methodology - Simulation Studies

In order to assess the quantitative accuracy of DOT reconstruction using registered Atlas models, simulations were designed using NIRFAST [63] and a series of simulated brain conditions were constructed to mimic a Valsalva Manoeuvre (VM). As discussed in Section 4.3, the VM produces dramatic alterations in ICP, a key parameter monitored in TBI cases, which combined with the fact that the VM will produce very different superficial and cerebral haemodynamic responses, makes it an ideal method to test the suitability of the proposed NIRS/DOT probe and Atlas reconstruction algorithm for use in TBI monitoring. This method section is split into the following areas:

1. Production of patient specific models for modelling forward data.
2. Registration of Atlas models to match patient models for use in data reconstruction.
3. Probe design and positioning on head models

4. Simulation of forward data
5. Atlas and Tomography based reconstructions

5.2.1 Production of Patient Specific head Models

The process of data simulation and image reconstruction starts with the creation of subject-specific models, the basis of which is a T1 weighted MRI scan (Figure 5.1A). The MRI scan provides accurate structural information of features within the head, which can be translated into an FEM to accurately predict the propagation of NIR light through the target volume. From this the MRI scans were segmented into 5 separate regions: skin, bone, cerebral spinal fluid (CSF), white matter and grey matter (Figure 5.1B), using the statistical parametric mapping (SPM) software package [58, 131] based on a pixel intensity probability function distribution.

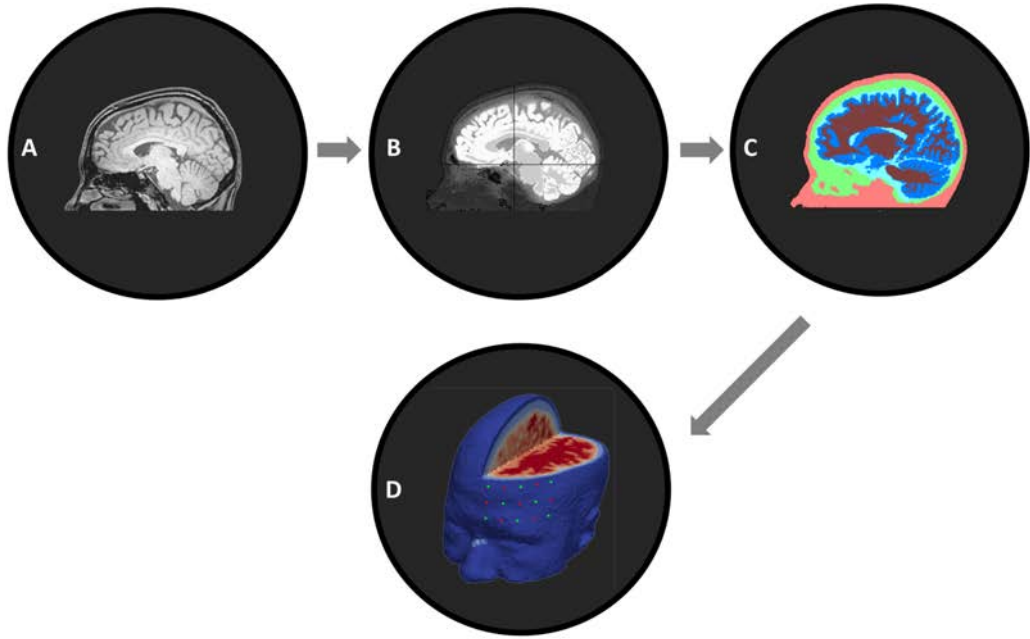


Figure 5.1: Flow chart of model generation from a patient MRI scan. A Original T1 weighted MRI scan. B MRI scan segmented into skin, bone, CSF, white matter and grey matter. C Masks created in NIRVIEW using the segmented MRI scan. D Mesh created in NIRFAST using masks.

Following the segmentation of the MRI scans, NIRVIEW [112] was used to create masks of the segmented scans (Figure 5.1C), which the final meshing process can be based on. NIRVIEW provides a vital checking step to ensure the segmentation process was correct, where any gaps of unassigned pixels can be filled to reduce the risk of holes in the final head model. Small gaps in the segmentation can be rectified using the iterative hole-filling algorithm built into NIRVIEW, which uses a voting algorithm at each iteration to determine where each pixel will be assigned based on the assignment of its surrounding pixels [112]. Large holes that were not filled using the automated routine were filled in manually through inspection of each segmented image slice. The end result of NIRVIEW processing was a stack of segmented masks that could be imported into NIRFAST and used as a basis for volumetric mesh creation (Figure 5.1D) [112, 63]. Once meshing in NIRFAST was complete, the models could be checked for consistency to ensure there were no holes present in the target forehead region.

5.2.2 Production of registered Atlas models

A widely used Atlas model in DOT studies is the ICBM152 [58, 110, 111], in which studies were primarily designed to look at brain activations and therefore segmentation accuracy was focused on the brain rather than superficial (skin and bone) regions. Preliminary data for the current study showed that there exists a large mismatch between the relative thicknesses of skin and bone within this Atlas and subject-specific models (see for example Figure 5.2), with this difference in layer thickness being enough to substantially reduce the accuracy of the model used. Therefore, for the purpose of this work a new Atlas was developed based on a tenth subject-specific MRI, which was segmented (as described in Section 5.2.1 and used as the new Atlas. While the layer thicknesses on the new Atlas were more representative of the 9 other models, future work will require a more comprehensive Atlas. The mismatch may not purely be due to the ICBM Atlas, there is also the possibility that the segmentation process used to create the patient specific models is also inaccurate in the superficial regions, thus selecting a new Atlas that would

also contain this error is a potential method to reduce its influence on the reconstructions.

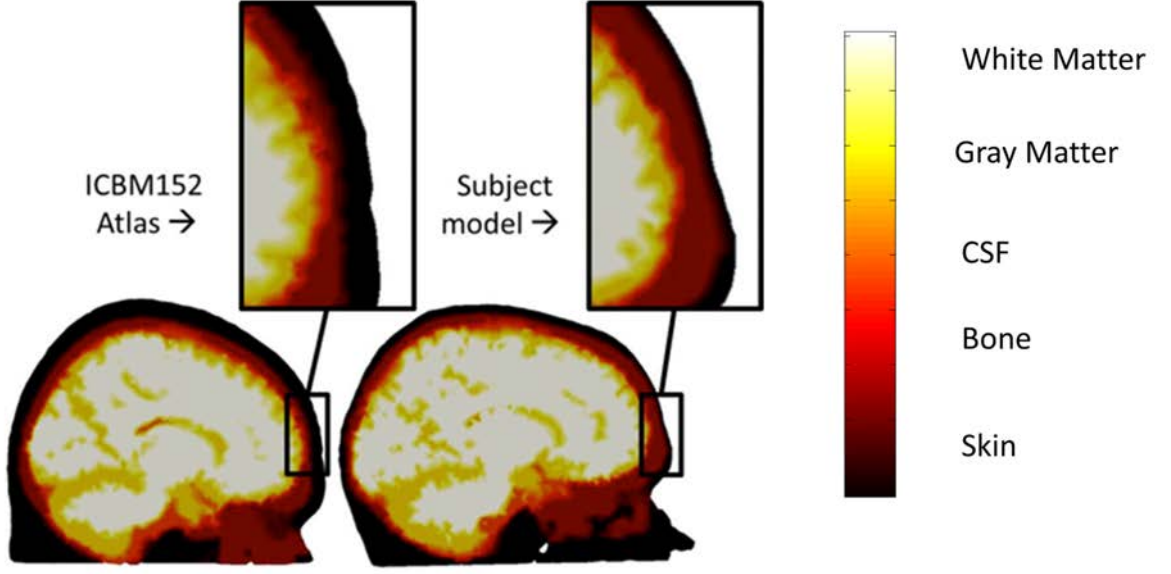


Figure 5.2: Comparison of the ICBM152 Atlas (Left) and the new Atlas used for the simulations (Right).

The registration of the Atlas model to each of the 9 subject-specific models was achieved using 687 evenly distributed landmarks based on a non-iterative point-to-point (nP2P) algorithm, to minimise the difference between the subject and the Atlas. This method has previously been shown to give a maximum surface registration error of 4.5 mm [58]. While this may appear as a large registration error based on the ~ 1 mm resolution of the initial MRI scans, it has been shown to be a successful method to provide an alternative to cases where subject-specific models are not available [132].

5.2.3 Proposed continuous wave probe design

The DOT probe being modelled (Figure 5.3) consisted of 8 triple wavelength LED sources (for example, L735/805/850-40C32, Ushio Epitex Inc., Japan) with peaks at 735, 805 and 850 nm with a bandwidth of 40 nm. There were 7 detectors (FDS100, Thorlabs) interspersed within the grid of sources and the spacing between each adjacent source/detector

was 15 mm, giving a total of 168 measurements with a minimum source-detector separation of 15 mm and a maximum of 62 mm. In real practical settings the maximum source-detector separation would probably be limited to ~ 40 mm, depending on the dynamic range of the detectors and the systematic noise levels. The modelled probe was set up to produce continuous wave intensity data only.

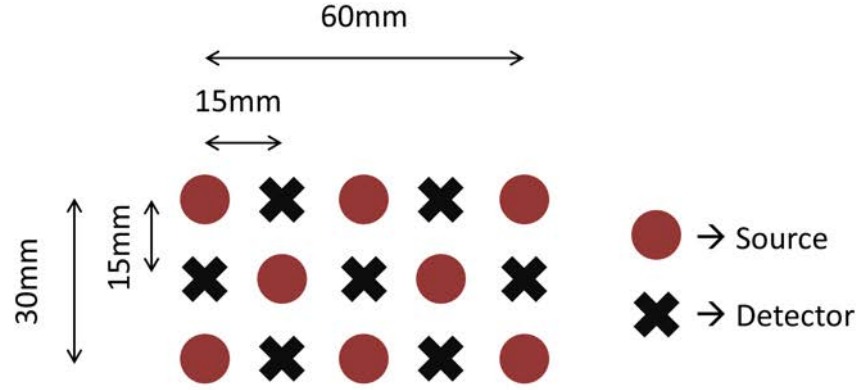


Figure 5.3: Design of high-density NIR spectroscopy probe

The probe pad was positioned relative to a user defined reference at the nasion point, as identified during the segmentation of MRI data (a process covered in Section 5.2.1). From this reference point a positioning algorithm was used to reduce the Euclidean distance between every source and detector to the desired 15 mm over an iterative cycle. From this point inbuilt routines within NIRFAST were used to move the sources one scattering distance beneath the surface of the model to account for the boundary conditions in the diffusion approximation (DA). For the simulation studies, the probe was positioned on the left hand side of the subject's forehead (Figure 5.4) with first point being placed 25 mm up and 1 mm left of the reference nasion point.

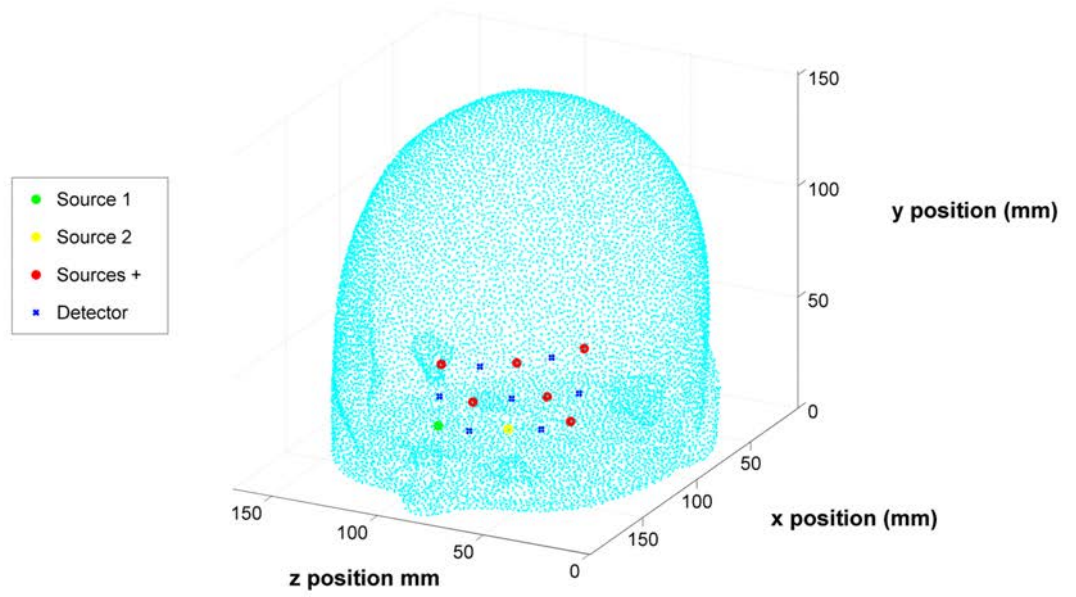


Figure 5.4: High-density NIR spectroscopy probe positioned on the forehead

5.2.4 Simulation of Forward Data

Forward (boundary) data for the VM (Section 4.3) was produced for 9 unique subject models using the FEM-based software package NIRFAST [63], with each time point on Figure 5.5 providing an individual dataset for a specific set of skin, bone and brain optical properties (Appendix .1). The simulation was designed to represent a continuous wave (CW) system, meaning that the forward dataset consists of a single boundary intensity measurement for each source-detector pair over three wavelengths.

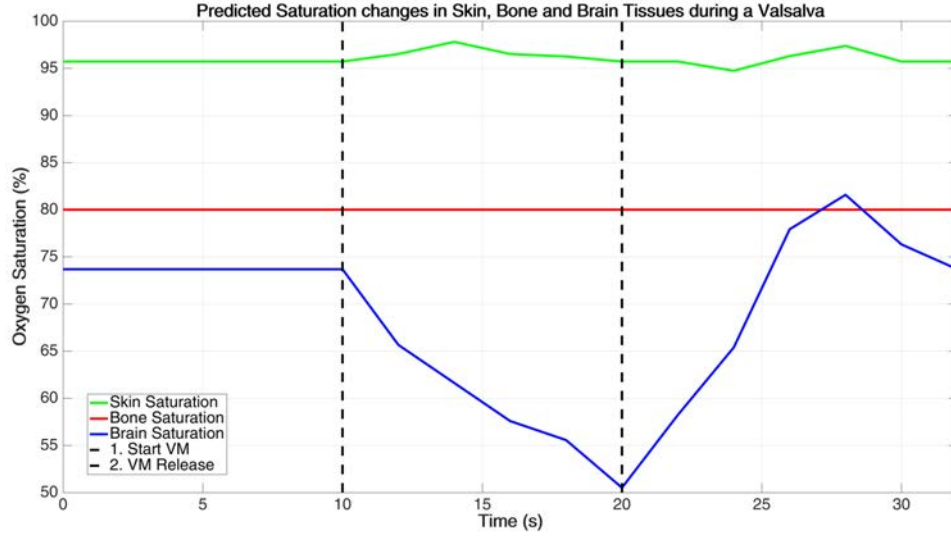


Figure 5.5: Predicted changes in oxygen saturation over a 30 s period including 10 s baseline, 10 s maximal VM and 10 s of recovery. Values are shown for three different tissues: Skin, Bone and Brain.

5.2.5 Reconstruction Routines - Simulation Studies

Reconstruction of the simulated data was performed using NIRFAST, which uses FEMs and the DA to produce data for the forward model within the reconstruction regime. The DA has been shown to be valid in mediums where scatter is the dominant interaction process and the source-detector separations are large enough to allow for multiple scattering events [63]. It may be argued that the use of the DA may not be the most accurate model for application in tomographic imaging of the brain, as there may exist regions where scattering does not dominate absorption (for example Cerebral Spinal Fluid), but the methodologies for parameter recovery outlined here are independent of the model of light propagation utilised. A full explanation of the basic reconstruction process used by NIRFAST is given in Chapter 2, any additional changes made for the purpose of the simulation studies will be covered in this section.

Several different reconstruction regimes were investigated for comparison, including

inverse crime and Atlas-based reconstructions, both utilising spatial priors for either full tomographic or region-based (one value for each layer) parameter recovery. The inverse crime involves using the same FEM for the forward and inverse modelling, which represents an idealised situation in which there is no error in source/detector positioning, the exact scattering properties are known and the spatial information in the model is accurate; whereas the Atlas-based reconstruction provides a more realistic setting. The tomographic reconstructions produce a set of spatially varying optical properties for every node in the FEM, which could then be averaged to give global parameter values per region (skin, bone, brain etc.) post reconstruction. However, the regional reconstructions produce a singular set of optical properties per predefined region, assuming each region is homogeneous. The region-based reconstruction uses a mapping function to make the values of the Jacobian matrix for each region the same value, this has the effect of reducing the number of unknowns in the inverse model, however, it is based heavily on the assumption that each region is homogeneous. Further details on the region-based reconstruction algorithm can be found elsewhere [133].

The inverse crime reconstructions had the most accurate prior information in terms of spatial and scattering properties; this was designed as a proof-of-concept. Atlas-based reconstructions, however, were designed to assess the ability to reconstruct brain saturation with only an estimate at absorption, scattering and spatial priors. NIRFAST allows for a reconstruction basis to be chosen in order to increase computational efficiency instead of using the original forward mesh (in this case the Atlas of subject-specific models). A reconstruction basis allows the model to be subdivided into sections (reconstruction pixels), reducing the number of unknowns in the matrix inversion process (further details found here [134]). Additionally, an increased computational efficiency was obtained by implementing a method of reducing the Jacobian calculation to utilise only sensitivity values greater than 1% of the total sensitivity for parameter recovery [135]. For this study the reconstruction basis was kept as the Atlas or subject-specific mesh (depending on the re-

construction type) with the starting values kept constant regardless of the reconstruction type for consistency. The 3 regions used the same scattering and water percentages as shown in Appendix .1, however the haemoglobin concentrations were set to be homogeneous at 0.0560 mM (Oxyhaemoglobin -HbO) and 0.0140 mM (Deoxyhaemoglobin - HHb) equating to a saturation of 80%.

The reconstruction process itself was split into two steps: (1) a global fit of optical properties based on boundary data for the whole model (i.e., assuming a homogeneous single layer model), which was limited to 20 iterations with a regularisation parameter of 10, and (2) using the bulk average value from the previous step as a basis for either the tomographic or regional reconstruction, which was limited to 40 iterations with a regularisation parameter of 0.01, the stopping criteria due to projection error change was a difference of less than 0.01 %.

For full tomographic-based reconstructions, in order to obtain an average value from each layer, the region of interest for each layer was define as those with a minimum of 2.5% sensitivity, and the reconstructed saturation values were then averaged over these regions of interest. This value was initially chosen based on prior knowledge of photon penetration for the initial homogeneous model, but the importance of model-based, subject-specific modifications are discussed below. For the regional reconstruction, a single saturation value was produced for each layer.

5.3 Results and Discussion - Simulation Studies

5.3.1 Registration Process

The principle of using a registered Atlas model for reconstruction requires that the registration methods applied are capable of giving an accurate fit to the patient-specific models, from which the simulated data are obtained.

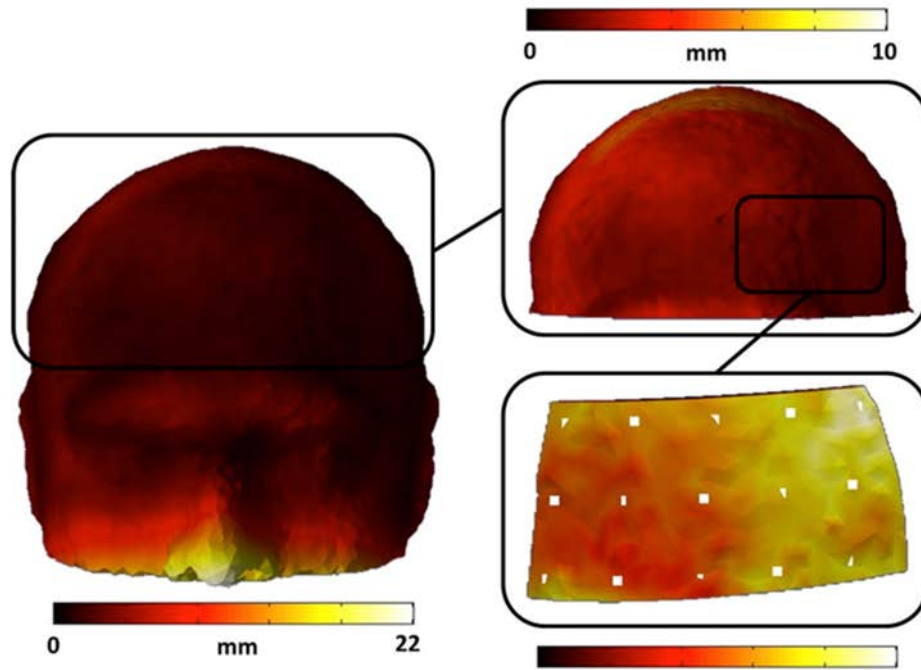


Figure 5.6: Heat map showing average registration error between each subject-specific and the corresponding registered Atlas model (Left). Cropped and rescaled heat map to show registration error on the desired region of interest (forehead) (Top Right). A zoom in on the region of the forehead where DOT pad is positioned (Bottom Right).

The registration accuracy was assessed for each of the 9 models used by measuring the Euclidean distance between nearest neighbour points on the original and registered Atlas models and averaging over all the models (Figure 5.6). The maximum registration error over the entire head was found to be 22 mm; however this takes into account anomalous regions such as large differences in nose features. Since the main focus of the study was the forehead, the calculated average results confined to the forehead region was found to be less than 10 mm, with errors in the pad region not increasing over 4.53 mm.

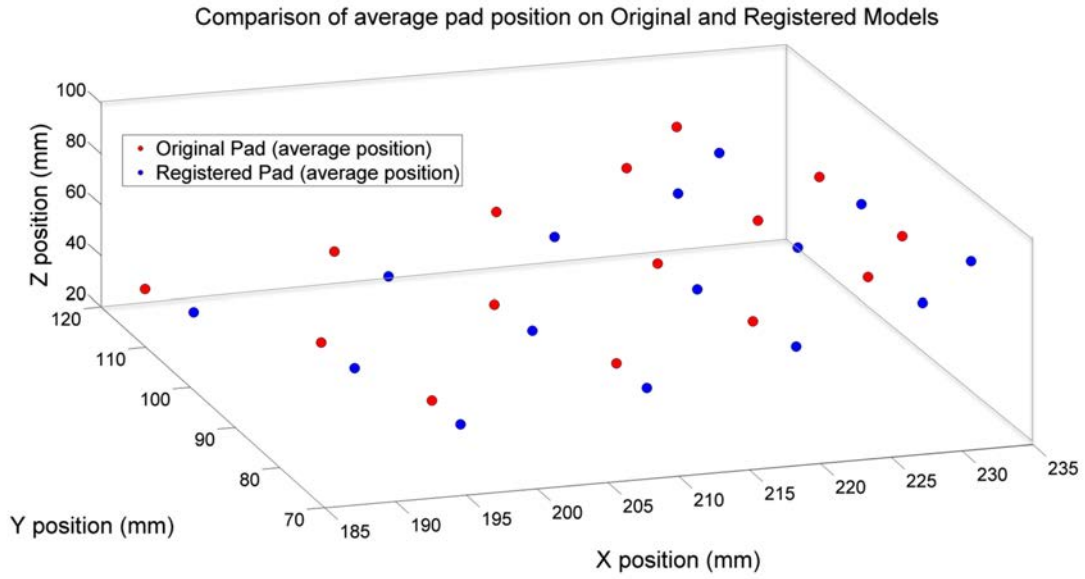


Figure 5.7: Average coordinates positions of the DOT pad on the original subject-specific models (red) and on the registered Atlas models (blue).

With confidence in the accuracy of the registered Atlas-models, the next step was to assess the positioning and layout of the DOT probe on the forehead region. The pad-positioning algorithm developed for this work uses a user defined reference point, at the nasion, from which the optode positioning initiates at a fixed x, y and z distance from the nasion. Figure 5.7 shows the average position of the pads from all models before and after registration, and it can be seen that although the conformity of the pad is correct in the x and z axes, the positioning in the y axis (as controlled by the user defined reference point) is not optimal. This has resulted in a shift of ~ 5 mm of the pad down the forehead towards the nose, which is not ideal as the probe will be sampling a different region of the cortex. Nevertheless, since the reconstruction averages over the whole pad area, a small change in sample area would be considered negligible in this study, and which represents a more realistic clinical situation where pad orientation and position will vary between

patients.

The more important issue, however, is the accuracy in layout of the sources and detector positions. If the spacing between sources and detectors used for the reconstruction model is different to that of the original model, there will be inaccuracies that will propagate through to the final reconstructed parameters. Figure 8 shows a contour plot of positioning accuracy for each source and detector across all the registered models, which was produced by stacking all the pads for all models, aligning their central point and calculating the spread in Euclidian distances between the original location of each source/detector and their position on the registered Atlas models. This gives a 2D representation of a 3D error. From the plot it can be seen that all the sources and detectors fall within 2.5 mm of their desired position.

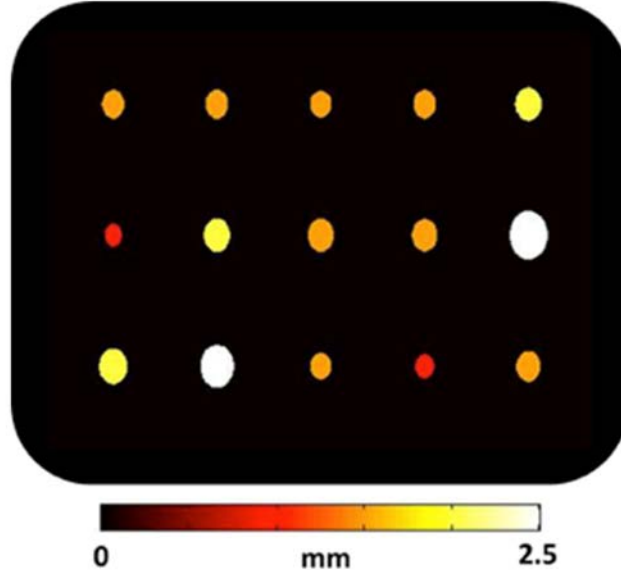


Figure 5.8: Maximum error in individual source/detector positioning across all the registered-Atlas models. This is a 2D representation of a 3D error.

Considering the system as a whole, the combination of errors in positioning of the pad and registration of the Atlas models produces a maximum mismatch of 7.5 mm. This is an area where refinements can be made, however, for the scope of the current study this mismatch provides a baseline level of numerical noise (error) for the reconstruction process, posing a worst-case scenario as a proof-of-concept. In a clinical situation, there

will be other confounding factors to reduce the accuracy of the reconstruction, such as detector noise, source variability, poor coupling between the head and probe, as well as human error in pad positioning. Human error in pad positioning has been observed in published literature observing the effect of test-retest NIRS studies [136]. Potential optimisation of the probe positioning through the use of a full head cap is impractical in the context of TBI, as there are often bandages and injuries, as well as other invasive probes obstructing the head. These factors are hard to reproduce in simulation; hence the baseline numerical noise from the registration is a good starting point from which future investigations can build and improve upon. With regard to the coupling efficiency between the probe and the scalp, as this simulation is designed as a proof-of-concept, the effect of coupling efficiency has not been considered, however it has been illustrated in other published literature that data can be calibrated to account for intensity and measurement variation effects [137, 14], as well as the recovery of these unknown coefficients as part of the image reconstruction [138]; both of which will be subject of further work when considering experimental data.

5.3.2 Reconstructions

After the registration process, the next step was to assess the reconstruction algorithms and its ability to provide quantitative measures of modelled changes from modelled measurements. The overall quality of the reconstruction was assessed on the accuracy of the recovered saturation values in the brain region, and while ideally all regions would be recovered to the same level of accuracy, in the interest of TBI the main concern is the quantitatively accurate reconstruction of brain saturation. All presented data are the average across all models with error bars showing the standard deviation calculated for the means of all models.

Reconstructed parameters from all models were analysed in terms of the recovered temporal changes of oxygen saturation for each layer of tissue, as shown in Figure 5.9. This

figure illustrates the recovered values as a function of time shown for the three layers under investigation (skin, bone and brain), prior to, during and immediately following a simulated VM. This reconstruction was an inverse crime, where the same model was used for both data simulation and reconstruction. From the results shown in Figure 5.9 it is evident that the region-based reconstruction (where a single parameter is recovered for each tissue type) has given the most accurate results in all three layers of the head. This result demonstrates the validity of the regional reconstruction algorithm (0.04% error for simulated values with a standard deviation of 0.07%), using a set of homogeneous starting properties and given accurate spatial priors.

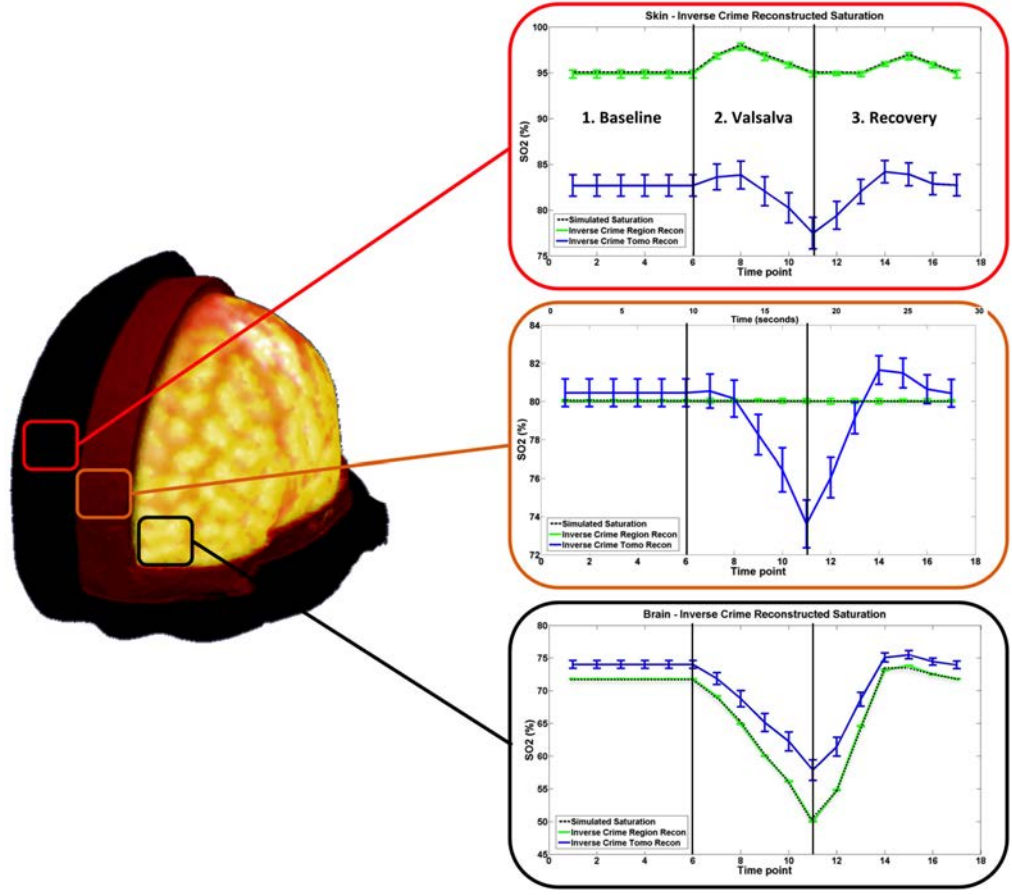


Figure 5.9: Inverse crime reconstructed saturation values for the skin (top), bone (centre) and brain (bottom) regions (outlined in Figure 4.15) using both regional (green) and tomography (blue) algorithms prior to, during, and immediately following a VM (time points 6-11) . The plotted results are the average over all models with the error bar showing the standard deviation of the dataset. The simulated saturation line (dashed) in the Brain results graph (bottom graph) is not visible as it overlaps the Inverse Crime Regional Reconstruction (Green) line.

The results when utilising spatially varying tomographic reconstruction are also shown in Figure 5.9 (blue line), and demonstrate that these do not perform to the same level of accuracy as the region-based reconstructions (green line). Recovered oxygen saturation in the skin, while showing the correct trend, is not quantitatively accurate. Bone region reconstructions show a closer resemblance to the expected changes in the brain rather than for the bone. Finally the brain reconstructions, while showing the correct trends (like the skin), lacked the desired quantitative accuracy, with maximum percentage difference between the average brain parameters and the simulated values of 15.7% (values quoted

are percentage error between recovered and simulated values as opposed to a change in oxygen saturation) with a standard deviation of 1.2%.

While these tomographic-based results are of lower accuracy, they are not unexpected for this set of simulations, since tomography gives a spatially varying saturation value throughout the model in comparison to the region-based reconstructions (Figure 5.9) that give a single saturation value for an entire region.

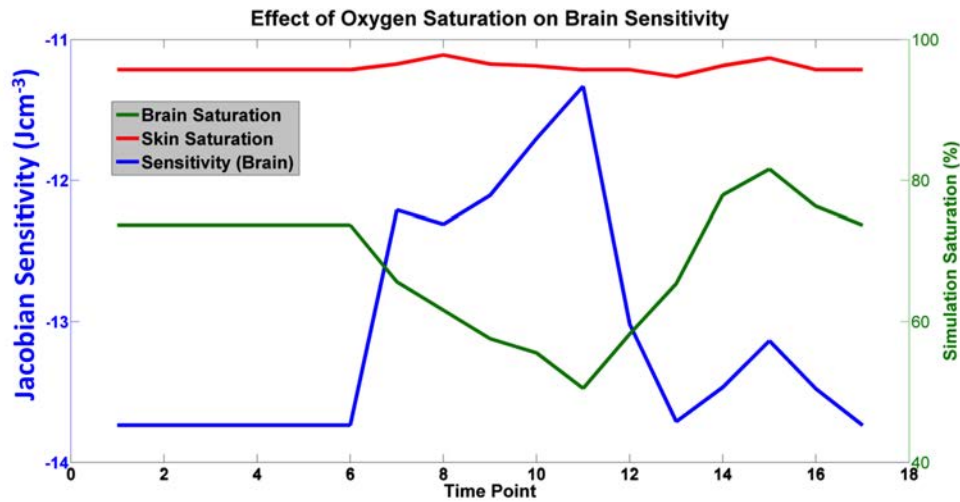


Figure 5.10: Graph illustrating how the sensitivity of DOT in the brain region alters as the saturation in all regions is varied during the VM. The sensitivity is a summation of the Jacobian values corresponding to brain nodes. More negative values indicate higher sensitivity.

To further analyse the tomographic reconstruction, the inaccuracy in the recovered parameters has two main potential factors; firstly, the simulation is biased to regional recovery as the simulation itself is for changes that are global to each region. Based on this information it can be speculated that in a clinical situation where changes in each region is heterogeneous, tomography may outperform the regional reconstruction. The second

source comes from how each FEM node and its optical properties are selected for averaging. The nodes as discussed earlier are selected in a pre-reconstruction step, where the Jacobian is calculated for the initial homogenous optical properties of the reconstruction model by thresholding to a minimum (at least 2.5%) sensitivity value. A retrospective view would show that this is not the most accurate way to define nodal region of interest. Instead a better method would be to reassesses the Jacobian matrix and the region assignments at the end of each time point reconstruction, and then look at an objective method of thresholding the Jacobian to determine a more accurate region of interest. This way the tomographic reconstruction would be better suited to keep up with any localised changes in sample area due to changes in optical properties. For example, Figure 5.10 shows that as the saturation in the brain decreases the overall sensitivity to the brain region itself is being decreased due to the increased concentration of deoxyhaemoglobin. This is why a decrease in the accuracy of the reconstruction at the peak desaturation of the VM is observed. It would also explain why the bone region is inaccurate around the VM; the change in sensitivity causes cross talk between the brain and bone regions as the region assignment becomes less accurate. In terms of improving the thresholding for region selection, defining a range of values based on a percentage (top 60-95%) of the maximum sensitivity value instead of a simple cut-off sensitivity at 2.5% could offer advantages. As evident in Figure 5.11, is it clear that by setting only a minimum sensitivity, and not a maximum, the average saturation in the superficial (skin and bone) regions will be inaccurate due to the hot spots of hyper sensitivity.

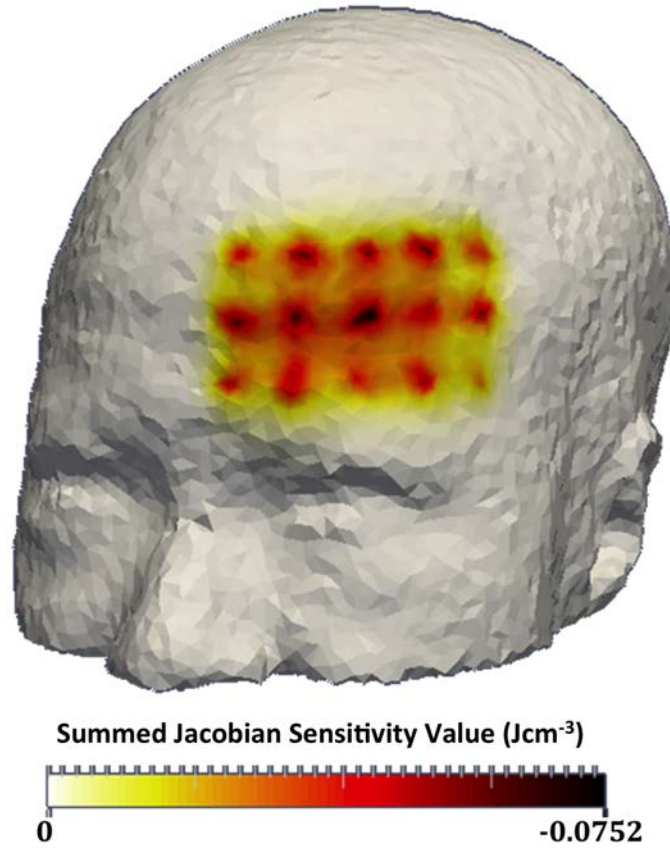


Figure 5.11: Plot of Jacobian (sensitivity) matrix values on the surface of a subject-specific model showing the hot spots of hyper sensitivity under each of the sources and detectors. A smaller sensitivity value represents a higher sensitivity.

While the studies to date utilising the inverse crime models demonstrate that a small scale DOT probe can be used to obtain quantitatively accurate brain saturation values, it is imperative to investigate the accuracy and validity of using the registered Atlas models as the basis for the reconstructions, bringing the simulations more in line with clinical conditions where there is no prior information about the internal structure of the head.

For the regional reconstruction based on registered Atlas models (Figure 5.12), the recovered saturation for both skin and bone are subject to poor quantitative accuracy and a large standard deviation. It is evident that fixing spatial priors, by giving absolute spatial information for each region (layer), the reconstruction is not able to accurately

recover the superficial saturation values. This indicates that despite the utilisation of the new Atlas model, the variation in superficial layer thickness between subjects and the Atlas is still confounding the reconstructions. Evidence of this cross talk within the superficial layers can also be seen with a simple comparison of the trends in the skin and bone regions, which both appear to follow the same trends as the simulated skin saturations, thus implying that the skin layer is too thin in the utilised Atlas model. Despite the mismatch in superficial layers, the region-based reconstruction recovered the brain saturation values with an average percentage difference of 11.2% (standard deviation 5.0%) between simulated and reconstructed values. While this does not seem overly accurate, in comparison to some of the existing NIRS techniques such as SRS reconstructions explored in previous work [139, 140, 54] and data from Chapter 4, region-based DOT shows a marked improvement.

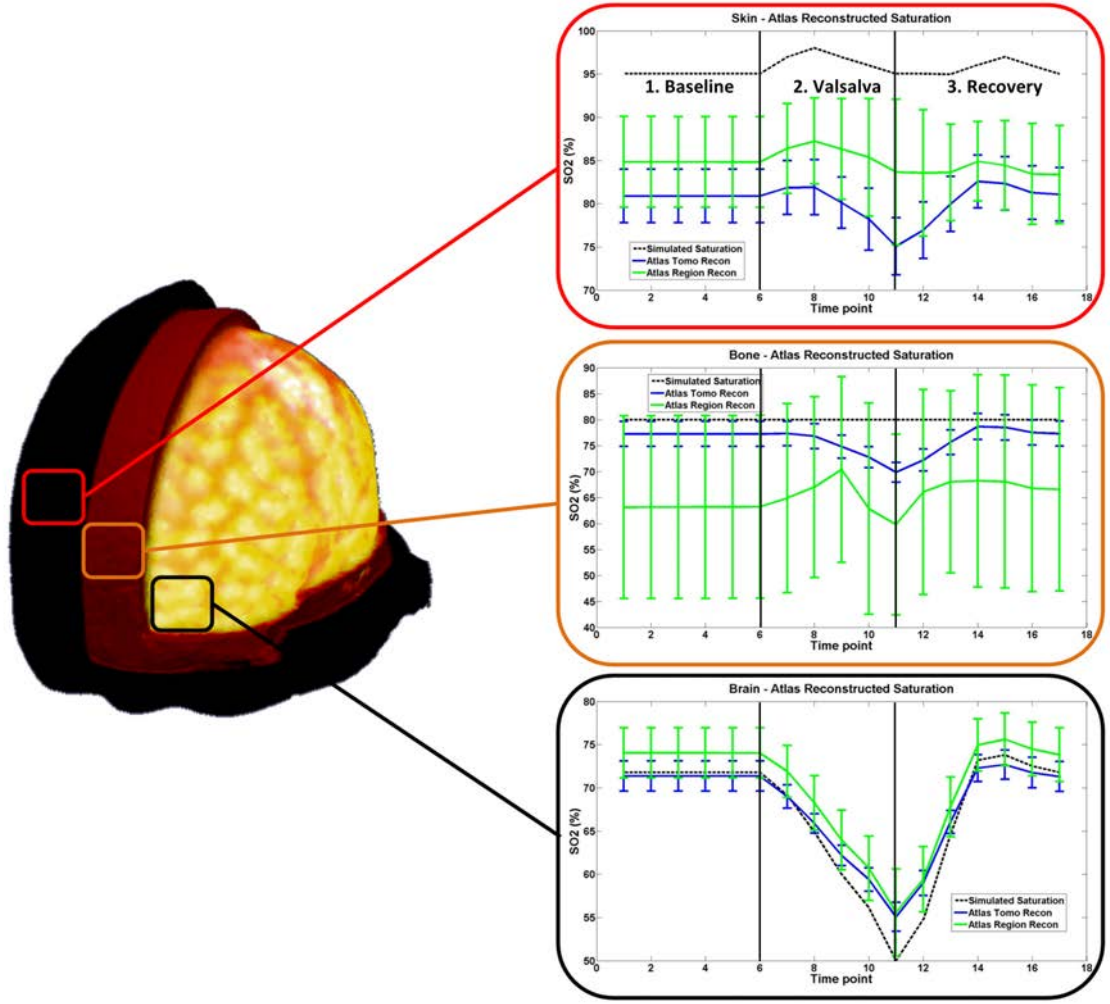


Figure 5.12: Atlas reconstructed saturation values for the skin (top), bone (centre) and brain (bottom) regions using both regional (green) and tomography (blue) algorithms. The plotted results are the average over all models with the error bar showing the standard deviation of the dataset

Unlike the inverse crime reconstructions, once the Atlas is employed, the quality of the tomographic reconstruction surpassed that of the regional in all layers, other than the skin (see Figures 5.12 and 5.9) in terms of both quantitative accuracy and the standard deviation of the recovered saturation values. The average percentage difference between the simulation and reconstructed brain values was 10.1% with a standard deviation of 1.8%. While the fixed region sizes posed an issue for the regional reconstructions, the tomographic process was not constricted in the same way. The Atlas tomography even performed better than its inverse crime counterpart, again highlighting issues with region

of interest (ROI) selection. The limiting factors in grouping nodes into a ROI via Jacobian thresholding still apply, however because of the mismatch in superficial layer size these errors appear to average out over the course of all the head models, smoothing the results.

The main consideration when assessing the quality of the registered-Atlas reconstructions is that the results were more quantitatively accurate than the current NIRS-based recovery techniques. While absolute quantification was never anticipated, the main goal of this study was to show the potential of DOT to improve on current NIRS limitations, which is clearly visible from the above results.

5.3.3 Conclusions - Simulation Studies

Currently the NIRS technology that is available in the clinic lacks the quantitative accuracy to monitor saturation changes in TBI patients. The global measures of saturation provided by NIRS probes mean that the target changes in the brain are often confounded by the haemodynamics of superficial layers such as skin and bone. While brain haemodynamic changes are observable, the saturation values obtained are not reliable enough to allow NIRS to be used as a clinical gold standard for TBI monitoring.

In the context of measuring quantitatively accurate brain saturation measurements in TBI patients, the technique of Atlas-guided reconstructions has shown significant potential. While there are many refinements to both the reconstruction algorithms and the realism of the simulations, which can be made, the data in this study present a first step towards clinical DOT measurements for TBI monitoring. Where previous studies implementing NIRS into the clinic have found that the superficial saturation changes can obscure accurate brain observation, current simulations for DOT have shown the potential benefits. Due to the iterative recovery process of DOT it is inherent that more prior information can be provided. Even though this information has proved inaccurate in terms of superficial layer size, the known depth of the cortex surface (roughly constant over all heads) has allowed for significant improvements in brain parameter recovery.

The next progression of this work comes in two forms. The first needs to focus on the

refinement of the reconstruction techniques. This will come in the form of redeveloping the Atlas so that the superficial layer mismatch provides less of an issue. Also in terms of improving the tomography reconstructions, thorough investigations into methods of selecting the correct regions of interest are required. The second is the practical implementation for a clinical DOT NIRS system. Simulations will never truly mimic clinical conditions, thus the probe needs to be characterised and tested on a mix of, well defined phantom models, healthy volunteers and TBI patients.

5.4 Direction Of Future Studies - Healthy Volunteer testing with existing DOT probe

Having demonstrated that the reconstructions based on registered-Atlas models were found to provide potential improvements, in terms of quantitative accuracy, when recovering cerebral saturation changes during a simulated VM, the following experiment aimed to extend this method for testing in a series of healthy volunteer studies. As well as extending the Atlas model reconstruction, where available, the Atlas reconstructions were compared to reconstructions using a subject-specific model (segmented MRI of the subject) as the reconstruction basis to improve the structural prior information. In comparing the two, the validity of the Atlas models in clinical situations can be assessed, as well as allowing the effects of superficial layer mismatch to be seen. With healthy volunteer studies, as well as potential mismatch in tissue layer thicknesses and the shape of the head, there is now also the possibility of scattering property mismatch. This is a potential limitation of this technique as continuous wave devices provide no specific scatter information during data reconstruction.

5.5 Methodology - *In Vivo* Testing

5.5.1 High-Density Probe for Data Collection

High-density probe used for these healthy volunteer studies was designed and built by the Nalecz Institute of Biocybernetics and Biomedical Engineering (Polish Academy of Sciences). The probe consisted of 8 source positions, illuminating at 750 and 850 nm with 6 detector locations. Each detector measured light from all 8 source positions resulting in 96 overlapping measurements at source-detector separations of 1.5, 3.4, 4.5 and 5.5 cm over a 16 cm² region of interest. The layout of the probe and position on the Atlas model and subject heads is shown in Figure 5.13

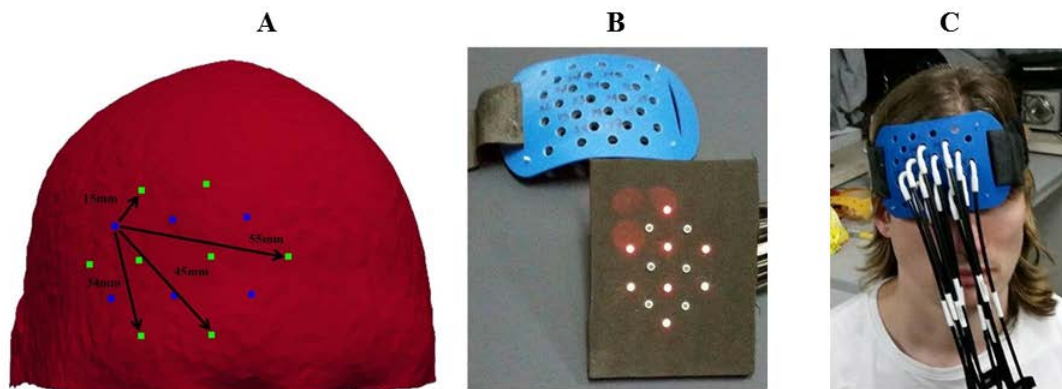


Figure 5.13: Layout of the high-density DOT probe on Atlas Model (A) and actual probe (B) designed and built by the Institute of Biocybernetics and Biomedical Engineering (IBIB). Detector positions are shown in blue and source positions in green with the maximum source-detector separations indicated. C shows the probe in position on a subjects forehead.

The pad holder was made from a curved and semi-flexible plastic that moulds to the subject's head and is held in place with an elasticated strap. The fibre optic cables channelling light to and from the sources/detectors could be individually moved to ensure they were all in direct contact with the skin, and as the target region was on the forehead

there was no risk of hair obstructing any of the fibres. The position of the pad was on the subjects right-hand side and was positioned such that the right most source/detector was 1 cm from the midline with probe base just above the superior orbital ridge. While this protocol was used for each of the subjects, variation in the shape and available space on the forehead meant the angle of the probe did vary, which may cause a mismatch between the 'real' probe and the probe positioned on the reconstruction models.

5.5.2 Recording *Valsalva* Data

Ten healthy volunteers (8 Male, 2 Female aged 35-50) performed a series of three, 10 s, standing maximal VMs under controlled laboratory conditions. The study conformed to the Declaration of Helsinki and was approved by the University of Birmingham Research Ethics Board (Ref.: ERN_30-1031). Individuals recruited had no significant prior medical history. As no blood pressure readings were available to judge the recovery to baseline between VMs, a 5 min rest period was taken between each recording. Each data acquisition consisted of a 30 s baseline reading, the 10 s VM with a 30 s recovery reading. Subjects were given instruction and practice trials to insure the VMs would be consistent.

5.5.3 Production and Registration of Head Models

The production of both the Atlas and subject-specific head models used the same method followed for the simulation studies in Section 5.3.1. The Atlas used for the reconstructions was the ICBM152 model, despite its discovered limitations in the simulation study. The Atlas and MRIs were segmented in NIRVIEW, where the landmarks for registration were also positioned. MRI data was available for two of the subjects, which was used to create subject-specific head models to compare to the registered-Atlas reconstructions. The meshing process used an average nodal distance of 3 mm and the total number of nodes in the mesh was 76,925 for the Atlas model

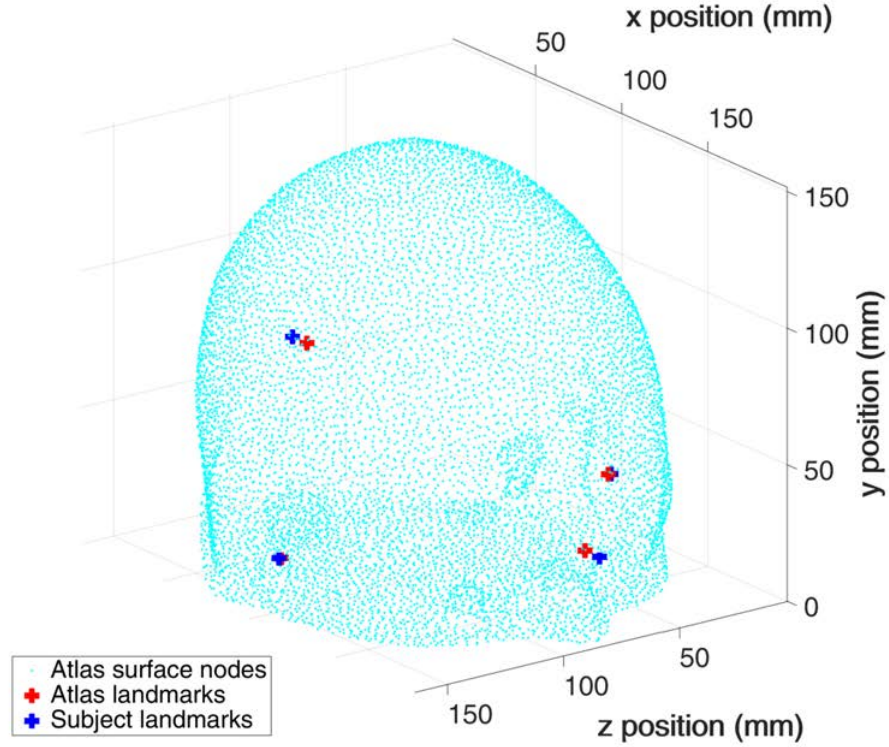


Figure 5.14: Example of the 4 landmark points used to register the Atlas model to the geometry of a subjects head.

Instead of the 687 registration point used in the simulations (which are usually collected with a digitizer pen that maps 3D coordinates), 2 sets of paired points were used to represent a simple set of measurements that would be easily obtainable in a clinical setting. Although only using 4 points will likely cause the registration accuracy to decrease, previous research into the use of different registration methods has shown that the basic 4-point registration did not provide a significantly reduced registration accuracy (~ 2 mm reduction in accuracy) [58]. The points used for registration were, nasion to inion (front to back) and pterion-pterion (side to side) as shown in Figure 5.14 and were measured using medical callipers. The 4 points were co-registered using the same non-iterative point-to-point algorithm used in the simulations study (Section 5.2.2). The probe positioning was done prior to registration using the same iterative algorithm from Section 5.2.5, with

updated information about the new probe layout. The transformation followed by the registration was used to deform both the head model and the source/detector coordinates at the same time. The baseline optical properties of the models were set to the values defined in Appendix .1.

Data exclusion - In the previous studies using the VM to induce superficial and cerebral changes the validity of each data set for inclusion in statistical analysis was assessed by monitoring blood pressure during the VM to insure enough effort was exerted by the participant to stop venous return. However, in this study blood pressure monitoring was not available and thus the assessment of the VM had to be performed empirically through inspection of the raw data before processing, as well as subjective notes taken during the data collection on the apparent visible effort (facial flushing, shaking etc). In order to increase the reliability of performing the maximal VM, each participant was shown an example maximal VM by an experience maximal VM performer. As well as being used as a demonstration, this performance was used for the subjective grading and was arbitrarily given a grade of 5. A maximal VM should cause strong facial flushing, shaking from the strain of force expiration and finally a fast audible release of breath as the glottis is opened. Using the example participant as a model, each subsequent volunteer was given a VM grade based purely on these physical attributes. Then once the VMs were complete the raw detector data was checked against the physical gradings. Only participants who showed both poor visible VM signs as well as poor detector response were excluded (see Figure 5.15 for examples of VM data grading).

While these metrics are no substitution for blood pressure monitoring there was correlation between the observed effort and the level of changes seen in the raw data. Figure 5.15 shows examples of how the VM data was graded from 1 to 5, with one being a poor VM (no change) and 5 being a strong VM with large visible changes in the data.

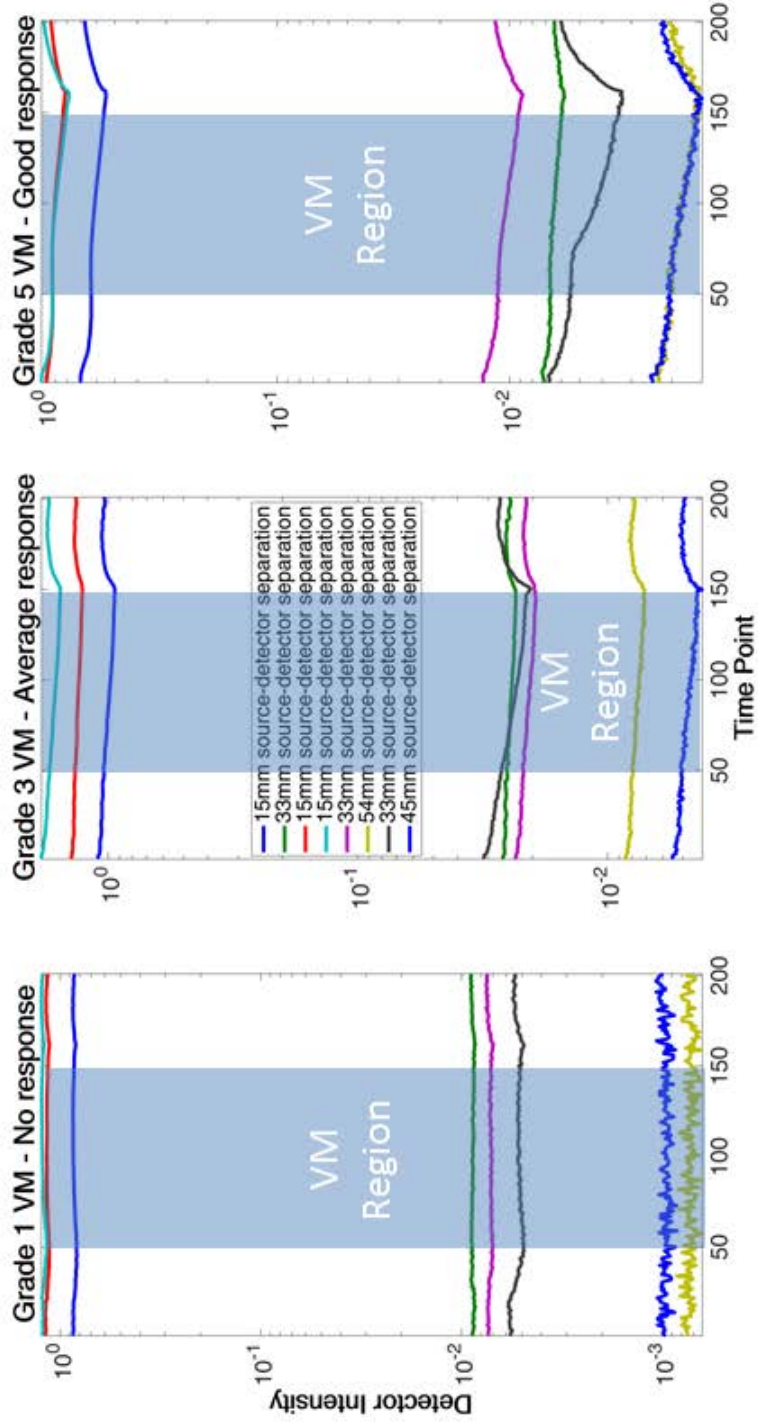


Figure 5.15: Examples of the VM grading system used for raw data where 1 is a poor VM, 3 is an good VM and 5 represents a strong VM. This is example data from one detector recording data from all sources at 750 nm source wavelength. The different coloured lines represent different source detector separations.

5.5.4 Reconstruction Regime

The reconstruction regime for the healthy volunteer study was altered from the original methodology used in the simulation studies as an additional step was required in terms of data processing and reconstruction sequence. Only the region reconstruction method, providing a single set of recovered optical properties for each region was used, with no 'global' reconstruction to provide an initial guess. The global reconstruction was removed as preliminary studies showed that it tended to force the reconstruction into a local minimum and finish with a high projection error after only 2 iterations. The outline of the reconstruction sequence for the healthy volunteer study are as follows:

1. Calibration of raw VM data.
2. Averaging of data into two time points. A) baseline and B) peak VM.
3. Three-region reconstruction for baseline and VM data

Data Calibration - The data calibration process used data obtained from a large homogeneous cylindrical phantom using the high-density probe (FEM shown in Figure 5.16). The phantom data was fitted to an analytical solution to the diffusion approximation, which is based on a infinite homogeneous medium (full details given in Section 3.1) using a 25 stage iterative fitting algorithm (Newton-Raphson). The calibration process fits the gradient of $(\frac{\delta \ln(rI)}{\delta r})$, where r is the source-detector distance and I is the detected intensity. The fit minimises the difference between the calibration dataset and a set of forward data produced by the analytical solution for the same probe geometry given a set of initial starting properties ($\mu_a = 0.01 \text{ mm}^{-1}$ and $\mu'_s = 1 \text{ mm}^{-1}$). This process is repeated for the 750 nm and 850 nm data.

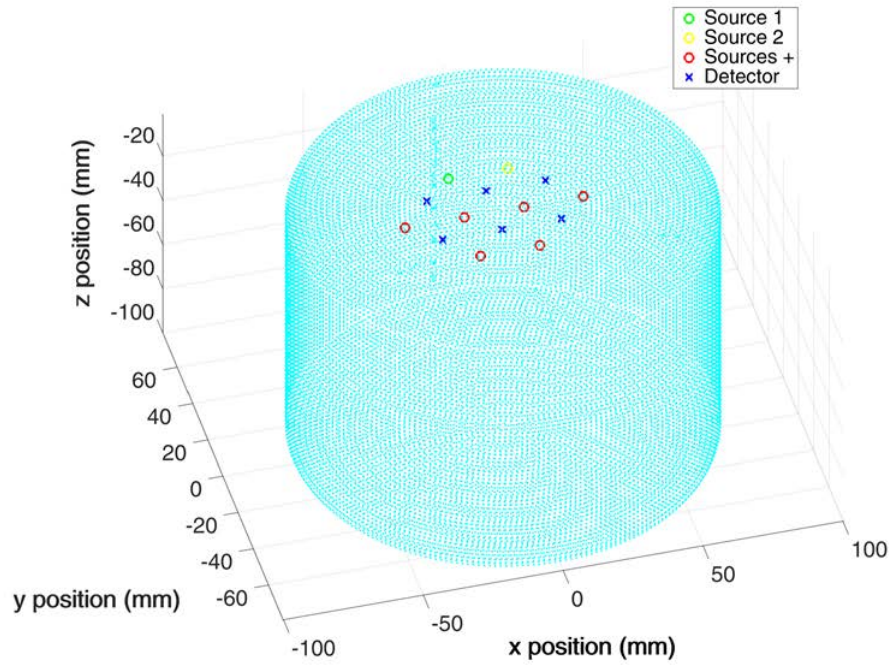


Figure 5.16: Surface point representation of cylindrical phantom mesh used for VM data calibration process.

To further improve the fitted optical properties, a second fitting process over 10 iterations was used in conjunction with the FEM (Figure 5.16) fit instead of the infinite medium solution. The result is an offset value for each source-detector pair for each wavelength that could be directly applied to the raw VM data, this is also a calibration for detector responsivity and source intensity.

Data Averaging - The data were recorded by the probe at 10 Hz so there were 10 data points available for each second of recording time. For the reconstruction, two sections of the recorded data were averaged to produce two data points, one for the baseline measurement and another for the peak desaturation just before the VM is released (Figure 5.17). The baseline was an average over a 20 s period (200 data points) and the peak

VM data were averaged over a 1 s (10 data points) period. Each data set was checked manually to make sure the data points taken for each section were in the correct location. Grade 1 VMs were removed from statistics on peak VM desaturation changes, however, the data were still valid for assessment of the baseline variation between participants. The assessment looked at the magnitude of the change as well as in which channels it occurred. For example, a poor VM has no response even in the short (15 mm) source-detector separations (channels); even a weak VM caused facial flushing that was enough to exhibit a change in detected intensity, therefore without this change the VM was not counted as a maximal effort.

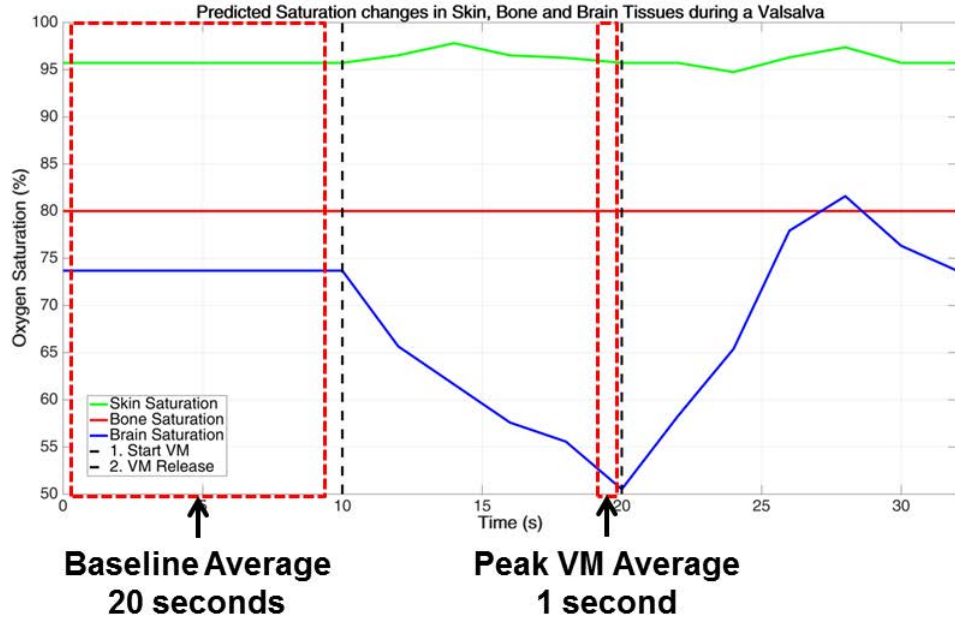


Figure 5.17: Illustrations of the sections of the recorded data used for the baseline and peak VM data sets.

Reconstruction - The reconstruction process consisted of a region-based reconstruction recovering a set of optical properties for 3-tissue layers of skin, bone and brain. The reconstruction basis for both the baseline and VM datasets was set to be the registered-Atlas model (or subject-specific model) with scattering properties and water content values shown in Appendix .1. The concentrations of HbO and HHb were

initially set as homogeneous being 0.0560 mM and 0.0140 mM, respectively. The reconstruction was allowed to run for a series of 40 iterations with the stopping criteria for the projection error being a change of less than 0.01 % between the current and previous model data. The regularisation value used for the reconstruction process was 1000. The use of this value was based on preliminary results what showed the reconstruction ran for a large number of iterations with a lower final projection error when the regularisation parameter was higher.

5.5.5 Results and Discussion

Valsalva Reconstructions - Atlas model

The Atlas-based regional reconstructions showed that the variation in baseline readings over the 10 participants was significantly higher than expected, with the standard deviation of the brain saturation across the group being 24% (Figure 5.18). This was a significantly higher variation than was seen with existing fNIRS probes testing in previous work where the NIRO-200NX and the ISS Oxiplex TS were found to have a mean baseline variation of 8.4 % and 9.7%, respectively. These results are not encouraging for the high-density probe as the large variation in brain saturation makes it very difficult to quantify what saturation value constitutes a healthy subject in the TBI monitoring context. It is unlikely that the results given are quantitatively accurate as some participants had recovered cerebral saturation values as low as 39%, a value that would be considered extremely dangerous in the clinic. The variation in the baseline is most likely due to mismatches between layer thickness and scatter properties from the Atlas to the participant, as was seen in the simulation studies. An explanation for this is that in the making of the reconstruction model more complex to improve its accuracy, this may have inherently left the process more open to influence these sources of error. The subject of mismatch between layer thickness and scatter between the Atlas model and the participant head is discussed later on in this section.

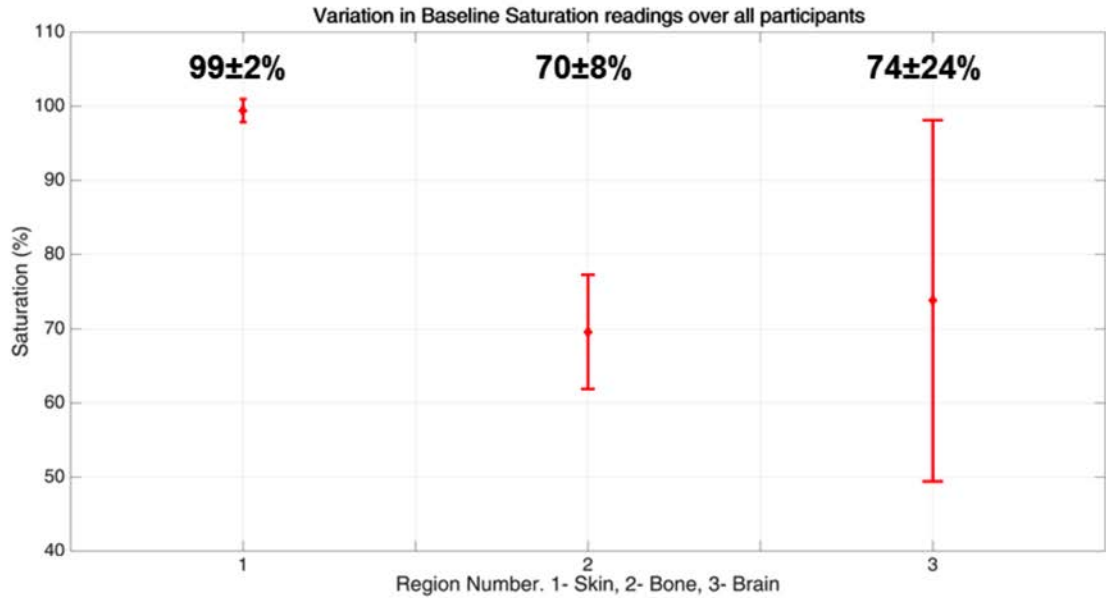


Figure 5.18: Baseline variation in saturation for the skin, bone and brain regions over all 10 participants.

Despite the lack of quantitative accuracy there are areas where the high-density probe showed improvements over the conventional fNIRS devices. The high-density probe was significantly better at mapping the magnitude of the desaturation expected during the VM. The predicted drop in saturation was approximately $\sim 20\%$ yet data recorded on the ISS Oxiplex TS fNIRS device during the experiments in Chapter 4 where a maximal effort VM was performed showed there was only a drop in saturation of $7 \pm 3\%$, less than half of the drop predicted in the VM model. The high-density probe on the other hand showed an average drop in saturation of $20 \pm 7\%$. So while the high-density probe still lacked the quantitative accuracy required to monitor TBI patients without a normative baseline measurement, they appear better at separating out changes between different

tissues on the head and recovering the magnitude of changes in the brain. The results of the reconstructed VM data are shown in Figure 5.19, where the average reconstructed values for each region are plotted for the baseline and the peak of the VM. Due to the high variability in the baseline the error bars overlap between the baseline and the peak VM values which makes the data hard to interpret, however there is a statistically significant desaturation over all the participants (Wilcoxon Signed rank test: $p < 0.001$, $z = 3.49$, number of samples - 16).

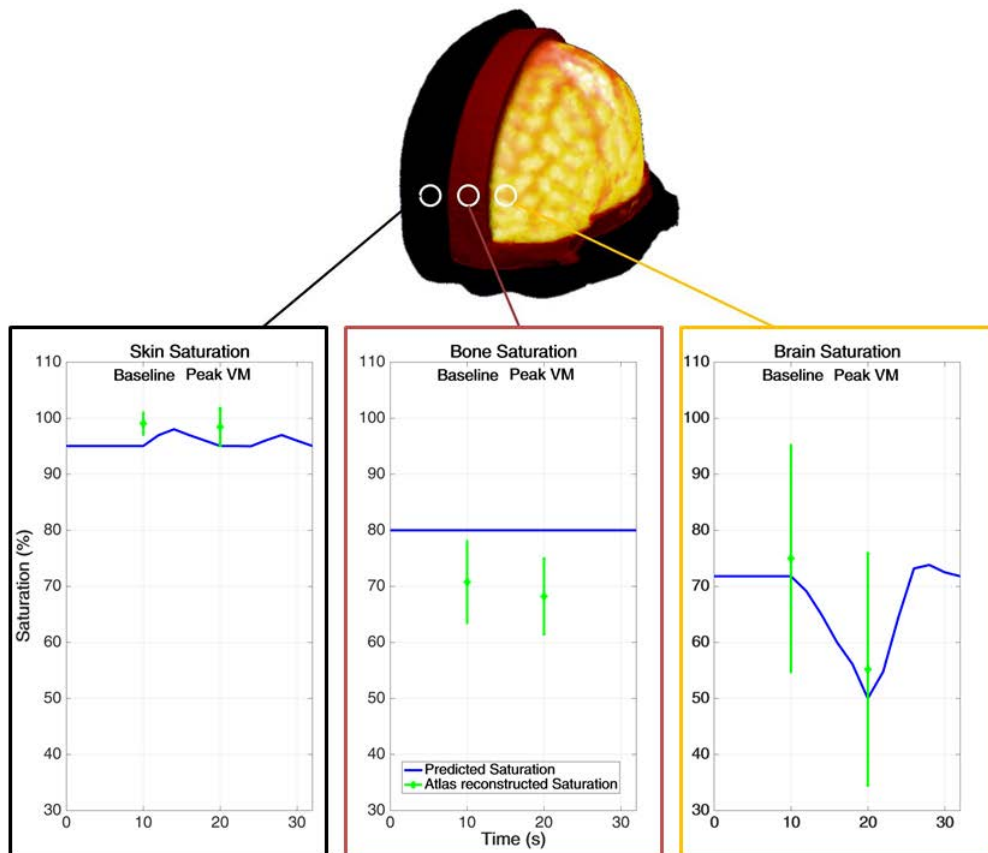


Figure 5.19: Average reconstructed saturation values for the skin, bone and brain regions.

It is clear that even though reconstructions using the Atlas model and high-density probe data are able to accurately map the cerebral changes occurring due to the VM without influence from the superficial tissues (as was seen with conventional fNIRS), there are still flaws in the model that are preventing it from being fully quantitatively accurate. As discussed in the simulation results, this is most likely due to a mismatch in the tissue layer

thickness between the Atlas model and the participant, or that the scattering properties in the model are different to the actual scatter properties of the participants head. As the probe only provides intensity measurements there is no way for scatter to be accurately updated in the reconstruction, for this a frequency domain device with phase measurements would be required. However, the layer mismatch, which would mean the spatial priors given to the reconstruction were inaccurate, is a theory that can be tested. For two of the participants who underwent the VM protocol there was MRI data available, which was segmented and used to create two subject-specific models that could be compared to the registered Atlas models when used as the reconstruction basis.

***Valsalva* Reconstructions - Patient Specific Models**

The two participants for whom the MRI data were available showed a marked difference in the saturation values reconstructed using the registered Atlas models. The reconstructed data for these participants are compared alongside the predicted saturation values in Table 5.1. While both of these participants show a large drop in saturation over the course of the VM, the baseline saturation values are markedly different.

Layer	Participant 1 Saturation (%)	Participant 2 Saturation (%)	Predicted Saturation (%)
Scalp Baseline	99.99	94.53	95
Skull Baseline	78.67	58.92	80
Brain Baseline	94.83	39.10	72
Scalp VM	99.99	91.67	95
Skull VM	72.90	57.54	80
Brain VM	66	18.80	50

Table 5.1: Comparison of reconstructed regional saturation values using registered Atlas models for two participants.

From the simulation studies the source of this error was thought to be the mismatch in superficial layer thicknesses. Figure 5.3 shows a comparison of the layer thicknesses and depth to the cortex for the Atlas and both the subject-specific MRI models. The measurement plane was taken as the central sagittal slice of the models, 4 cm above the nasion point. The measurements show that there is a difference between the layer thicknesses in the models with the Atlas having a thicker scalp layer and a greater depth to the cortex, however, as the resolution of the models is 3 mm, it is hard to draw any firm conclusions from this data, it can only be taken as a guideline. Measurements taken from the MRI data using specialised clinical software (AGFA, Impax) showed that the distance from the skin surface to the grey matter surface to be 16.0 ± 1 mm and 15.6 ± 1 mm for participants 1 and 2 respectively. While this cannot be directly compared to the measurements taken on the models it confirms that there may be limitations to the segmentation process and the meshing resolution being used to translate the MRI data into the reconstruction models.

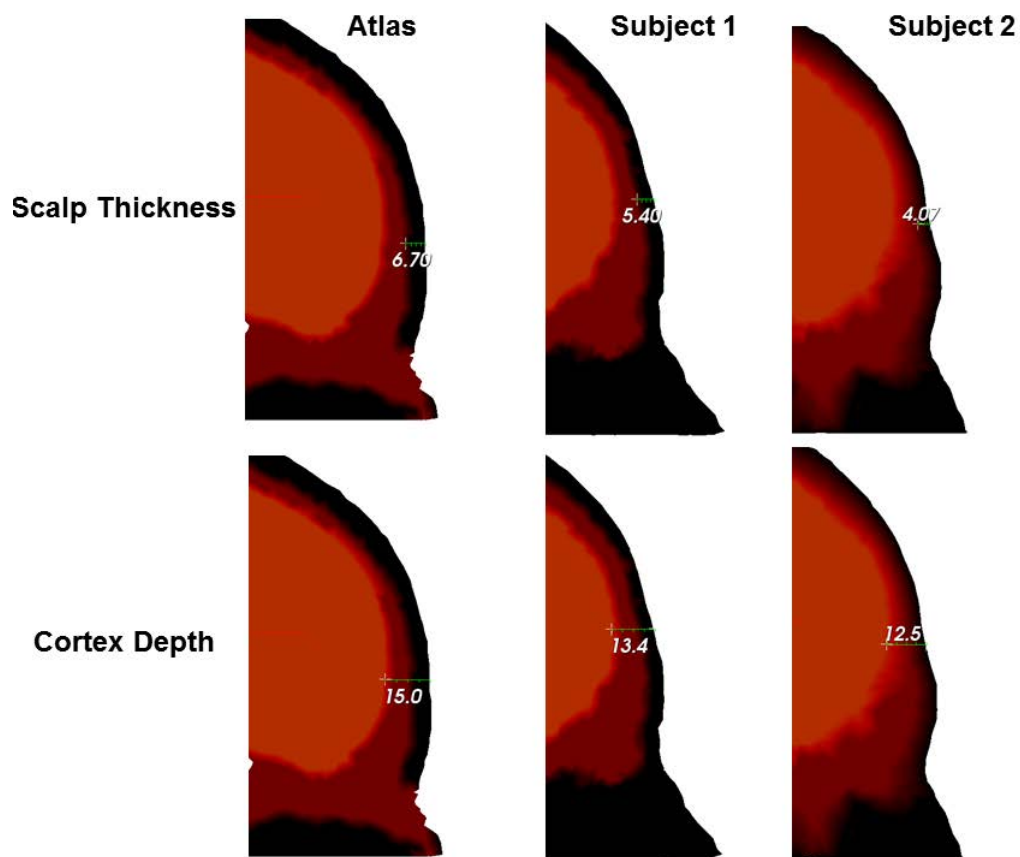


Figure 5.20: Comparison of superficial layer thicknesses between the Atlas model and two subject-specific models made from segmented MRI data. All distances are measured in millimetres (mm) and the distances shown are skin thickness (top) and cortex depth (bottom).

Layer	Participant 1 Saturation (%)	Participant 2 Saturation (%)	Predicted Saturation (%)
Scalp Baseline	99.99	99.92	95
Skull Baseline	79.65	60.31	80
Brain Baseline	86.54	55.20	72
Scalp VM	99.99	99.14	95
Skull VM	74.54	57.70	80
Brain VM	71.76	39.15	50

Table 5.2: Comparison of reconstructed regional saturation values using registered MRI models for two participants.

When the reconstructions were reprocessed using the MRI models as the reconstruction basis, the results showed a marked improvement with the average values becoming closer to the predicted saturation values and the standard deviation between the two models decreasing, as shown in Figure 5.21, dropping from 39% to 22%. The average desaturation during the VM changed from 25 ± 6 % with the Atlas models to 15 ± 1 % for the MRI models, showing a much smaller variation and on average closer to the predicted 22% drop (when considering the variation). This showed that even though the measurements of superficial thickness did not show much variability (when considering measurement accuracy) there were clearly differences between the Atlas and MRI models within the layer sizes or the surface geometry. Overall, the saturation in participant 1 still higher than expected and the saturation in participant 2 was still lower than expected despite the use of accurate spatial priors (Table 5.2). Therefore, it can be hypothesised that the superficial mismatch in tissue layer thickness is not the limiting factor in achieving quantitatively accurate results as the two tested healthy participants should not show this degree of variation at baseline. The most significant other factor capable of affecting the light propagation in tissue is the scattering properties; a parameter that is not reconstructed for when using continuous wave systems. So, it is possible that although the correct

spatial prior information is being used the light propagation in the forward model is not representative of the true model as scatter is being incorrectly calculated through under or over estimation of scatter. This is entirely possible as the scattering values being used were average values taken from literature sources [113], and hence may not represent all heads sufficiently to get quantitative accurate data.

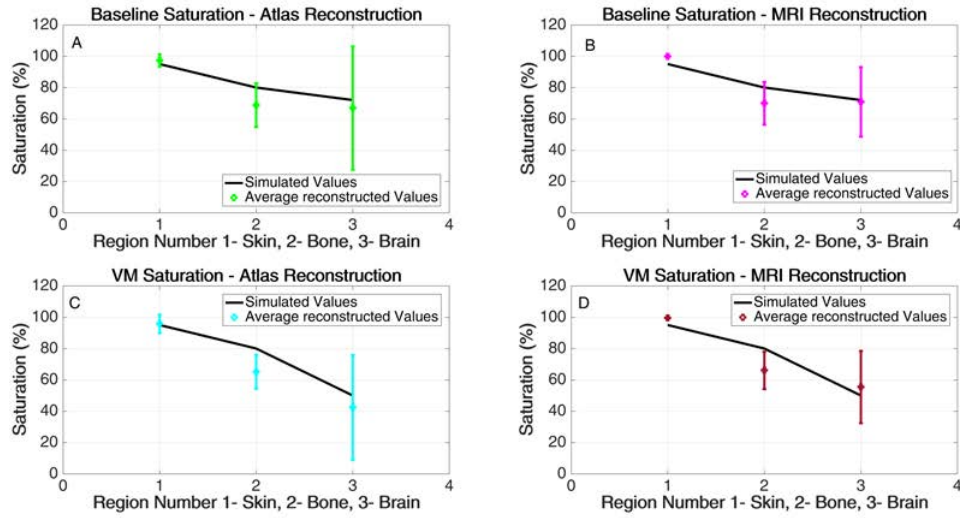


Figure 5.21: Comparison of average reconstructed saturation for all tissue layers using the registered Atlas models and the subject-specific models for 2 participants. A and B show the baseline values for the Atlas and MRI models, respectively, and C and D show the VM values for the Atlas and MRI models, respectively.

5.5.6 Conclusions - Healthy Volunteer Testing

Testing on healthy volunteers with a high-density probe showed that the registered-Atlas model-based reconstructions is not currently capable of quantitatively accurate cerebral oxygen saturation values using continuous wave measurements. The standard deviation

in the baseline cerebral saturation between subjects was 24%, which is greater than the variation seen in testing on commercial fNIRS devices of 8.4% and 9.7% [54]. It is apparent that increasing the complexity of the reconstructions to give regional values rather than just global changes, as with conventional fNIRS, has opened up the potential for both improvements and further inaccuracies in reconstructed results. Despite the increased variability and the lack of quantitative accuracy, the high-density probe along with the Atlas-based reconstruction has shown potential improvements over conventional fNIRS techniques, in the sense that it can more accurately map the predicted magnitude of saturation changes during a VM. There was a statistically significant desaturation over all the participants, with an average drop in saturation of $20 \pm 7\%$, almost double that of the $7 \pm 3\%$ drop shown with a conventional fNIRS probe in Chapter 4. This result is also more in line with the predicted 22% drop in saturation predicted during a VM. Therefore, even though the results are not quantitatively accurate, the knowledge that the magnitude of the change can be more accurately mapped is an advantage for TBI monitoring.

The inaccuracies in the healthy volunteer reconstructions are greater than in the simulation studies as there are now errors due to the scatter and spatial errors in the Atlas models, as well potential differences in the magnitude of patient effort during the VM. While future testing on the patient effort could be monitored with beat-to-beat blood pressure monitoring, scatter and spatial mismatches in the models require a different approach. The use of segmented MRI data to provide subject-specific models in two participants showed that the accurate spatial information did bring the reconstructed saturation values more in line with the predicted values, however the variation between the two subjects was still too high to indicate the results were quantitatively accurate. Therefore, it can be concluded that as well as errors in the spatial accuracy of the models (tissue layer thickness), there must also be a difference in the scatter properties of the head between participants that are confounding results, an issue that was not present in the simulation studies. As the continuous wave measurements with this probe cannot be

used to accurately update scatter and absorption properties simultaneously, there is no way to improve this error unless a more representative set of baseline scatter properties for the skin, bone and brain regions can be found. Alternatively, if frequency-domain data could be obtained phase measurements could be used to update the scatter properties during the reconstruction.

The two main issues highlighted by this study have been inaccuracies in the spatial information given by the Atlas model and the scatter properties being used. Therefore, to improve the quantitative accuracy the following section will explore the use of frequency domain measurements in updating scatter properties as part of the Atlas-based reconstruction. Also, the spatial errors in the Atlas model are clearly having an influence on the reconstruction accuracy, thus further investigation is required into the creation of more representative Atlas models.

5.6 Frequency Domain Simulations

One of the primary aims of this research was to design and build a high-density continuous wave probe that was capable of obtaining the quantitatively accurate saturation measurements needed for monitoring TBI patients in the clinical and pre-clinical setting. The combination of the simulation studies and the healthy volunteer studies indicate that while cerebral haemodynamics are being more precisely mapped, the quantitative accuracy of the results is still confounded. While superficial mismatch has been shown to have an influence on results in both cases, it is clearly not the overriding source of error. The scatter parameters in the simulations were kept constant and therefore were not present as a source of error, however in the healthy volunteer studies it has become apparent its effects are more pronounced. Research by Michaelsen *et al* showed that if the scatter estimate was out by 20%, then the error in the reconstructed HbT concentration could be out by up to 22.6% or 35.1%, for over or under estimating scatter respectively

[141]. The same study also showed that using phase data from a frequency-domain device, to recover scatter information, allowed for more accurate reconstruction of optical properties as scatter estimates were being updated in reconstruction data from human breast imaging. Therefore to extend this theory the concept of using phase data to recover scatter information and thus improve the quantitative accuracy of the Atlas-based reconstructions is explored in a preliminary set of frequency domain simulations.

5.6.1 Methodology

The probe used for the frequency domain simulations was the one described in the previous simulations (Section 5.2.3), utilising the same absorption changes to simulate a VM. The difference was the use of different scattering properties and spatial prior information between the data simulation and the reconstruction basis model. Three scenarios were tested to assess the contribution from superficial layer thickness mismatch (spatial mismatch) and scatter property mismatch.

1. Layer mismatch - Example MRI used to simulate data and Atlas model used for reconstruction with the same scatter properties
2. Scatter mismatch - Atlas model used for both data simulation and reconstruction with different scatter properties
3. Scatter and Layer Mismatch - Example MRI model used for both data simulation with 'Original' scatter and reconstruction performed using the Atlas model with 'New' scatter properties

Frequency-domain data was modelled at 100 MHz modulation frequency and both frequency domain and continuous wave reconstructions were carried out on the data sets for comparison, the 'New' and 'Original' scatter properties are shown in Table 5.3 with the new values being obtain from the literature (i.e., [142]).

Layer	Skin Scatter (mm ⁻¹)	Bone Scatter (mm ⁻¹)	Brain Scatter (mm ⁻¹)
Original - 735 nm	0.33	2.20	0.68
Original - 805 nm	0.26	1.93	0.64
Original - 850 nm	0.22	1.78	0.61
New - 735 nm	1.74	2.66	2.49
New - 805 nm	1.63	2.34	2.19
New - 850 nm	1.56	2.17	2.03

Table 5.3: New ([142]) and Original ([113]) scattering properties used for the frequency domain simulations.

The reconstruction of the data followed the same outline as the VM data with the IBIB high-density probe (detailed in Section 5.5).

5.6.2 Results and Discussion

The results of the frequency domain simulations were variable, however, there were areas where the more complex reconstruction process proved superior to the previous continuous wave results. Figure 5.22 shows the saturation values reconstructed for the baseline and VM datasets for the skin, bone and brain regions over the 3 different simulation conditions. As these are a preliminary set of simulations, there is not enough data for a rigorous assessment of the technique, however, there are a number of deductions that can be made to inform future studies.

For the first set of reconstructions the reconstruction basis had the correct scatter properties however the shape of the mesh and the internal layers was different (spatial mismatch). The results are shown as the red line on the graphs in Figure 5.22, and show a poor correlation with the simulated saturation values (dashed black line) over all three regions of the head. Even though the FD reconstructions used phase to calculate updates

to the scatter properties of the model, the quantitative accuracy of the reconstructed saturation values showed no improvement over the CW reconstructions of previous simulations and healthy volunteer testing. This could be due to the region-based nature of the reconstruction, where even though the scatter properties are being updated for a more accurate estimate, the fact that the parameters are being 'forced' into the inaccurate spatial layers of the model is undoing any improvements the scatter information may provide. Future investigation in this area could reassess the use of the tomographic reconstructions explored in the first set of simulations so the reconstruction process is less constrained.

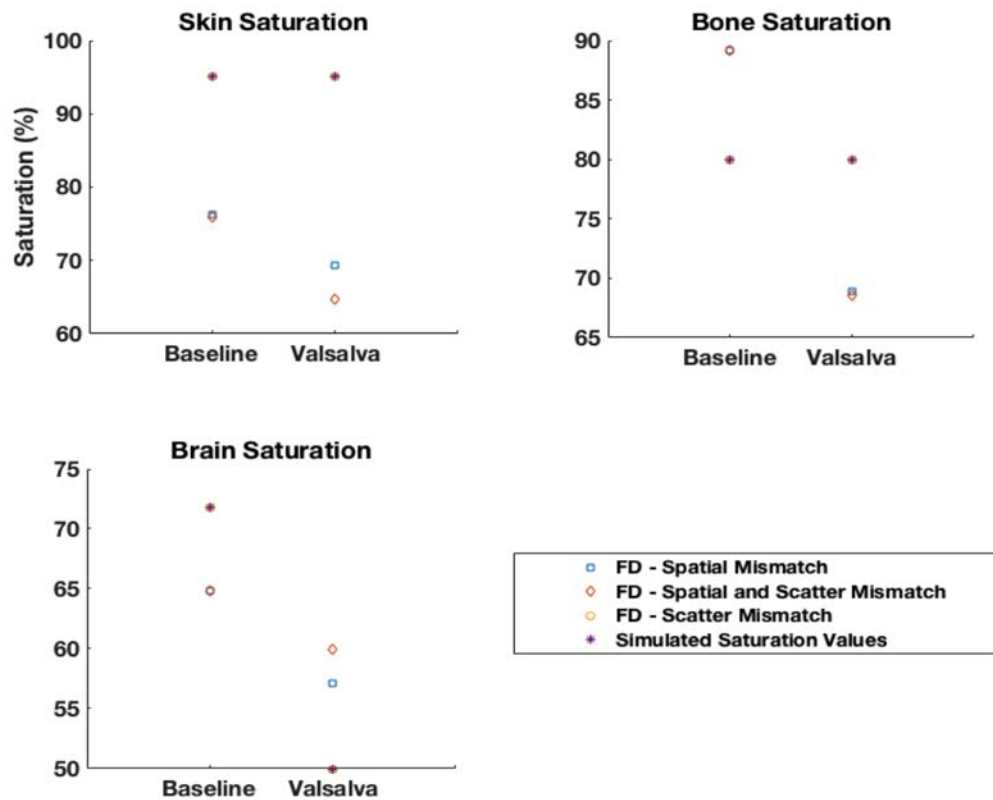


Figure 5.22: Reconstructed saturation values for the 3 different frequency domain simulations. The blue line representing the FD reconstructions with on a scatter mismatch and the black line representing the simulated values overlay each other.

The second set of reconstructed values (shown by the green line) use a reconstruction basis that has both inaccurate scatter and spatial properties and theoretically should have

the least quantitative accuracy, however, the saturation values obtained were similar to the reconstructions with just a spatial mismatch. This would indicate that the mismatch in scatter properties are not causing the inaccuracies in the frequency domain reconstructions and it is still the spatial mismatch causing a majority of the errors. This theory is confirmed by the third set of FD results that used a reconstruction basis containing only scatter property mismatch; these results are shown by the blue line and show an almost perfect match to the simulated saturation values.

While the overall results of the frequency-domain simulations showed that the quantitative accuracy is still limited, the results were compared to a set of continuous wave simulations based on the same parameters to check the magnitude of change of the desaturation seen during a simulated VM. This comparison aimed to see if FD reconstructions maintained this advantage, which showed in the previous CW testing in this Chapter.

The continuous wave results indicate that in the situations where scatter and spatial mismatch were simulated, the magnitude of the desaturation was $\sim 17\%$, which is much more significant than the $\sim 5\%$ seen in the FD reconstruction and much closer to the simulated 22% . The reconstructions with spatial inaccuracies only showed the magnitude of change was under estimated in the FD reconstructions and over estimated in the CW reconstruction. The only time when FD reconstructions outperformed the CW reconstructions in all metrics was when scatter mismatch was the only form of inaccuracy in the reconstruction model.

This would suggest that in a situation where the Atlas model could be improved, so as to be more representative of a subject's internal tissue layer thickness, the FD reconstruction would theoretically improve the quantitative accuracy of the reconstructions, and make the technique more viable for use as a TBI monitoring modality. There is also the possibility that if a frequency domain probe was used it would have better results if it was combined with a tomography-based Atlas rather than a fixed layer-based region

reconstruction.

5.6.3 Conclusions - Frequency Domain Simulations

From the simulations explored with frequency-domain reconstructions, the inclusion of phase data only increased the quantitative accuracy of the reconstructed saturation values when the only inaccuracy in the reconstruction model was scatter mismatch. However when the reconstruction model includes inaccuracies in spatial information, the frequency domain reconstruction does not provide any improvements over the continuous wave methodology, in fact, in the example tested here the continuous wave reconstruction provides a better insight into the magnitude of cerebral saturation changes, although they are still quantitatively inaccurate.

The data indicates that a frequency-domain device could have the ability to make the Atlas reconstruction method more quantitatively accurate if the Atlas model itself could be improved, to be more representative of the patient tissue layer thicknesses. If this could be achieved then a frequency-domain probe could provide the additional quantitative accuracy needed for TBI patient monitoring. The probe designed as part of this research (covered in Chapters 6 and 7) is controlled by an Arduino Due, which has the ability to modulate its LED output signal and therefore theoretically be adapted to make a low cost frequency domain probe to provide a cheap and portable form of TBI monitoring.

5.7 Summary

The overall findings from this Chapter show that the current state of high-density measurements and the Atlas-based reconstruction are not yet sufficient to achieve quantitative accuracy in the context of TBI patient monitoring. Despite this, the technique does provide a more accurate mapping of cerebral saturation values during a VM than conventional fNIRS probes and thus the use of tomography can be considered a step in the

right direction.

The initial simulations with the high-density probe showed that the continuous wave measurements were capable of semi-quantitative accuracy even when there is a spatial mismatch of the internal layers between the subject and the Atlas model. However, when a different high-density probe was tested on healthy volunteers, the semi-quantitative accuracy of reconstructed parameters seen in simulations broke down. This was down to the addition of scatter mismatch as well as the spatial mismatch to the Atlas models, which is confounding the continuous wave reconstructions and limiting them to observing only accurate changes in cerebral saturation values. Another explanation for the reduction in the quality of the reconstructions in healthy volunteers is the design and features of the probe being used. The probe being simulated (the one built as part of this research - Chapter 6) theoretically provides a higher measurement density (168 for a 18 cm^2 region) and number of wavelengths (3), which could improve on the quality of the reconstructions obtained using the IBIB probe, which only had 2 measurement wavelengths (96 measurements for a 16 cm^2 region). This suggests that the high-density probe simulated does contain enough data for semi-complex reconstruction, however, the accuracy of the Atlas models is clearly still a limiting factor in terms of both its spatial and scattering properties. There is a large amount of variation in the literature values of scatter properties for skin, bone and brain tissues, which means that the values being used cannot necessarily be trusted in all situations, which was the basis for the preliminary testing with frequency domain simulations.

Initial testing with the frequency-domain measurements obtained on the high-density probe designed in this research indicate that the use of phase data can lead to improved quantitative accuracy of the reconstructed saturation values in the situation where there is only scatter mismatch and not spatial mismatch. In the event that both mismatches are present, the frequency-domain reconstructions provide no improvements over continuous wave results and in some cases could potentially be less accurate in observing the magnitude of cerebral changes. Therefore, a key area for further research in this area

is improving the spatial accuracy of the Atlas model so it is more representative of the internal structure of patient heads. Improving the spatial accuracy could then potentially provide the additional information required to improve the scatter estimates with frequency-domain measurements and make a viable monitoring method of TBI patients.

CHAPTER 6

HIGH-DENSITY NEAR INFRARED SPECTROSCOPY PROBE DESIGN AND VALIDATION STUDIES

The overriding aim of this research was the adaptation and development of high-density NIR devices for use in monitoring patients with a traumatic brain injury (TBI), in both clinical and pre-clinical settings. While Chapter 5 explored potential algorithmic developments during data reconstruction to improve the suitability of high-density near infrared spectroscopy (HDNIRS) as a TBI monitoring modality, it is not the only area the technique needs further research and development. The cost and portability of the devices is a key consideration if they are to be used for widespread patient monitoring. The aim of this chapter is to show that a small scale HDNIRS device can be built from off the shelf components such as silicon photodiodes (SPDs) and light emitting diodes (LEDs), designed specifically for use with the Atlas-based reconstruction algorithm outlined in Chapter 5. As mentioned in Chapter 5 there are probes available that could be used for this purpose, however this study is a proof of concept to demonstrate it can be achieved at minimal cost, increased portability and increased measurement density.

In this Chapter the design and building of the new probe is outlined and testing carried out to characterise the system response so it can be calibrated before use in *in vivo* studies in Chapter 7.

6.1 Probe design

The probe design is the same as the one outlined for the simulation studies in Chapter 5, which is a simple rectangular, high-density grid (Figure 6.1), a design which has been shown previously to have high sensitivity and localisation errors when reconstructing cerebral data [88]. The probe consists of 8 triple wavelength LED sources (L735/805/850-40C32, Ushio Epitex Inc., Japan) with peaks at 735, 805 and 850 nm with a bandwidth of 40 nm.

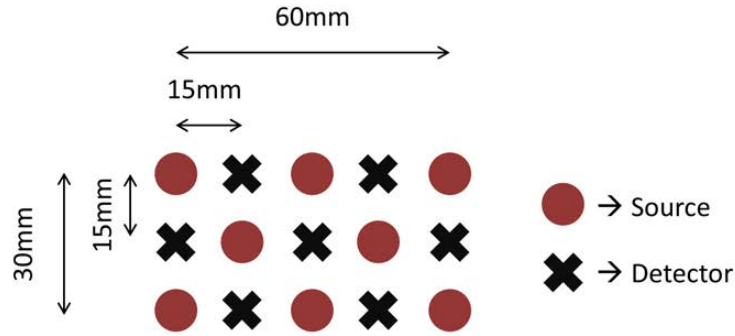


Figure 6.1: Design of high-density NIR spectroscopy probe

The wavelengths are similar to those used in the NIRO-200NX. The choice of wavelengths is essential for unmixing spectral signals as 805 nm is at the isobestic point in the HbO and HHb spectra (Figure 6.2), the point at which absorption is equal for both chromophores. Then 735 nm is to the left of this point being more strongly absorbed by HHb and 850 nm is to the right and is more strongly absorbed by HbO.

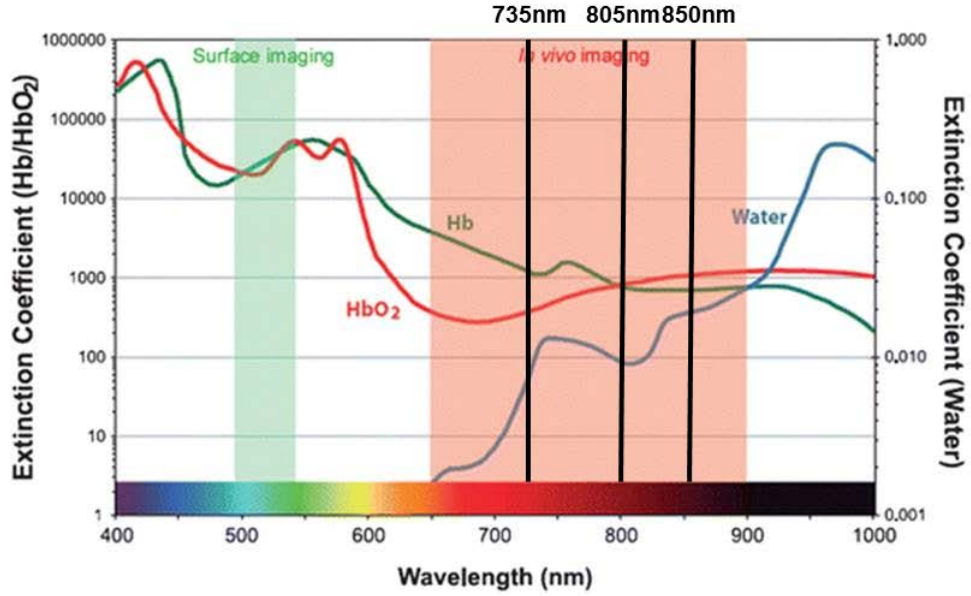


Figure 6.2: Absorption spectra for oxyhaemoglobin (HbO₂), deoxyhaemoglobin (Hb), and water, showing the relatively low absorption levels in the NIR region and the location of the LED wavelengths used in the probe [18].

There were 7 photodiode detectors (FDS100, Thorlabs) interspersed within the grid of sources and the spacing between each adjacent source/detector was 15 mm, giving a total of 168 measurements with a minimum source-detector separation of 15 mm and a maximum of 62 mm. These components along with the printed circuit board and the Arduino Due (Arduino, USA) give the probe a cost of $\sim \pounds 300$.

6.1.1 Electronics

The electronic setup of the probe was made as simplistic as possible consisting of a grid of LEDs and SPDs controlled directly via an Arduino Due board. Each LED consisted of a single anode and three cathode pins, one for each wavelength, therefore, to control

each LED and wavelength individually, would have required at least 25 output ports on the Arduino. To reduce the number of Arduino pins required to drive the LED sources, the LEDs were arranged in a grid where each of the columns shared a common anode and each of the rows shared a common cathode. By multiplexing the LEDs in this way all 24 source positions/wavelengths could be activated individually using only 12 output pins on the Arduino as shown in Figure 6.3. As the current available from the Arduino ports was less than the maximum forward current over the LEDs, no current limiting resistors were required in the circuit.

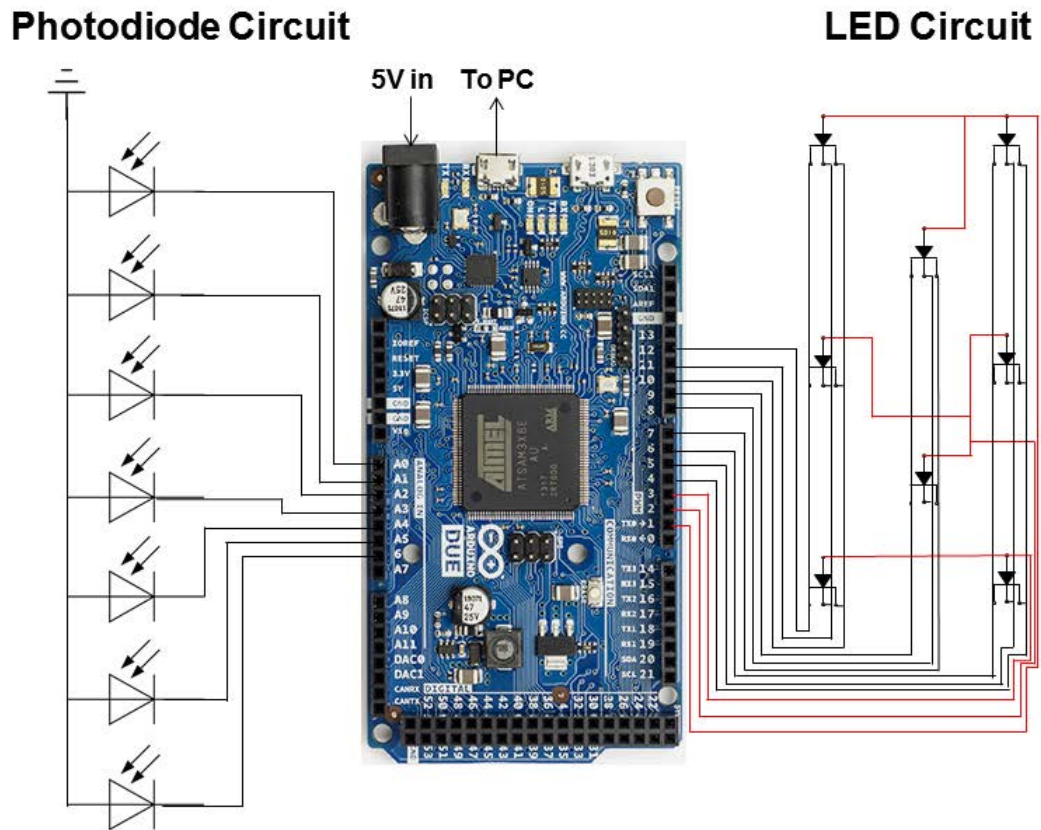


Figure 6.3: Circuit diagram for the LED and SPD grids and their connection to the Arduino Due control board.

The SPDs were connected directly to the analogue input ports of the Arduino that con-

tains a 12 bit analog to digital converter in zero bias (photovoltaic) mode (Figure 6.3). In photovoltaic mode the current flow in the diode is restricted so a voltage builds up, this is the basis of solar panels and is used here in order to decrease the dark-noise level. Operating the photodiode with a reverse bias voltage applied across it will increase the sensitivity of the detector however it comes at the cost of high dark noise. Photovoltaic mode allows the SPD to become a voltage source where the anode is connected to ground and the voltage can be measured by the Arduino at the cathode. In this configuration there should be an exponential relationship between voltage and incident light intensity. It is common practice to connect SPDs in series with a resistor or as part of a pre-amplifier circuit to linearise the response of voltage with light intensity, however as the detector response could be calibrated with this setup it was therefore not necessary for the prototype probe as it is being assessed as a proof of concept device. As the maximum input to the Arduino ports was 3.3 V the minimum observable change by this system is a change of $\frac{3.3V}{2^{12}} = 0.8mV$. The output from the Arduino ADC is simply a value from 0 to 4096 that can be translated into a Voltage reading using the value of 0.8 mV per unit.

For this probe to be used for monitoring the brain, the components would need to be soldered onto a flexible circuit board and encased in a flexible silicon or plastic casing, however for the initial testing of the device a rigid version was built using a solid circuit board and case with the view to testing on solid phantoms and a human arm where no curvature is present. The circuit was printed on a 2 layered board to allow for the complex LED circuit wiring and the components soldered in place as shown in Figure 6.4. The circuit board was then connected to the Arduino using flexible 1.6 mm coated wire.

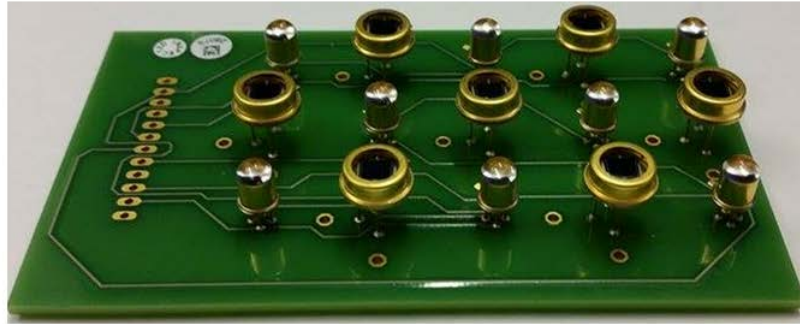


Figure 6.4: Circuit board for probe with component soldered in place.

The Arduino was programmed to illuminate each source in sequence, wait 5ms (integration time per detector) and then take a recording from each of the 7 detectors. The detector data at each source was then concatenated and set as a string of data via USB to a PC where the data were formatted in MATLAB, using inbuilt serial function, ready for processing. One read cycle consisting of 7 detector readings for 24 source wavelength could be transferred into MATLAB at a rate of 1.3 Hz (773 ms total acquisition time per read cycle).

6.1.2 Probe Casing

The design for the case sections that made up the circuit board housing are shown in Figure 6.5, the sections were designed using OpenSCAD (Freeware CAD package). The designs were translated into .stl format so they could be manufactured using a 3D printer (Mendel - RepRapPro) in solid black plastic.

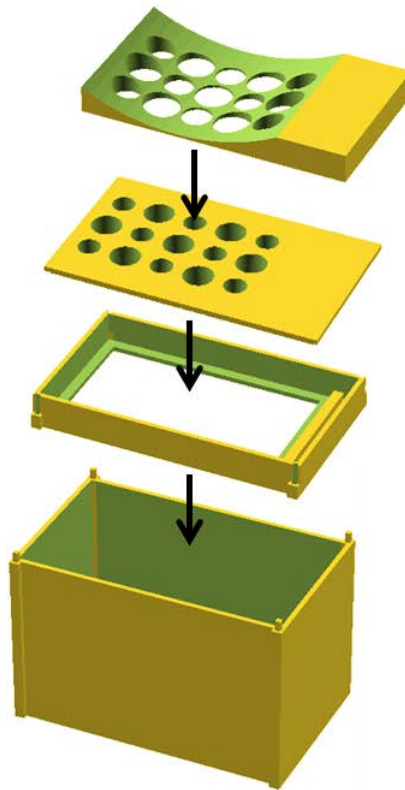


Figure 6.5: Sections of probe casing that fit together to house the circuit board. The top curved section is removable to allow for data collection of curved or flat target media.

The finished probe housing is shown in Figure 6.6. This version of the probe was designed for use on flat targets, however, a curved light guide was constructed to allow preliminary measurements to be made on curved surfaces such as the head.

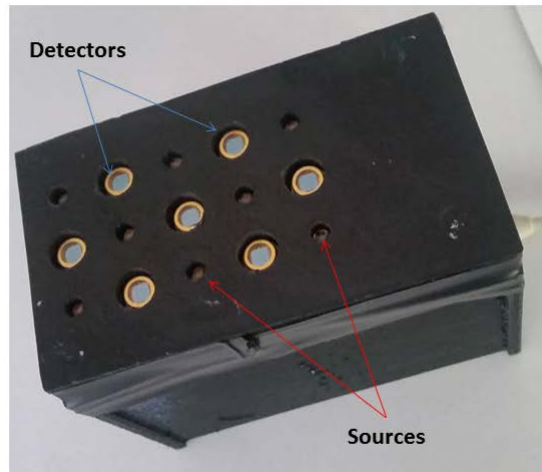


Figure 6.6: Fully assembled prototype probe with flat top.

6.2 Probe Characterisation

In order to test the validity of the probe setup a series of characterisation experiments were carried out that will be covered in Sections 6.2.1 - 6.2.8, data from these measurements can then be used to calibrate the probe before experimental use.

6.2.1 Dark Noise

A silicon photodiode consists of two types of semiconductor material placed alongside each other, one will be an electron rich N-type semiconductor and the other will be an electron deficient, P-type semiconductor. At the interface between the two semiconductor a depletion region forms with electrons and electron holes being drawn towards their respective sides of the junction as seen in Figure 6.7, the depletion region sits in a state of dynamic equilibrium. When a photon with sufficient energy (3.62 eV for Silicon [143]) is incident on this region it is absorbed and an electron-hole pair is produced with both drifting to their respective sides of the junction, this causes a build up of positive charge in the N region and a negative build up in the P region giving an overall increased potential difference (voltage). However it is possible for thermally excited electrons to drift across

the depletion region and induce a current flow irrespective of incident light, this is known as dark current and the associated change in detector signal due to this current is known as dark noise.

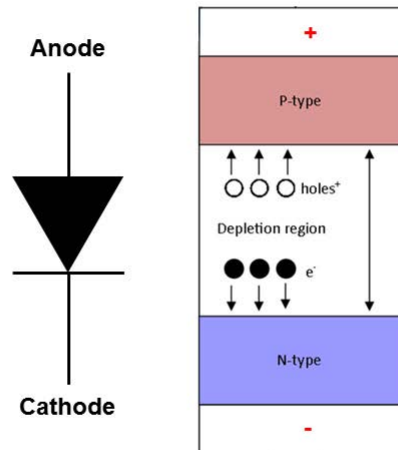


Figure 6.7: Illustration of the P-N junction of a Silicon Photodiode and the depletion region formed between them. The left of the figure shows the component symbol for a SPD and how it orientates with the P and N type junction.

Correction for dark noise is relatively simple however it can be complicated if the temperature of the detectors is changing over time; the higher the temperature the more thermal electrons will have the energy to drift across the depletion region. This is one of the reasons why photovoltaic mode was selected to minimise the dark current so the effect of temperature change from influences such as contact with the skin, would have a smaller effect on the overall readings. As the experiments done with the probe were short in duration the dark noise correction factor was based on the assumption that dark noise levels would remain constant over the course of the data collection process.

Method - The dark noise was assessed by averaging the response from each detector over a series of 7 reads (a total of 2200 read cycles) under blackout conditions. The LED

sources were set to remain off while the rest of the acquisition process remained constant. Then a solid homogeneous phantom (ISS calibration phantom A - details in Appendix .3) was placed on the probe and was further covered in a black out cloth (Figure 6.8), all readings were performed in a dark room, care was taken to shield the detectors from outside light sources such as the acquisition laptop.

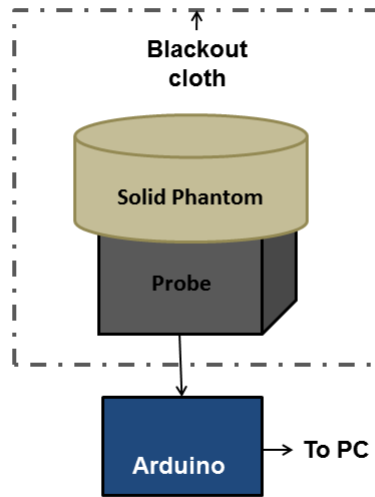


Figure 6.8: Setup used for dark measurements as well as phantom and repeatability measurements for later sections.

Results - Figure 6.9 shows the average dark noise (in mV) for each detector. These data are used at the first form of calibration for the raw detector measurements and can be applied through direct subtraction.

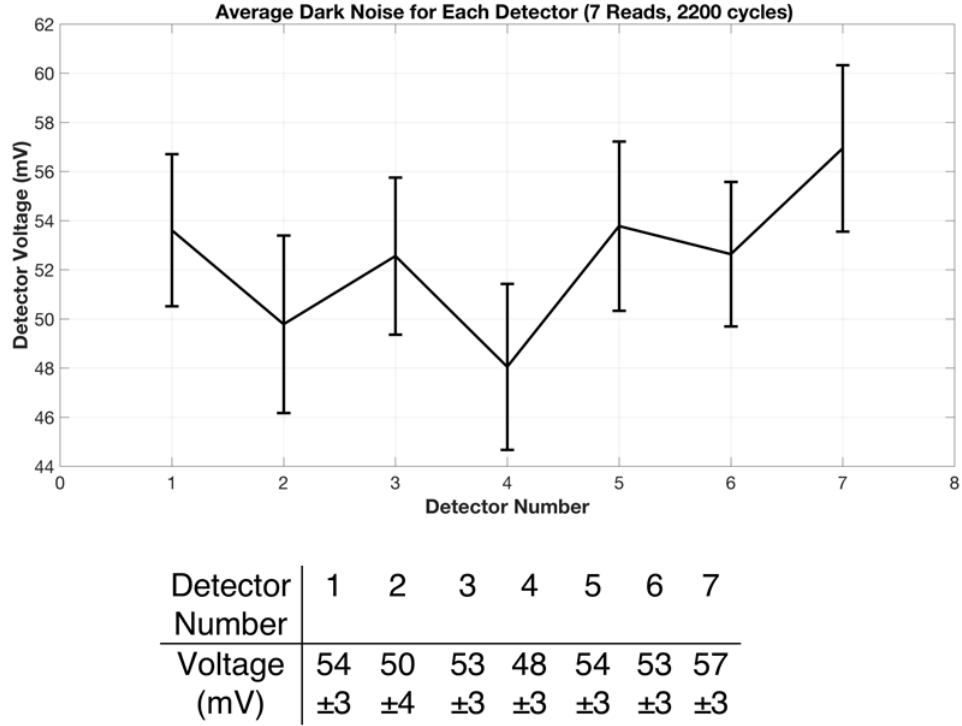


Figure 6.9: Top - Graph showing the dark noise of each detector along with the standard deviation from the average measurement. Bottom - Table of numerical values of Dark correction factors.

6.2.2 Silicon Photodiode responsivity

The response from each detector with respect to the wavelength of incident light should be equal, however due to differences in the manufacturing process it is possible that detectors being used will respond differently to the same incident light. This could be due to aspects such as small changes in the size of the detector or changes in the uniformity of the semiconductors materials making up the photodiode. Therefore, the response of all the detectors was measured in order to provide a calibration factor that would normalise the response for all detectors prior to the data reconstruction process.

Method - The response of the detectors in the probe was measured while being illuminated by a single LED source at each of the source wavelengths. Even though the LED being used as the reference source is not calibrated, it is sufficient to normalise the response of all the probe detectors with respect to each other.

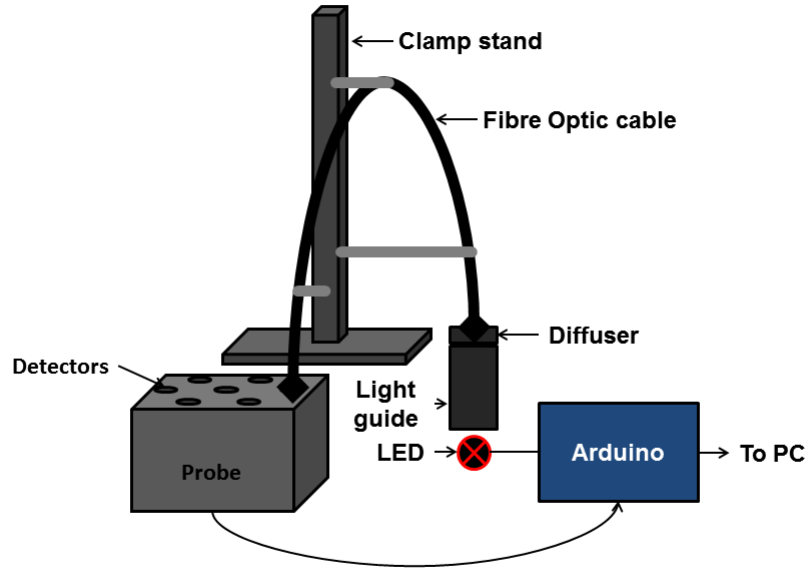
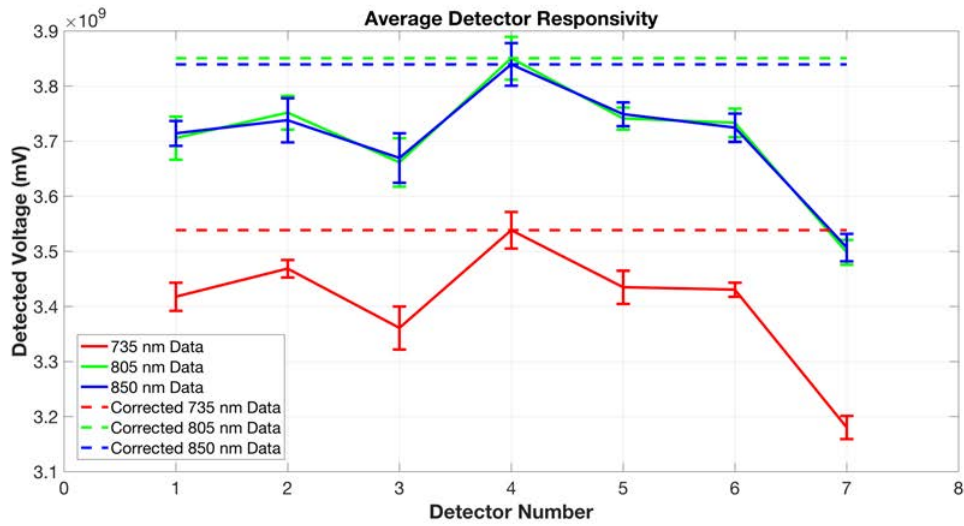


Figure 6.10: Setup of SPD responsivity test for probe.

The setup of the responsivity experiment is shown in Figure 6.10, light from the LED was channelled to each of the detectors in turn using $\frac{1}{4}$ " , 91cm optical fibre. A diffuser (Thorlabs) was placed between the source and the optical fibre to account for any small variations in the positioning of source between data acquisition cycles. The fibre optic was held in place using a series of clamps and the opposing end of the fibre was placed directly on top of the target SPD.

A series of 5 repeat reads for each detector were recorded with 29 read cycles in each, resulting in 3625 measurements per detector for calculation of the responsivity.

Results - The results showed that there was a maximum variation in the detector responsivity of 3.5% from the maximum reading, with the response consistent across all three wavelengths on each detector. The average responses for each detector, after dark noise correction, is shown in Figure 6.11, the calibration factor was calculated by dividing each average response by the maximum detector response at each wavelength. The calibration can be applied after the dark correction by dividing each detector reading by the wavelength specific correction factor.



Detector Number		1	2	3	4	5	6	7
Correction Factor	735nm	0.996	0.985	0.979	0.988	1.000	0.994	0.965
	805nm	0.993	0.981	0.980	0.990	1.000	0.993	0.969
	850nm	0.993	0.980	0.980	0.986	1.000	0.990	0.969

Figure 6.11: Results of detector responsivity testing with calibration factors shown below the graph.

6.2.3 Light Emitting Diode intensity variation

The light output of each LED in the probe is not identical and can therefore influence the detector readings and propagate through the reconstruction process as an error. The

changes in LED intensity can be due to small differences in the semiconductor material making up the LED, small changes in supply current (due to position in the multiplexed LED grid), and the mounting angle of the LED on the circuit board.

There LED intensity has an angular dependence, with a zero angle providing the maximum intensity. Therefore if the LED has been soldered into the board at a slight angle then the apparent intensity of the LED will appear lower.

Method - To assess the intensity of each LED in the probe an EMCCD (Hamamatsu, Japan) camera was used to measure the photon counts per second at each source wavelength so all the LEDs could be calibrated to the maximum value.

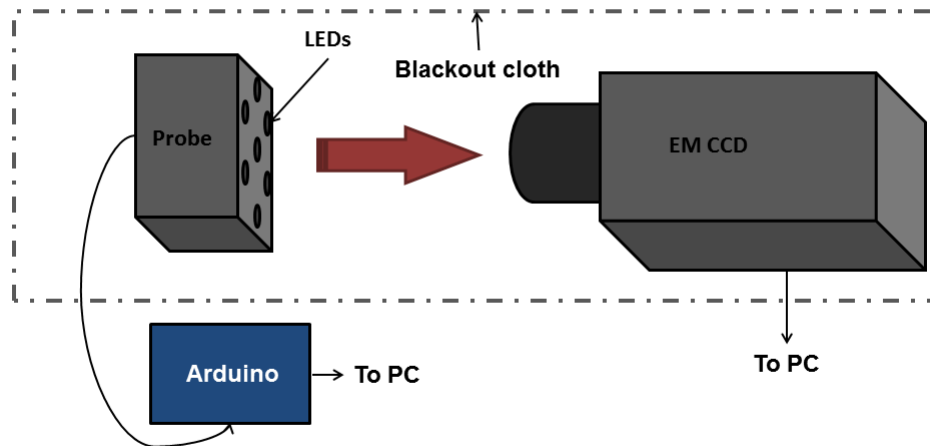


Figure 6.12: Setup of LED intensity testing for probe.

Figure 6.12 shows the setup of the experiment used to measure the intensity the probe LEDs. The front face of the probe was positioned 20 cm from the front of the camera and then the probe was raised so the central point on the front face lined up with the centre of the camera lens.

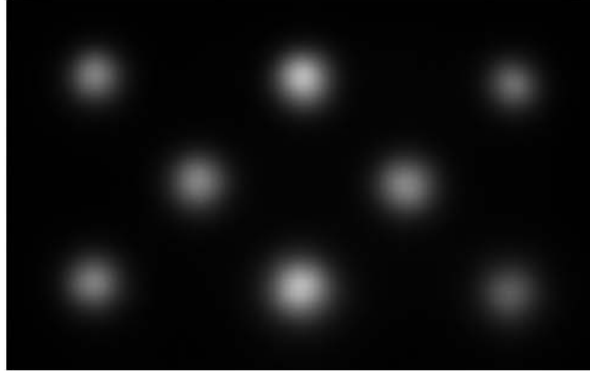
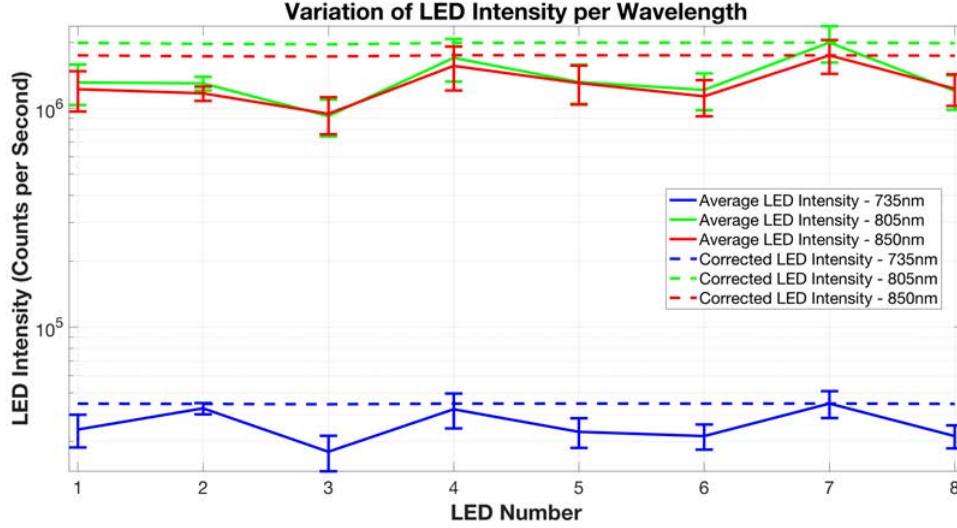


Figure 6.13: Image taken of 735nm sources using EM CCD.

Six repeat readings were taken for each LED position and wavelength. Each source was captured individually with the exposure times set to 1 s for the 735 nm wavelength and 0.03 s for the 805 and 850 nm sources. Figure 6.13 shows the combined images of all the 735 nm sources. The source images were dark corrected by subtracting a dark image taken over the same exposure time. The peak intensity, measured in photon counts, was extracted by fitting a 2D Gaussian to the source image in MATLAB. The intensity readings were translated into counts per second so they could be plotted on the same axis.

Results - The results of the LED intensity calibration test (Figure 6.14) showed that the largest variation in LED intensity is 54% from the maximum value. The patterns in the intensity variation were also consistent across the three wavelengths. The calibration factor to normalise the LED intensity can be applied to the detector readings simultaneously through division, as it maps a percentage change and can therefore be used interchangeably regardless of the detector being used. As a separate set of calibration factors was calculated for each source wavelengths, the spectral response and quantum efficiency of the EMCCD did not need to be considered. The calibration factor

was designed only to normalise across sources of the same wavelength.



Source Number		1	2	3	4	5	6	7	8
Correction Factor	735nm	0.76	0.95	0.60	0.94	0.74	0.71	1.00	0.71
	805nm	0.66	0.65	0.46	0.85	0.66	0.61	1.00	0.60
	850nm	0.70	0.67	0.54	0.89	0.75	0.65	1.00	0.70

Figure 6.14: Results of LED intensity testing with calibration factors shown below the graph.

6.2.4 Light Emitting Diode spectra response

Since the probe detectors have been calibrated for their response at the specified source wavelengths of 735, 805 and 850 nm, it is important to confirm that each source is emitting light around these peak wavelengths. As well as having effects on the detector response a large change in the peak wavelength of the sources has a knock on effect in the reconstruction of data as the extinction coefficients used will be specific to a given wavelength. By measuring the true peak wavelengths of each source the reconstruction models can be updated to match, improving the overall accuracy of the reconstruction.

Method - The emission spectra of the probe LEDs was measured using a spectrometer (BSR112E-VIS/NIR CCD Spectrometer, Edmund Optics) and the setup shown in Figure 6.15. Light was channel through a $\frac{1}{4}$ ", 91 cm optical fibre, held in place with a series of clamps, from each of the source LEDs to the detector of the spectrometer. Three spectra were taken for each LED (and source wavelength) in the probe.

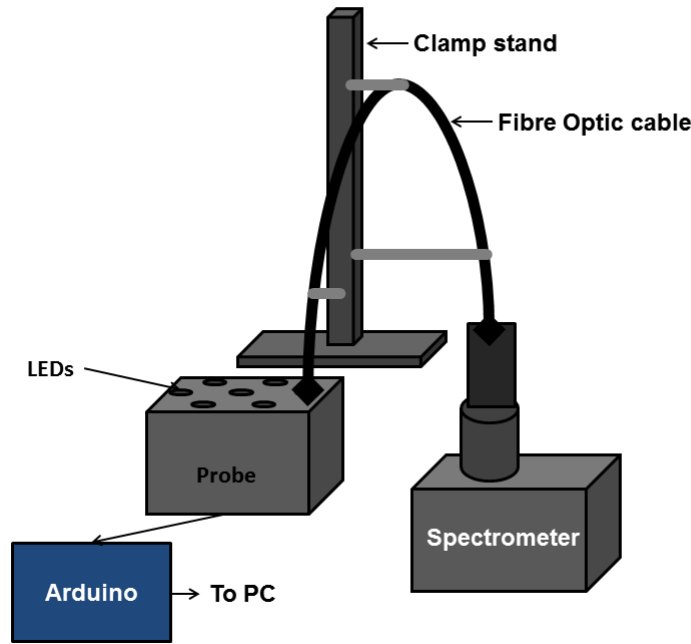


Figure 6.15: Setup of LED Spectral testing for probe.

The measured spectra were recorded over a 75 ms integration time and were dark corrected for the given exposure time within the spectrometer software. The spectral data were imported into MATLAB for processing where the response was averaged over all 8 LEDs at the 3 different source wavelengths. The peak wavelength was found by extracting the maximum value from each spectrum.

Results - The peaks wavelength of the LEDs were found to be 728 ± 1 nm, 803 ± 2 nm and 850 ± 1 nm for the advertised source wavelengths 735, 805 and 850 nm respectively (shown in Figure 6.16). Within the bounds of the standard deviation only the 735

nm sources did not match up with the results showing that the peak wavelength was potentially 7 nm lower than expected.

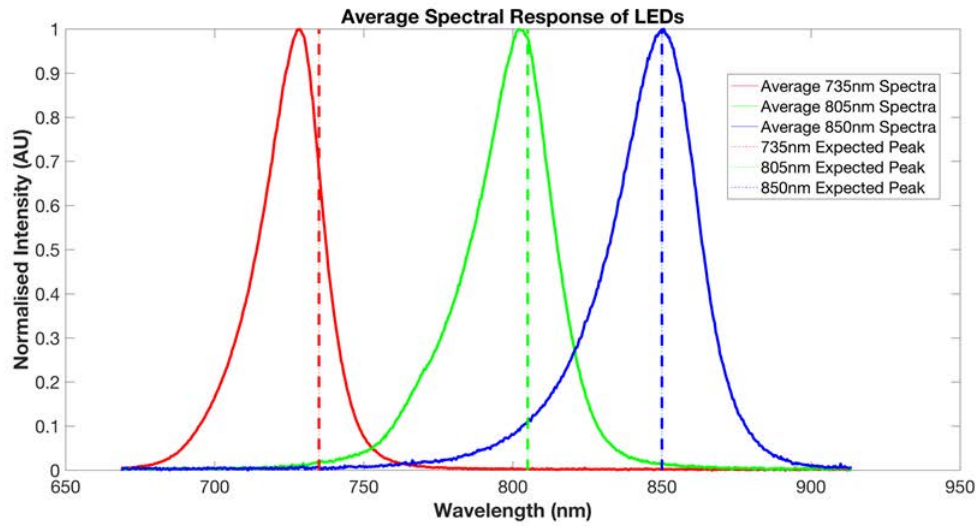


Figure 6.16: Average spectral response over all LEDs in the probe compare to the expected peak wavelengths.

As the spectra response across all LEDs in the probe was mainly consistent (Figure 6.17), the calibration of the detector responsivity performed earlier in this section is still valid as the tested LED was from the same batch.

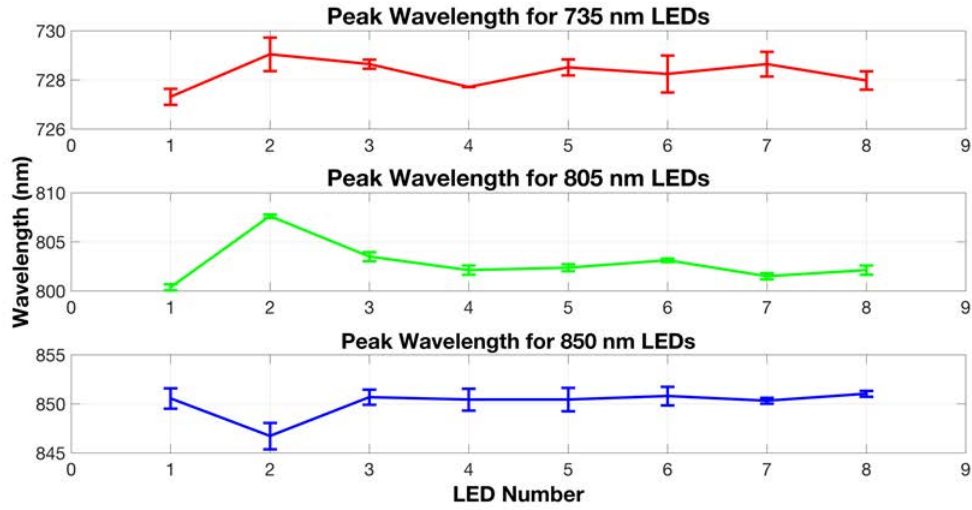


Figure 6.17: Peak wavelengths for all the sources in the probe.

6.2.5 Voltage - Intensity Calibration

As discussed in Section 6.1.1, the detected voltage from the SPDs is not linear with the incident light intensity as the photodiodes are connected directly to the Arduino without the use of a preamplifier. Therefore, to estimate the intensity of light being observed by each detector a calibration factor between the output voltage of the detector on the Arduino and the input light intensity is beneficial. It will also confirm that the detectors are responding as expected.

Method - To assess the detector response to different input light intensity a source of known intensity, a Thorlabs High-Intensity Halogen Lamp Light Source (OSI-1-EC), with a maximum light output of 40,000 foot candles that is equivalent to $\sim 0.064 \text{ Wcm}^{-2}$ was used. This process is not exact as the light source itself is not calibrated, however it is possible to take relative, intensity change, measurements. The intensity of the input light is altered through the use of neutral density filters. The intensity of the light transmitted

(I) through the neutral density filter (of value nd) from initial intensity I_0 is calculated using Equation 6.1. The neutral density filters used had values of 0 (no filter), 0.1, 0.2, 0.3, 0.4, 0.5, 0.6, 3, and 4.

$$\frac{I}{I_0} = 10^{-nd} \quad (6.1)$$

The setup on the experiment is shown in Figure 6.18. Light from the source was directed to a single detector on the probe using a $\frac{1}{4}$ " optical fibre held in place using a clamp stand. The neutral density filter was applied above the light guide positioned over the detector.

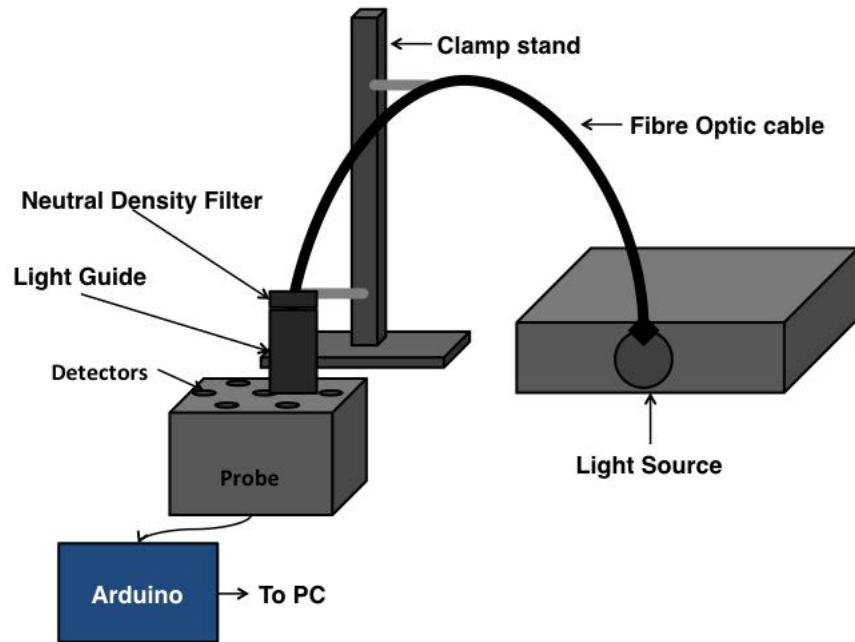
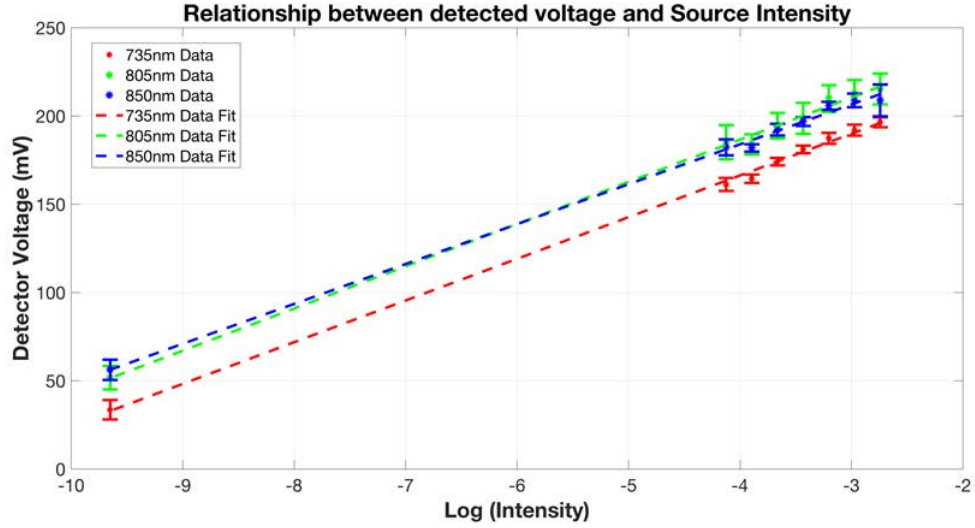


Figure 6.18: Setup of voltage-intensity calibration experiment using an external light source.

A series of 5 repeat measurements with each neutral density filter were obtained for processing.

Results - The average detector intensity readings from the Arduino (in mV) were plotted against the log of input light intensity and showed a linear relationship (Figure 6.19). This confirmed the expected exponential relationship between light intensity and SPD response (in mV).



$$I_{735} = e^{\left[\frac{V_{735}-261}{24}\right]}$$

$$I_{805} = e^{\left[\frac{V_{805}-417}{30}\right]}$$

$$I_{850} = e^{\left[\frac{V_{850}-408}{28}\right]}$$

Figure 6.19: Voltage - Intensity calibration plot with fitted equations to convert mV detector readings into intensity for using in NIRFAST reconstructions.

To obtain a conversion factor between voltage and intensity the polyfit function in MATLAB was used to fit the data plotted in Figure 6.19 and provide the conversion equations for each wavelength (shown under the plot). Although the intensity of the light source is known approximately because the source is not calibrated we can only produce a 'relative intensity' value for the photodiode response, which is unitless.

6.2.6 Probe repeatability tests

It is essential that the response of the probe is consistent over a number of read cycles with detector readings remaining constant (within a certain margin). A constant set of detector readings would mean that data recorded in different sessions on different days would be directly comparable.

Method - To test the probes repeatability a series of 20 acquisitions consisting of 30 read cycles each taken over a 2-day period. The data were taken using the probe and a solid homogeneous phantom (ISS phantom A - details in Appendix .3) using the setup shown previously in Figure 6.8.

Results - The average results over the 20 reads (Figure 6.20) showed that the maximum variation in detector measurements was 0.67%, which is an acceptable amount of variation as it is below the variation in dark noise measurements found in Section 6.2.1

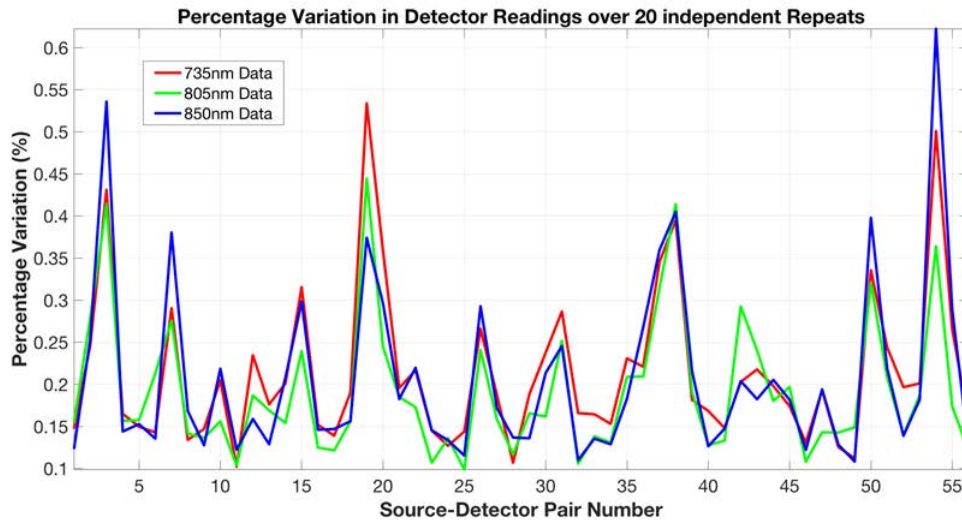


Figure 6.20: Percentage variability in detector measurement over 20 independent read cycles on a solid phantom

To further assess the variation data the percentage variation was grouped by source-detector separation (Figure 6.21). These data showed that the variation in the detector signals increases with increasing source-detector separation. This is expected as the lower the incident light intensity the higher noise level in comparison to the signal (signal-to-noise ratio) with the error on photon counting (intensity \propto number of photons) scale with \sqrt{n} , where n is the number of photons.

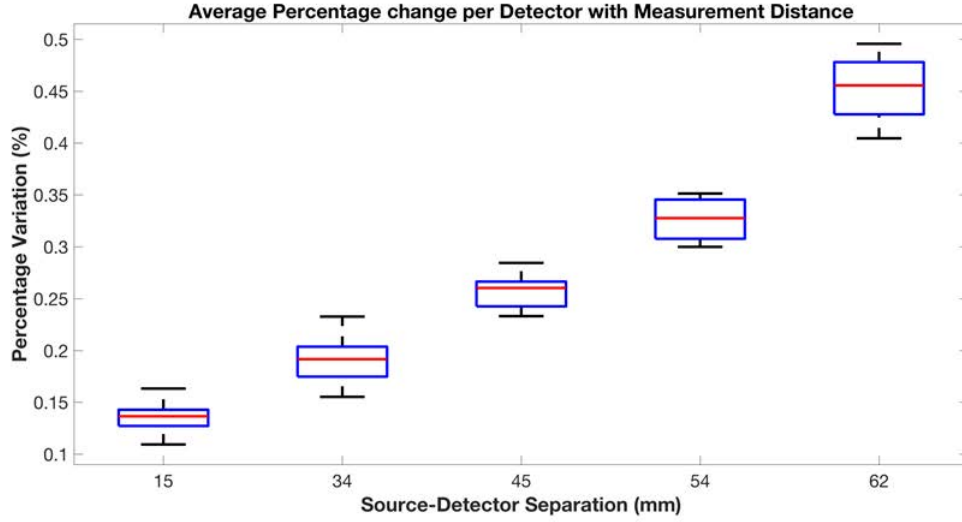


Figure 6.21: Average percentage variation in 735 nm detector measurements, separated by source-detector distance, over 20 repeat reads on a solid phantom

6.2.7 Solid phantom measurements

With the components of the probe now individually calibrated the response of the probe as a whole system must also be assessed to ensure that the correct response is seen on a homogeneous phantom model. The detected intensity of light recorded on a reflection geometry should decrease exponentially with increasing source-detector separation.

Method - The data were taken using the probe and a solid homogeneous phantom (ISS phantom A - details in Appendix .3) using the setup shown previously in Figure 6.8. The data acquisition was run over 60 cycles and averaged into a single dataset as the phantom is homogeneous and not changing over time. The calibration factors calculated previously in this Chapter were applied to the data before processing.

Results - To check the detector response matches the expected exponential drop off with increasing source-detector separation, a box plot of intensity vs source-detector separation is shown in Figure 6.22. To make the results easier to interpret the intensity axis is given a logarithmic scale so the ideal response is a linear drop off in intensity with increasing distance. The first 3 source-detector separation, 15, 33 and 45 mm follow a linear decrease, however at 54 mm and 62 mm the linearity breaks down. This indicates that the large source-detector separations are not useable in the data reconstruction process as they are clearly subject to high noise levels that are limiting their accuracy. As well as the noise effects at the higher source-detector separations there is also the issues of the boundaries of the phantom itself. At this separation the source and corresponding detector are within 2cm of the edge of the phantom, this could lead to photon loss through the edges of the phantom and potentially contamination from external photon sources.

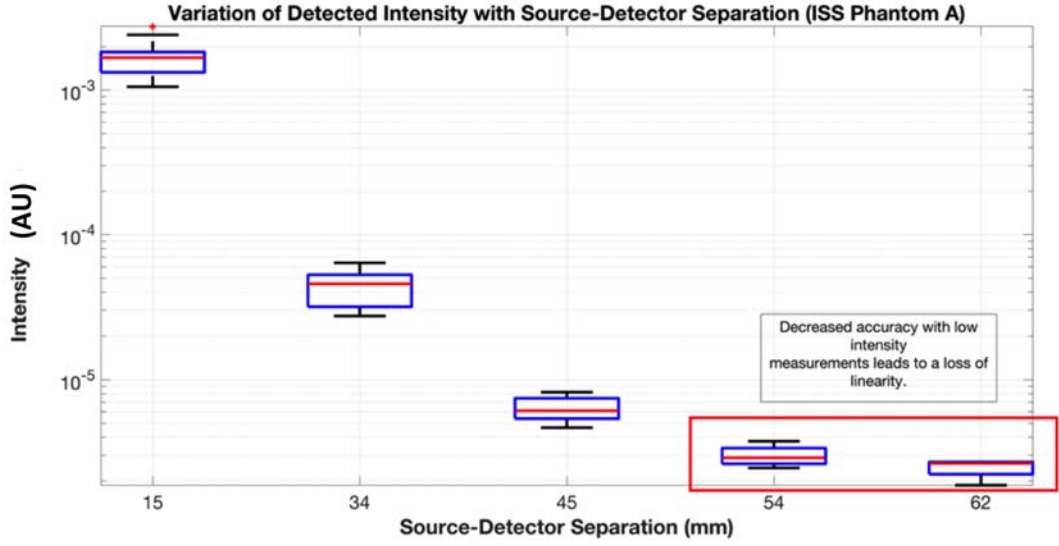


Figure 6.22: Plot of detector intensity (on logarithmic scale) vs source-detector distance on solid phantom A for 735 nm wavelength

The quality of the data was further assessed by running it through the data calibration process outlined in section 3.1 where the log of source-detector distance multiplied by intensity is plotted against source-detector separation and fitted to expected values generated from an analytical model. This response should again show a linear decrease with increasing source-detector distance. The results of this calibration, seen in Figure 6.23, confirm that the 54 and 62 mm data points are inaccurate and should not be used in reconstruction processes.

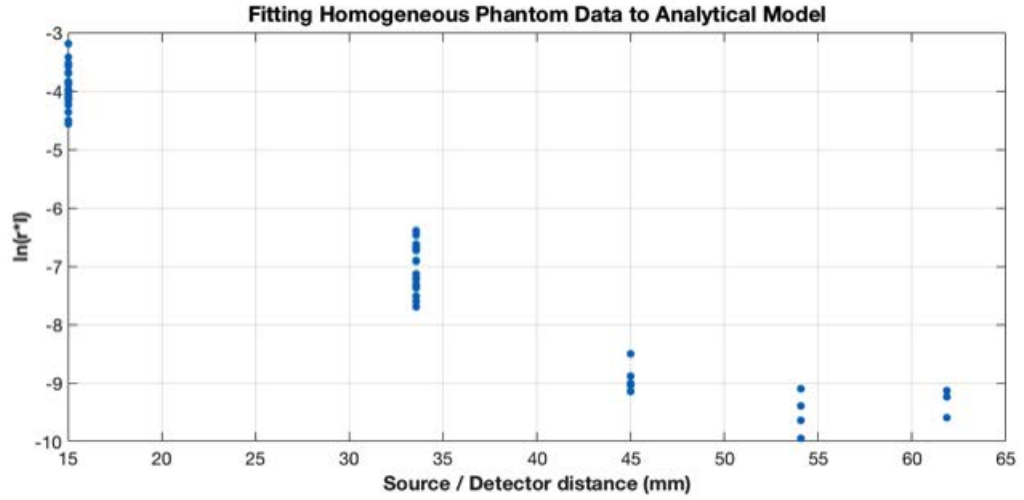


Figure 6.23: Example of a calibration plot fitting homogeneous phantom data (from 735nm source) to an analytical model to estimate absorption properties - Process explained in Section 2.

6.2.8 Pre-amplifier testing

The break down of the relationship between detected intensity and source-detector separation is due to the limited dynamic range and sensitivity of the detector configuration being used, as mentioned previously in Section 6.1.1. The lack of pre-amplifiers and the direct connection of the detectors to the Arduino result in a exponential relationship between voltage and intensity which limits the dynamic range of the setup and reduces sensitivity to low light levels. As this probe was built a proof of concept the limitations of the detectors were not a major hindrance however to prove that the low cost components used in the system were capable of more accurate measurements the SPDs were tested with a ready built pre-amplifier.

Method - The pre-amplifier testing was carried out in preliminary tests before the probe was built, thus the LED light source used was a 780nm (Thorlabs LED780E) with a similar optical power to those used in the prototype probe ($\sim 9\text{mW}$). The pre-amplifier used was the PowerLab 16 channel analog-to-digital converter (ADC). The setup of the experiment is shown in Figure 6.24. The SPD was held in place by a black plastic holder, then there were 6 different slots for the LED to sit in at 10, 20, 30, 40, 50 and 60 mm from the detector, with measurements being taken across a solid homogeneous phantom (ISS phantom A - details in Appendix .3). The LED source was powered using an Arduino Due and the PowerLab data were recorded using LabChart software.

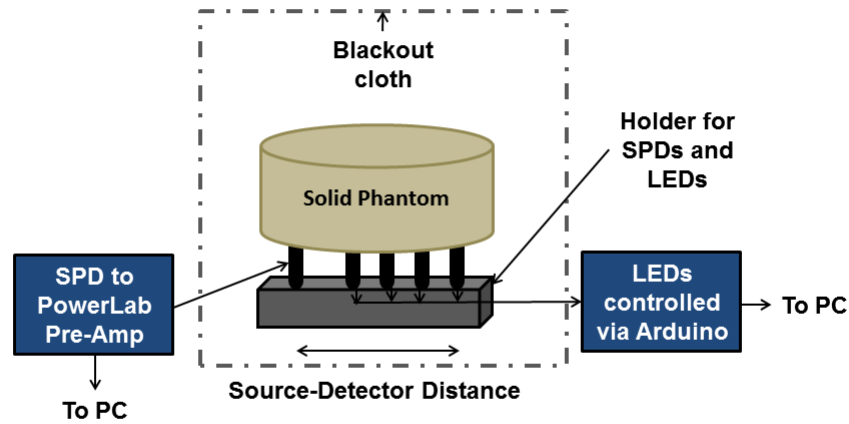


Figure 6.24: Setup of preamplifier testing experiment using PowerLab pre amplifier for a single detector while measuring sources at varying distance along a solid phantom.

Results - The results of the pre-amplifier testing are plotted in Figure 6.25 alongside a set of example detector measurements from the prototype probe. Intensity is plotted against source-detector separation distance on the intensity axis that was given a logarithmic scale. Although the results are not directly comparable as the source LEDs are different, the data shows that the pre-amplified detectors have a much greater dynamic range and sensitivity to low intensity light. The prototype probe detector setup under

responds to changes in light intensity and therefore it can be theorised that the probe will be less sensitive to absorption changes within a given target medium.

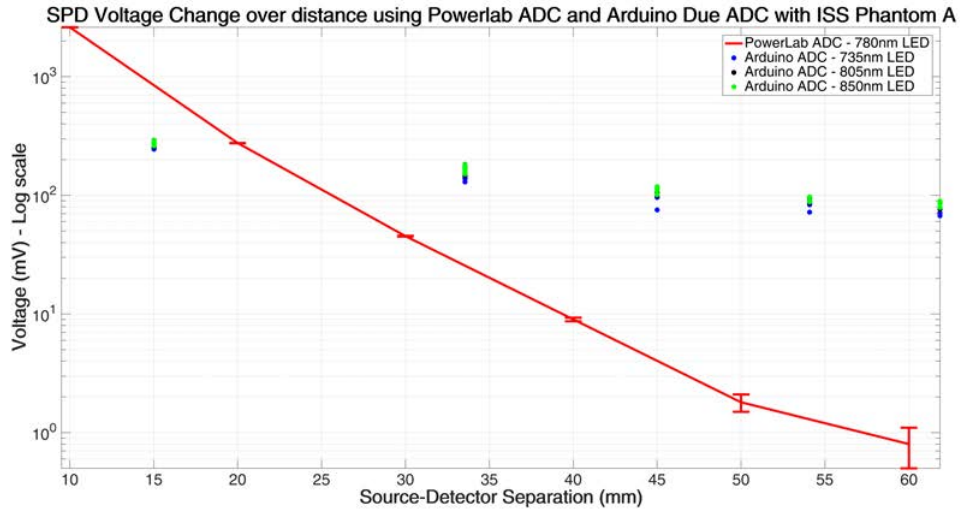


Figure 6.25: Plot of detector intensity vs source-detector separation distance recorded using a PowerLab pre-amplifier. The error bars on the pre-amplifier detector measurements are ± 0.03 mV which was the smallest measurable change in voltage.

While these data shows that the current probe design will function with a reduced sensitivity to chromophore concentration changes, it will still function as a proof-of-concept device and the testing with the pre-amplifier has shown that the components are capable of producing good data. Upgrading the probe to use pre-amplifiers in the future is achievable at a low cost so the aim of a low cost probe would still be feasible.

6.2.9 Curved probe calibration

The prototype probe was designed for use on solid flat target volumes, however, a curved plastic mould was produced to act as a light guide so measurements could be made on a curve surface such as the forehead. With the curved mount on the probe the sources and detectors were no longer in direct contact with the target medium. To account for this

and any decrease in detected intensity due to the curved surface a coupling calibration is required.

Method - The solid homogeneous ISS phantoms have a curved side for calibration of flexible probes. This feature was used to provide a comparison between the detector measurements when the phantom was imaged on the flat probe and the measurements when the curved probe was used. An average of 30 read cycles were taken for the curve and flat probes on the solid phantom (ISS phantom A - details in Appendix .3) - detailed in Figure 6.26.

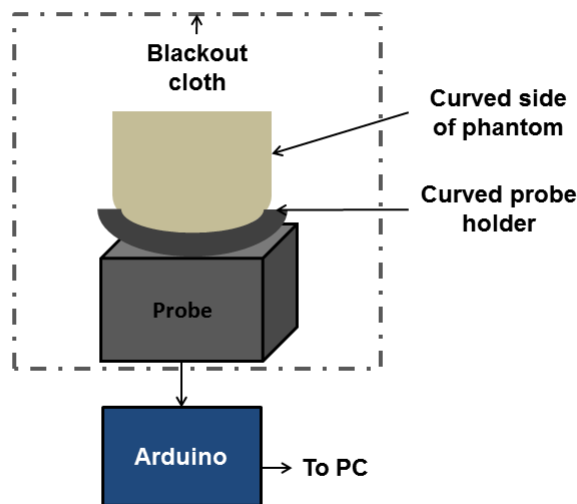


Figure 6.26: Setup of curved probe phantom testing.

Results - The percentage difference between the detector readings on the flat and curve side of the phantom was calculated in order to give a calibration factor to account for any changes in detector intensity. As the same phantom was used for both measurements the only external change is the non-contact nature of the curved probe, hence it can be

concluded that any change in measurement data is a result of the curvature.

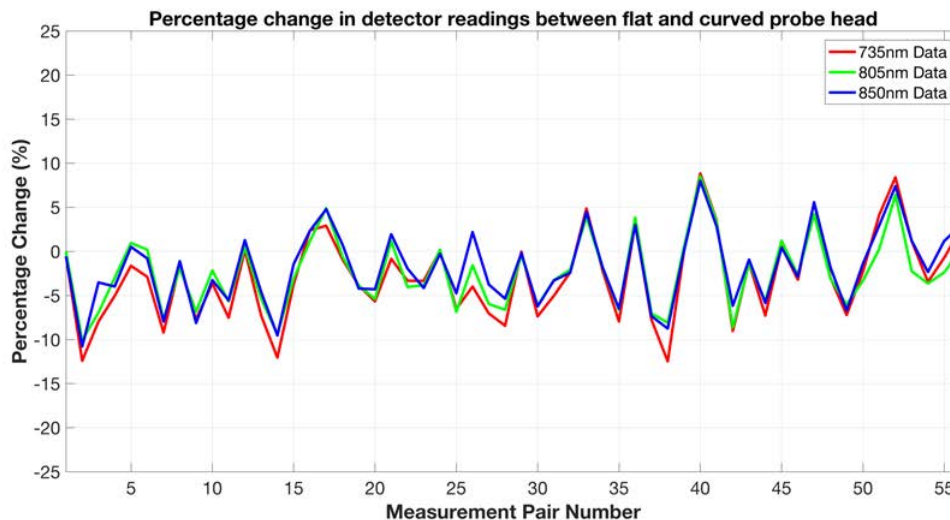


Figure 6.27: Plot of correction factor to compensate for intensity drop due to curvature in the probe mount.

The variation in detector intensity varies from +8.5 to -12.5 % (Figure 6.27), and the percentage change is converted into a decimal so a calibration factor can be applied to each source-detector measurement taken on the curved probe.

6.3 Conclusions

The data in this Chapter has demonstrated that a low cost high-density probe, produced for approximately £300, can use Arduino Due controlled LEDs and SPDs to measure changes in detected light intensity from a solid homogeneous phantom that follow the predicted patterns of an exponential drop off in intensity with increasing source-detector separation.

The probe built was a simplistic prototype built as a proof-of-concept device and is therefore limited in terms of its sensitivity. Despite this, the probe was calibrated

for dark noise and detector responsivity as well as peak LED wavelength and intensity. Investigations into the use of pre-amplifiers with the SPD showed that the current probe setup has a limited sensitivity and dynamic range. This will have an effect on data reconstruction as the probe will under respond to changes in absorption, however changes will still be observed, but they will just be blunted, this will be explored in Chapter 7.

Although the prototype probe was designed for use on flat surfaces only, the addition of the curved mount allows for data collection on a curved surface. The effect of the non-contact nature of the curve probe was assessed by direct comparison of phantom data taken on the flat and curved probes to provide a calibration for each source-detector pair in order to allow preliminary data to be taken on different geometries such as the forehead.

Assessment of the prototype probe has shown the potential of a low cost high-density probe to provide meaningful data for semi-complex reconstructions. While the current probe may lack the sensitivity and ergonomics to provide cerebral measurements required for TBI monitoring, it has shown the technology is available in a much more cost effective form than current commercially available NIR devices. The ability of the probe to provide meaningful oxygen saturation values under *in vivo* conditions will be explored in the form of arm cuff and VM studies in Chapter 7.

CHAPTER 7

HIGH-DENSITY NEAR INFRARED SPECTROSCOPY PROBE TESTING

Registered Atlas-based reconstructions have shown improvements in terms of observing the magnitude of changes in cerebral haemodynamics when tested using an existing high-density DOT system. While the variation in baseline measurements between subjects was too high to yield the quantitatively accurate chromophore concentrations required for monitoring traumatic brain injury (TBI) patients, the correct mapping of cerebral desaturation during a *Valsalva* showed potential improvements over existing fNIRS techniques.

Improving the reconstruction methods is only half of the challenge in developing NIR techniques for TBI monitoring. The second issue is making the high-density probe small, cost effective and portable so they can be used on a large scale in both the clinical and pre-clinical settings. To date the high-density probes that have been produced that would be suitable to provide the measurement data needed for the Atlas reconstruction method have either lacked the low cost, compact nature or portability required for TBI monitoring. The probe built and calibrated in Section 6 was designed to fulfil the low cost and portable requirements needed for a TBI monitoring device. Preliminary calibration of the prototype device showed that the system followed the expected response trends, however, the configuration of the electronics requires fine tuning for the probe to match data reconstructions performed on the IBIB probe in Section 5.

The following chapter assesses the prototype probe under *in vivo* conditions by measuring oxygen saturation on the forearm and the forehead during physiological procedures that changed oxygen saturation within the targeted tissue. If the prototype probe can obtain meaningful data in its current form then there is potential for the probe to be developed further for more accurate measurements. This combined with the progress in the Atlas-based reconstruction is a step forward for NIR TBI monitoring. These experiments were only a preliminary assessment of the high-density probes' performance, and were only carried out on 3 healthy volunteers. Further, while a protocol was followed for the data acquisition they were not rigorous in terms of repeat measurements due to time constraints and the suitability of the prototype probe for this manner of such testing.

7.1 Arm Cuff Studies

Arm cuff experiments are a fast and simple way of inducing large changes in blood oxygen saturation for assessment via NIR. There are experiments within the literature where arm cuff/occlusion studies have been used to test or compare fNIRS devices (Examples - [144, 145, 146]). The effect of clamping blood flow at the top of the arm (with pressure high enough to restrict both arterial and venous flow) results in a steady reduction in the oxygen saturation of the blood over time. When the clamp is release there is a hyperaemia response, which floods the occluded tissues with blood giving a sharp rise, or rebound in oxygen saturation.

By acquiring the fNIRS data on the forearm the region of interest can be considered roughly homogeneous as the target area will be skeletal muscle, therefore the fitting of blood concentration parameters is theoretically more accurate as there is no influence from superficial contamination all changes are global in the target volume.

Within the context of assessing the prototype probe, arm cuff experiments are a sim-

ple way to illicit large saturation changes as a measure of how well it is functioning in comparison to conventional fNIRS devices.

7.1.1 Methodology

The following arm occlusion protocol was carried out on 2 healthy volunteers. The custom high-density probe was tested along side the NIRO-200NX (Hamamatsu, Japan) as a reference fNIRS device.

Figure 7.1 shows the position of the probe and the cuff on the subjects arm. A blood pressure monitoring cuff was positioned around the bicep on the upper section of the subject's left arm. The probe was positioned over the brachioradialis muscle on the underside of the forearm just below the elbow joint. As it was the larger probe, the position of the high-density probe was marked so the NIRO probe could be positioned at the centre of the acquisition area.

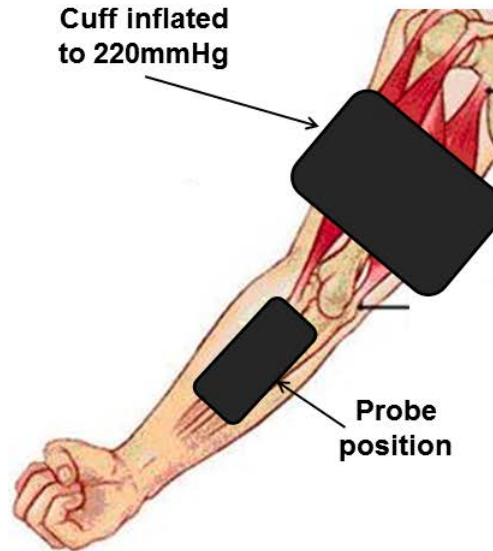


Figure 7.1: Setup for taking arm cuff measurements on the NIRO-200NX and the in-house high-density probe.

Once positioned, a baseline reading of 60 s was recorded, at the end of the baseline the cuff was inflated to a pressure of 220 mmHg over a 10 s period. Once fully inflated the cuff pressure was maintained for 5 min. After 5 min of cuff occlusion the pressure was released using the quick release function on the pressure monitor and the recovery process was recorded for a further 60 s at which point the data acquisition was terminated.

This process was repeated for both the custom probe and the NIRO probe. A reference reading was taken with a second NIRO-200NX probe on the right forearm to show there were no other systemic influences on the occluded arm measurements.

Parameter Reconstruction - The data from the NIRO comes in the form of chromophore changes (HbO, HHb and HbT) and also the tissue oxygenation index (a

surrogate for deep tissue oxygen saturation). Therefore, to provide a comparison the high-density probe data was processed in the following ways.

1. Difference Data using the modified Beer-Lambert Law.
2. Spatially Resolved Spectroscopy.
3. Spectral minimisation of difference data - FEM basis.

Before the data were processed the calibration factors calculated in Chapter 6 were applied, starting with the dark noise subtraction and then dividing through by the LED intensity and SPD responsivity factors. As discussed in Chapter 2, there are several sources of physiological noise present in all fNIRS data, such as mayer waves (blood pressure) and cardiac changes that will cause small, predictable fluctuations in detected light intensity. Therefore, to smooth the raw data a frequency domain filtering process was used to removed signals with frequencies of 1 Hz (cardiac) or 0.08-0.12 Hz (Mayer) [107]. After the noise filtering, a secondary smoothing process consisting of a 5-point moving average was also applied. After the smoothing process the intensity data for the 60 s baseline measurement was averaged to provide a reference measurement (Θ_{ref}) from which changes could be measured.

The modified Beer-Lambert law can be used to calculate changes in chromophore (HbO and HHb) concentration with reference to a set of reference baseline measurement intensities (Θ_{ref}). Using the relationship $\Theta_{anom} - \Theta_{ref}$, the change in optical density (ΔOD) at a given time point can be found, where Θ_{anom} is a non-reference measurement point [107]. Using the OD from each wavelength (λ) and the extinction coefficients (ϵ) of the chromophores at each wavelength, Equation 7.1.1 can be used to work out changes in HbO and HHb.

$$\begin{bmatrix} \Delta Hb02 \\ \Delta HHb \end{bmatrix} = \frac{1}{L \times DPF} \begin{bmatrix} \epsilon_{Hb02\lambda_1} & \epsilon_{Hb02\lambda_2} \\ \epsilon_{HHb\lambda_1} & \epsilon_{HHb\lambda_2} \end{bmatrix}^{-1} \begin{bmatrix} \Delta OD_{\lambda_1} \\ \Delta OD_{\lambda_2} \end{bmatrix} \quad (7.1)$$

As the differential pathlength factor (DPF) at the source wavelengths is not known, an average literature value of 5.5 was used based on forearm data [147] and L is the distance between the source and detector.

As the high-density probe has multiple measurements at a range of source-detector separations, they were grouped and averaged by separation distances of 15, 34, 45, 54 and 62 mm for reconstruction.

Spatially resolved spectroscopy is discussed in detail in Chapter 2. For the arm cuff measurements the TOI data was calculated for each data point using Equations 7.2 and 7.3.

$$k\mu_a(\lambda) = \frac{1}{3(1 - 6.3E^{-4}\lambda)} \left(\ln(10) \frac{\delta A(\lambda)}{\delta \rho} - \frac{2}{\rho} \right) \quad (7.2)$$

where k is an unknown constant, λ is wavelength, μ_a is the absorption coefficient, A is the detector measurement, ρ is the distance between detectors, and ϵ is the extinction coefficient. From the relative concentrations of HbO and HHb the TOI can be produced ($TOI = (\frac{kHbO}{kHbO+kHHb}).100$).

$$\begin{bmatrix} kHbO \\ kHHb \end{bmatrix} = \begin{bmatrix} \epsilon_{i,j}^{-1} \end{bmatrix} \begin{bmatrix} k\mu_a(\lambda_1) \\ k\mu_a(\lambda_2) \\ k\mu_a(\lambda_2) \end{bmatrix} \quad (7.3)$$

The SRS method is only valid for small changes in detector separation, ρ , the high-density dataset could not be combined to reconstruction in one value. Instead the detector measurements were separated into their nearest neighbour groups, 15-34 mm, 34-45 mm, 45-54 mm and 54-62 mm, with the 34-45 mm pairing the closest to the NIRO detector setup of 37-43mm. All the detector pairs over the high-density grid were averaged in order to calculate a single TOI value at each time point for each of the detector distance groupings.

The spectral minimisation of the data was done using a rectangular FEM produced using NIRFAST measuring 60x100x60 mm (Height x Width x Depth) with 15417 nodes (shown in Figure 7.2). The model was set to have homogeneous scatter and absorption properties with HbO concentration at 0.0560 mM, HHb at 0.0140 mM, a water percentage of 50% (mimicking the properties of muscle tissue found in [113]) and scatter power and amplitude values of 1.

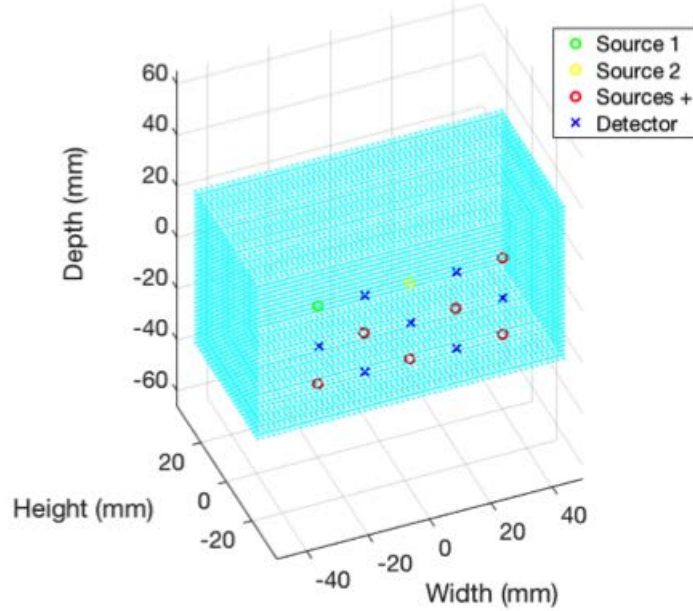


Figure 7.2: Mesh used for spectral minimisation of arm cuff data.

The minimisation process uses the difference data between a give time point and the average baseline measurement intensity ($\Theta_{anom} - \Theta_{ref}$ [19]) and the inverted Jacobian

matrix (J) to calculate the nodal changes in chromophore concentration (ΔC) as shown in Equation 7.4

$$\Delta C = J^{-1} \Delta \Theta = J^{-1} \ln \left(\frac{\Theta_{anom}}{\Theta_{ref}} \right) \quad (7.4)$$

As the minimisation provides a change at all nodes, a small region of interest central in the probes acquisition field was chosen over which the chromophore changes could be averaged. The region of interest was take 5 mm below the surface to avoid the hypersensitivity spots under each source and detector and was 5x10x10 mm in size (Height x Width x Depth).

7.1.2 Results and Discussion

The following data was from a single subject and is aimed at proving the prototype probe is observing sensible signals. An example of the raw data from a single source-detector pair in the probe at 735 nm is shown in Figure 7.3. The raw data is also plotted alongside the filtered and smooth data, which can be seen to remove a proportion of the high frequency noise in the signal. The data shows that there is a large change in detected intensity over the course of the arm occlusion followed by a large rebound in the signal strength on release of the cuff. As 735 nm is most strongly absorbed by HHb this is the pattern that would be expected to be seen as more HHb will be present over the occlusion as saturation decreases then as HbO returns after the cuff is released, the HHb absorption decreased and more light is detected again.

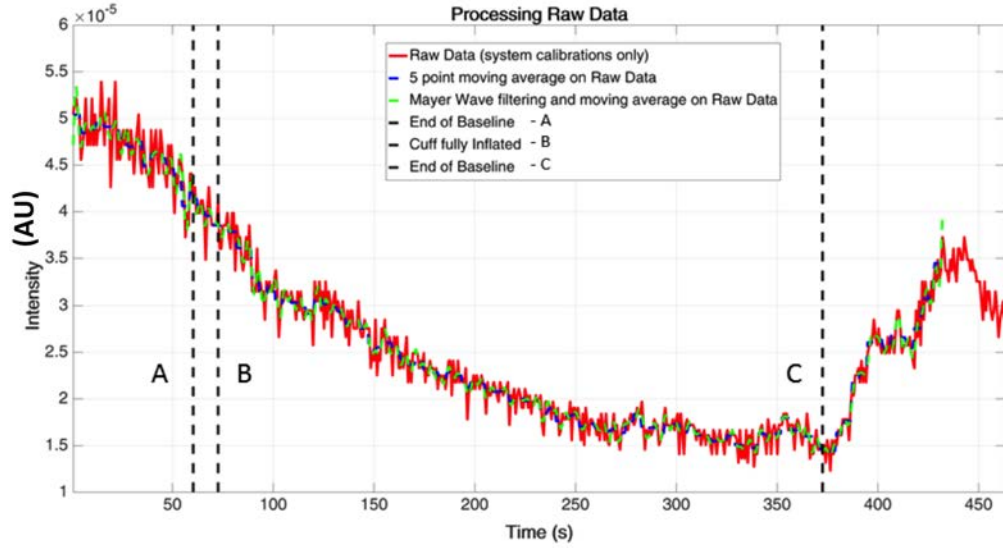


Figure 7.3: Raw data from built high-density probe before and after moving average, and frequency domain filtering.

A noticeable feature of the raw data is the obvious drift in the baseline measurement before the cuff was inflated. It is possible that this change is due to the photodiode being in direct contact with the skin and hence the temperature change is affecting the response. To test this, the drift of the probe was measured on a solid homogeneous phantom over 20 minute period so the change in intensity over time could be calculated to provide a calibration factor for the raw data. Figure 7.4 shows the drift data for the same source-detector pair as the raw data in Figure 7.3. Given that the change in intensity over the entire 20-minute period is $\sim 12\%$ and the baseline drift is $\sim 20\%$ over a 60 s period it is likely that it is body heat affecting the detectors which is an issue that will need to be addressed in future probe development. Calibration factors for the intrinsic probe drift were applied to all raw data measurements for processing after this point, however it did not make a significant impact because ΔI (intensity change) measurements were being

used.

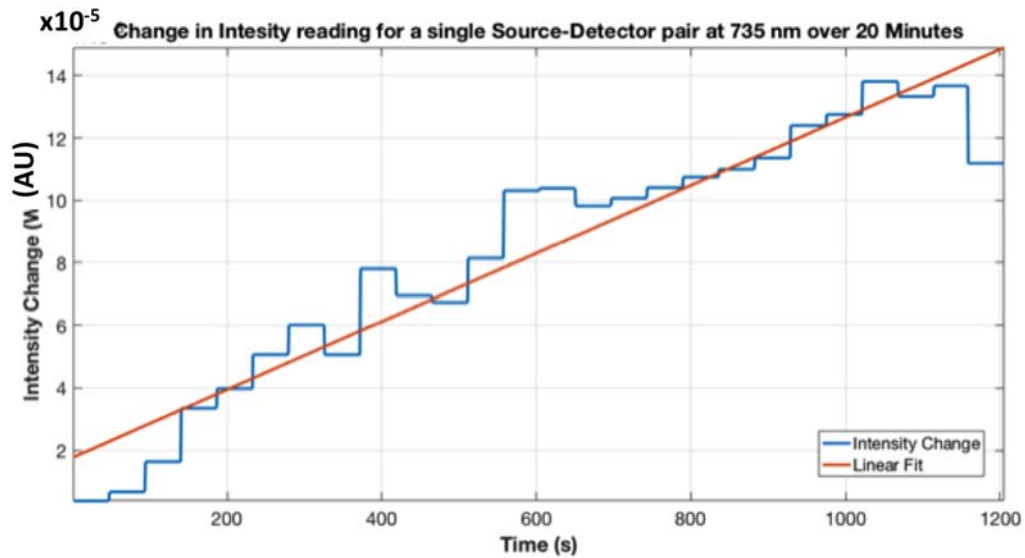


Figure 7.4: Data from measurement of probe drift over a 20-minute period with fitted line used to calculate a correction factor for drift.

Figure 7.5 shows the average change in optical density from the baseline measurement. The results follow the expected trends with the 735 nm data showing an increase in density from increasing HHb during the occlusion, 805 nm data shows a minimal change as the total amount of HbT is not changing and the 850 nm data shows a decrease in optical density during occlusion as HbO concentration is decreasing. Then on release of the cuff the optical density in all channels rises due to the influx of blood back to the arm. The data are separated by source-detector distance and indicates that the 3 mm channels are showing the greatest changes, representing a depth of approximately 2 cm into the target tissue. As discussed in the previous chapter, the dynamic range and sensitivity of the current detector setup is suboptimal the correct level of change may not be seen over all the detectors.

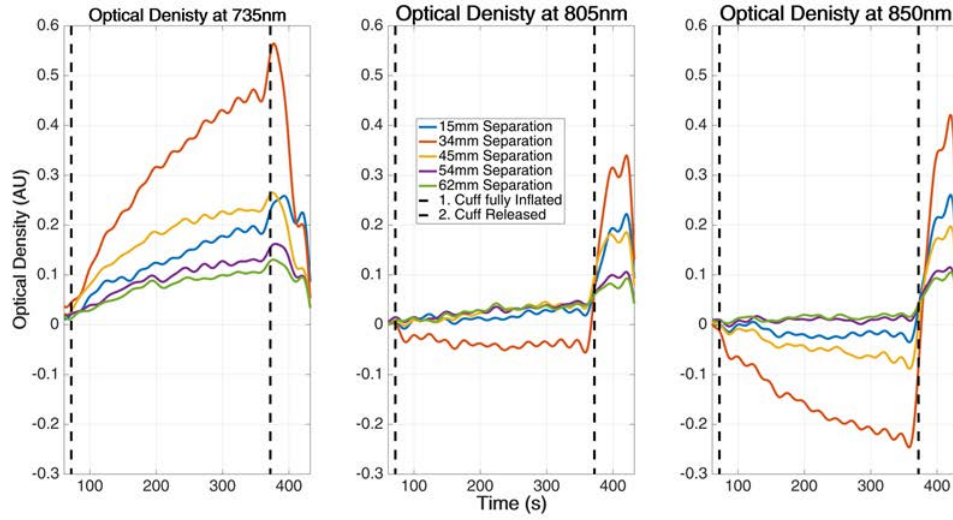


Figure 7.5: Graphs of optical density change from baseline over the duration of data collection for each respectively source-detector distance and wavelength.

The changes in optical density and the modified Beer-Lambert Law were used to estimate the changes in HbO and HHb over the arm cuff acquisition, with the results being displayed in Figure 7.6 along side the data set obtained using the NIRO-200NX under the same conditions. While all the data channels show the correct trends in comparison to the NIRO probe, it is clear that on the whole the probe response between channels is not consistent. For a homogeneous medium such as forearm muscle, it is expected that the changes with depth are roughly similar however the results show a distinct drop in the magnitude of change as the source-detector separation increases. It is also clear that the 54 and 62 mm readings are noisier. Using the 34 mm channel as an example, the concentration change of approximately 12 μM in both HbO and HHb over the course of the occlusion and assuming the literature values for baseline chromophore concentrations at correct at 56 μM for HbO and 14 μM for HHb [113], the saturation change on the high-density probe would be 80-63 % which is a more realistic value than the $\sim 400\mu\text{M}$ change in HbO and HHb shown by the NIRO, however this is likely due to the use of

literature values for differential pathlength factor used in the current reconstructions. All channels also showed a slight increase in HbT over the course of the occlusion, which is theoretically not possible as the blood supply is blocked and so HbT should stay constant as it does in the NIRO data. A slowly increasing HbT can be explained by the intensity drift discussed earlier in this section, where the intensity slowly decreases over time and propagated through the reconstruction as a small increase in absorption uniform over all wavelengths. This highlights a limitation of the current probe electronics.

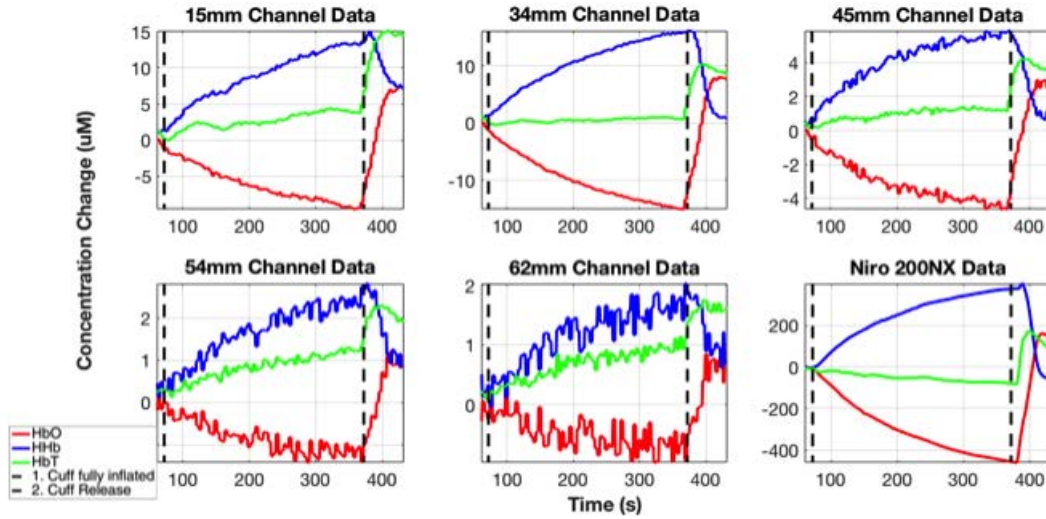


Figure 7.6: Changes in chromophore concentration calculated using the modified Beer lambert law for each source detector separation.

The results of the SRS reconstruction are shown in Figure 7.7, where it can again be seen that there is one channel outperforming the rest. The 34-45 mm channel shows the greatest change in TOI over the course of the arm occlusion with a drop of approximately 7% observed. All channels follow the expected trend of steadily decreasing saturation

during the occlusion followed by a saturation spike when the cuff is released. This is supported by the trends shown in the NIRO TOI data shown in Figure 7.8.

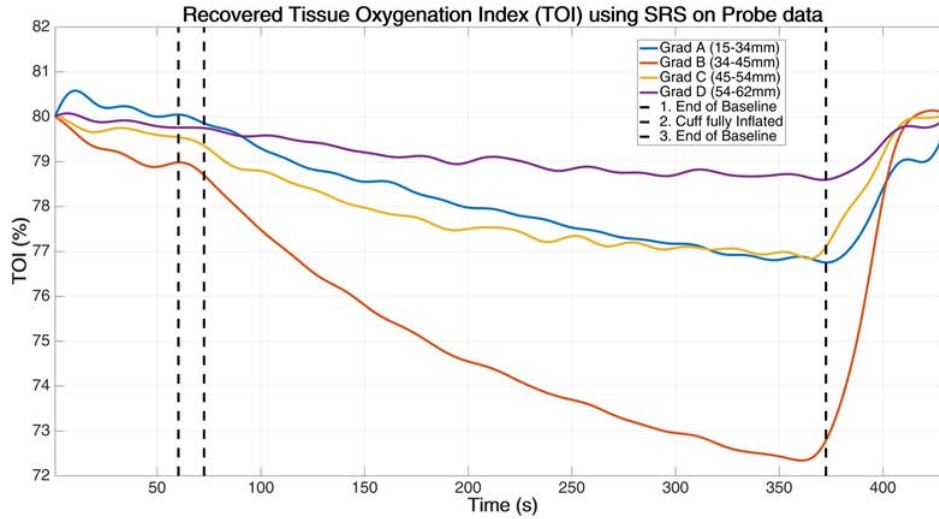


Figure 7.7: Reconstructed spatially resolved spectroscopy parameter - tissue oxygenation index during arm cuff measurement. Results are shown for each pair of source-detector separations.

The magnitude of the desaturation over the course of the arm occlusion is significantly greater in the NIRO TOI data (Figure 7.8), with a TOI drop of approximately 35% which is similar to previous literature values [144]. However, simulations using the SRS method on homogeneous models presented in Chapter 4 showed that the method overestimated saturation changes in the medium under homogeneous, globally changing, conditions. This would indicate that even though the prototype probe is clearly underestimating saturation changes, the NIRO data may also be an overestimate of the true saturation change. The over response could be due to the scatter assumptions that are made in the SRS equation, which would lead to the constant 'k' value not cancelling out correctly when calculating TOI.

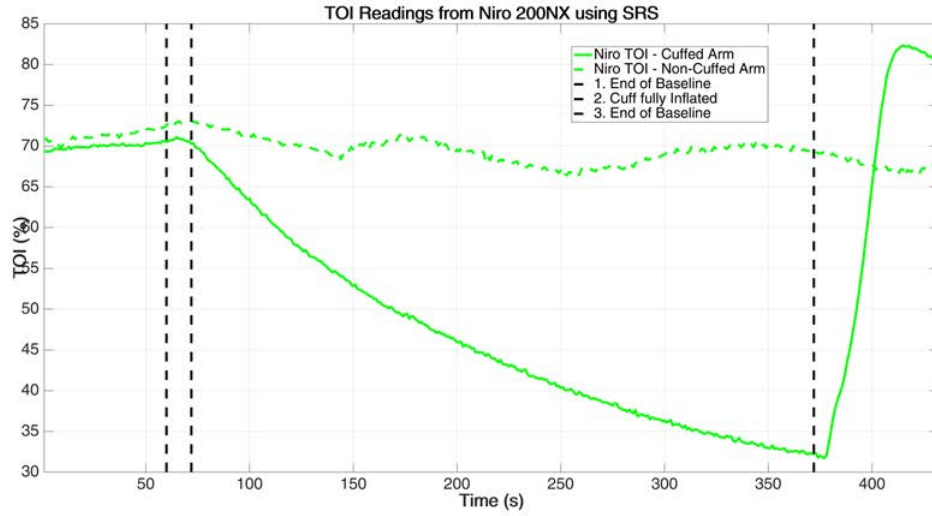


Figure 7.8: Tissue oxygenation index values obtained from the forearm with a NIRO-200NX probe.

The final form of data reconstruction is spectral minimisation of the data using the Jacobian matrix from the FEM shown in Figure 7.9. The reconstructed chromophore changes are based on the entire set of high-density measurements providing 3D tomographic changes, which have been averaged into a singular concentration value based on the assumption that the medium is homogeneous. While the reconstructed data appear noisy, it is still following the same trends as the previous data. Considering that the predicted HbT concentration in the forearm is 70 μM , the changes in HbO and HHb of approximately 80 μM seem to be overestimates of the actual change, however this is assuming the literature values are correct and the medium is homogeneous. The raw data for the FEM results were processed with a 20-point moving average in order to smooth the data, which is why the plot in Figure 7.9 is more 'stepped' than the previous results.

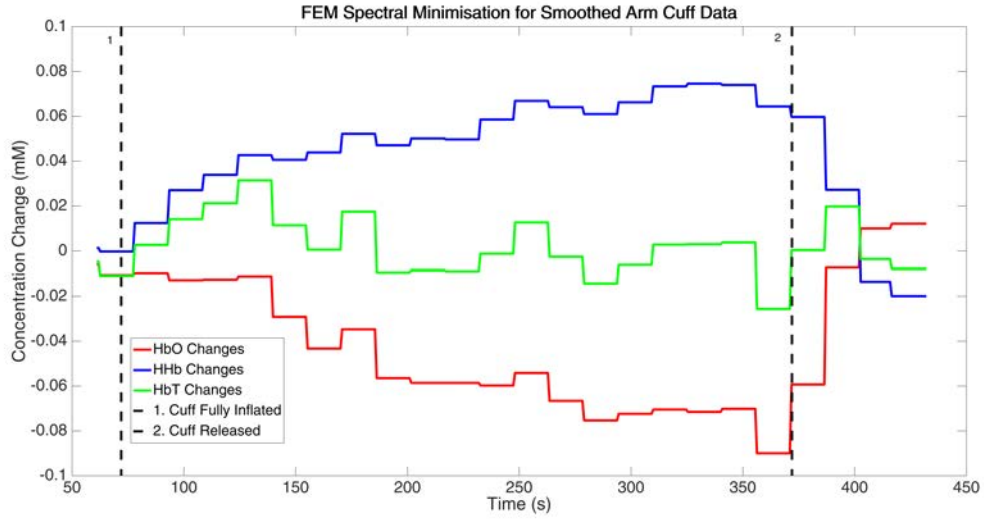


Figure 7.9: Changes in chromophore concentration during arm cuff study obtained through minimisation of spectral data.

7.1.3 Conclusions

The results of the arm cuff measurements confirmed findings from the previous chapter that the detector setup is not sensitive enough to monitor the true changes in absorption within a medium and therefore cannot accurately detect the magnitude of haemodynamic changes. The drift in the intensity measurements over time and the effects of body heat on detector readings are a significant limitation for the prototype probe, and will need development if the probe is ever going to be a viable TBI monitoring device.

Despite the apparent limits in the probe sensitivity and issues with long-term drift, these arm cuff studies show that the prototype probe is capable of observing sensible changes in haemodynamics on simple homogeneous media (muscle tissue), which is an important first step in the development of a low cost probe.

7.2 Valsalva Studies

The second stage in the prototype probe testing recording data on the head, the protocol for this assessment was the same *Valsalva Manoeuvre* used to test the IBIB probe and the Atlas reconstruction process. While the data on the probe so far indicates it is limited in its sensitivity, if the prototype is capable of tracking the haemodynamics of a VM and differentiating between the superficial and cerebral changes then it will be a significant step forward in the development of a low cost, portable probe with a more spatially assessment of saturation than that provided by conventional fNIRS devices.

7.2.1 Methodology

For the VM testing of the probe the curved attachment was used to improve the fit of the probe to the curvature of the forehead. As these were again preliminary tests data were recorded for 2 repeat VMs over 2 healthy volunteers following the protocol for a 10 s maximal VM outlined in Chapter 5. The probe was positioned on the left hand side of the subjects head (Figure 7.10) and held in place manually for the duration of the recording due to the size of the prototype, meaning a physio bandage wrap (as used in a clinical setting) could not be used to secure it to the head. The data were recorded first on the high-density probe and then after a minimum of 5 minutes recovery time the experiment was repeated with the NIRO-200NX probe in the same position for comparison. The acquisition consisted of 60 s of baseline readings, 10 s of maximal effort VM followed by a further 60 s of recovery measurements.

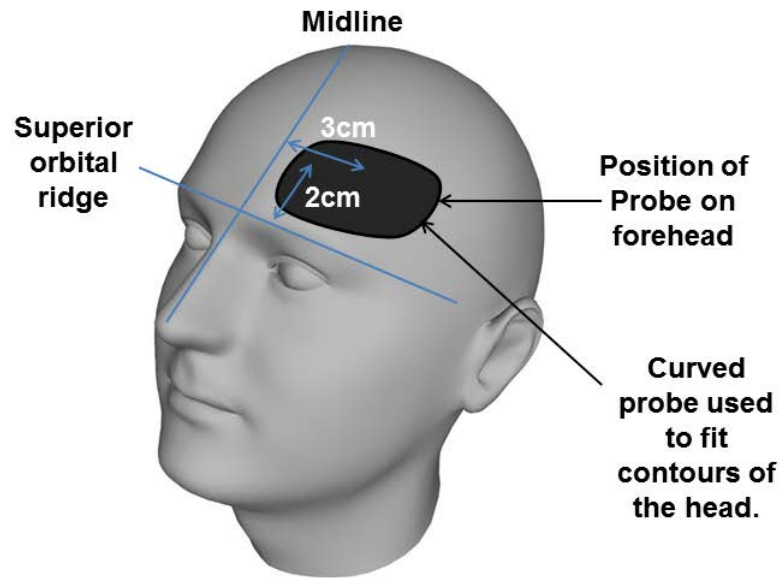


Figure 7.10: Position of high-density and NIRO probe of the subjects head.

Before reconstruction of the data, the calibration factors were applied to the raw data to correct for dark noise, detector responsivity, LED intensity, and to convert the data into intensity units. As the curved probe was being used, the coupling correction factor was also applied. As the time scale of the VM was over 10 s, performing the normal frequency domain removal of Mayer waves resulted in the response to the VM being blunted. Therefore, the frequency filtering was only performed on 1 Hz signals from cardiac noise. The smoothing of the data was done with a 3-point moving average as to not affect the signal drop in the VM.

Parameter Reconstruction - For comparison to the NIRO-200NX and previous experimental results using the VM, the data were reconstructed using 2 different routines.

1. Spatially Resolved Spectroscopy.

2. Spectral minimisation of difference data - FEM basis.

The spatially resolved spectroscopy method used was identical to the procedure followed in the arm cuff reconstructions with the detector measurements being separated into their nearest neighbour groups, 15-34 mm, 34-45 mm, 45-54 mm and 54-62 mm. All the detector pairs over the high-density grid were averaged in order to calculate a single TOI values at each time point for each of the detector distance groupings.

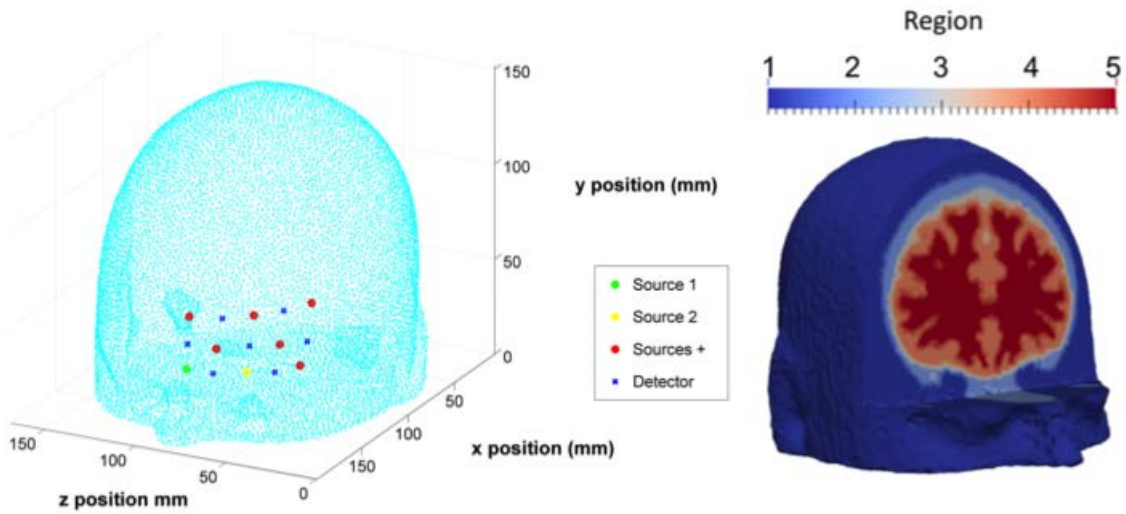


Figure 7.11: Mesh used for spectral minimisation of high-density VM data. Left - Surface mesh showing the position of the sources and detectors on the model. Right - Internal tissue structure of the head model, region 1 is skin, region 2 is bone and regions 3-5 are brain.

The spectral minimisation for the VM data used a more spatially accurate model than the arm cuff data. Instead of having a homogeneous slab model, the Atlas model was used as the basis for the minimisation so the chromophore changes could be separated into the skin, bone and brain regions. The scatter and absorption properties of the model are based on literature values for muscle shown in Appendix .2. The model consisted of 131,545 nodes and the minimisation process is outlined by Equation 7.5. This is the same

minimisation method used for the arm cuff studies for consistency, no regularisation was included.

$$\Delta C = J^{-1} \Delta \Theta = J^{-1} \ln \left(\frac{\Theta_{anom}}{\Theta_{ref}} \right) \quad (7.5)$$

The 60 s baseline reading was averaged into a single reference dataset, (Θ_{ref}) , then each time point after the baseline was taken as the 'anomaly' measurement, (Θ_{anom}) , from which the change in intensity could be found in order to calculate changes in chromophore concentration over time.

7.2.2 Results and Discussion

The following data gives example measurements from a single subject during a VM to show the prototype probe is capable of obtaining useful data when positioned on the head. As the probe was solid, even with the curved head piece the coupling with the head of the subjects was not ideal. The following dataset was for a subject where the probe made the best contact with the forehead and therefore represents a best case scenario for the prototype probe; a successful reconstruction of the data will prove that the concept of the low cost probe is viable and will form the basis for progression of the design and electronics.

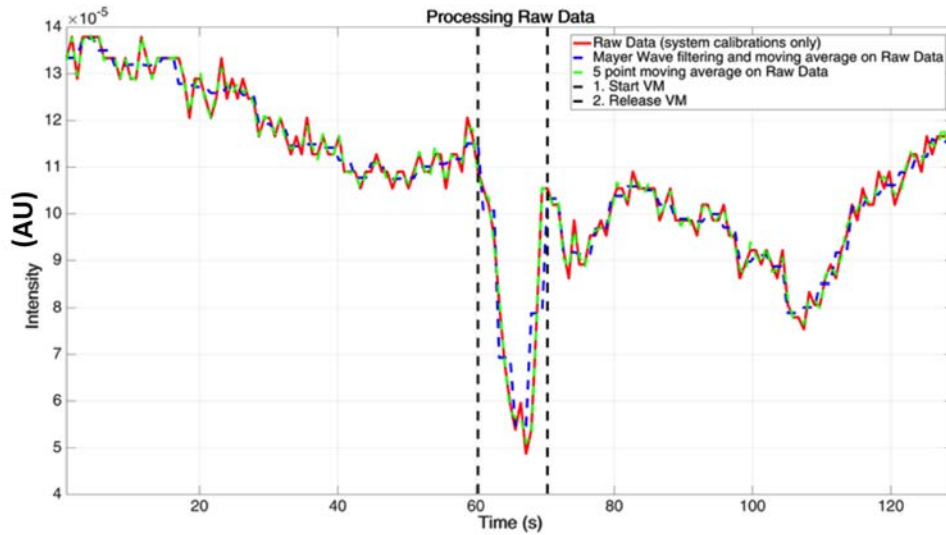


Figure 7.12: Raw data recorded on the forehead during a 10 s VM plotted alongside moving average and frequency domain filter data.

Figure 7.12 shows a set of raw data from a single source-detector pair over the course of the VM measurement. The data comes from a 735 nm source and the separation between the source and detector is 34 mm. There is a large drop in detected light intensity after the onset of the VM, which quickly recovers to baseline when the VM is released. Given that this data is at 735 nm, the drop in intensity indicates an increase in the concentration of HHb and which would be consistent with the predicted decrease in oxygen saturation in the brain. The raw data is also shown alongside the frequency filtered and smoothed datasets, showing that the noise removal process is not obscuring the dynamics of the VM.

The results of the reconstructed TOI values are shown in Figure 7.13 for the 4 different source-detector gradient pairs. Unlike the arm cuff measurements, the pair showing the greatest change in the VM data is the 15-34 mm. This make sense conceptually as the

15 mm detector readings will be mainly sampling skin and the 34 mm readings will be sampling both skin and the surface of the brain, therefore the difference between them will be mainly brain changes. Also, as these are the two shortest source-detector separations the sensitivity of the probe is less of a limiting factor as it is with the other measurement pairs. The data from the second participant is shown in Appendix .6.

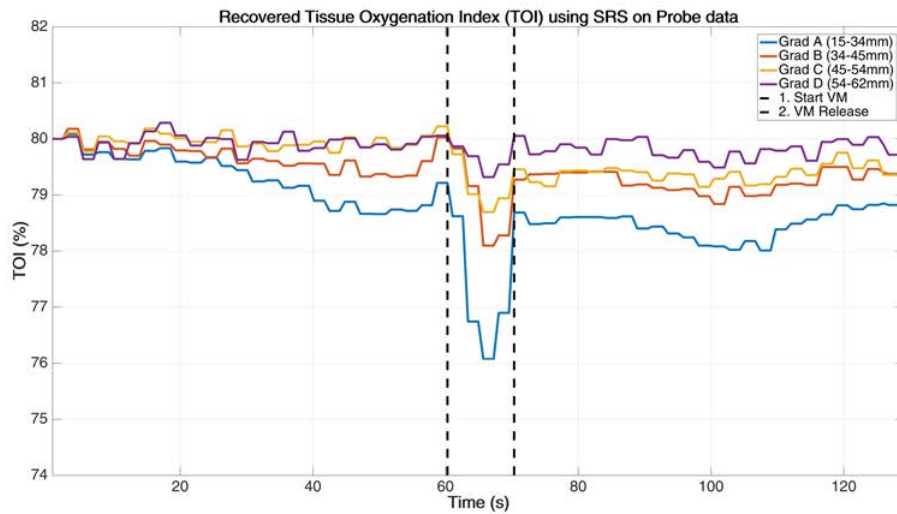


Figure 7.13: Reconstructed TOI for 10 s VM using high-density probe.

The maximum reconstructed drop in TOI over the course of the VM was 3%, which is significantly lower than the predicted 22% drop expected in a VM. However, considering the current limitation of the prototype probe in terms of detector sensitivity the TOI drop is comparable to the 6% seen on the same subject using the NIRO-200NX probe (Figure 7.14). Regardless, the probe is clearly detecting cerebral changes during the VM, which is a promising step for the low cost probe that could be easily improved upon with design changes to improve contact with the subjects head, for example.

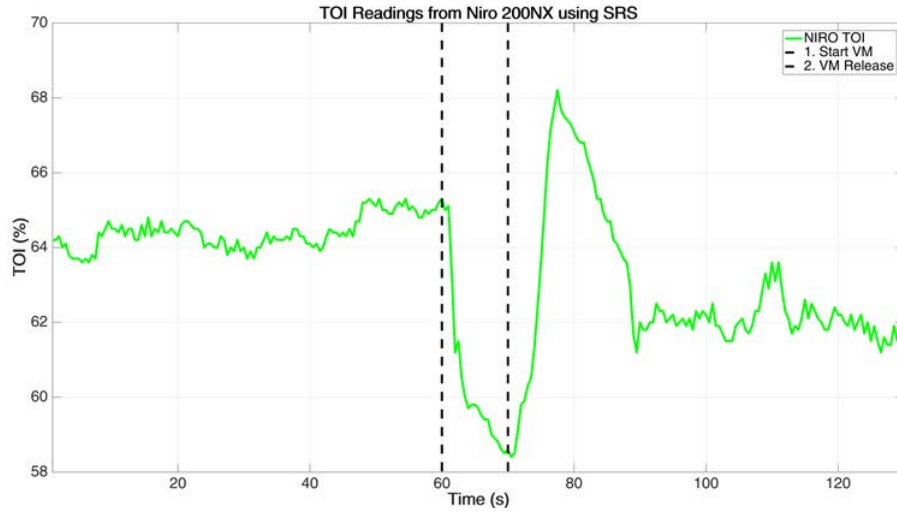


Figure 7.14: Tissue oxygenation index values obtained from the forehead with a NIRO-200NX probe during a 10 s VM.

The spectral minimisation of the data aimed to provide a semi-complex form of data reconstruction, as the Atlas model used as the basis for the Jacobian can be separated into distinct tissue regions of skin, bone and brain in order to assess chromophore concentration changes in the different regions. However the data taken using the curved probe during a VM proved too noisy to provide meaningful results using this form of semi-complex reconstruction.

7.3 Conclusions

The purpose of this chapter was to verify whether the prototype high-density probe was capable of observing sensible changes in haemodynamics from measurements taken on the forearm and forehead. For development of NIR techniques for monitoring TBI patients there are changes necessary in both the hardware and the reconstruction algorithms. The results of the Atlas-model based reconstructions in Chapter 5 showed the potential benefits of the semi-complex reconstruction method underpinned by high-density overlapping measurements. The experiments in this chapter represent the testing of a low cost and

portable high-density probe that could, with further development and refinement, provide the measurement data required for the semi-complex Atlas-based reconstructions.

From the probe characterisation work performed in Chapter 6 it was known that the prototype probe did not have the sensitivity to perform quantitatively accurate measurements and as the dynamic range of the detectors was narrow, the chances of observing accurately the magnitude of changes within a target medium were also low. Therefore, the success of the prototype probe was measured by its ability to map qualitative changes in superficial and cerebral haemodynamics.

Arm cuff studies confirmed that even under homogeneous conditions the prototype probe lacked the sensitivity to accurately map changes in TOI, with only a 7% drop over 5 minutes in comparison to the 35% drop seen on the NIRO-200NX. Nevertheless, the 34 mm data channels showed that when the data was reconstructed using the modified Beer-Lambert law, a more realistic change of 17% was observed. Spectral minimisation of all the data measurements also showed the correct desaturation trends. Consequently, the results do indicate that the probe is definitely capable of observing saturation changes, however, the detector sensitivity is the limiting factor as the probe is failing to match the results from commercially available fNIRS probes.

The VM measurements of TOI were at the very limit of the prototype probes capability due to the inflexible nature of the head piece, which prevented complete contact with the forehead. Despite this major limitation and the sensitivity issue highlighted above the high-density probe was still able to map the expected trends in TOI during the VM. The Atlas-based spectral minimisation however was unsuccessful even the noise level in the data and the more complex form of reconstruction relative to the SRS method used to calculate TOI.

While the prototype probe is clearly in need of further development in terms of pre-amplifiers for the detectors and flexible circuit boards for conforming to curved surfaces

it has shown the potential for a low cost and portable probe to be built that could be applied in a TBI monitoring environment.

CHAPTER 8

CONCLUSIONS AND FUTURE WORK

8.1 Conclusions

The validity of NIR spectroscopy as a monitoring modality for patients with traumatic brain injury has been investigated and presented. Within the context of traumatic brain injury the following hypotheses have been addressed as stated in Chapter 1.3:

1. Signals from superficial tissues are not preventing fNIRS from measuring haemodynamic changes in the brain that would be necessary for guiding TBI patient therapy.
2. Contamination from superficial tissues is limiting the quantitative accuracy of fNIRS measurements and thus it cannot currently be used as a standalone TBI monitoring modality when no normative baseline measurements are available.
3. A small scale hybrid fNIRS/DOT probe and Atlas-based reconstruction algorithm can be used to recover superficial and cerebral haemodynamics simultaneously and thus produce quantitatively accurate results.
4. A low cost, portable, fNIRS device capable of producing these measurements can be built using off-the-shelf components.

Investigations into existing fNIRS probes, in both healthy volunteer studies and numerical simulations, confirmed that despite the presence of superficial contamination from facial

tissue, they still have the capability to observe the changes in cerebral haemodynamics. It was demonstrated that a maximal VM was a good method of inducing profound changes in cerebral haemodynamics in healthy volunteers; similar to those that would be expected in brain trauma patients, making it suitable for validation of fNIRS probes and reconstruction algorithms. Using this technique it was shown that while the fNIRS devices that were tested identified the anticipated changes, the magnitude of the change, as well as the quantitative accuracy of the reconstructed data, was not sufficient to support clinical decisions on trauma patients. Specifically, without first obtaining a healthy normative baseline reading from which to reference changes against, fNIRS alone cannot currently be used to guide patient therapy. Furthermore, the high variation in measured oxygen saturation at baseline between participants makes it difficult to put a firm number on what saturation level constitutes a healthy brain.

In reference to the first two hypotheses, superficial contamination does not prevent fNIRS from observing cerebral changes however, its presence obscures the ability to produce quantitatively accurate results. Hence it was concluded that in order to develop fNIRS as a monitoring modality for traumatic brain injury, a high-density probe and more complex recovery process was required. A more complex dataset and reconstruction algorithm allows the move from a global parameter recovery over a region of interest, to a more spatially resolved parameter recovery, capable of separating out changes from different tissues within the region of interest.

With regards to the third hypothesis posed, using an Atlas-model registered to the measurements of subject's head, the reconstruction algorithm for parameter recovery can be enhanced to provide more quantitative results. The Atlas model gives more accurate structural prior information as a basis for the reconstruction so that changes from different tissue regions (skin, bone and brain) can be separated.

In simulations, the use of a high-density fNIRS probe utilising multiple overlapping measurements, at three wavelengths, showed an improvement in terms of quantitative accuracy and also in the magnitude of the recovered saturation changes when compared to the fNIRS geometries tested previously. Even with this improvement, however the results could still not be considered to be truly quantitative and findings showed that mismatches in the internal tissue thicknesses and scattering properties between the subject and the Atlas were now contributing factors to the quantitative inaccuracies. As such, making the reconstruction process more complex is a double-edged sword, as there is clearly an improved ability to separate out signal contributions from different tissue regions in some cases, however, this also introduces additional error sources; including inaccuracies in scatter properties and internal tissue structure within the Atlas model that have the potential to obscure recovered parameters.

This was confirmed in the healthy volunteer studies where the recovered cerebral saturation data were found to not be quantitatively accurate. Despite this the probe mapped drops in cerebral saturation ($20 \pm 7\%$) that were much more representative of the expected values (22%) than current fNIRS devices ($7 \pm 3\%$). Extending this probe and reconstruction process to frequency domain measurements (in simulation) showed that in situations where the Atlas model was accurate, then the new phase data was sufficient to update the scatter properties and provide much more accurate cerebral saturation values.

Finally the fourth hypothesis was covered by the work presented in Chapters 6 and 7. Findings indicate that it is possible to build a portable high-density fNIRS probe for less than £300. The prototype probe using triple wavelength LEDs (735, 805 and 850 nm) and SPD detectors provided 168 measurement channels over an 18 cm^2 region of interest. While the prototype did not have sufficient sensitivity to provide a dataset that could be used for the semi-complex Atlas-based reconstruction algorithm it was shown to be able to qualitatively map the expected changes in oxygen saturation during arm cuff occlusions

and *Valsalva Manoeuvre* studies. Further development of such a probe and reconstruction algorithms could potentially lead to a viable TBI monitoring device.

Overall this research has shown the benefits of using Atlas models for providing semi-complex reconstruction of high-density NIR spectroscopy data. While the quantitative accuracy of the results is not sufficient to guide TBI patient therapy, it can more accurately map cerebral changes than a standard fNIRS setup.

8.2 Future Work

While this project has provided a basis for the application of high-density fNIRS to monitoring patients with traumatic brain injury, the lack of quantitative accuracy means that further improvements are needed in order to make it a viable tool for clinicians. The research on Atlas-based reconstruction process can progress in multiple directions. Firstly, there is the accuracy of the model itself; the model being used currently was produced for brain activation studies and hence the focus was put on accuracy of segmentation in the brain region, not the superficial skin and bone regions. It was found that there was a marked difference between superficial tissue thicknesses in segmented subject MRIs and the Atlas model, indicating that the Atlas is not truly representative. Therefore, investigating the use of the technique with other Atlas models, such as the Colin27 MRI Atlas, to assess the impact on the results would be beneficial. There is, however, no guarantee that the Colin27 Atlas would be any better. The Atlas models could also be extended to cover different age ranges as this can also lead to different average head structures. The ideal situation would be to produce a model specific to each TBI patient, however this is only possible for the clinical environment where CT and MRI scans can be produced. Therefore as we also require pre-clinical monitoring the best way to approach the Atlas problem could be to use the 'big data' approach. If thousands of 3D CT/MRI head images could be processed along with other demographic data, such as age and gender, it may be possible to build up a new set of generalised head models to use, instead of the Atlas

models that are currently available. The high-density probe and reconstruction methods also need to be tested on TBI patients in the clinic. Running a clinical trial where a high-density fNIRS probe is used alongside current invasive monitoring modalities (ICP and oxygen tension monitor) for an extended period (e.g. 24 hours) would provide an ideal opportunity to validate the reconstruction technique and Atlas models. The clinical trial scenario would mean that CT scans of TBI patients could also be segmented and used to create models for the reconstruction. This way the registered Atlas could also be compared to patient specific models.

In addition to the need for testing on different Atlas models, the choice of baseline optical properties (both absorption and scatter) in the model needs to be addressed. Currently these are based on a single set of literature values with no guarantee they are representative of the general population. There is also a large variation in scattering properties for the given tissues types (skin, bone and brain) across the literature (reviewed by Jacques et al [142]). Consequently, combining incorrect scattering properties with poor structural priors in a reconstruction based on continuous wave measurements, where no information about scatter can be accurately reconstructed, is a large potential error source. Therefore if the Atlas model can be improved to make the internal structure more representative, then progression on the scattering properties can be made by extending the high-density probe to take frequency domain measurements that could allow for scatter to be reconstructed as well as absorption. Although this may provide advantages to the reconstructions, this would need to be balanced against the likely increase in cost of the probe.

One of the differences between the Atlas-model simulation studies and the healthy volunteer testing was the number of wavelengths in the probe. The simulations used the design of the in-house probe that was constructed during this project, which used 3 wavelengths instead of the 2 that the Institute of Biocybernetics and Biomedical Engineering (IBIB) probe used. Therefore, the Atlas-reconstruction method should be tested on a high-density probe, which uses more than 2 wavelengths.

Finally, the high-density probe built in this project was a proof-of-concept and is subsequently in need of further development. The first issue is its lack of flexibility. Printing flexible circuit boards and low profile LEDs and SPDs would allow the probe to conform to the shape of a subject's forehead and minimise the contact error. Also much greater sensitivity could be obtained from the detectors if pre-amplifiers were incorporated into the circuits.

While the Atlas-based reconstructions provided a step in the right direction for fNIRS as a TBI monitoring tool, there is another aspect on top of the quantitative accuracy that was not addressed in this project. The reconstruction time for the Atlas-based reconstructions is not yet real time, however there is on-going work within the University of Birmingham group that aims to use the multiple processing cores on graphics cards to speed up the matrix calculations performed in the reconstruction (within NIRFAST) in a move towards real time reconstruction. This will also add significant value and increase the likely translation of this advancement in fNIRS technology into the clinical and pre-clinical setting for TBI care.

.1 Appendix 1 - Near Infrared Spectroscopy Probe Geometries for Simulation

Probe	Wavelengths (nm)	Source-Detector Separation (mm)	No. Sources	No. Detectors	No. Measure- ments
ISS	690,830	30,35,40,45	4	1	8
INVOS	730,810	30,40	1	2	4
EQUANOX	730,810,880	20,40	2	2	12
Foresight	690,780,805,850	15,50	1	2	8
NIRO- 200NX	735,810,850	37,43	1	2	6

Table 1: Information about the five commercial probes being modelled. Note - Due to the curvature of the head the Euclidean distance between a given source-detector pair with vary by approximately ± 1 -2 mm

.2 Appendix 2 - Atlas model Optical Properties

Layer	Region No.	HbO (μ M)	HHb (μ M)	H ₂ O (%)	Scatter Amplitude	Scatter Power
Scalp	1	0.0560	0.0140	50	0.14	2.82
Skull	2	0.0392	0.0098	15	1.40	1.47
Brain	3-5	0.0540	0.0220	78	0.54	0.76

Table 2: Optical properties for scalp, skull and brain used for simulations [113]

.3 Appendix 3 - Optical Properties of ISS Calibration Phantoms

Wavelength (nm)	Absorption Coefficient (mm ⁻¹)	Scattering Coefficient (mm ⁻¹)
690	0.141	5.22
830	0.140	4.72

Table 3: Optical properties of ISS calibration Phantom A

Wavelength (nm)	Absorption Coefficient (mm ⁻¹)	Scattering Coefficient (mm ⁻¹)
690	0.105	10.9
830	0.102	9.7

Table 4: Optical properties of ISS calibration Phantom B

.4 Appendix 4 - Blood pressure comparisons from Vasopressor studies

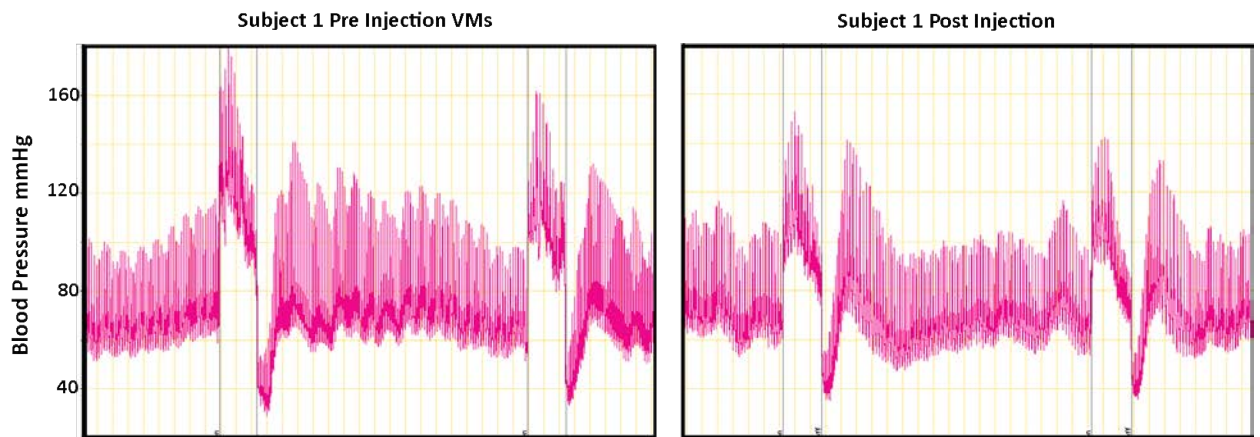


Figure 1: Comparison of blood pressure during the VMs pre and post injection for subject 1.

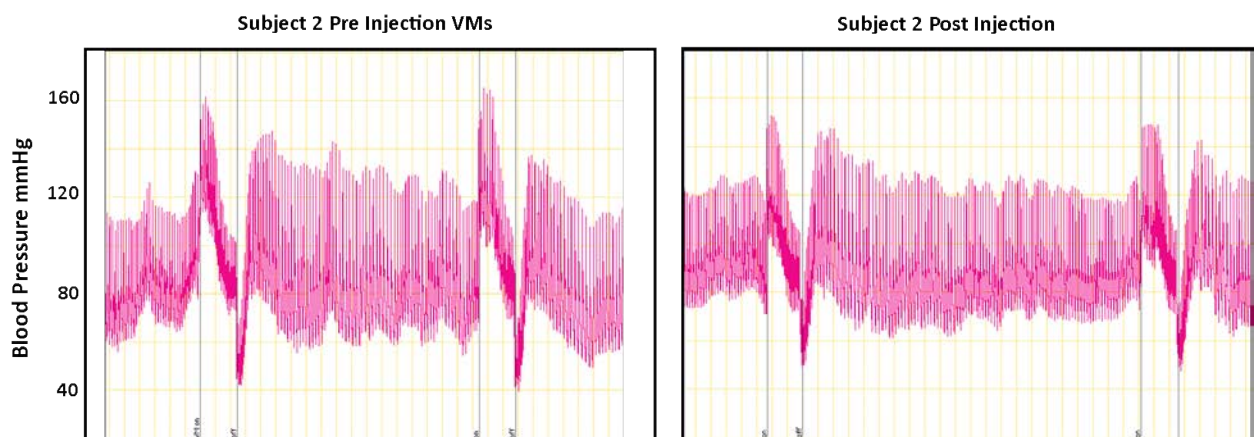


Figure 2: Comparison of blood pressure during the VMs pre and post injection for subject 2.

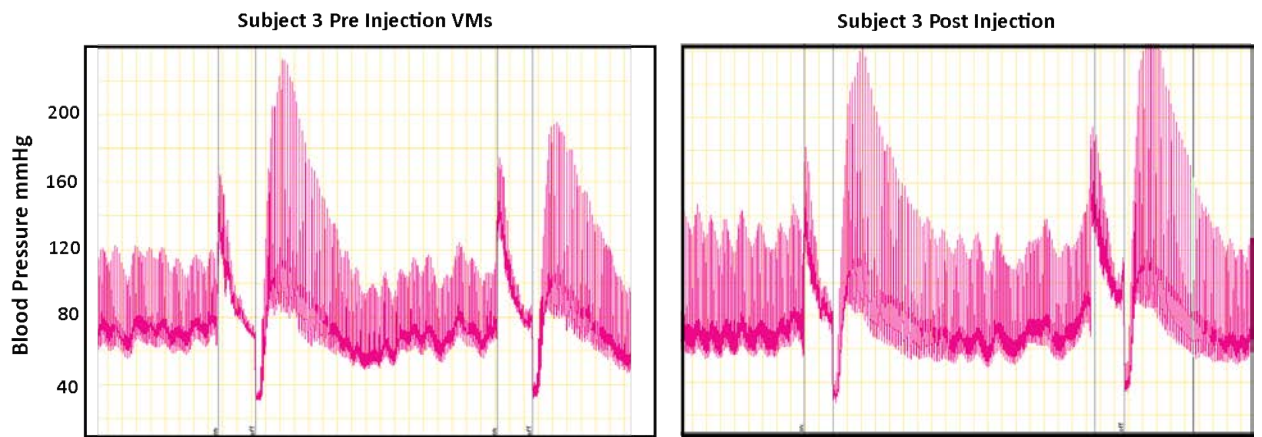


Figure 3: Comparison of blood pressure during the VMs pre and post injection for subject 3.

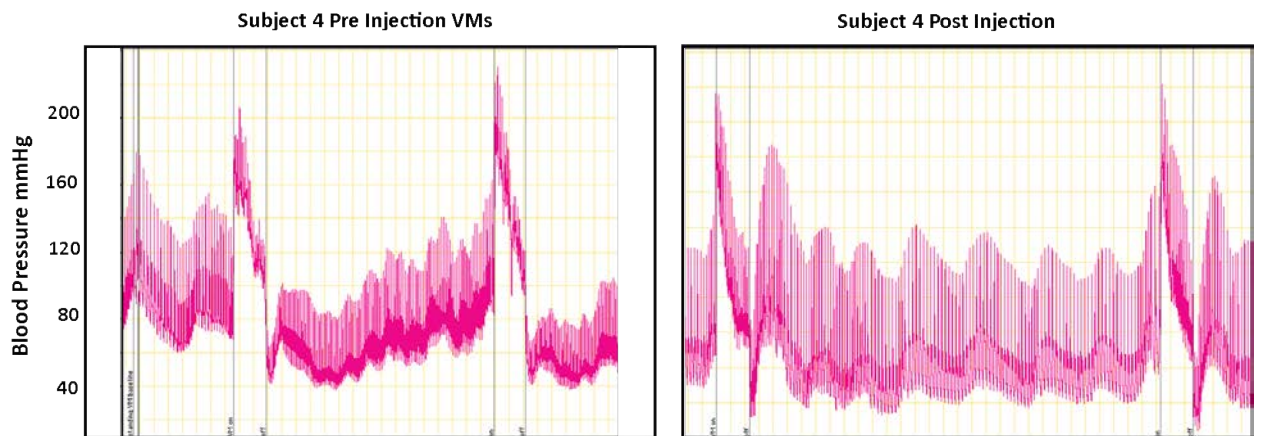


Figure 4: Comparison of blood pressure during the VMs pre and post injection for subject 4.

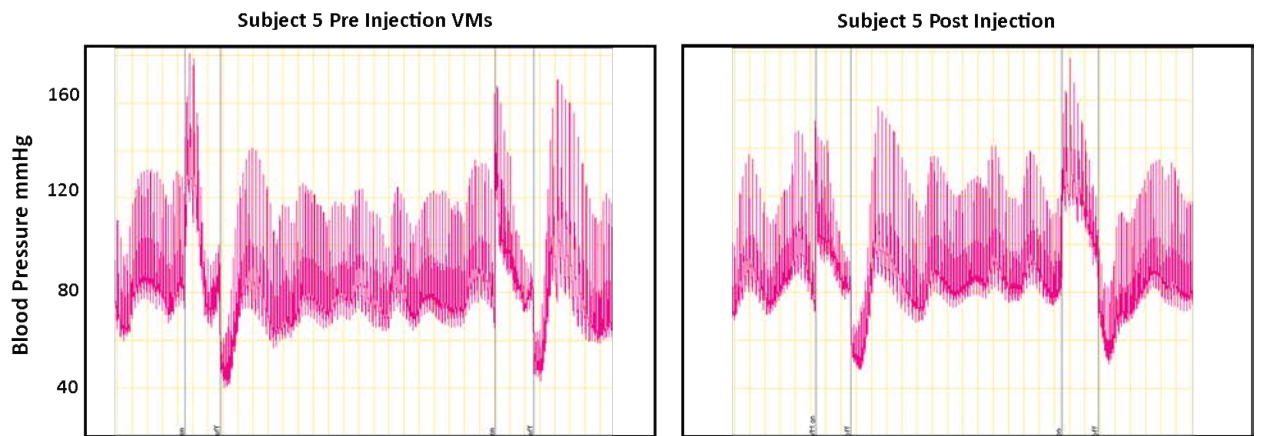


Figure 5: Comparison of blood pressure during the VMs pre and post injection for subject 5.

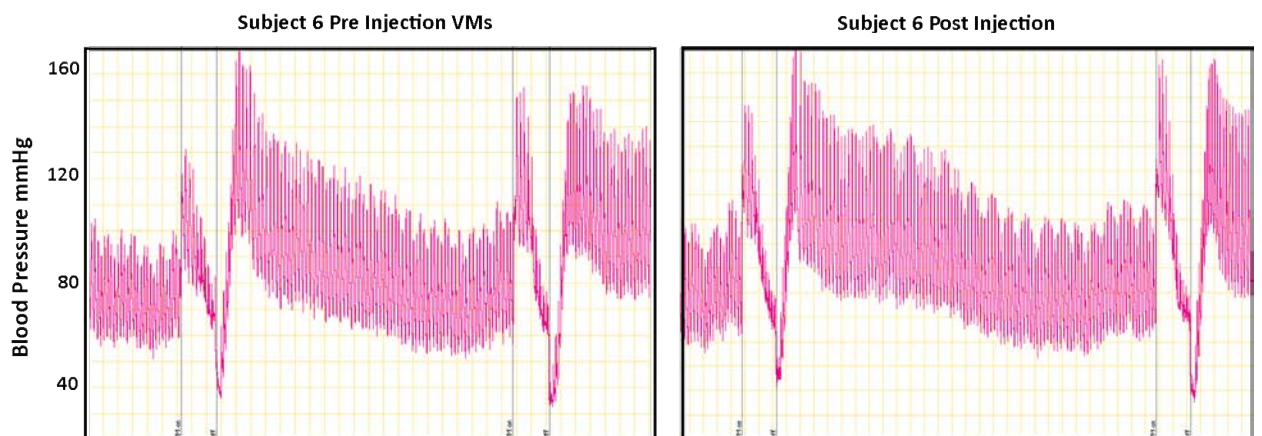


Figure 6: Comparison of blood pressure during the VMs pre and post injection for subject 6.

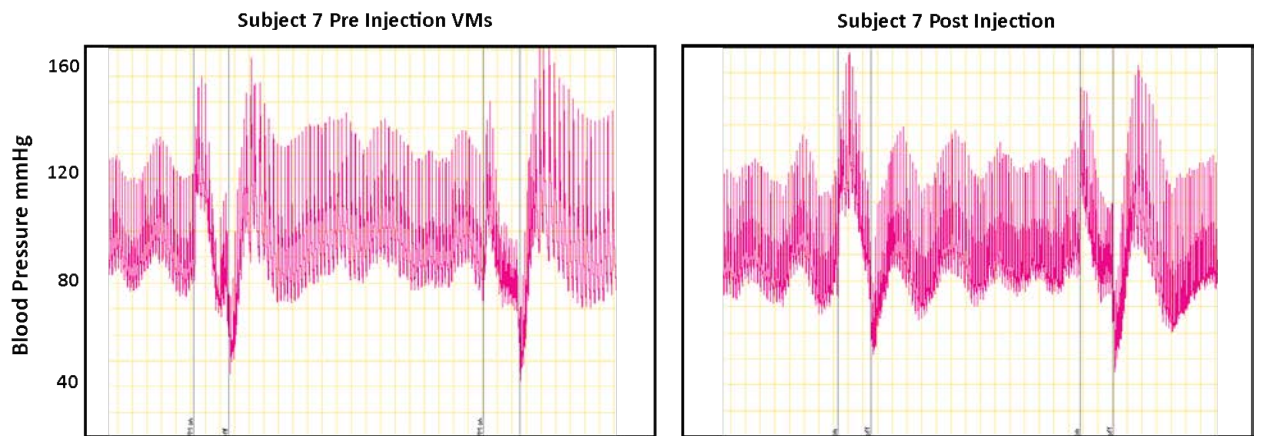


Figure 7: Comparison of blood pressure during the VMs pre and post injection for subject 7.

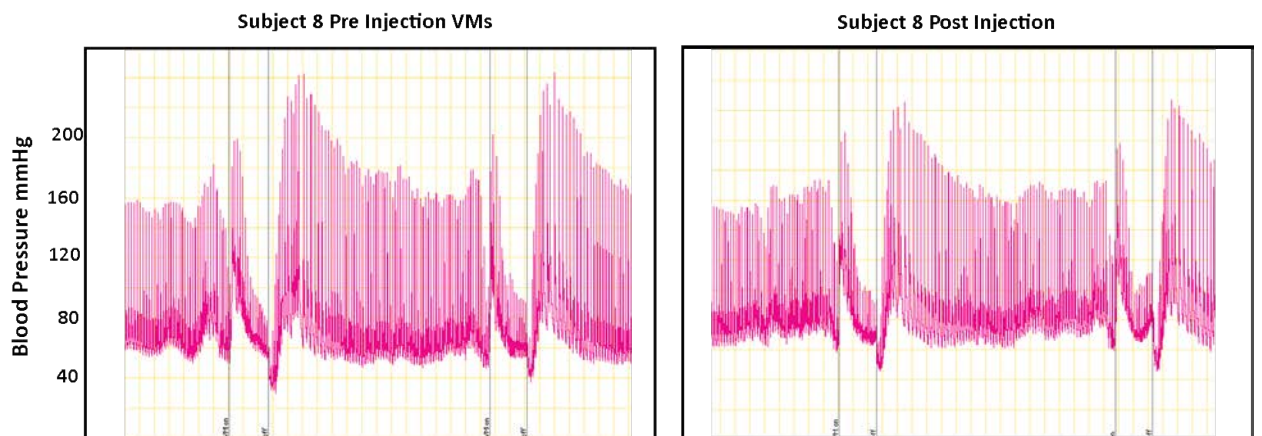


Figure 8: Comparison of blood pressure during the VMs pre and post injection for subject 8.

.5 Appendix 5 - Reconstructed arm cuff data from second participant

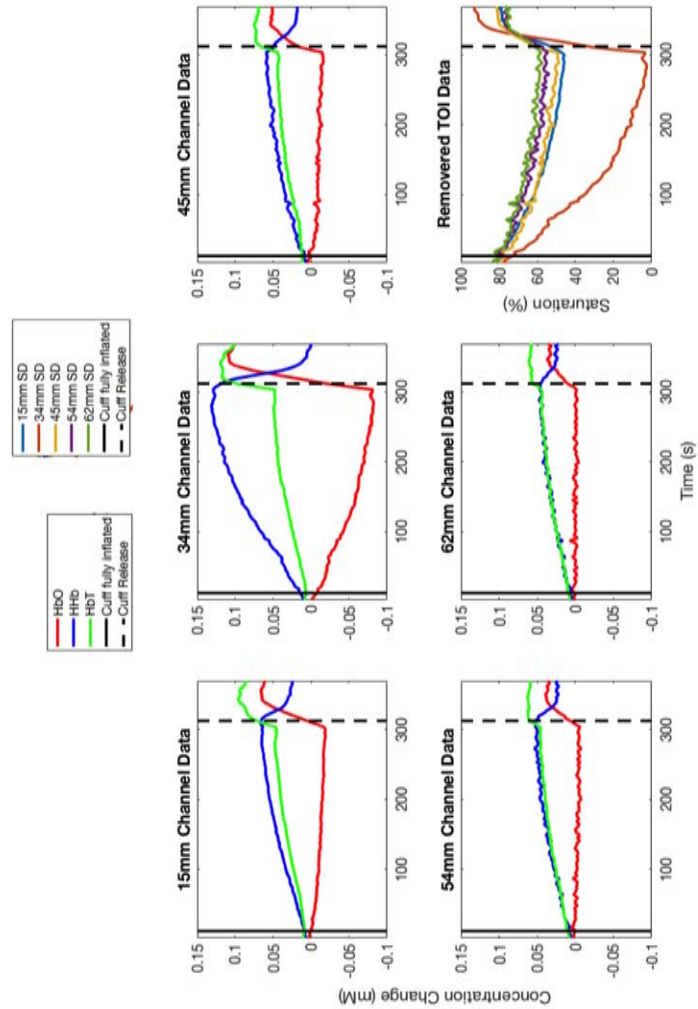


Figure 9: Reconstructed concentration values and TOI values (using SRS) for second participant in arm cuff studies with the prototype high-density probe.

.6 Appendix 6 - Reconstructed VM data from second participant

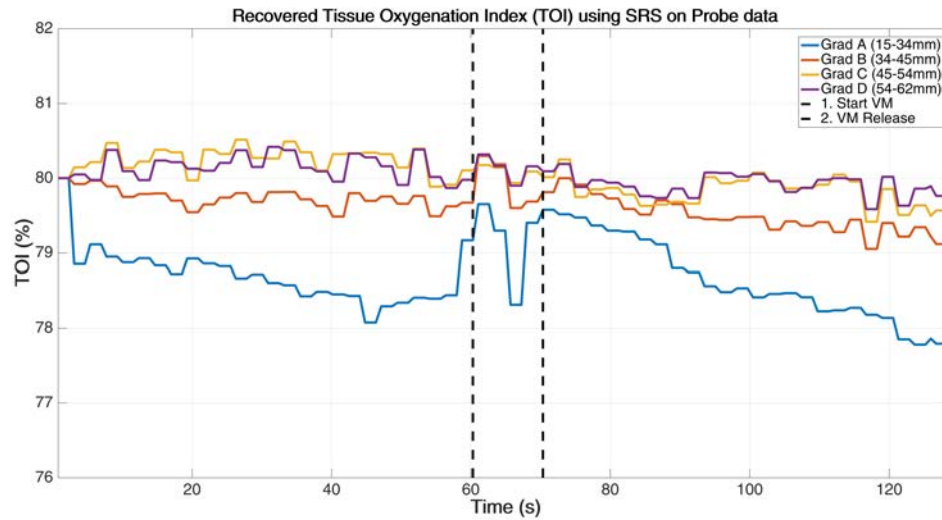


Figure 10: Reconstructed TOI for 10 s VM using high-density probe for second participant

LIST OF REFERENCES

- [1] Michael F Stiefel, Alejandro Spiotta, Vincent H Gracias, Alicia M Garuffe, Oscar Guillaumondegui, Eileen Maloney-Wilensky, Stephanie Bloom, M Sean Grady, and Peter D LeRoux. Reduced mortality rate in patients with severe traumatic brain injury treated with brain tissue oxygen monitoring. *Journal of neurosurgery*, 103(5):805–811, 2005.
- [2] Sarah Hodgkinson, Vicki Pollit, Carlos Sharpin, Fiona Lecky, et al. Early management of head injury: summary of updated nice guidance. *Bmj*, 348, 2014.
- [3] Eileen Maloney-Wilensky, Vicente Gracias, Arthur Itkin, Katherine Hoffman, Stephanie Bloom, Wei Yang, Susan Christian, and Peter D LeRoux. Brain tissue oxygen and outcome after severe traumatic brain injury: A systematic review*. *Critical care medicine*, 37(6):2057–2063, 2009.
- [4] David F Signorini, Peter JD Andrews, Patricia A Jones, Joanna M Wardlaw, and J Douglas Miller. Adding insult to injury: the prognostic value of early secondary insults for survival after traumatic brain injury. *Journal of Neurology, Neurosurgery & Psychiatry*, 66(1):26–31, 1999.
- [5] Pippa G Al-Rawi and Peter J Kirkpatrick. Tissue oxygen index thresholds for cerebral ischemia using near-infrared spectroscopy. *Stroke*, 37(11):2720–2725, 2006.
- [6] TWL Scheeren, P Schober, and LA Schwarte. Monitoring tissue oxygenation by near infrared spectroscopy (nirs): background and current applications. *Journal of clinical monitoring and computing*, 26(4):279–287, 2012.
- [7] Santiago R Leal-Noval, Aurelio Cayuela, Victoria Arellano-Orden, Antonio Marín-Caballeros, Vicente Padilla, Carmen Ferrándiz-Millón, Yael Corcia, Claudio García-Alfaro, Rosario Amaya-Villar, and Francisco Murillo-Cabezas. Invasive and noninvasive assessment of cerebral oxygenation in patients with severe traumatic brain injury. *Intensive care medicine*, 36(8):1309–1317, 2010.

- [8] Arnab Ghosh, Clare Elwell, and Martin Smith. Cerebral near-infrared spectroscopy in adults: A work in progress. *Anesthesia & Analgesia*, 115(6):1373–1383, 2012.
- [9] Yoko Hoshi. Functional near-infrared optical imaging: Utility and limitations in human brain mapping. *Psychophysiology*, 40(4):511–520, 2003.
- [10] Frans F Jobsis. Noninvasive, infrared monitoring of cerebral and myocardial oxygen sufficiency and circulatory parameters. *Science*, 198(4323):1264–1267, 1977.
- [11] Thomas Muehlemann, Daniel Haensse, and Martin Wolf. Wireless miniaturized in-vivo near infrared imaging. *Optics express*, 16(14):10323–10330, 2008.
- [12] Etienne Lareau, Frederic Lesage, Philippe Pouliot, Dang Nguyen, Jerome Le Lan, and Mohamad Sawan. Multichannel wearable system dedicated for simultaneous electroencephalography/near-infrared spectroscopy real-time data acquisitions. *Journal of biomedical optics*, 16(9):096014–096014, 2011.
- [13] Stéphane Perrey. Non-invasive nir spectroscopy of human brain function during exercise. *Methods*, 45(4):289–299, 2008.
- [14] Hamid Dehghani, Brian W Pogue, Steven P Poplack, and Keith D Paulsen. Multi-wavelength three-dimensional near-infrared tomography of the breast: initial simulation, phantom, and clinical results. *Applied Optics*, 42(1):135–145, 2003.
- [15] Maxim Fradkin, Matthias C Hofmann, Jean-Michel Rouet, Richard H Moore, Daniel B Kopans, Keith Tipton, Sankar Suryanarayanan, David A Boas, and Qian-qian Fang. Diagnosing breast cancer using independent diffuse optical tomography and x-ray mammography scans. In *SPIE BiOS*, pages 85740G–85740G. International Society for Optics and Photonics, 2013.
- [16] Tao Zhang, Junli Zhou, Paul R Carney, and Huabei Jiang. Detecting epileptic seizures in awake rats with diffuse optical tomography. In *Biomedical Optics*, pages BT5B–4. Optical Society of America, 2014.
- [17] Jeremy C Hebden, Robert J Cooper, Adam Gibson, Nick Everdell, and Topun Austin. Simultaneous eeg and diffuse optical imaging of seizure-related hemodynamic activity in the newborn infant brain. In *SPIE Photonics Europe*, pages 84271N–84271N. International Society for Optics and Photonics, 2012.

- [18] Rami Nachabé, Benno HW Hendriks, Marjolein van der Voort, Adrien E Desjardins, and Henricus JCM Sterenborg. Estimation of biological chromophores using diffuse optical spectroscopy: benefit of extending the uv-vis wavelength range to include 1000 to 1600 nm. *Biomedical optics express*, 1(5):1432–1442, 2010.
- [19] Hamid Dehghani, Subhadra Srinivasan, Brian W Pogue, and Adam Gibson. Numerical modelling and image reconstruction in diffuse optical tomography. *Philosophical Transactions of the Royal Society A: Mathematical, Physical and Engineering Sciences*, 367(1900):3073–3093, 2009.
- [20] T Durduran, R Choe, WB Baker, and AG Yodh. Diffuse optics for tissue monitoring and tomography. *Reports on Progress in Physics*, 73(7):076701, 2010.
- [21] Marco Ferrari and Valentina Quaresima. A brief review on the history of human functional near-infrared spectroscopy (fnirs) development and fields of application. *Neuroimage*, 63(2):921–935, 2012.
- [22] David A Boas, Anders M Dale, and Maria Angela Franceschini. Diffuse optical imaging of brain activation: approaches to optimizing image sensitivity, resolution, and accuracy. *Neuroimage*, 23:S275–S288, 2004.
- [23] Richard B Buxton, Kâmil Uludağ, David J Dubowitz, and Thomas T Liu. Modeling the hemodynamic response to brain activation. *Neuroimage*, 23:S220–S233, 2004.
- [24] Adam Liebert, Piotr Sawosz, Daniel Milej, Michał Kacprzak, Wojciech Weigl, Marcin Botwicz, Joanna Mkaczewska, Katarzyna Fronczewska, Ewa Mayzner-Zawadzka, Leszek Krolicki, et al. Assessment of inflow and washout of indocyanine green in the adult human brain by monitoring of diffuse reflectance at large source-detector separation. *Journal of biomedical optics*, 16(4):046011–046011, 2011.
- [25] Saeid Zanganeh, Yan Xu, Carl V Hamby, Marina V Backer, Joseph M Backer, and Quing Zhu. Enhanced fluorescence diffuse optical tomography with indocyanine green-encapsulating liposomes targeted to receptors for vascular endothelial growth factor in tumor vasculature. *Journal of biomedical optics*, 18(12):126014–126014, 2013.
- [26] Sophie N Davie and Hilary P Grocott. Impact of extracranial contamination on regional cerebral oxygen saturation: a comparison of three cerebral oximetry technologies. *The Journal of the American Society of Anesthesiologists*, 116(4):834–840, 2012.

- [27] Timothy J Germon, AE Young, Alexander R Manara, and Richard J Nelson. Extracerebral absorption of near infrared light influences the detection of increased cerebral oxygenation monitored by near infrared spectroscopy. *Journal of Neurology, Neurosurgery & Psychiatry*, 58(4):477–479, 1995.
- [28] Hilary P Grocott and Sophie N Davie. Future uncertainties in the development of clinical cerebral oximetry. *Cerebral oxygenation in health and disease*, page 139, 2015.
- [29] Jennifer C Hirsch, John R Charpie, Richard G Ohye, and James G Gurney. Near infrared spectroscopy (nirs) should not be standard of care for postoperative management. In *Seminars in Thoracic and Cardiovascular Surgery: Pediatric Cardiac Surgery Annual*, volume 13, pages 51–54. Elsevier, 2010.
- [30] Angelos G Kolias, Mathew R Guilfoyle, Adel Helmy, Judith Allanson, and Peter J Hutchinson. Traumatic brain injury in adults. *Practical neurology*, pages practneurol–2012, 2013.
- [31] Jamshid Ghajar. Traumatic brain injury. *The Lancet*, 356(9233):923–929, 2000.
- [32] Hayden White and Bala Venkatesh. Traumatic brain injury. *Oxford Textbook of Neurocritical Care*, page 210, 2016.
- [33] Andrew IR Maas, Nino Stocchetti, and Ross Bullock. Moderate and severe traumatic brain injury in adults. *The Lancet Neurology*, 7(8):728–741, 2008.
- [34] Jeffrey J Fletcher, Karen Bergman, Paul A Blostein, and Andreas H Kramer. Fluid balance, complications, and brain tissue oxygen tension monitoring following severe traumatic brain injury. *Neurocritical care*, 13(1):47–56, 2010.
- [35] Marek Sykora, Marek Czosnyka, Xiuyun Liu, Joseph Donnelly, Nathalie Nasr, Jennifer Diedler, Francois Okoroafor, Peter Hutchinson, David Menon, and Peter Smielewski. Autonomic impairment in severe traumatic brain injury: a multimodal neuromonitoring study. *Critical care medicine*, 44(6):1173–1181, 2016.
- [36] Gillian S McHugh, Doortje C Engel, Isabella Butcher, Ewout W Steyerberg, Juan Lu, Nino Mushkudiani, Adrián V Hernández, Anthony Marmarou, Andrew IR Maas, and Gordon D Murray. Prognostic value of secondary insults in traumatic brain injury: results from the impact study. *Journal of neurotrauma*, 24(2):287–293, 2007.

- [37] Nino Stocchetti, Adriano Furlan, and Franco Volta. Hypoxemia and arterial hypotension at the accident scene in head injury. *Journal of Trauma and Acute Care Surgery*, 40(5):764–767, 1996.
- [38] Pradeep K Narotam, John F Morrison, and Narendra Nathoo. Brain tissue oxygen monitoring in traumatic brain injury and major trauma: outcome analysis of a brain tissue oxygen-directed therapy: Clinical article. *Journal of neurosurgery*, 111(4):672–682, 2009.
- [39] Randall M Chesnut, Nancy Temkin, Nancy Carney, Sureyya Dikmen, Carlos Rondina, Walter Videtta, Gustavo Petroni, Silvia Lujan, Jim Pridgeon, Jason Barber, et al. A trial of intracranial-pressure monitoring in traumatic brain injury. *New England Journal of Medicine*, 367(26):2471–2481, 2012.
- [40] Arash Farahvar, Linda M Gerber, Ya-Lin Chiu, Nancy Carney, Roger Härtl, and Jamshid Ghajar. Increased mortality in patients with severe traumatic brain injury treated without intracranial pressure monitoring: Clinical article. *Journal of neurosurgery*, 117(4):729–734, 2012.
- [41] Catherine Ract, Sophie Le Moigno, Nicolas Bruder, and Bernard Vigué. Transcranial doppler ultrasound goal-directed therapy for the early management of severe traumatic brain injury. *Intensive care medicine*, 33(4):645–651, 2007.
- [42] D Davies, M Clancy, Z Su, H Denghani, and A Belli. Choosing a cerebral near-infrared spectroscopy system for use in traumatic brain injury: deriving the ideal source detector layout. *Critical Care*, 18(Suppl 1):P468, 2014.
- [43] R Boushel, H Langberg, J Olesen, J Gonzales-Alonzo, J Bülow, and M Kjaer. Monitoring tissue oxygen availability with near infrared spectroscopy (nirs) in health and disease. *Scandinavian journal of medicine & science in sports*, 11(4):213–222, 2001.
- [44] KP Budohoski, C Zweifel, M Kasproicz, E Sorrentino, J Diedler, KM Brady, P Smielewski, DK Menon, JD Pickard, PJ Kirkpatrick, et al. What comes first? the dynamics of cerebral oxygenation and blood flow in response to changes in arterial pressure and intracranial pressure after head injury. *British journal of anaesthesia*, 108(1):89–99, 2012.
- [45] Ruwan Alwis Weerakkody, Marek Czosnyka, Christian Zweifel, Gianluca Castellani, Peter Smielewski, Ken Brady, John D Pickard, and Zofia Czosnyka. Near infrared spectroscopy as possible non-invasive monitor of slow vasogenic icp waves. In *Intracranial Pressure and Brain Monitoring XIV*, pages 181–185. Springer, 2012.

- [46] Claudia S Robertson, Eric L Zager, Raj K Narayan, Neal Handly, Alok Sharma, Daniel F Hanley, Homero Garza, Eileen Maloney-Wilensky, Justin M Plaum, Carolyn H Koenig, et al. Clinical evaluation of a portable near-infrared device for detection of traumatic intracranial hematomas. *Journal of neurotrauma*, 27(9):1597–1604, 2010.
- [47] M Thavasoathy, M Broadhead, C Elwell, M Peters, and M Smith. A comparison of cerebral oxygenation as measured by the niro 300 and the invos 5100 near-infrared spectrophotometers. *Anaesthesia*, 57(10):999–1006, 2002.
- [48] C Michael Dunham, Kenneth J Ransom, Laurie L Flowers, Joel D Siegal, and Chander M Kohli. Cerebral hypoxia in severely brain-injured patients is associated with admission glasgow coma scale score, computed tomographic severity, cerebral perfusion pressure, and survival. *Journal of Trauma and Acute Care Surgery*, 56(3):482–491, 2004.
- [49] Louis Gagnon, Meryem A Yücel, David A Boas, and Robert J Cooper. Further improvement in reducing superficial contamination in nirs using double short separation measurements. *Neuroimage*, 85:127–135, 2014.
- [50] Marco Ferrari, Leonardo Mottola, and Valentina Quaresima. Principles, techniques, and limitations of near infrared spectroscopy. *Canadian journal of applied physiology*, 29(4):463–487, 2004.
- [51] David J Davies, Zhangjie Su, Michael T Clancy, Samuel JE Lucas, Hamid Dehghani, Ann Logan, and Antonio Belli. Near-infrared spectroscopy in the monitoring of adult traumatic brain injury: a review. *Journal of neurotrauma*, 32(13):933–941, 2015.
- [52] B Kessel, I Jeroukhimov, I Ashkenazi, T Khashan, M Oren, J Haspel, M Medvedev, V Nesterenko, A Halevy, and R Alfici. Early detection of life-threatening intracranial haemorrhage using a portable near-infrared spectroscopy device. *Injury*, 38(9):1065–1068, 2007.
- [53] Quan Zhang, Hongyan Ma, Shoko Nioka, and Britton Chance. Study of near infrared technology for intracranial hematoma detection. *Journal of biomedical optics*, 5(2):206–213, 2000.
- [54] Daniel Lighter, Michael Clancy, David Davies, George M Balanos, Samuel J Lucas, and Hamid Dehghani. Assessing the quantitative accuracy of continuous wave and frequency domain near infrared spectroscopy for detecting hypoxia in patients with traumatic brain injury. In *Clinical and Translational Biophotonics*, pages JW3A–44. Optical Society of America, 2016.

- [55] Alessandro Torricelli, Davide Contini, Antonio Pifferi, Matteo Caffini, Rebecca Re, Lucia Zucchelli, and Lorenzo Spinelli. Time domain functional nirs imaging for human brain mapping. *Neuroimage*, 85:28–50, 2014.
- [56] Brian W Pogue, Steven P Poplack, Troy O McBride, Wendy A Wells, K Sunshine Osterman, Ulf L Osterberg, and Keith D Paulsen. Quantitative hemoglobin tomography with diffuse near-infrared spectroscopy: Pilot results in the breast 1. *Radiology*, 218(1):261–266, 2001.
- [57] Robert J Cooper, Matteo Caffini, Jay Dubb, Qianqian Fang, Anna Custo, Daisuke Tsuzuki, Bruce Fischl, William Wells, Ippeita Dan, and David A Boas. Validating atlas-guided dot: a comparison of diffuse optical tomography informed by atlas and subject-specific anatomies. *NeuroImage*, 62(3):1999–2006, 2012.
- [58] Xue Wu, Adam T Eggebrecht, Silvina L Ferradal, Joseph P Culver, and Hamid Dehghani. Quantitative evaluation of atlas-based high-density diffuse optical tomography for imaging of the human visual cortex. *Biomedical optics express*, 5(11):3882–3900, 2014.
- [59] Anna Custo, David A Boas, Daisuke Tsuzuki, Ippeita Dan, Rickson Mesquita, Bruce Fischl, W Eric L Grimson, and Williams Wells III. Anatomical atlas-guided diffuse optical tomography of brain activation. *Neuroimage*, 49(1):561–567, 2010.
- [60] David A Boas, Dana H Brooks, Eric L Miller, Charles A DiMarzio, Misha Kilmer, Richard J Gaudette, and Quan Zhang. Imaging the body with diffuse optical tomography. *IEEE signal processing magazine*, 18(6):57–75, 2001.
- [61] Martin Schweiger. Gpu-accelerated finite element method for modelling light transport in diffuse optical tomography. *Journal of Biomedical Imaging*, 2011:10, 2011.
- [62] Adam T Eggebrecht, Silvina L Ferradal, Amy Robichaux-Viehoever, Mahlega S Hassanpour, Hamid Dehghani, Abraham Z Snyder, Tamara Hershey, and Joseph P Culver. Mapping distributed brain function and networks with diffuse optical tomography. *Nature Photonics*, 2014.
- [63] Hamid Dehghani, Matthew E Eames, Phaneendra K Yalavarthy, Scott C Davis, Subhadra Srinivasan, Colin M Carpenter, Brian W Pogue, and Keith D Paulsen. Near infrared optical tomography using nirfast: Algorithm for numerical model and image reconstruction. *Communications in numerical methods in engineering*, 25(6):711–732, 2009.

- [64] Rami Nachabé, Daniel J Evers, Benno HW Hendriks, Gerald W Lucassen, Marjolein van der Voort, Jelle Wesseling, and Theo JM Ruers. Effect of bile absorption coefficients on the estimation of liver tissue optical properties and related implications in discriminating healthy and tumorous samples. *Biomedical optics express*, 2(3):600–614, 2011.
- [65] Lihong V Wang and Hsin-i Wu. *Biomedical optics: principles and imaging*. John Wiley & Sons, 2012.
- [66] Pierre Bouguer. *Traité d’optique sur la gradation de la lumière*. 1760.
- [67] Johann Heinrich Lambert. *Photometrie: Photometria, sive De mensura et gradibus luminis, colorum et umbrae (1760)*, volume 31. W. Engelmann, 1892.
- [68] August Beer. Bestimmung der absorption des rothen lichts in farbigen flüssigkeiten. *Annalen der Physik*, 162(5):78–88, 1852.
- [69] DT Delpy and M Cope. Quantification in tissue near-infrared spectroscopy. *Philosophical Transactions of the Royal Society of London. Series B: Biological Sciences*, 352(1354):649–659, 1997.
- [70] Gunnar Naulaers, Bart Meyns, Marc Miserez, Veerle Leunens, Sabine Van Huffel, Paul Casaer, Michael Weindling, and Hugo Devlieger. Use of tissue oxygenation index and fractional tissue oxygen extraction as non-invasive parameters for cerebral oxygenation. *Neonatology*, 92(2):120–126, 2007.
- [71] Michael Firbank. *The design, calibration and usage of a solid scattering and absorbing phantom for near infra red spectroscopy*. PhD thesis, University of London, 1994.
- [72] Andreas H Hielscher. Optical tomographic imaging of small animals. *Current opinion in biotechnology*, 16(1):79–88, 2005.
- [73] Judith R Mourant, Tamika Fuselier, James Boyer, Tamara M Johnson, and Irving J Bigio. Predictions and measurements of scattering and absorption over broad wavelength ranges in tissue phantoms. *Applied optics*, 36(4):949–957, 1997.
- [74] Xin Wang, Brian W Pogue, Shudong Jiang, Hamid Dehghani, Xiaomei Song, Subhadra Srinivasan, Ben A Brooksby, Keith D Paulsen, Christine Kogel, Steven P Poplack, et al. Image reconstruction of effective mie scattering parameters of

- breast tissue in vivo with near-infrared tomography. *Journal of biomedical optics*, 11(4):041106–041106, 2006.
- [75] Simon R Arridge, M Cope, and DT Delpy. The theoretical basis for the determination of optical pathlengths in tissue: temporal and frequency analysis. *Physics in medicine and biology*, 37(7):1531, 1992.
 - [76] Susumu Suzuki, Sumio Takasaki, Takeo Ozaki, and Yukio Kobayashi. Tissue oxygenation monitor using nir spatially resolved spectroscopy. In *BiOS'99 International Biomedical Optics Symposium*, pages 582–592. International Society for Optics and Photonics, 1999.
 - [77] Gary Strangman, David A Boas, and Jeffrey P Sutton. Non-invasive neuroimaging using near-infrared light. *Biological psychiatry*, 52(7):679–693, 2002.
 - [78] Scott C Bunce, Meltem Izzetoglu, Kurtulus Izzetoglu, Banu Onaral, and Kambiz Pourrezaei. Functional near-infrared spectroscopy. *Engineering in Medicine and Biology Magazine, IEEE*, 25(4):54–62, 2006.
 - [79] Davide Contini, Lucia Zucchelli, Lorenzo Spinelli, Matteo Caffini, Rebecca Re, Antonio Pifferi, Rinaldo Cubeddu, and Alessandro Torricelli. Review: Brain and muscle near infrared spectroscopy/imaging techniques. *Journal of Near Infrared Spectroscopy*, 20(1):15–27, 2012.
 - [80] Adelina Pellicer and María del Carmen Bravo. Near-infrared spectroscopy: a methodology-focused review. In *Seminars in Fetal and Neonatal Medicine*, volume 16, pages 42–49. Elsevier, 2011.
 - [81] Martin Wolf, Marco Ferrari, and Valentina Quaresima. Progress of near-infrared spectroscopy and topography for brain and muscle clinical applications. *Journal of biomedical optics*, 12(6):062104–062104, 2007.
 - [82] Brian W Pogue, Markus Testorf, Troy McBride, Ulf Osterberg, and Keith Paulsen. Instrumentation and design of a frequency-domain diffuse optical tomography imager for breast cancer detection. *Optics express*, 1(13):391–403, 1997.
 - [83] Juliette Selb, Jonathan J Stott, Maria Angela Franceschini, A Gregory Sorensen, and David A Boas. Improved sensitivity to cerebral hemodynamics during brain activation with a time-gated optical system: analytical model and experimental validation. *Journal of biomedical optics*, 10(1):011013–01101312, 2005.

- [84] Louis Gagnon, Claudine Gauthier, Rick D Hoge, Frédéric Lesage, Juliette Selb, and David A Boas. Double-layer estimation of intra-and extracerebral hemoglobin concentration with a time-resolved system. *Journal of biomedical optics*, 13(5):054019–054019, 2008.
- [85] Felix Scholkmann, Stefan Kleiser, Andreas Jaakko Metz, Raphael Zimmermann, Juan Mata Pavia, Ursula Wolf, and Martin Wolf. A review on continuous wave functional near-infrared spectroscopy and imaging instrumentation and methodology. *Neuroimage*, 85:6–27, 2014.
- [86] David A Boas, Constantinos Pitris, and Nimmi Ramanujam. *Handbook of biomedical optics*. CRC press, 2011.
- [87] Alistair M Howseman, Oliver Josephs, Geraint Rees, and Karl J Friston. Special issues in functional magnetic resonance imaging. *SPM course, short course notes*, 1997.
- [88] Brian R White and Joseph P Culver. Quantitative evaluation of high-density diffuse optical tomography: in vivo resolution and mapping performance. *Journal of biomedical optics*, 15(2):026006–026006, 2010.
- [89] NIRx Medical Technologies. Nirxport.
- [90] Fabrizio Martelli, Angelo Sassaroli, Yukio Yamada, and Giovanni Zaccanti. Analytical approximate solutions of the time-domain diffusion equation in layered slabs. *JOSA A*, 19(1):71–80, 2002.
- [91] Troy O McBride. *Spectroscopic reconstructed near infrared tomographic imaging for breast cancer diagnosis*. PhD thesis, Citeseer, 2001.
- [92] William H Press, SA Teukolsky, WT Vetterling, and BP Flannery. Numerical recipes in c. *Cambridge University Press*, 1:3, 1988.
- [93] Yuxuan Zhan. *Model-based high-density functional diffuse optical tomography of human brain*. PhD thesis, University of Birmingham, 2013.
- [94] David Boas, J Culver, J Stott, and A Dunn. Three dimensional monte carlo code for photon migration through complex heterogeneous media including the adult human head. *Optics express*, 10(3):159–170, 2002.

- [95] LH Wang and Steven L Jacques. Monte carlo modeling of light transport in multi-layered tissues in standard c. *The University of Texas, MD Anderson Cancer Center, Houston*, 1992.
- [96] Qianqian Fang and David A Boas. Monte carlo simulation of photon migration in 3d turbid media accelerated by graphics processing units. *Optics express*, 17(22):20178–20190, 2009.
- [97] Anton V Gorshkov and Mikhail Yu Kirillin. Acceleration of monte carlo simulation of photon migration in complex heterogeneous media using intel many-integrated core architecture. *Journal of Biomedical Optics*, 20(8):085002–085002, 2015.
- [98] Wenxiang Cong, Durairaj Kumar, Yi Liu, Alexander Cong, and GE Wang. A practical method to determine the light source distribution in bioluminescent imaging. In *Optical Science and Technology, the SPIE 49th Annual Meeting*, pages 679–686. International Society for Optics and Photonics, 2004.
- [99] SR Arridge, M Schweiger, M Hiraoka, and DT Delpy. A finite element approach for modeling photon transport in tissue. *Medical physics*, 20(2):299–309, 1993.
- [100] Qianqian Fang and David A Boas. Tetrahedral mesh generation from volumetric binary and grayscale images. In *2009 IEEE International Symposium on Biomedical Imaging: From Nano to Macro*, pages 1142–1145. IEEE, 2009.
- [101] H Dehghani and DT Delpy. Linear single-step image reconstruction in the presence of nonscattering regions. *JOSA A*, 19(6):1162–1171, 2002.
- [102] Chein-Shan Liu. A dynamical tikhonov regularization for solving ill-posed linear algebraic systems. *Acta applicandae mathematicae*, 123(1):285–307, 2013.
- [103] Roger Penrose. A generalized inverse for matrices. In *Mathematical proceedings of the Cambridge philosophical society*, volume 51, pages 406–413. Cambridge Univ Press, 1955.
- [104] Louis Gagnon, Robert J Cooper, Meryem A Yücel, Katherine L Perdue, Douglas N Greve, and David A Boas. Short separation channel location impacts the performance of short channel regression in nirs. *Neuroimage*, 59(3):2518–2528, 2012.
- [105] Nicholas M Gregg, Brian R White, Benjamin W Zeff, Andrew J Berger, and Joseph P Culver. Brain specificity of diffuse optical imaging: improvements from superficial signal regression and tomography. *Frontiers in neuroenergetics*, 2, 2010.

- [106] Xue Wu, Adam T Eggebrecht, Silvina L Ferradal, Joseph P Culver, and Hamid Dehghani. Fast and efficient image reconstruction for high density diffuse optical imaging of the human brain. *Biomedical optics express*, 6(11):4567–4584, 2015.
- [107] Theodore J Huppert, Solomon G Diamond, Maria A Franceschini, and David A Boas. Homer: a review of time-series analysis methods for near-infrared spectroscopy of the brain. *Applied optics*, 48(10):D280–D298, 2009.
- [108] Sinem B Erdougan, Meryem A Yukio Kobayashicel, and Ata Akin. Analysis of task-evoked systemic interference in fnirs measurements: Insights from fmri. *NeuroImage*, 87:490–504, 2014.
- [109] Blake G Perry, James D Cotter, Gaizka Mejuto, Toby Mündel, and Samuel JE Lucas. Cerebral hemodynamics during graded valsalva maneuvers. *Cerebral oxygenation in health and disease*, page 110, 2015.
- [110] John Mazziotta, Arthur Toga, Alan Evans, Peter Fox, Jack Lancaster, Karl Zilles, Roger Woods, Tomas Paus, Gregory Simpson, Bruce Pike, et al. A four-dimensional probabilistic atlas of the human brain. *Journal of the American Medical Informatics Association*, 8(5):401–430, 2001.
- [111] John Mazziotta, Arthur Toga, Alan Evans, Peter Fox, Jack Lancaster, Karl Zilles, Roger Woods, Tomas Paus, Gregory Simpson, Bruce Pike, et al. A probabilistic atlas and reference system for the human brain: International consortium for brain mapping (icbm). *Philosophical Transactions of the Royal Society of London B: Biological Sciences*, 356(1412):1293–1322, 2001.
- [112] Michael Jermyn, Hamid Ghadyani, Michael A Mastanduno, Wes Turner, Scott C Davis, Hamid Dehghani, and Brian W Pogue. Fast segmentation and high-quality three-dimensional volume mesh creation from medical images for diffuse optical tomography. *Journal of biomedical optics*, 18(8):086007–086007, 2013.
- [113] Hamid Dehghani, Brian R White, Benjamin W Zeff, Andrew Tizzard, and Joseph P Culver. Depth sensitivity and image reconstruction analysis of dense imaging arrays for mapping brain function with diffuse optical tomography. *Applied optics*, 48(10):D137–D143, 2009.
- [114] JP Culver, V Ntziachristos, MJ Holboke, and AG Yodh. Optimization of optode arrangements for diffuse optical tomography: A singular-value analysis. *Optics letters*, 26(10):701–703, 2001.

- [115] Yuxuan Zhan, Adam T Eggebrecht, Joseph P Culver, and Hamid Dehghani. Singular value decomposition based regularization prior to spectral mixing improves crosstalk in dynamic imaging using spectral diffuse optical tomography. *Biomedical optics express*, 3(9):2036–2049, 2012.
- [116] Phaneendra K Yalavarth, Hamid Dehghani, Brian W Pogue, and Keith D Paulsen. Critical computational aspects of near infrared circular tomographic imaging: Analysis of measurement number, mesh resolution and reconstruction basis. *Optics express*, 14(13):6113–6127, 2006.
- [117] Frank Pott, Johannes J Van Lieshout, Kojiro Ide, Per Madsen, and Niels H Secher. Middle cerebral artery blood velocity during a valsalva maneuver in the standing position. *Journal of Applied Physiology*, 88(5):1545–1550, 2000.
- [118] Blake G Perry, Toby Mündel, Darryl J Cochrane, James D Cotter, and Samuel JE Lucas. The cerebrovascular response to graded valsalva maneuvers while standing. *Physiological reports*, 2(2):e00233, 2014.
- [119] Frank P Tiecks, Colleen Douville, Sheila Byrd, Arthur M Lam, and David W Newell. Evaluation of impaired cerebral autoregulation by the valsalva maneuver. *Stroke*, 27(7):1177–1182, 1996.
- [120] Rong Zhang, Julie H Zuckerman, Kenichi Iwasaki, Thad E Wilson, Craig G Crandall, and Benjamin D Levine. Autonomic neural control of dynamic cerebral autoregulation in humans. *Circulation*, 106(14):1814–1820, 2002.
- [121] Pedro M Castro, Rosa Santos, João Freitas, Ronney B Panerai, and Elsa Azevedo. Autonomic dysfunction affects dynamic cerebral autoregulation during valsalva maneuver: comparison between healthy and autonomic dysfunction subjects. *Journal of Applied Physiology*, 117(3):205–213, 2014.
- [122] H Prabhakar, PK Bithal, A Suri, GP Rath, and HH Dash. Intracranial pressure changes during valsalva manoeuvre in patients undergoing a neuroendoscopic procedure. *min-Minimally Invasive Neurosurgery*, 50(02):98–101, 2007.
- [123] Walter E Judson, JD Hatcher, and ROBERT W WILKINS. Blood pressure responses to the valsalva maneuver in cardiac patients with and without congestive failure. *Circulation*, 11(6):889–899, 1955.

- [124] Manuel Ignacio Monge García, Anselmo Gil Cano, and Juan Carlos Díaz Monrové. Arterial pressure changes during the valsalva maneuver to predict fluid responsiveness in spontaneously breathing patients. *Intensive care medicine*, 35(1):77–84, 2009.
- [125] G Michael Felker, Phillip S Cuculich, and Mihai Gheorghiade. The valsalva maneuver: a bedside biomarker for heart failure. *The American journal of medicine*, 119(2):117–122, 2006.
- [126] Arenda HEA Van Beek, Jurgen AHR Claassen, Marcel GM Olde Rikkert, and René WMM Jansen. Cerebral autoregulation: an overview of current concepts and methodology with special focus on the elderly. *Journal of Cerebral Blood Flow & Metabolism*, 28(6):1071–1085, 2008.
- [127] G de J Lee, MB Matthews, and EP Sharpey-Schafer. The effect of the valsalva manoeuvre on the systemic and pulmonary arterial pressure in man. *British heart journal*, 16(3):311, 1954.
- [128] Mansour Razminia, Atul Trivedi, Janos Molnar, Monther Elbzour, Mayra Guerrero, Yasser Salem, Aziz Ahmed, Sandeep Khosla, and David L Lubell. Validation of a new formula for mean arterial pressure calculation: the new formula is superior to the standard formula. *Catheterization and cardiovascular interventions*, 63(4):419–425, 2004.
- [129] David Davies, Shaun Evans, Michael Clancy, Zhangjie Su, Peter Hansen, Hamid Dehghani, Antonio Belli, and Samuel Lucas. Comparison of near infrared spectroscopy with functional mri for detection of physiological changes in the brain independent of superficial tissue. *The Lancet*, 387:S34, 2016.
- [130] Zachary B Rodgers, Varsha Jain, Erin K Englund, Michael C Langham, and Felix W Wehrli. High temporal resolution mri quantification of global cerebral metabolic rate of oxygen consumption in response to apneic challenge. *Journal of Cerebral Blood Flow & Metabolism*, 33(10):1514–1522, 2013.
- [131] Karl J Friston. Statistical parametric mapping. In *Neuroscience Databases*, pages 237–250. Springer, 2003.
- [132] Silvina L Ferradal, Adam T Eggebrecht, Mahlega Hassanpour, Abraham Z Snyder, and Joseph P Culver. Atlas-based head modeling and spatial normalization for high-density diffuse optical tomography: in vivo validation against fmri. *Neuroimage*, 85:117–126, 2014.

- [133] Hamid Dehghani, Brian W Pogue, Jiang Shudong, Ben Brooksby, and Keith D Paulsen. Three-dimensional optical tomography: resolution in small-object imaging. *Applied Optics*, 42(16):3117–3128, 2003.
- [134] Scott C Davis, Hamid Dehghani, Jia Wang, Shudong Jiang, Brian W Pogue, and Keith D Paulsen. Image-guided diffuse optical fluorescence tomography implemented with laplacian-type regularization. *Optics express*, 15(7):4066–4082, 2007.
- [135] Matthew E Eames, Brian W Pogue, Phaneendra K Yalavarthy, and Hamid Dehghani. An efficient jacobian reduction method for diffuse optical image reconstruction. *Optics express*, 15(24):15908–15919, 2007.
- [136] Anna Blasi, Sarah Lloyd-Fox, Mark H Johnson, and Clare Elwell. Test–retest reliability of functional near infrared spectroscopy in infants. *Neurophotonics*, 1(2):025005–025005, 2014.
- [137] Kelly E Michaelsen, Venkataramanan Krishnaswamy, Linxi Shi, Srinivasan Vedantham, Steven P Poplack, Andrew Karellas, Brian W Pogue, and Keith D Paulsen. Calibration and optimization of 3d digital breast tomosynthesis guided near infrared spectral tomography. *Biomedical optics express*, 6(12):4981–4991, 2015.
- [138] David Boas, Thomas Gaudette, and Simon Arridge. Simultaneous imaging and optode calibration with diffuse optical tomography. *Optics express*, 8(5):263–270, 2001.
- [139] Michael Clancy, Antonio Belli, David Davies, Samuel JE Lucas, Zhangjie Su, and Hamid Dehghani. Comparison of neurological nirs signals during standing valsalva maneuvers, pre and post vasoconstrictor injection. In *European Conferences on Biomedical Optics*, pages 953817–953817. International Society for Optics and Photonics, 2015.
- [140] Michael Clancy, Antonio Belli, David Davies, Samuel JE Lucas, Zhangjie Su, and Hamid Dehghani. Monitoring the injured brain: registered, patient specific atlas models to improve accuracy of recovered brain saturation values. In *European Conferences on Biomedical Optics*, pages 95381C–95381C. International Society for Optics and Photonics, 2015.
- [141] Kelly Michaelsen, Venkat Krishnaswamy, Brian W Pogue, Steven P Poplack, and Keith D Paulsen. Near-infrared spectral tomography integrated with digital breast tomosynthesis: Effects of tissue scattering on optical data acquisition design. *Medical physics*, 39(7):4579–4587, 2012.

- [142] Steven L Jacques. Optical properties of biological tissues: a review. *Physics in medicine and biology*, 58(11):R37, 2013.
- [143] John Lilley. *Nuclear physics: principles and applications*. John Wiley & Sons, 2013.
- [144] Simon Hyttel-Sorensen, Trine Witzner Hessel, and Gorm Greisen. Peripheral tissue oximetry: comparing three commercial near-infrared spectroscopy oximeters on the forearm. *Journal of clinical monitoring and computing*, 28(2):149–155, 2014.
- [145] Troy James Cross, M van Beekvelt, Keren Constantini, and Surendran Sabapathy. Measurement of regional forearm muscle haemodynamics via the near-infrared spectroscopy venous occlusion technique: the impact of hand circulatory occlusion. *Physiological measurement*, 35(12):2563, 2014.
- [146] Neil B Hampson and Claude A Piantadosi. Near infrared monitoring of human skeletal muscle oxygenation during forearm ischemia. *Journal of Applied Physiology*, 64(6):2449–2457, 1988.
- [147] Arlene Duncan, Judith H Meek, Matthew Clemence, Clare E Elwell, Lidia Tyszczuk, Mark Cope, and D Delpy. Optical pathlength measurements on adult head, calf and forearm and the head of the newborn infant using phase resolved optical spectroscopy. *Physics in medicine and biology*, 40(2):295, 1995.